Optimal Planning and Resilient Operation of Microgrids with Renewable Energy Sources

By

MINGJIA YIN

A thesis submitted for the degree of
Doctor of Philosophy

School of Electronic & Electrical Engineering
Faculty of Engineering
UNIVERSITY OF LEEDS

MAY 2022

Abstract

Modern societies are highly dependent on electric power supply systems which are however becoming increasingly complex due to the exponential increase of load demand in the last decades. The increase of fossil fuel fired thermal power plants is no longer sustainable, not only because of the rising costs of non-renewable fuel sources, but more significantly the substantial increase of greenhouse gas (GHG) and pollutant emissions from the plants, which is detrimental to the sustainable development of mankind. Therefore, recent years have seen profound changes in both the electric power supply and demand sides along with the global effort to decarbonize the whole energy chain from top to tail. One of the most significant changes is the widespread adoption of distributed energy resources (DES). UK has set ambitious climate targets to reduce at least 68% GHG emissions by 2030 compared to 1990 levels and achieve net zero emissions by 2050 [1]. Researches have revealed the dispersion of small and medium scale generators fed from renewable sources is promising to fully take over the conventional fossil fuel based large power plants.

In this context, the concept of microgrid is proposed as a self-healing unit aiming at reducing the dependence on fuel consumption as well as improving the system resilience. Although research topics relating to centralized or decentralized control of power systems with significant penetration of renewable energy and energy storage have been investigated intensively in recent years, these isolated solutions with limited scope may potentially deteriorate existing system performance and request frequent changes of devices settings. In turn, a systematic study in this work will explore existing and potential microgrid technologies and opportunities in the electricity market by multiple optimization formulations and solving methodologies for the sustainable future. The purpose of the work presented in this thesis aims to justify the functionality of microgrids by adopting optimal energy planning and operation strategies for infrastructure investors, utilities and police makers. Within this context, this thesis has addressed the challenge of uncertainty from both renewable generation and loads into the microgrid planning.

NOMENCLATURE

Abbreviation

ALA	Advanced Lead-Acid
BD	Benders decomposition
BFS	Backward/Forward Sweep
BM	Balancing Mechanism
CC&G	Column and constraint generation
CERTS	Electric Reliability Technology Solutions
CHP	Combined Heat and Power
CMA-ES	Covariance Matrix Adaptation Evolution Strategy
CPP	Critical-Peak Pricing
D-FACTS	Distributed Flexible AC Transmission System
D-STATCOM	Distributed Static Synchronous Compensator
DAP	Day-ahead Pricing
DDARDGP	Data-driven adaptive robust distributed generation planning
DE	Differential Evolution
DES	Distributed Energy Resources
DG	Distributed Generation
DOE	Department of Energy
DP	Dynamic Programming
DPMM	Dirichlet process mixture model
DR	Demand Response
EPLEPR	ESS Planning with Low Energy Procurement Risks
ERCOT	Electric Reliability Council of Texas

ES	Evolution Strategy
ESS	Energy Storage System
GA	Genetic Algorithm
GHG	Greenhouse Gas
IEA	International Energy Agency
IPOP-CMA-ES	Increasing Population Size Covariance Matrix Adaptation Evolution Strategy
ISO	Independent System Operator
Li-ion	Lithium-ion
LP	Linear Programming
LR	Lagrangian Relaxation
LT	Lithium-titanate
MILP	Mixed-integer Linear Programming
MIP	Mixed-integer Programming
MPPT	Maximum power point tracking
MT	Microturbine
NG-ESO	National Grid ESO
O&M	Operation and Maintenance
OPF	Optimal Power Flow
PCC	Point of common coupling
PSO	Particle Swarm Optimization
PV	Photovoltaic
QP	Quadratic Programming
RES	Renewable Energy Source
RO	Robust optimization
ROCOF	Rate Of Change Of Frequency
RTO	Regional Transmission Organization
RTP	Real-time Pricing
SA	Simulated Annealing
SCADA	Supervisory Control and Data Acquisition

SO	Stochastic optimization
SOP	Soft Open Point
SUMP	Sustainable Urban Mobility Plan
SVC	Support vector clustering
TESS	Transportable Energy Storage System
TLBO	Teaching Learning Based Optimization
ToU	Time-of-Use
TSN	Time-space Network
UoS	Use Of System
URFC	Unitized Regenerative Fuel Cell
VPP	Virtual Power Plants
VRB	Vanadium Redox Flow Battery
WOA	whale optimization algorithm
WSM	Weighted Sum Model
XBID	Cross-border Intraday

Chapter 3 - Sets and Indices

i	Index for buses.
j	Index for types of a certain DG category.
l	Index for incremental number of a certain DG type.
t	Index for time period.
k	Index for basic uncertainty set.
$\mathbb{F}$	Binary feasible set for binary indicators $f_{i,j,l}^{mt,wt,pv}$.
$\mathbb{Y}$	Feasible set for continues variables $P_{i,t}^{mt,wt,pv}$, $Q_{i,t}^{mt,wt,pv}$, $P_{1,t}^{+,-}$, $P_{i,t}$,$Q_{i,t}$ and $V_{i,t}$.
$\mathbb{U}$	Uncertainty Set for wind power output $\omega_{i,j,l,t}^{wt}$, solar power output $\omega_{i,j,l,t}^{wt}$ and load demand $P_{i,t}^{c}$, $Q_{i,t}^{c}$. It is an union of T basic uncertainty sets $\mathbb{U}_k$.

Chapter 3 - Parameters for DDARDGP framework

$\alpha^{fc,emi}$	Fuel price and emission penalty price of MT (\$/kWh).
ρ^{c}	Price for selling electricity to customers (\$).

$\rho^{s,b}$	Selling price and purchasing price at which the electricity is traded from microgrid to the main grid ($).
σ	Emission factor of MT (kg/kWh).
τ	Minimum requirement for DG Capacity in microgrid for islanded operation.
$C^{mt,wt,pv}$	One discrete increment of capacity of MT, WT and PV (kW).
FF	Fill factor of solar cell.
I_{max}	Line current limit (kA).
$inv^{mt,wt,pv}$	Capital cost of MT,WT and PV ($/kW).
K_v/K_i	Voltage temperature coefficient ($V/^\circ C$) and current temperature coefficient ($A/^\circ C$).
$om^{mt,wt,pv}$	O&M cost of MT,WT and PV ($/kWh).
$pf_{min}^{mt,wt,pv}$	Lower limit of power factor of MT, WT and PV.
r_i/x_i	Resistance and reactance between bus i to bus $i+1$.
$s_{av,t}$	Average solar irradiance at time t (kW/m^2).
T_a	Ambient temperature of PV cells at time t ($^\circ C$).
T_c/T_{no}	Cell temperature and nominal operating temperature of cell ($^\circ C$).
$v_{av,t}$	Average wind speed (m/s) at time t.
$v_{ci}/v_{ci}/v_r$	Cut-in speed, cut-off speed and rated wind speed of WT (m/s).
V_{min}/V_{max}	Lower and upper limit of voltage (kV).
V_{MPP}/I_{MPP}	Voltage (V) and current (A) at maximum power point
V_{oc}/I_{sc}	Open-circuit voltage (V) and short circuit current (A).
$\mathbf{A},\mathbf{J}$	Parameter matrices for binary variables **f** in the DDARDGP framework
$\mathbf{B},\mathbf{G}$	Parameter matrices for continues variables **y** in the DDARDGP framework
$\mathbf{C},\mathbf{E},\mathbf{H}$	Parameter matrices for uncertain variables **u** in the DDARDGP framework
$\mathbf{m},\mathbf{n}$	Vectors of scalars in the DDARDGP framework

Chapter 3 - Variables for DDARDGP framework

$\omega_{i,j,l,t}^{mt,wt,pv}$	lth incremental active power generation from jth type of MT,WT and PV of bus i at time t, respectively.
C^{EMI}	Emission penalty cost of MT ($).
C^{FC}	Fuel cost of MT ($).
C^{INV}	Investment cost of all DG units($).
C^{OM}	O&M cost of all DG units ($).
C^{REV}	Total revenue by selling electricity to customers and the main grid ($).
$f_{i,j,l}^{mt,wt,pv}$	Binary indicators that represent whether the lth increment of jth type of MT,WT or PV is installed at bus i. 1 if installed, otherwise 0.
$P_{i,t}^{c}/Q_{i,t}^{c}$	Active/reactive load demand of bus i at time t.
$P_{1,t}^{+,-}$	Power surplus and deficiency of microgrid at time t.
$P_{i,t}/Q_{i,t}$	Active/reactive power flow from bus i to bus $i+1$ at time t.
$P_{i,t}^{mt,wt,pv}$	Total Active power generation from MT,WT and PV of bus i at time t.
$Q_{i,t}^{mt,wt,pv}$	Total Reactive power generation from MT,WT and PV of bus i at time t.
$V_{i,t}$	Voltage of bus i at time t.

Chapter 3 - Other symbols for data-driven uncertainty set

λ_k	Weight of kth mixture component of DPMM.
λ_{th}	Truncation threshold value of the weight.
$\mu_k, \kappa_k, \nu_k, \Psi_k$	Parameters of kth normal Wishart pior distribution.
$\mu_k', \kappa_k', \nu_k', \Psi_k'$	Parameters of kth normal Wishart posterior distribution.
$\overline{x_k}$	mean value of kth mixture component of DPMM.
ζ	Scaling factor to adjust the size of the basic uncertainty set.
a_k, b_k	Parameters of kth beta distribution.
n_k	Data size of kth mixture component of DPMM.

Chapter 4 - Sets and Indices

t	Index for hours.
d	Index for days.

i, j	Index for buses.
y	Index for years.
s	Index for ESS.
k	Index for scenarios.
$\mathbb{D}_i$	The set of downstream lines attached to bus i.
$\mathbb{K}$	The set of all scenarios.
$\mathbb{X}$	The set of first-stage variables $\mathbf{x}$.

Chapter 4 - Parameters for EPLEPR model

$\bar{\rho}^{DA}$	Average day-ahead electricity price ($/kWh).
β_{max}	Upper boundary index of electricity price.
β_{min}	Lower boundary index of electricity price.
$\Delta P_t^{NET\_DA}$	The adjustment amount of energy procurement in the day-ahead market (kW).
η_c	Charging efficiency (%).
η_d	Discharging efficiency (%).
γ_y	Net present value factor.
ρ_t^{DA}	Forecasted day-ahead electricity price ($/kWh).
ρ^{fr}	Average price of fast reserve service ($/kWh).
ρ_t^{buy}	Buy price of imbalance charges ($/kWh).
ρ_t^{sell}	Sell price of imbalance charges ($/kWh).
$\rho_{y,t}^{UoS}$	Electricity price to cover power losses ($/kWh).
DOD	Depth of discharge (DOD) of ESS (%).
dr	Annual discount rate (%).
inv_s^{ESS}	Capital cost of ESS ($/kWh).
om_s^{ESS}	O&M cost of ESS ($/kWh).
$P_t^{\prime NET\_DA}$	Final energy procurement in the day-ahead market (kW).
P_{max}^{ch}	The maximum charge power of ESS (kW).
$P_i^C, Q_{i,t}^C$	Active/reactive load demand at bus i (kW).
$P_t^{D\_DA}$	Forecasted day-ahead power consumption (kW).
$P_t^{D\_RT}$	Actual real-time power consumption (kW).

P_i^{DG}, Q_i^{DG}	Active/reactive power generations of distributed generators at bus i (kW).
$P_{max}^{dis\_fr}$	The maximum discharge power allocated for fast reserve service (kW).
P_{max}^{dis}	The maximum discharge power of ESS (kW).
$P_t^{G\_DA}$	Forecasted day-ahead power production (kW).
$P_t^{G\_RT}$	Actual real-time power production (kW).
$P_t^{NET\_DA}$	Forecasted day-ahead net load (kW).
$P_t^{NET\_RT}$	Actual real-time net load (kW).
$r_{l_{i\to j}}/x_{l_{i\to j}}$	Resistance and reactance between bus i to bus j.

Chapter 4 - Variables for EPLEPR model

$\mathbf{x}$	The first-stage variables including C_s^{ESS} and L_s^{ESS}.
$\mathbf{y}$	The second-stage variables including $E_{s,t}^{ESS}$ and D_s^{AR}.
C^{DA}	Cost of day-ahead energy procurement ($).
C_s^{ESS}	Energy capacity of ESS (kWh).
C^{IB}	Real-time imbalance charges ($).
C^{INV}	Investment cost of all ESSs ($).
C^{OM}	O&M cost of all ESSs ($).
C^{UoS}	Use of system (UoS) cost ($).
D_s^{AR}	Allowed depth of ESS for arbitrage in day-ahead market (%).
D_s^{FR}	Assigned depth of ESS for fast reserve service (%).
$E_{s,t}^{ESS}$	Energy stored in ESS (kWh).
$I_{l_{i\to j,y,t}}$	line current flowing from bus i to j (A).
L_s^{ESS}	Location of ESS (kWh).
LC_s^R	Remaining life cycles of ESS.
LC_S	life cycles of ESS.
P_t^{ch}	Power charged from the grid to ESS (kW).
P_t^{dis}	Power discharged from the grid to ESS (kW).
$P_{l_{d_i}}, Q_{l_{d_i}}$	Active and reactive power flowing from bus i.

$P_{l_{i\to j}}, Q_{l_{i\to j}}$	Active and reactive power flowing from bus i to bus j.
$P_{l_{u_i}}, Q_{l_{u_i}}$	Active and reactive power flowing to bus i.
R^{FR}	Revenues of fast reserve service (\$).
R^{RV}	Residual values of ESSs (\$).
SOC_t	State-of-charge (SOC) of ESS (%).
V_i	Voltage of bus i.

Chapter 4 - Other symbols for the fast IPOP CMA-ES algorithm

$\boldsymbol{\sigma}, \boldsymbol{p_\sigma}, \boldsymbol{p_c}, \mathbf{C}$	Dynamic parameters for the fast IPOP-CMA-ES algorithm.
$\boldsymbol{c_\sigma}, d_\sigma, \boldsymbol{c_c}, \boldsymbol{c_\mu}$	Static parameters for the fast IPOP-CMA-ES algorithm.
λ	Number of samples.
$\mathbf{m}$	Mean value vector.
w_h	Weight of the sample h.

Chapter 5 - Sets and Indices

b	Index for TESSs.
i	Index for buses.
k	Index for reconfiguration topologies.
l	Index for DG units.
t	Index for hours.
p, q	Index for stations.
$\mathbb{B}$	The Set of TESSs.
$\mathbb{E}$	The Set of braches.
$\mathbb{P}$	The Set of reconfiguration topologies.
$\mathbb{Q}$	The Set of arcs.
$\mathbb{Q}_p^+$	The Set of arcs starting from the station p.
$\mathbb{Q}_p^-$	The Set of arcs ending at station p.
$\mathbb{S}$	The Set of buses.
$\mathbb{T}$	The Set of hours.
$\mathbb{Y}$	The Set of all stations including real stations and virtual stations.
$\mathbb{Y}^+$	The Set of real stations.

Chapter 5 - Parameters

η_b^{ch}	Charging efficiency of TESS b (%).
η_b^{dis}	Discharging efficiency TESS b (%).
ρ_t^b	Sell price of the electricity from the main grid to the microgrid ($/kWh).
ρ^c	Sell price of the electricity to the customers of the microgrid ($/kWh).
ρ^{WC}	The price of wind curtailment ($/kWh).
$E_{b,t}^{TESS}$	Energy stored in TESS b at time interval t (kWh).
int_i	The unit interruption cost for the load at bus i ($/kWh).
$om^{DG,TESS}$	O&M cost of DG units and TESS ($/kWh).
$P_{i,t}^c/Q_{i,t}^c$	Active/reactive load demand of bus i at time t.
P_{max}^{ch}	The maximum charge power of TESS (kW).
$P_{max,l,t}^{DG}$	The maximum dispatched wind generation of WT l at time t (kW).
P_{max}^{dis}	The maximum discharge power of TESS (kW).
$pob_{b,t}$	Transport cost of TESS b per unit of time ($).
S_i^{SOP}, Q_i^{SOP}	Rating power of the SOP connecting bus i (kVA).
$SOC_{b,t}$	State-of-charge (SOC) of TESS b at time interval t (%).

Chapter 5 - Variables

$\delta_{b,p,t}$	Binary variable indicates the position of TESS b at time interval t. It is 1 if TESS b locates at station p at time interval t.
$\gamma_{b,(p,q),t}$	Binary variable indicates the state of TESS b at time interval t. (p,q) represents the transit arc/park arc. It is 1 if TESS transits from station p to station q. If p is the same as q, the TESS stays at the station p.
$\varphi_{b,t}^{ch}, \varphi_{b,t}^{dis}$	Binary variable indicates the charging/discharging state of TESS b at time interval t.
C^{INT}	Interruption cost of the unserved loads ($).
C^{OM}	O&M cost of all DG units and TESSs ($).
C^{POS}	Repositioning cost of TESS ($).

C^{WC}	Wind curtailment cost ($).
$P^{c}_{i,t}/Q^{c}_{i,t}$	Active/reactive restored load demand of bus i at time t.
$P^{ch}_{b,p,t}$	Power charged from the grid to TESS b in the station p at time interval t (kW).
P^{DG}_{l}, Q^{DG}_{l}	Actual active and reactive dispatched generation of WT l at time t (kW).
$P^{dis}_{b,p,t}$	Power discharged from the grid to TESS b in the station p at time interval t (kW).
$P_{(i,j),t}, Q_{(i,j),t}$	Active and reactive power flowing from bus i to bus j.
P^{SOP}_{i}, Q^{SOP}_{i}	Active and reactive power of the SOP entering bus i (kW).
R^{REV}	Total revenues that are achieved by selling the electricity its customers at price ρ^{c} ($/$kWh$) and profits through the energy transactions with the main grid ($).
V_i	Voltage of bus i.

ACKNOWLEDGEMENTS

It has been an extraordinary experience for me in the last four years. Words cannot express my grateful to those who have offered me encouragement and support during the course of my study.

First and foremost I would like to thank my supervisor, Professor Kang LI, who always instruct with patience and share with selflessness. Without his continuous suggestions and guidance, I can not make it this far. Far beyond academic support, I would like to thank him for creating a warm scientific team in which I feel welcomed and know where to turn to for help.

I would also like to thank my friends and colleges for their kindness and company. Although most of the time since last year I have to work from home, I still have many precious memories in the office.

Finally, I would especially like to thank my family for supporting and encouraging me throughout this endeavour. Without them this would not have been possible.

Declaration

I declare that the work in this dissertation was carried out in accordance with the requirements of the University's Regulations and Code of Practice for Research Degree Programmes and that it has not been submitted for any other academic award. Except where indicated by specific reference in the text, the work is the candidate's own work. Work done in collaboration with, or with the assistance of, others, is indicated as such. Any views expressed in the dissertation are those of the author.

TABLE OF CONTENTS

List of Tables

List of Figures

Figure **Page**

CHAPTER 1

INTRODUCTION

The highly interconnected power systems are among the largest and most complex networks built by mankind. They have been operated under a high degree of reliability for over a century since 1882 when the first power plant - Pearl Street Station - was opened by Thomas Edison in New York city. After more than one hundred years of development, the annual worldwide electricity consumption has grown from an initial 400 lamps (approximately 6,000 kWh) to 23,398 billion kWh in 2018 [6]. Although there was an about 1% reduction in global demands of 2020 due to the impacts of the Covid-19 pandemics, a strong recovery of more than 6% boost has been seen in 2021 based on the latest Electricity Market Report published by the International Energy Agency (IEA) in Jan, 2022 [7]. To meet the exponential growth of the power consumption due to global trends of urbanization and industrialization as well as recent decarbonization commitments, the mature power grid features long-distance high voltage transmission lines and gigawatt-scale generation units which traditionally rely on carbon-based fossil fuels as the primary energy resources. As a result, the operation of power systems is relentlessly pressured by the exponential complexity of network interlinks.

Conventionally, the electricity grid is recognized as a complex "macrogrid" which connects all power plants, the infrastructures such as wires and transformers, and

the consumers. In the recent decade, a paradigm shift from centralized "macrogrid" to decentralized microgrids draws people's attention. Although there is no universal definition of the concept, a broadly cited explanation from the US Department of Energy (DOE) defines an microgrid as "a group of interconnected loads and distributed energy resources (DER) within clearly defined electrical boundaries that acts as a single controllable entity with respect to the grid. A microgrid can connect and disconnect from the grid to enable it to operate in both grid-connected or island mode [8]." Although the self-contained operation method seems like a "retro" of the Edison's Pearl Street Station that has been in parts of the industry for many years, politicians in charge didn't realize its importance until the most destructive catastrophe - Hurricane Sandy - in 2002, during which more than 130 people were killed, and over 7 millions people in the Northeast of the US lost electrical power for many weeks. Fortunately, despite the extreme devastation, microgrids or distributed generation (DG) of some buildings kept lights on, which inspires the DOE to introduce microgrids as "plug-and-play" components to improve the power reliability and security as well as the robustness of flexibility of grid operations. Meanwhile, a demonstration project in Japan, namely Sendai Microgrid shows extraordinary achievements on continuing to provide power for customers during 311 Great East Earthquake and Tsunami of 2011 [9].

In Europe, environmental and economic concerns are main drivers for microgirds. According to the statistic data from IEA, fossil fuel accounted for 79.676 % of total energy consumption globally in 2015 [10], resulting in the serious problem of greenhouse gas (GHG) emissions. In 2015, more than 170 nations passed the Paris agreement, focusing on strengthening the consensus of climate change on the 2030 Agenda [11]. It requires a significant commitment on innovation in utilizing alternative energy supply sources - renewable energy sources (RESs) - that naturally replenish themselves without being depleted in the earth. The most common ones include hydro power, wind power, solar energy, geothermal energy and bio energy. UK saw the share of electricity generated from renewable sources increase up to 37.3% in Quarter 2 of 2021. Offshore and onshore wind is the biggest source of renewable energy in the UK [12]. The geographical dispersion

nature of wind resources as well as other RESs, such as solar and hydro power makes the microgrid an economically efficient option to integrate thousands or even millions of RESs due to advantages such as reductions in the power loss. Similar motivations are found in China. As the world's second-largest economy, China has long relied on fossil fuels for almost of its energy mix — much of it generated from high-polluting coals. Since 2011, national investments on the microgrid technology are adopted as parts of its 12th Five Year Plan to reduce the reliance on centralized coal power plants [13].

Today, over 1 billion people in developing and underdeveloped regions and countries still lack of adequate electricity infrastructures to meet their essential needs. The microgrid provides a great opportunity for people living in remote communities such as mountainous areas with good hydro power or small islands with strong solar power, rather than to import expensive diesel fuels from outside.

In this chapter, the background of microgrids will be first introduced. Then, an overview of research challenges will be presented. Finally, the research scope and contributions of the thesis will be discussed.

1.1 Background: Representative Microgrid Projects and Their Developments

According to the recent report of Guidehouse Insights [2], the total global microgrid capacity surges from 3.5 GW, totaling a $ 8.1 billion market in 2009 to 23.6 GW in the 3rd quarter of 2021 with an estimated market opportunity of $ 24.6 billion.

As shown in Figure 1.1, Asian Pacific takes the largest share, accounting for 39.6% of microgrid installation in 2021. The domination position comes from several reasons. Large populations in the region lack of stable electricity supply, which include communities in India, Australia, South Korea, Vietnam and many other southeastern Asia countries. Remote microgrid systems serve the customers who would otherwise never gain access to traditional utility grids. China has become a force to be reckoned with due to an initiative for market-oriented DG installation in response to power sector reform

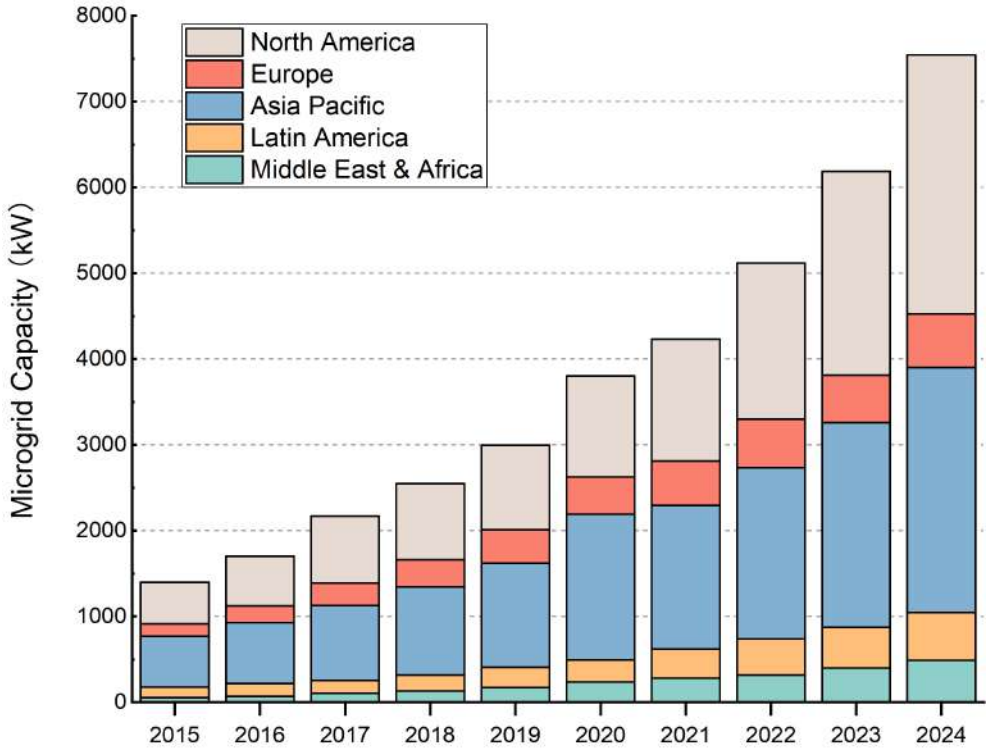

Figure 1.1: Annual total microgrid capacity by region: 2015-2024 [2]

since 2017. Japan, as a leading country in DG research and innovation mainly focuses on grid-connected projects and new technologies for resilient operation such as virtual power plants (VPP).

The North America, especially relying on contributions from the US, takes the second leading position with around 33.55% of worldwide microgrid demonstrations in 2021 and is expected to take the first place by the end of 2024. A comprehensive insight into microgrid projects in the US is shown in Figure 1.2 (Source: US DOE [14]). The prosperity and thriving developments of microgrid are inseparable from federal, state and local supports [3]. Noticeably, although the other regions including Europe, Latin America and Middle East & Africa are not historically leading the innovation in microgrids, the rapid expansion in these areas should not been ignored.

It is very difficult to trace exactly when and where microgrids started, it is believed that systematical analysis and research began with the Consortium for Electric Reliability Technology Solutions (CERTS) in the US in 1999. In the white paper "The CERTS

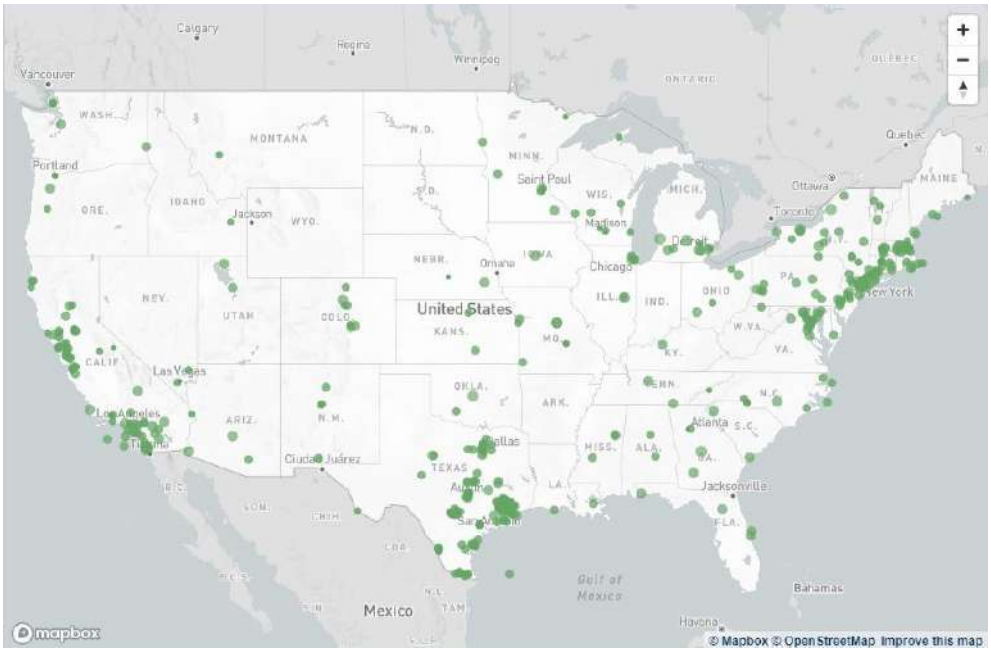

Figure 1.2: The microgrid installation map in the US [3]

MicroGrid Concept" [15], microgrid concept in terms of technologies, structure, control methods, protective relaying and economics is firstly declared as a significant potential in integrating DERs. Six initiatives sharing the common benefits of microgrids are presented by Table 1.1. The technical trends exhibited underneath these demonstration projects are fallen into following aspects:

- The primary goal of a test-bed system is the implementation of advanced technologies, including but not limited to new generation and storage methods, novel power-electronic devices, and planning, analysis & operation tools.

- The promotion of microgrid helps the transition from federal programs to utilities to private investors, ranging from tax incentives, financial subsidies and communities' awareness of cost saving. Microgrid is possible to be a game changer in deregulated electricity market.

- In response to contingency such as power outages, the reliability of isolated operation must be enhanced accordingly. Meanwhile, islanded-to-grid-connected switching control strategies are also evolving.

- The interaction with smart grid technology is important, which makes the microgrid more efficient and reliable to support existing centralized main grids, such as deferral of transmission and distribution upgrade, voltage/VAR control, ancillary services and power quality improvement.

1.2 Challenges: Uncertainties, Complexity and Resilience

With the development of the microgrid, there are emerging challenges to address. In the following section, several predominant characteristics which distinguish the operation of microgrid from conventional power grid will be presented.

Uncertainties - In the power system, uncertainties refer to those factors introducing imbalances in real-time operation. Prevailing uncertainties fall into two groups: the normal operation uncertainties and the contingency-based uncertainties [16]. Uncertainties such as forecast errors of solar power, wind power, load and market prices belong to the normal operation uncertainties.

Great efforts have been made in the research of load profile and weather forecast based on which the economical and reliable operation takes place [17, 18]. However, one remarkable characteristic of RES is the intermittent nature. It is hard to accurately predict the power production over specific time scales, especially for long terms [19]. High penetration of RES in microgrids requires the capability of quick response to stochastic power integration. Similarly, usage patterns have been altered significantly with the electrification of transport systems, including electrical vehicles and electrified railways. When large scale of such loads are connected to the microgrid, the load profiles will fluctuate dramatically. Failure to foreseen these changes leads to an unsuccessful configuration design. A classical example is the “duck curve” problems in California, US. Unchartered expansion of solar power plants due to the increasingly generous subsides in the area results in a dramatic drop of the net load in the mid-day. A steep rise in the

Table 1.1: Summary of representative microgrid demonstrations

Project name	Case Study	Country	Year	Capacity	Technologies	Fund	Characteristics
-	Sendai Microgrid	Japan	2004	>1MW	Gas engines (2*350 kW), PV (50 kW), phosphoric acid fuel cell (200 kW)	NEDO	Demo of experimental study of multi-power quality supply system; continue supply power after earthquake
FP6	Kythnos Microgrid	Greece	2006	<100kW	PV (11 kW), lead-acid battery bank (1,000 Ah/48V & 480 Ah/60V), diesel generator (9 kW)	National Technical University of Athens, CRES, SMA, ISET	First microgrid in Europe mostly supplied by 100% renewable generation; advanced control strategies
-	Wallstadt microgrid	Germany	2006	<100kW	Fuel cell (4.7kW), PV (23.5kW), flywheel storage unit (1.2kW), CHP (14.5kW)	MVV Energie	Demo of residential test system including islanding; develop by utility company; assess consumer attitudes
RDSI	Illinois Institute of Technology Microgrid	US	2008	12MW	Gas turbines (8 MW), PV (1.4 MW), wind turbine (8 kW), diesel generator (4 MW),Flow battery (500 kWh)	IIT, DOE, and other partners	First self-healing and efficient smart microgrid; enhanced reliability; sustainable energy sources; smart automation technology; advanced metering infrastructure
CERTS, RDSI	Santa Rita jail	US	2012	4MW	PV (1.2 MW), diesel generation (2.4 MW), molten carbonate, fuel cell (1 MW), Li-ion battery (2 MW/4 MWh)	Alameda Country, DOE	Demo of multiple DERs integration; seamlessly islanding operation; peak demand reduction; high reliability;
BMG	Brooklyn Microgrid	US	2016	-	-	LO3 Energy	Demo of community-driven microgrid; peer-to-peer energy transactions; reducing customer costs; new business models

ramp rate of dispatchable generation units is needed to fully support the utilization of solar energy [20]. However, inadequate power generation and limited energy storage lead to occasional negative market prices in the region.

Another emerging uncertainty associates with environmental and operational failures. Random component failures and weather-related incidents need rescheduling or reconfiguration to withstand severe disturbances. With the implementation of microgrid, several autonomous regions can disconnect from the main grid and operate properly in islanded mode. The seamless transition between grid-connected and islanded modes require a sophisticated control scheme to guarantee the transient stability. So far, little has been done in investigating the reliability and performance indicators which are essential to evaluate the impacts of different levels of uncertain events [21].

Complexity - The complexity of the microgrid arises from the planning and operation of the system. It requires smart grid technology to advance the monitor and control of the microgrid. A smart grid features advanced metering infrastructures such as smart meters and phasor measurement units, new communication technologies and smart circuit breakers e.g. load control switches and smart appliances, which facilitates the connection of critical components and raises people's awareness of real-time operational states. On account of sustainable innovations on DG, energy storage devices, supervisory control and data acquisition (SCADA) , weather forecasting, etc., huge amount of data are generated, driving the power system towards the big data era. Attractive applications using smart grid technologies involve asset management, renewable energy prediction, demand forecasting, customer service analysis, peer-to-peer energy transactions, fault diagnosis and decision-making support [22].

Tradition data processing and computational methods are not sufficient enough to analyze the heterogeneous petabytes level data in areas such as renewable energy integration, real-time operation monitoring and data backup and recovery after catastrophic damage. The complexity increases not only with the size but also with the format and structure. IBM proposed a micro-siting solution to wind farm location selection based

on four massive environmental streaming data [23]. The project reveals the need of high-precision models and high efficient parallel processing for long-term revenues based on big data.

Resilience - The resilience of the power grid refers to the ability to recover from or withstand the high-impact low frequency events. To maintain a high power quality operation on account of economic and environmental influences to meet the challenges arisen from climate change and ever-increasing power demands and DG installation, the following fundamental requirements need to be satisfied [24] :

- The system must match power production to consumption (including load and transmission loss), both of which vary drastically over time. Failure to meet the balance may lead to poor power quality and significant security issues such as blackout. Therefore, adequate capacity should be reserved and capable of response within the planned time when needed.

- The system should operate at the least economic costs and with minimum environmental influences.

- The power quality of the system should meet the standards regarding the constancy of frequency, voltage and the level of reliability.

However, the ever-increasing power demands and DG installation might pose new challenges, such as unexpected transmission congestion, protection coordination issues and voltage control problem. To solve them, the energy management system plays an important role in the operation of a power electronics based microgrid. The computer-aided tools are used to control and optimize the performance of the whole system. When an unexpected event is detected, the energy management system either automatically adjusts the system to normal conditions or helps the operators make decisions with minimum loss.

1.3 Research Motivations and Contributions

Along with the remarkable political pressure and public awareness of emission control, microgrid development has evolved from initial prototype demonstration and pilot projects to current commercial projects. The study of microgrid incorporates multidisciplinary approaches. This research aims to provide an optimal strategies for the planning and operation of the microgrid system by considering latest technologies that has not been fully analysed.

The main contributions of this work can be summarized as follows:

- A novel data-driven approach for DG planning considering both grid-connected and islanded modes of microgrids is introduced. The proposed framework is appealing to system planner that it makes good use of spatio-temporal data of historical weather and grid information based on Bayesian nonparametric method. Compared with existing work, the total cost of the utility is decreased while the microgrid is capable to accommodate more renewable energy.

- A multi-objective stochastic two-stage stochastic energy storage system (ESS) planning. The proposed model integrates energy procurement risk into the optimal sizing and sitting problem , which emphasizes on the economic potential of ESS in day-ahead and balancing market. A novel algorithm fast IPOP-CMA-ES is proposed and proven to be suitable for the non-convex optimization problem with fast convergence rate and superior performance in find the optimum.

- A joint scheme of resilient operation and post-disaster restoration of a microgrid is formulated. The system under study include one transportable energy storage system (TESS) and a novel power electronic device, namely soft open point (SOP) with active and reactive power flow capabilities. Simulation results reveal the improvement of the system resilience and load restoration rate due to the mobility of TESS and suitable network topology reconfiguration. Besides, there is a significant reduction on power losses with the integration of SOP.

The following is the list of my publication of journals and conference papers on the field:

Journal

1. M. Yin, K. Li, and Y. James, "A data-driven approach for microgrid distributed generation planning under uncertainties," *Applied energy*, in press

2. M. Yin, K. Li, and X. Cheng, "A review on artificial intelligence in high-speed rail," *Transportation Safety and Environment*, vol. 2, no. 4, pp. 247–259, 2020

3. Y. Li, K. Li, M. Yin, and X. Cheng, "Advances in fault diagnosis for high-speed railway: A review," in *2019 6th International Conference on Frontiers of Industrial Engineering (ICFIE)*. IEEE, 2019, pp. 67–72

4. H. Zhang, D. Yue, W. Yue, K. Li, and M. Yin, "Moea/d-based probabilistic pbi approach for risk-based optimal operation of hybrid energy system with intermittent power uncertainty," *IEEE Transactions on Systems, Man, and Cybernetics: Systems*, 2019

Conference Paper

1. M. Yin and K. Li, "Optimal allocation of distributed generations with sop in distribution systems," in *2020 IEEE Power & Energy Society General Meeting (PESGM)*. IEEE, 2020, pp. 1–5

2. M. Yin, K. Li, and M. Zheng, "Spectrum utilization of cognitive radio in industrial wireless sensor networks-a review," *Intelligent Computing and Internet of Things*, pp. 419–428, 2018

1.4 Thesis Structure

The thesis is organised in six chapters. The layout follows the Preparation-Plan-Operation-Discussion-Feedback order as shown in Figure 1.3.

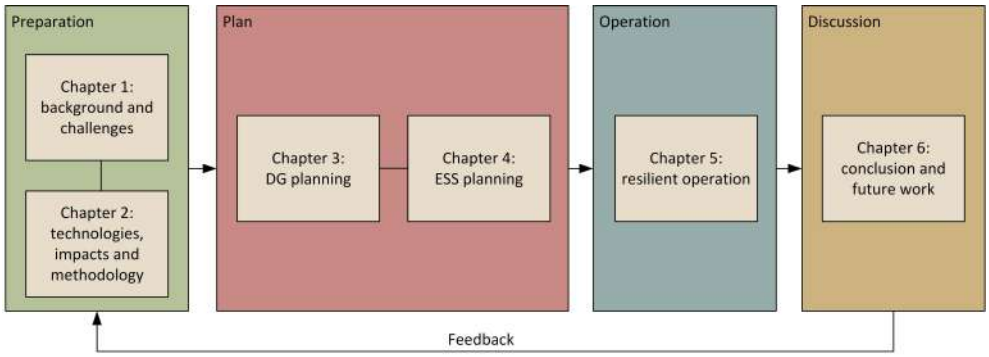

Figure 1.3: The correlation of chapters

- **Preparation**: Chapter 1 briefly introduces the background of microgrid development, followed with a discussion of challenges and issues on uncertainties, smart grid and energy management from top to tail. An overview of microgrid planning and scheduling is provided in Chapter 2 which include the comparisons of various microgrid technologies, impacts and state-of-art optimization methods.

- **Plan:** Following the preparation stage of literature review, Chapter 3 and 4 constitute the planning stage. In Chapter 3, an optimal solution of sizing, sitting and mix of DG are determined when considering investment cost, operation and maintenance (O&M) cost, fuel cost, emission penalty cost, and system revenue from energy transactions. The obtained DG configuration in Chapter 3 is used in Chapter 4 which solve a ESS planning problem associated with energy procurement risks.

- **Operation:** In Chapter 5, three case studies are carried out to evaluate the microgrid planning proposed in Chapter 3 and 4 based on a joint resilient operation and post-disaster restoration scheme.

- **Conclusion and Discussion** Chapter 6 concludes the thesis, which summarises the existing work. Reflections and suggestions for future work are presented.

CHAPTER 2

LITERATURE REVIEW: AN OVERVIEW OF MICROGRID PLANNING AND SCHEDULING

The evolutionary transition towards microgrids is driven by a range of distributed energy resources (DERs). The emergence of smaller generating units has reconstructed the way of energy utilization. For instance, small-scale natural gas power generation is appealing to some regions in the US because of lower natural gas costs than electricity. In addition, some traditional engines can still remain competitiveness for the roles to play in microgrids with suitable power electronics. In this section, some examples of technologies used in microgrids will be outlined first, followed by an review of influencing factors and methodologies.

2.1 Microgrid Technologies

2.1.1 Generation Technologies

In context of a micrigrid, the generation refers particularly to those small-scale energy supplies which are placed near the consumption sites, in contrast to large-scale centralized power plants.

Diesel generator A diesel generator is a combination of an internal combustion engine and an electric generator that converts chemical energy of fuel to mechanical energy and then to electricity. It is widely adopted in the early research of microgrid due to the highest thermal efficiency of among all practical internal or external combustion engines [31–33]. Coupling with a synchronous generation, a diesel engine is capable to interface with loads. The general efficiency value for converting fuel to electricity of diesel generator is 38% to 44% [34]. It is popular for combined heat and power (CHP) applications with the advantages of quick startup and dispatchable characteristic. However, the most significant drawback of this type of technology is nitrogen oxide emissions and GHG emissions. In [31], a case study of using diesel generator as DER for UW Micrgrid is introduced, which aims at developing a modeling and control framework to coordinate with other inverted-based sources. A control scheme was first proposed in [32] for a seamless switch from grid-connected mode to islanded mode for a PV-Diesel microgrid. The structure realizes the maximum power points tracking of PV at any setting power of the diesel genset. A sizing model of the diesel genset in a Wind-Diesel microgrid was proposed in [33] to improve the wind penetration and diesel fuel consumption and efficiency. The model is validated with two years of observed data from a remote community in Canada.

Microturbine Microturbine (MT) is an alternative option of dispatchable generation units that suits the CHP application. The tiny gas turbines are driven by the flow of gas that outputs power varing from 25 kW to 250 kW [35]. The efficiency of MT generation is about 17% to 22% [34]. Despite its mechanical simplicity, the integration of MTs with grid relies on power electronics which will be discussed separately in the following section. Compared with diesel generators, MTs are more environmentally-friendly with lower GHG emissions as the natural gas is the primary source. However, they are still not be categorised as clean generation. The study of Sendai Microgrid validates a 14%- 30% energy cost reduction, a 23% and 42% equipment space saving and 12% GHG emission cut owing to the integration of MTs and other RESs [36]. A dynamic

model was proposed by Huang et. al. [37] to design the coordinated control strategy of the MT and power electronic system. Simulations on an experimental prototype of microgrid indicate that the proposed mathematical model can efficiently implement the set points of real and reactive power in both normal operation and perturbed run such as a sudden load change or voltage drop. In [38], MTs are considered to act as the mollifier to flatten the load profiles of the microgird based on a market/regulatory structure. A hourly scheduling plan was formulated and a supervision framework at the minute time scale was developed based on economic model predictive control. The proposed hierarchical approach was investigated in an office building in Minneapolis, US, serving as a microgrid and shows its effectiveness of operating cost reduction and intelligent decision making at the scheduling time scale.

Renewable generation Renewable generation technologies especially photovoltaic (PV) cells and wind turbines (WTs) are one of the primary drivers of microgrids, which have been extensively studied. The energy efficiency of PV and WT is 15%-20% and 20% to 40%, respectively [34, 39]. Renewable generation is superior with respect to GHG emissions and fuel costs. In other words, the operation cost of this types of generation is near zero once installed. Although the integration of power electronics facilitates a limited capability of power adjustment, renewable generation without storage are regarded as non-dispatchable units. In [40], high penetration of wind power has been investigated in the weak Electric Reliability Council of Texas (ERCOT) grid. Voltage stability issues such as voltage oscillations and overvoltage were observed, which would affect the power quality of their customers. A study of the microgrid in the University of California, US explains how tariff structure will affect the operation strategies and renewable integration [41]. It also brings an insight into the "missing money" problem which refers to the situation that low electricity prices in wholesale electricity market or ancillary service contracts are not adequate to cover the capital expenditure or stimulate the investment of renewable energies. Protection and control scheme have been studied for a residential community with considerable PV panels installed [42]. The microgrid

implemented the operation and protection in islaneded mode and bi-directional power flow in grid-connected mode. Solar uncertainty and variability based on forecast data have been modeled at the 5-min time scale in [43] to demonstrate the reliability and cost-efficiency of the microgrid. In [44], the issues of wind and solar curtailment were reviewed across eleven countries. The problem was caused by the mismatch between power generation and consumption. The curtailment levels ranged from 1-3% of wind generation in most regions covering up to 10% of China, Italy and the US. Energy management of the microgrid with renewable penetration is therefore always related to storage systems.

2.1.2 Energy Storage Technologies

The strict real-time power balance constraint between production and consumption makes electricity a unique commodity in the market. The grid-scale energy storage does not come into view until the large-scale integration of renewable generation. The growing interest and popularity of energy storage are also found in the microgrid applications. As one of the fastest growing DERs, energy storage is capable for load shifting, peak shaving, load following, black start, energy arbitrage, frequency regulation and voltage support. There are numerous types of energy storage available and a classification based on principles is presented in Figure 2.1. In this section, several popular energy storage technologies used for microgrid applications are introduced.

Fuel Cell & Electrolyzer A fuel cell converts the chemical energy of fuel into electricity by means of continuous chemical reaction of fuel and oxidant. Individual fuel cells are "stacked" or connected in series and are capable to produce hundreds of kW power [45]. Compared with the dispatchable generation units described above, fuel cell is an emerging generation technology with 100% theoretical maximum efficiency. Unitized regenerative fuel cell (URFC) stack technology which implements a forward and reversed duel electrochemical process make fuel cell a storage unit for electrified systems [46].

An overview of different types of fuel cell technology is presented in [47]. There

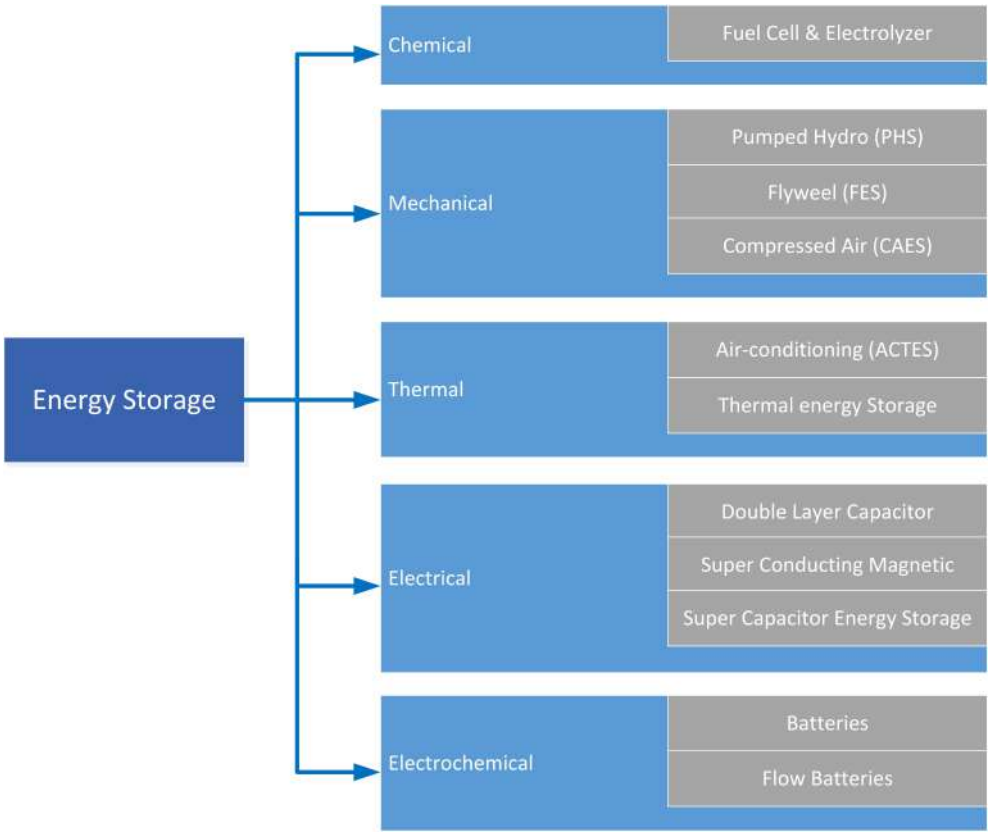

Figure 2.1: Classification of energy storage technologies [4]

are various types of fuel cells, such as biological fuel cells and direct methanol fuel cells. Compared with most other materials, hydrogen fuel cells are of particular interest because of the potential to store the energy in the hydrogen form with high energy density by weight and low energy density by volume. It is presumed to work as a form of clean energy storage that only releases water vapor to the environment when burned. A review of hydrogen fuel cells with different electrolytes is presented in [45]. The authors focused on providing details of the energy conversion efficiency, life span, energy density, power density, energy cost, power cost and working temperature. In addition, a summary of fuel cells in grid-connected, grid-parallel, stand-alone, back-up power applications is provided. An interesting application of hydrogen fuel cell is the development of portable energy storage systems for power sources and automobiles [48]. However, the disadvantages of the technology are the expensive capital cost, limited lifetime and safety issues related to hydrogen processing and transportation.

Pumped Hydro Pumped hydroelectric energy storage is not a new idea. Large-scale hydro power plants have been used successfully in the centralized power grid for many years. The energy is stored by pumping water up to a high elevation and released through turbines in a low elevation. The generator is then driven by the kinetic energy of turbines to produce electricity. The efficiency of hydro power plant can reach as high as 90%. The question remains for the pumped hydro power energy storage is that does the small-scale form still hold the advantages of low-cost, high reliability in a microgrid with the integration of renewable energy. A sustainable feasibility evaluation was studied by authors in [49] for the microgrid in rural areas of Africa. The results show the economic potential to install hydro power in a bottom-up concept of development. Compared with other energy storage technology, pumped hydro power is extremely hydrology-related and does not have mobility, leading to specialized designs for each system. A spectrum of research was done in fields of modeling of the turbine and the generator [50], load frequency control [51], reliability assessment [52], energy management with hybrid renewable energy in the grid-connected and islanded operation of mirogrids [53–55] .

Battery Battery energy storage has long history of research and a wide spread of deployments in power systems due to its fast response, geographical independence, cost-effective features. Battery is different from the fuel cell in the working principle. Other than continuously supplying energy through chemical reactions, batteries work as a "tank" that store the electric energy from other primary resources and discharge as requested. In terms of structure, battery energy storage is similar to fuel cell energy storage that needs to be connected in series to form a battery pack. There are several promising battery technologies extensively studied for the microgrid applications, including lead-acid batteries, nickel-cadmium batteries, lithium-ion (Li-ion) batteries and vanadium redox flow battery (VRB) [56]. Table 2.1 illustrates the features of different battery energy storage technologies [57, 58]. For some batteries like lead-acid batteries, the power capacity and energy capacity are highly correlated, which simplifies the size determination problem by only accounting for energy capacity. However, to deal with the

sizing of the de-coupled energy density and power density model for batteries such as VRB, an analytical method has been proposed in [59] based on the cost-benefit analysis. Li-ion batteries are reckoned as the most suitable technology for the islanded operation of microgrid in [60]. It has characteristics of high efficiency, high energy density, rapid response time and relatively low self-discharge rate [58]. However, depleted batteries may cause water and air pollution if improperly disposed. Conventional Li-ion batteries are criticized for short service life compared with other clean energy storage technologies. A new member of Li-ion battery family, $Li_4Ti_5O_{12}$ based lithium titanate oxide, shows attractive properties such as high life cycles, high charge/discharge capability and low operation temperature [61]. With the technological breakthroughs in the development of batteries, the integration of transportable or called mobile battery energy storage for rolling stocks [62] and plug-in electric vehicles [63] is practically possible. In [64], a two-stage stochastic optimal investment model of mobile energy storage units was proposed. The stationary energy storage units were re-routed to blackout areas caused by disasters as back-up resources to enhance the system resilience. A power transaction-based flexibility enhancement strategy with transportable energy storage for multi-microgrid system was analyzed in [65]. Numerical studies show a 23.58% reduction in the operation cost of diesel generator and a total 7.17% rise on renewable energy penetration after the integration of transportable energy storage.

2.1.3 Demand Response Technologies

The ever-growing load demand is constantly one step ahead of the development of generation in capacity. In underdeveloped countries, recent interest in household electrification has the priority in order to meet the people's life-improving needs [66]. Automotive electrification is the overwhelming global trend owing to the sustainability and environmental concerns. The concept of Sustainable Urban Mobility Plan (SUMP) is introduced by the European Commission, which aims at replacing fuels of gasoline and diesel with clean ones [67]. UK provides an official grant "The Electric Vehicle Homecharge Scheme" to stimulate families shifting to electric powered automobile. However, load rich will

Table 2.1: Characteristics of battery energy storage technologies

Battery	Lead-acid bateries	Nickel-cadmium batteries	Lithium-ion batteries	Vanadium redox flow batteries
Energy density (W.h/kg)	30~50	75	75~200	20~70
Power density (W/L)	200	300	200-300	10–20
Life cycles (times)	300	80	>1000	>12000
Operating temperature (°C)	-10~50	-20~60	-20~60	15~55
Response time	millisecond	millisecond	millisecond	$\leqslant$ 10min
Advantages	Low cost	low cost	high energy density	quick charge/discharge
	mature technology	quick charge/discharge	high voltage	high life cycles
			great stability	
	low energy density	memory effect	high cost	low energy and power density
	pollution	cadmium pollution	low life cycles	low response time
Disadvantages	low life cycles	very low life cycles		complex structure

decrease the system frequency. In the worst case when there is an unexpected power outage or a feeder failure, the whole microgrid might collapse.

There are several demand response (DR) technologies applied to the microgrids for the balance between power supply and consumption: load shedding and load shifting. It follows the principle that critical loads such as hospitals and traffic controls receive service priority. Other non-critical loads nominated as controllable loads are determined when, where and how much to be curtailed or shifted based on traditional [68], semi-adaptive [69] and adaptive [70] methods. The main objective of DR techniques is to provide an efficient way for end-users to sense and react according to the pricing and energy signals. In general, there are two major approaches: namely incentive-based DR program and price-based DR programs [71]. Smart pricing incentives electricity customers to lower their usage during peak time, or shift their electricity usage from peak time to off-peak time. There are various smart pricing schemes: Time-of-Use (ToU) Pricing, Critical-Peak Pricing (CPP), Real-time Pricing (RTP) and Day-ahead Pricing (DAP). A review of load shedding scheme in microgrids during islanded operation was provided in [72]. In [73], responsive loads under incentive-based programs for load reduction cooperated in day-ahead scheduling. Authors of [74] proposed a RTP scheduling model to maximize the operation profit. In addition to participate in the energy scheduling, DR programs were investigated for providing ancillary services such as system voltage control [75] and security enhancements [76] in recent years.

2.1.4 Power Electronics Technologies

Power electronic devices are the interface for the renewable generation to supply local demand loads. A simple schematic diagram of a microgrid with a WT, PV, fuel cell and battery storage system is shown in Figure 2.2. The power electronic converters are capable to convert DC (the PV, fuel cell and battery storage system) or variable frequency AC (WT) to 50/60 Hz AC to fit the main grid. Jamil et. al. present a comprehensive review of operations of converters in grid connected, islanded and battery charing modes for microgrid in [77]. Some of the most widely used DG integration interface configurations

are summarised in Table 2.2 [78]. It can be seen that the bidirectional converters are superior than the conventional synchronous or induction generators due to the abundant power flow control abilities.

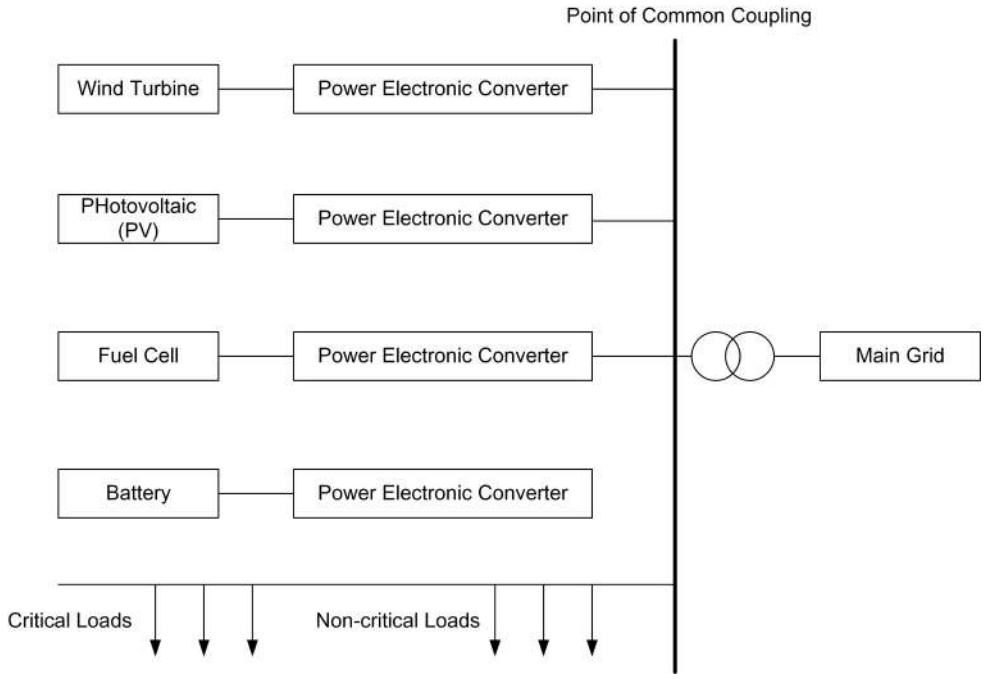

Figure 2.2: Schematic diagram of a microgrid

Table 2.2: DG interface configurations and power flow control abilities

Generation technology	Interfacing technology	Power flow control ability
Diesel engine	Synchronous generator	AVR +P,±Q
Microturbine	Power electronic converter (AC-DC-AC)	Turbine speed and DC link voltage +P,±Q
Fixed speed wind turbine	Induction generator	Turbine pitch +P,-Q
Variable speed wind turbine	Power electronic converter (AC-DC-AC)	Turbine speed and DC link voltage +P,±Q
Photovoltaic (PV)	Power electronic converter (DC-DC-AC)	Maximum power point tracking and DC link voltage +P,±Q
Fuel cell	Power electronic converter (DC-DC-AC)	Maximum power point tracking and DC link voltage +P,±Q
Pumped Hydro	Synchronous or induction generator	AVR +P,±Q
Battery	Power electronic converter (DC-DC-AC)	State of charge and output voltage/frquency ±P,±Q

In [79], the challenges arising from widespread use of power electronic converters were put forward. The interactions with other passive components, mechanical parts and

other converters will cause converter interaction issues, reliability issues and protection issues. The restructuring of conventional synchronous generator based power system results in a decrease in the inertia which refers to the energy stored in the large rotating machines [80]. For instance, the inertia of WTs is decoupled from the grid with variable frequency AC-DC-AC converters. The frequency stability of the microgrid is weakened by the high rate of change of frequency (ROCOF). A robust virtual inertia control technique was proposed in [81] to minimize the frequency measurement effects of a low-inertia microgrid. The proposed H_∞ control design was proved to have better robustness and the stabilizing performance than the conventional virtual inertia control and optimum proportional-integral (PI) control under different operation disturbances.

Despite the converters, several distributed flexible AC transmission system (D-FACTS) devices can participate in the microgrid to improve the power quality and stability [82], In [83], distribution static synchronous compensator (D-STATCOM) was proposed to provide harmonic composition due to increasing non-linear loads in the microgrid. Another D-FACTS component, soft open point (SOP), is regarded as a promising power electronics technology to provide power flow control, reactive power compensation and voltage regulation. The applications consist the economical dispatch for AC microgrid [84], restoration schedules [85] and peer-to-peer energy trading schemes [86] for the networked microgrids.

2.2 Techno-economic Impacts

System-level planning and operation schedule of microgrids is complex. There are a plenty of discussions and researches by academia, industry, utilities, regulators and policy makers. A good plan takes into account system structure, technologies, weather information and operational data to achieve technical, economic and environment objectives.

The power flow analysis, also called load-flow analysis is critical for the successful operation of a microgrid with dual modes (grid-connected and islanded mode). The

analysis involves the calculation of power flows and voltage of a microgrid network for specified terminal or bus conditions. Such calculations are required for the analysis of steady-state as well as dynamic performance of power systems [87]. The Optimal Power Flow (OPF) solves power system load flow, optimizes system operating conditions, and adjusts control variable settings, while ensuring system constraints are not violated. It was first introduced by Carpentier in 1962 [88]. The goal of OPF is to find the optimal settings of a given power system network that optimizes the system objective functions such as total generation cost, system loss, bus voltage deviation, emission of generating units, number of control actions, and load shedding while satisfying its power flow equations, system security, and equipment operating limits. The general framework encompasses dozens of optimization problems for power system planning and operation. OPF may be applied to decision-making at nearly any planning horizon - from long-term system capacity planning to minute-by-minute adjustment of real and reactive power dispatch [89].

2.2.1 Bus Classification

In conventional power flow, each bus has four quantities: active power P, reactive power Q, voltage magnitude V, and voltage angle θ. All system buses are assigned to one of the following types of buses.

- Voltage-controlled (PV) bus: Active power and voltage magnitude are specified. In addition, limits to the reactive power are specified depending on the characteristics of the individual devices. Examples are buses with generators, synchronous condensers, and static var compensators.

- Load (PQ) bus: Active and reactive power are specified. Normally loads are assumed to have constant power. If the effect of distribution transformer operation is neglected, load P and Q are assumed to vary as a function of bus voltage.

- Device bus: Special boundary conditions associated with devices such as HVDC converters are recognized.

- Slack (swing) bus: Voltage magnitude and phase angle are specified. Because the power losses in the system are not known a priori, at least one bus must have unspecified P and Q. Thus the slack bus is the only bus with known voltage.

2.2.2 Network Equations

The network equations in terms of the node admittance matrix can be written as follows

$$\begin{bmatrix} \dot{I}_1 \\ \dot{I}_2 \\ \cdots \\ \dot{I}_n \end{bmatrix} = \begin{bmatrix} Y_{11} & Y_{12} & \cdots & Y_{1n} \\ Y_{21} & Y_{22} & \cdots & Y_{2n} \\ \cdots & \cdots & \cdots & \cdots \\ Y_{n1} & Y_{n2} & \cdots & Y_{nn} \end{bmatrix} \begin{bmatrix} \dot{V}_1 \\ \dot{V}_2 \\ \cdots \\ \dot{V}_n \end{bmatrix} \tag{2.1}$$

where n is the total number of nodes. Y_{ii} is self admittance of node i which is equal to the sum of all the admittance terminating at node i. Y_{ij} is mutual admittance between nodes i and j which is equal to the negative of all the sum of all admittance between nodes i and j. $\dot{V}_i$ is the voltage at node i and $\dot{I}_i$ is the current flowing into the network at node i.

The current at any node k is related to P,Q and $\dot{V}$ as follows:

$$\dot{I}_k = \frac{P_k - jQ_k}{\dot{V}_k{}^*} \tag{2.2}$$

where $\dot{V}_k{}^*$ is the conjugate of voltage of node k. For the PQ nodes, P and Q are specified while for the PV nodes, P and the magnitude $\dot{V}$ are specified. As to other types of nodes, the relationship between P,Q,$\dot{V}$,$\dot{I}$ are defined by the characteristics of the devices connected to the nodes.

Clearly the boundary conditions imposed by the different types of nodes make the problem nonlinear and therefore traditional power-flow equations are solved iteratively using techniques such as Gauss-Seidel or Newton-Raphson method [90].

Gauss-Seidel Method - The method is based on the iterative approach which is proposed by Seidel in 1874. The current of node k can be written as

$$\frac{P_k - jQ_k}{\dot{V}_k{}^*} = Y_{kk}\dot{V}_k + \sum_{i=1, i\neq=k}^{n} Y_{ki}\dot{V}_i \tag{2.3}$$

Rearrange the expression for $\dot{V}_k$, the following formulation holds:

$$\dot{V}_k = \frac{P_k - jQ_k}{Y_{kk}\dot{V}_k^*} - \frac{1}{Y_{kk}} \sum_{i=1, i\neq k}^{n} Y_{ki}\dot{V}_i \tag{2.4}$$

Equation (2.4) is used to compute the voltage $\dot{V}_k$ by using the best available voltages of all buses for a load bus when its P and Q are known. If bus k is a generator bus, the following procedure is used:

(a) Rearrange Equation (2.3) and get

$$Q_k = -Im\left[\dot{V}_k^* \sum_{i=1}^{n} \dot{V}_i\right] \tag{2.5}$$

where Q_k is calculated by using the best available values of bus voltage. If Q_k is within the limits Q_{kmax} and Q_{kmin}, equation (2.4) is used to update the value of $\dot{V}_k$.

(b) If Q_k exceeds either the maximum or minimum limit, it is set equal to the limit. The updated value of $\dot{V}_k$ is computed by treating the generator bus as a PQ bus node.

The iterations are continued until the real and imaginary components of voltages at each bus computed converge to a specified tolerance.

Newton-Raphson (N-R) Method - P and Q at each bus are functions of voltage magnitude V and angle θ. The expressions for P_k and Q_k can be written as follows:

$$P_k = V_k \sum_{m=1}^{n} (G_{km}V_m cos\theta_{km} + B_{km}V_m sin\theta_{km}) \tag{2.6}$$

$$Q_k = V_k \sum_{m=1}^{n} (G_{km}V_m cos\theta_{km} - B_{km}V_m sin\theta_{km}) \tag{2.7}$$

where G is the conductance and B is the susceptance.

If the active power and reactive power at each bus are specified, it can be expressed as follows: using superscript sp to denote specified values, we may write the equation as

follows:

$$\begin{aligned}
P_1 &= (\theta_1, \cdots, \theta_n, V_1, \cdots, V_n) = P_1^{sp} \\
&\cdots \quad \cdots \quad \cdots \quad \cdots \quad \cdots \quad \cdots \quad \cdots \\
P_n &= (\theta_1, \cdots, \theta_n, V_1, \cdots, V_n) = P_n^{sp} \\
Q_1 &= (\theta_1, \cdots, \theta_n, V_1, \cdots, V_n) = Q_1^{sp} \\
&\cdots \quad \cdots \quad \cdots \quad \cdots \quad \cdots \quad \cdots \quad \cdots \\
Q_n &= (\theta_1, \cdots, \theta_n, V_1, \cdots, V_n) = Q_n^{sp}
\end{aligned} \tag{2.8}$$

where the superscript sp denotes specified values of P and Q.

Following the general procedure of Newton-Raphson method, the power flow equations can be expressed as follows:

$$\begin{bmatrix}
P_1^{sp} - P_1(\theta_1, \cdots, \theta_n, V_1, \cdots, V_n) \\
\cdots \quad \cdots \quad \cdots \quad \cdots \quad \cdots \quad \cdots \\
P_n^{sp} - P_n(\theta_1, \cdots, \theta_n, V_1, \cdots, V_n) \\
Q_1^{sp} - Q_1(\theta_1, \cdots, \theta_n, V_1, \cdots, V_n) \\
\cdots \quad \cdots \quad \cdots \quad \cdots \quad \cdots \quad \cdots \\
Q_n^{sp} - Q_n(\theta_1, \cdots, \theta_n, V_1, \cdots, V_n)
\end{bmatrix} =
\begin{bmatrix}
\frac{\partial P_1}{\partial \theta_1} \cdots \frac{\partial P_1}{\partial \theta_n} \frac{\partial P_1}{\partial V_1} \cdots \frac{\partial P_1}{\partial V_n} \\
\cdots \quad \cdots \quad \cdots \quad \cdots \quad \cdots \\
\frac{\partial P_n}{\partial \theta_n} \cdots \frac{\partial P_n}{\partial \theta_n} \frac{\partial P_n}{\partial V_1} \cdots \frac{\partial P_n}{\partial V_n} \\
\frac{\partial Q_1}{\partial \theta_1} \cdots \frac{\partial Q_1}{\partial \theta_n} \frac{\partial Q_1}{\partial V_1} \cdots \frac{\partial Q_1}{\partial V_n} \\
\cdots \quad \cdots \quad \cdots \quad \cdots \quad \cdots \\
\frac{\partial Q_n}{\partial \theta_n} \cdots \frac{\partial Q_n}{\partial \theta_n} \frac{\partial Q_n}{\partial V_1} \cdots \frac{\partial Q_n}{\partial V_n}
\end{bmatrix}
\begin{bmatrix}
\Delta\theta_1 \\ \cdots \\ \Delta\theta_n \\ \Delta V_1 \\ \cdots \\ \Delta V_n
\end{bmatrix} \tag{2.9}$$

The iteration is repeated until the errors are lower than a specified tolerance.

The Gauss-Seidel method is the oldest power flow solution method. It is simple, reliable and usually tolerant of poor voltage and reactive power conditions. In addition, it has low computing requirements. However, the computation time increases rapidly with system size. It also has a slow convergence rate and exhibits convergence problems when the system is stressed by massive active power transfer.

The Newton-Raphson method has a very good convergence rate. The computation time increases only linearly with system size. This method has convergence problems when the initial voltages are significantly different from their true values. Once the voltage solution is close to the true solution,however, the convergence is very rapid. The Newton-Raphson method is therefore particularly suited for applications involving large systems requiring very accurate solutions.

The convergence properties of the Newton-Raphson method complements the Gause-Seidel method. Therefore, many power flow programs provide both solutions techniques. The solution may be started with the Gauss-Seidel method and then switched to the New-Raphson method to obtain a rapid well-converged solution.

2.2.3 Standard AC OPF

The classic formulation of OPF considers about power generation limits, system operation limits such as reactive power constraints, voltage magnitude and angle constraints. The applications of OPF involves economic dispatch, unit commitment, optimal reactive power flow and optimal allocation of power source planning, that aims at minimizing either system power losses or total costs. For example, a schematic formulation of OPF based on economic dispatch is as follows:

$$min \quad \sum_{i \in \mathbb{G}} C_i(P_i^G) \tag{2.10}$$

$$\tag{2.11}$$

$$s.t. \qquad P_i(V,\theta) = P_i^G - P_i^C \qquad \forall i \in \mathbb{N} \tag{2.12}$$

$$Q_i(V,\theta) = Q_i^G - Q_i^C \qquad \forall i \in \mathbb{N} \tag{2.13}$$

$$P_{i,min}^G \leq P_i^G \leq P_{i,max}^G \qquad \forall i \in \mathbb{G} \tag{2.14}$$

$$Q_{i,min}^G \leq Q_i^G \leq Q_{i,max}^G \qquad \forall i \in \mathbb{G} \tag{2.15}$$

$$V_{i,min} \leq V_i \leq V_{i,max} \qquad \forall i \in \mathbb{N} \tag{2.16}$$

$$\theta_{i,min} \leq \theta_i \leq \theta_{i,max} \qquad \forall i \in \mathbb{N} \tag{2.17}$$

where $C_i(P_i^G)$ is the operating cost function of its real real output power. $\mathbb{G}$ is a subset of generator buses. $\mathbb{G} \subseteq \mathbb{N}$ which is the subset of all buses. P^G and Q^G are active and reactive generation, respectively. P^C and Q^C represent active and reactive load.

Constraints (2.12) and (2.13) are the power flow equations which is a shorthand of Equation (2.8). The remaining Constraints (2.14)-(2.17) represent bounds on the nodal voltage and power.

For microgrids, the network topology is normally simple radial network. Therefore, the non-linear power flow equations (2.12) and (2.13) power flow equations can be simplified as DistFlow Equations [91]. DistFlow Equations are the most popular power flow formulation for the planning problem in a radial distribution system. It is proposed by Baran and Wu in 1999 [91]. The voltage phase angle is omitted and are written as follows:

$$\sum_{l_{d_i} \in \mathbb{D}_i} P_{l_{d_i}} = P_{l_{u_i}} - r_{l_{u_i}} \frac{P_{l_{u_i}}^2 + Q_{l_{u_i}}^2}{V_i^2} - P_i^C \tag{2.18}$$

$$\sum_{l_{d_i} \in \mathbb{D}_i} Q_{l_{d_i}} = Q_{l_{u_i}} - x_{l_{u_i}} \frac{P_{l_{u_i}}^2 + Q_{l_{u_i}}^2}{V_i^2} - Q_i^C \tag{2.19}$$

$$V_j^2 = V_i^2 - 2(r_{l_{i\to j}} P_{l_{i\to j}} + x_{l_{i\to j}} Q_{l_{i\to j}}) + (r_{l_{i\to j}}^2 + x_{l_{i\to j}}^2) \frac{P_{l_{i\to j}}^2 + Q_{l_{i\to j}}^2}{V_i^2} \tag{2.20}$$

$\mathbb{U}_i$ denote the set of upstream lines attached to bus i and $\mathbb{D}_i$ the set of downstream lines. For each bus i, the upstream lines are $l_{u_i} \in \mathbb{U}_i$ while downstream lines are $l_{d(i)} \in \mathbb{D}_i$. Note that for a radial network, only the downstream lines attached to a bus can split up to be more than one branch. $l_{i\to j}$ refers to a line connecting bus i and bus j. $r_{l_{i\to j}}$ and $x_{l_{i\to j}}$ are corresponding transimission line resistance and reactance. $P_{l_{i\to j}}$ and $Q_{l_{i\to j}}$ represent the active and reactive power flowing from bus i to bus j, respectively.

To overcome the complexity of quadratic equations of DistFlow, the linearized formulation LinDistFlow in (2.21) to (2.23) is formulated as an approximate model.

$$\sum_{l_{d_i} \in \mathbb{D}_i} P_{l_{d_i}} = P_{l_{u_i}} - P_i^C \tag{2.21}$$

$$\sum_{l_{d_i} \in \mathbb{D}_i} Q_{l_{d_i}} = Q_{l_{u_i}} - Q_i^C \tag{2.22}$$

$$V_j^2 = V_i^2 - 2(r_{l_{i\to j}} P_{l_{i\to j}} + x_{l_{i\to j}} Q_{l_{i\to j}}) \tag{2.23}$$

An equivalent approximation (2.24) is derived from the equation (2.23) as the magnitude of the voltage at each bus is assumed to be close to the reference bus V_0 at the point of common coupling (PCC) and the phase angle differences among the buses are small enough to be neglected. The model has been widely adopted for the planning of

distribution system and microgrid [92, 93] because of its simplicity and availability.

$$|V_i| - |V_j| \simeq Re\left\{z_{l_{i\to j}} I_{l_{i\to j}}\right\} = \frac{Re\left\{z_{i\to j} S^*_{l_{i\to j}}\right\}}{V_0^*} \simeq \frac{r_{l_{i\to j}} P_{l_{i\to j}} + x_{l_{i\to j}} Q_{l_{i\to j}}}{V_0} \tag{2.24}$$

Therefore, for a radial network, the OPF with LinDistFlow form is formulated as:

$$min \quad \sum_{i\in G} C_i(P_i^G) \tag{2.25}$$

$$\tag{2.26}$$

$$s.t. \qquad \sum_{l_{d_i}\in \mathbb{D}_i} P_{l_{d_i}} - P_{l_{u_i}} = P_i^G - P_i^C \qquad \forall i \in \mathbb{N} \tag{2.27}$$

$$\sum_{l_{d_i}\in \mathbb{D}_i} Q_{l_{d_i}} - Q_{l_{u_i}} = Q_i^G - Q_i^C \qquad \forall i \in \mathbb{N} \tag{2.28}$$

$$V_j = V_i - (r_{l_{i\to j}} P_{l_{i\to j}} + x_{l_{i\to j}} Q_{l_{i\to j}})/V_0 \qquad \forall i,j \in \mathbb{N} \tag{2.29}$$

$$P_{i,min}^G \le P_i^G \le P_{i,max}^G \qquad \forall i \in \mathbb{G} \tag{2.30}$$

$$Q_{i,min}^G \le Q_i^G \le Q_{i,max}^G \qquad \forall i \in \mathbb{G} \tag{2.31}$$

$$V_{i,min} \le V_i \le V_{i,max} \qquad \forall i \in \mathbb{N} \tag{2.32}$$

$$\tag{2.33}$$

An application of OPF is the security-constrained optimal power flow. It considers the situation when one or more generators or transmission lines are out of service. The microgrid is regarded as a resilience source for power system to remain reliable operation under a set of contingency events. In [94], a resiliency-oriented scheduling is proposed based on a two-stage stochastic programming to mitigate adverse impacts of electricity interruptions. An extended power flow model is proposed in [95]. Combined with a mixed-integer linear programming (MILP) formulation, the effectiveness of the proposed iterative solution is validated to to enhance the voltage and frequency regulation based on a optimal sizing, sitting and schedules of the battery energy storage system.

2.3 Electricity Market Impacts

The integration of small and medium-sized DERs such as renewable WTs, residential PV panels, electric vehicles and battery storage systems in the microgrid has provided opportunities for utilities and other system owners to re-evaluate their energy practices [96]. The distribution and liberalization of power system synchronously deregulates the electricity market which undergoes a rapid evolution towards a greener, more flexible and more efficient mechanism. Figure 2.3 shows several main electricity markets in Europe [5]. It is critical for policymakers and system planner to consider the potential revenue streams into their decision making. The timeline of different electricity markets is illustrated in Figure 2.4 which highly depends on the interaction between market operators and system operators. Several representative markets will be introduced in the following section.

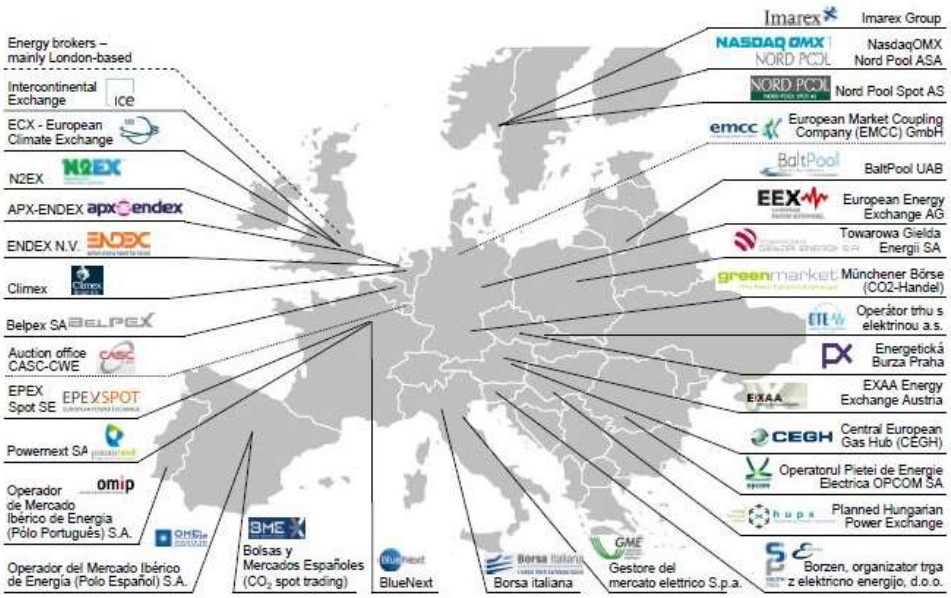

Figure 2.3: Electricity markets in Europe [5]

2.3.1 Day-ahead Market

In the UK, there are two predominant day-ahead markets, which are N2EX Day-Ahead Auction under the Nord Pool and Epex Spot UK Power Auction under Epex Spot [97].

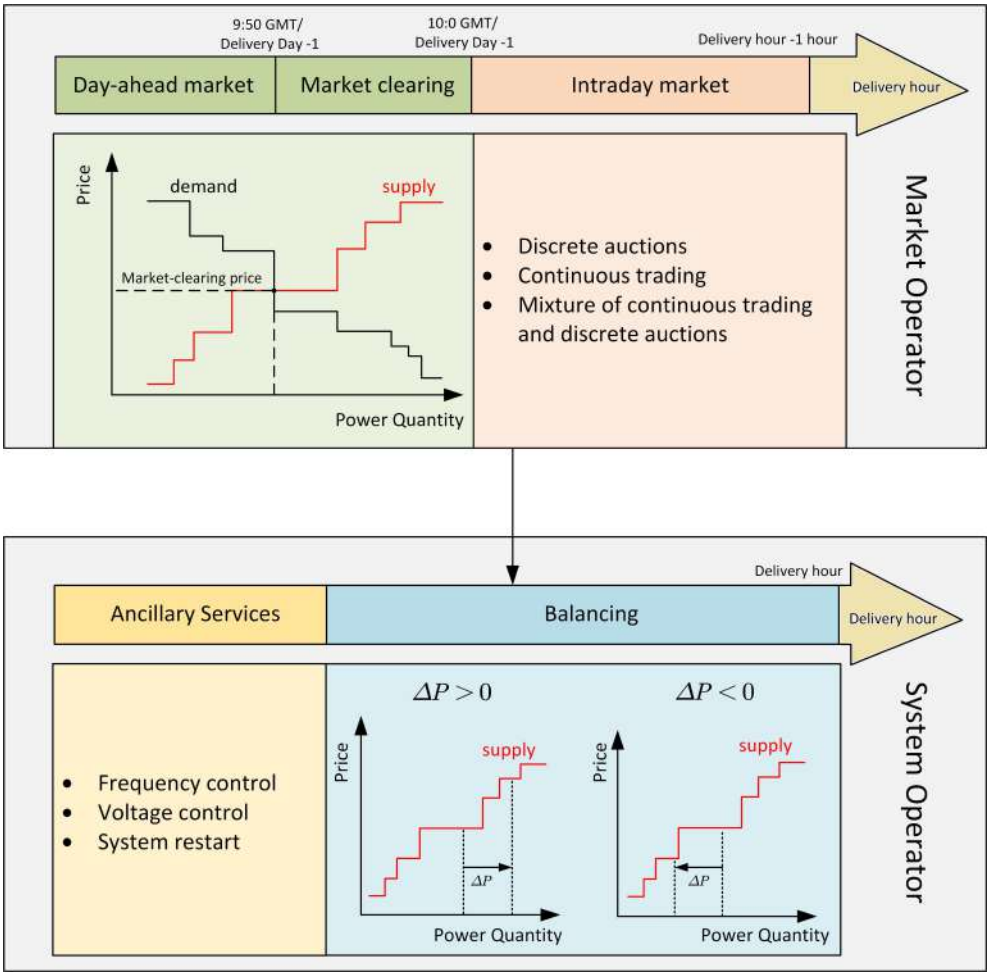

Figure 2.4: Timeline of electricity markets

Market participants make the energy transactions by auctions one day prior to delivery time in the day-ahead market or a pool mechanism. All generation bids and consumption offers are placed at the same time without knowing others' bids and offers. A centralized market-clearing algorithm is used to decide which bids and offers are retained. As shown in the green block of Figure 2.4, the generation or consumption provide an offer with power quantity and corresponding price at which they are willing to transfer. The demand offers are ranked in decreasing price order while the supply bids are ranked in the opposite order. The cross point is nominated as the equilibrium point when demand and supply are balanced. The price at the equilibrium point is the market-clearing price. After the market-clearing process, the system operator is informed about the trade results. For instance, the gate closure time of N2EX Day Ahead Auction is 9:50 GMT the

day before the delivery and results are published in 15 minutes.

2.3.2 Intraday market

After the closure of day-ahead market clearing, the intraday trading begins and lasts until one hour or even shortly before the delivery time. It allows market participants to correct the energy mismatch based on latest forecast of renewable generation or consumption between day-ahead market clearing and real-time operation. There are three existing forms of intraday trading in Europe: discrete auctions, continuous trading and mixture of continuous trading and discrete auctions. The discrete actions mimics the settlement of day-ahead market, determining the uniform prices for all market participants, The method is implemented by regional transmission organization (RTO) and independent system operator (ISO) in the US to complement the centralized dispatch systems [98]. The continuous trading follows the first-come-first-serve basis that bilateral contracts are continuously made whenever bids and offers are matched. Nord Pool provides intraday services for 16 European countries including Sweden, Denmark, Finland, Norway, UK, Germany, Poland, France, Netherlands, Belgium, Austria, etc. [99]. MIBEL - Iberian electricity market - adopts the mixture of continuous trading and discrete auctions. A comprehensive comparisons of bidding price strategies are given in [100]. In addition, the authors emphasize the trading research of transnational energy trading market - the European cross-border intraday (XBID) project - that will address the weakness of low market liquidity in the future.

2.3.3 Balancing Market and Ancillary Services

Balancing market is a trading platform to balance the demand and supply closer to real-time operation. Market participants can either increase or decrease generation (or consumption) to help system operator mitigate the power imbalance. If the power supply exceeds the demand, downward regulation is needed. If the power supply is less than the demand, upward regulation takes place. In the UK, it is called " Balancing Mechanism "

(BM) which is managed and administered by Elexon. BM operates under the balancing & settlement code on a half-hourly basis.

Ancillary services belongs to a broader concept which are also related to the actual power balance. They are provided by the system operator rather than the market operator. In general, ancillary services can be categorised as frequency control, voltage control and system restart. The conventions of this type of services vary from region to region. In the UK, National Grid ESO (NG-ESO) is the system operator that procures energy for ancillary services which involves frequency response service, reserve services, system security services, reactive power services, etc. [101]. The technical requirement for market access specifies minimum capacity and response times. For instance, firm frequency reserve services refer to the products with at least 1MW capacity and 10-30s response time to maintain the system frequency at 50Hz (± 1%) by NG-ESO [97].

2.4 Methodology: Optimization Methods in Microgrids

The planning and operation of power systems is an optimization problem. In particular, most of the problems have many constraints to to satisfy for secure and reliable operation and offer contingency measures for events such as a sudden loss of power plant. In this section, the conventional optimization methods will be reviewed exclusively from the perspective of specific applications in power economics and planning, followed by meta-heuristic methods which are generally more flexible and do not need gradient information. In addition, the methodology such as stochastic optimization and robust optimization used to handle uncertainty is provided. The corresponding simulation tools and software are discussed in the end.

2.4.1 Conventional Methods

A general optimization problem is express as follows:

$$\begin{aligned} min \quad & f(\mathbf{x}) \\ s.t. \quad & h(\mathbf{x}) \leqslant 0 \end{aligned} \tag{2.34}$$

where $\mathbf{x}$ denotes the vector of decision variables. $f(\mathbf{x})$ is called the objective function and $h(\mathbf{x})$ is the constraint for the decision variables. In this kind of formulation, all other parameters are deterministic. However, there is no single solution method for all problems. Structural simplification such as convexity are needed to make problems tractable. The simplified tractable optimization methods are called conventional methods.

The most widely used conventional optimization methods include linear programming (LP), quadratic programming (QP), mixed-integer programming (MIP), dynamic programming (DP) and Lagrangian relaxation (LR) method. A brief comparison is shown in Table 3.1.

Table 2.3: A brief comparison of optimization methods in microgrids

Method	Advantage v.s. Disadvantage		Applications
Linear programming	A	Easy implementation	Security-constrainted economic dispatch
		Multiple platform support	Optimal power flow
		Low computational cost	Steady-state security problem
	D	Limited framework	Operational cost minimization
		Low flexibility	with specific power price
Quadratic programming	A	Higher flexibility	Power loss minimization
		Multiple platform support	Econimic dispatch without valve-effect
	D	Limited framework	
		Specific solver requirement	
Mixed-integer programming	A	Higher flexibility	Unit commitment
	D	High computational cost	Generation planning
Dynamic programming	A	Dynamic features of each step	Unit commitment
		Low computational cost	Operational cost minimization
	D	Curse of dimensionality	with time-varying power price
Lagrangian relaxation	A	Easy implementation	Unit commitment
	D	Limited framework	Econimic dispatch with constraints
		Low flexibility	

2.4.1.1 Linear Programming

LP-based techniques use the linear forms of objective functions and constraints of microgrid planning and operation optimization problems. The straightforward implementation

offers several advantages [102]. Firstly, it is reliable, especially in regard to the convergence properties. Secondly, it is fast and easy to program and requires little computing storage. Thirdly, it accommodates many operating limits of power systems [103]. The simplex method [104] and interior point method [105] are known to be two of the effective methods for LP problems. A variety of LP-based practical applications such as security-constrained economic dispatch [106, 107], optimal power flow [108, 109] and steady-state security problems [109] have been found in the literature, which is deemed to meet the engineering precision. However, the disadvantages of these techniques are that the evaluation model of the system is not accurate enough compared with a nonlinear power model.

2.4.1.2 Quadratic Programming

QP is a special type of nonlinear program whose objective function is quadratic, and the constraints are in linear form. QP is generally more precise than LP approaches. One example of QP problem that is widely used in power system optimization is the fuel consumption function. An efficient QP technique used is to convert the QP problem into a LP formula based on the Kuhn-Tucker condition [110]. In most cases, conventional LP-based methods are not capable for nonlinear and quadratic objective functions. The extended quadratic interior point method [111] can accommodate the nonlinearity in objectives and constraints. Improved quadratic interior point method [112] features a general starting point (rather than a good point as in the general interior point method) and fast convergence. QP is widely used for solving the global or local optimization problems of the generation scheduling and finding optimal power flow solution considering transformer tap ratios, bus voltages, and reactive compensation [111–115].

2.4.1.3 Mixed-integer Programming

MIP solves problems with integer variables to formulate extensive management as discrete devices involved. One MIP application in microgrid is the generation planning problem in which binary variables indicate the unit connected or disconnected decisions.

MIP consumers more computing resource compared with other methods introduced earlier. When considering the integration of large-scale DGs, the high dimension framework makes the problem very complicated. Generally, to solve the MIP problem, the target is often decomposed into an integer master problem and a continuous subproblem. Various decomposition methods have been introduced in the literature, among which Benders decomposition (BD) method [116] is a method that can significantly increase the computing efficiency for the large-scale network. The advantage of the method is that it can reduce the dimensions of the separate subproblem and the number of iterations.

2.4.1.4 Dynamic Programming

DP is used implicitly in feasible schedules by splitting the whole optimization process into a series of time slots and determine the state at each moment. DP can be used to solve the economic dispatch for microgrid with time-varying prices [117]. One major advantage lies on the capability of producing a scheduling solution in a short time, which is very important particularly for intra-day scheduling of microgrid. The minimum cost at time t with state I can be expressed by a recursive expression [89], shown as below:

$$F_{tc}(t,I) = \min_{I \in \mathbf{L}} [F(t,I) + S_c(t-1, L \Rightarrow t, I) + F_{tc}(t-1,I)] \tag{2.35}$$

where $F_{tc}(t,I)$ is the total cost from the initial state to state I at time t. $F(t,I)$ is the production cost of state (t,I). $S_c(t-1,L \Rightarrow t,I) + F_{tc}(t-1,I)$ is the transition cost from state $(t-1,L)$ to state (t,I). $\mathbf{L}$ is the set of feasible states at time $t-1$.

It can easily add constraints within one interval, such as changing the reserve requirement at a particular time interval to compensate the rise in the electricity demand. However, it has difficulty to deal with continuous time interval constraints. The weakness of DP is called 'curse of dimensionlity' that the computation is in exponential growth with the increase of the dimensions. Other applications of DP include charging/discharging strategy for ESS [118, 119], unit commitment [120, 121], etc..

2.4.1.5 Lagrangian Relaxation

LR method involves decomposition of the problem into a primal problem and a dual problem [122]. The dual problem is a relaxed version of the primal problem, and more likely to be solved by adding the constraints to the objective function. Hence, the constrained prime problem is transformed into an unconstrained problem, and yields a lower boundary for the feasible solution of the primal problem. A simple formulation of Lagrangian function for an economic dispatch with power balance is obtained

$$F = \sum_i f_i(P_i^G) + \lambda \left(P^C - \sum_i P_i^G \right) \tag{2.36}$$

where λ is Lagrangian multiplier The optimality criteria of the Lagrange function is as follows

$$\frac{\partial F}{\partial P^C} = \frac{df_i}{dP^C} + \lambda \tag{2.37}$$

$$\frac{\partial F}{\partial P_i^G} = \frac{df_i}{dP_i^G} - \lambda \tag{2.38}$$

LR is a traditional approach which has been widely used to solve economic dispatch problems with constraints [123, 124].

2.4.2 Meta-heuristic Methods

Meta-heuristic optimization algorithms can be used to solve all optimization problems despite they are convex or non-convex. Compared with the convectional methods, meta-heuristic methods do not need to simplify the problem formulation. However, the methods do not guarantee the optimal solution and the solutions might vary in different runs.

in recently years, the methods are becoming more and more popular to deal with problems such as economic decisions [125, 126], engineering designs and planning [127] because of the following features:

- Simple concepts and easy implementation
- No requirement for gradient information of the cost function
- Easy to jump out of local optima

- Capable of solving a wide range of objectives with different constraints

By mimicking biological or physical phenomena, meta-heuristic algorithms can solve non-smooth, high dimensional optimization problems, which can meet the requirements of the complex power systems. In recent years, the development of meta-heuristic methods flourishes, and basically these approaches can be categorised into four groups as shown in Figure 2.5: evolution-based methods such as genetic algorithm (GA), and differential evolution (DE); physics-based methods including simulated annealing (SA); swam-based methods such as particle swarm optimization (PSO) and whale optimization algorithm (WOA) and human-based methods including teaching learning based optimization (TLBO).

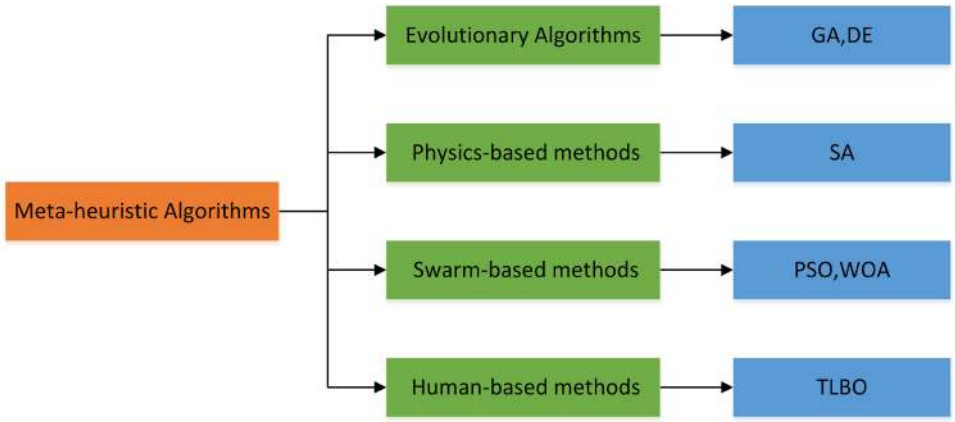

Figure 2.5: Classification of some popular meta-heuristic algorithms

2.4.3 Optimization Methods Dealing with Uncertainties

In practice, there are enormous questions are not deterministic, which would be formulated as a optimization problem with uncertainties in mathematical language. Specific applications in microgrid are optimal planning or scheduling problems with the intermittent renewable generations such as wind generation or solar generation. A general expression of optimization mathematical model with uncertainty could be

$$\begin{aligned} min \quad & f(\mathbf{x},\xi) \\ s.t. \quad & h(\mathbf{x},\xi) \leqslant 0, \forall \xi \in \mathbb{U} \end{aligned} \tag{2.39}$$

In equation (2.39), ξ represents the vectors of all uncertain variables which belong to uncertainty set $\mathbf{U}$. ξ could be either in objective function or constraints. The reasons of uncertainty are varied, but include: the missing or deviation in data collection process, the effect of weather factors, the simplification of models. Since 1950s, researchers such as Bellman and Charnes has been working on the optimization methods for problems with uncertainty [128, 129]. In this section, two dominated methods are introduced, which are stochastic optimization and robust optimization.

2.4.3.1 Stochastic Optimization

Stochastic optimization (SO) is recognised as a pre-analysis method. For problems expressed like Equation (2.38), the core of the method is to determine the distribution of uncertain variables ξ. The discrete scenarios can be clustered by modern machine learning algorithms. Therefore, the uncertain variables can be replaced by the relevant expect values. The method converts the original uncertain problems to deterministic problems by a number of discrete probabilistic scenarios. The converted problem can be solved by the conventional methods in section 2.4.1 or the meta-heuristic methods in section 2.4.2.

In a particular situation when there are only uncertain variables in constraints, the chance-constrained approach that restricts the probability of a constraint to be above a certain confidence level is reliable and widely adopted in the literature [130]. The model can be expressed as follows:

$$\begin{aligned} &min \quad f(\mathbf{x},\xi) \\ &s.t.\ P\{h(\mathbf{x},\xi) \leqslant 0\} \geqslant \alpha \end{aligned} \tag{2.40}$$

where α is the predefined confidence level.

2.4.3.2 Robust Optimization

Robust optimization (RO) is another pre-analysis method which is a derivative of robust control theory. If $\mathbb{U}$ in Equation (2.39) is a closed set, it can be viewed as a RO model. Compared with SO, RO does not need to know the distribution of uncertain variables

and the obtained results are often more conservative. Moreover, the constraint of RO is strictly true, that is, as long as the uncertain parameter ξ belongs to the uncertain set $\mathbb{U}$, the optimal solution can satisfy the constraint condition. The characteristics guarantee the strong robustness of RO in the region of $\mathbb{U}$ and the optimal solution has low sensitivity to parameter changes. A more general expression of RO is as follows:

$$\begin{aligned} & min \quad F \\ s.t. \quad & f(\mathbf{x},\xi) \leqslant F, \forall \xi \in \mathbb{U} \\ & h(\mathbf{x},\xi) \leqslant 0, \forall \xi \in \mathbb{U} \end{aligned} \tag{2.41}$$

The choice of uncertainty set that describe the uncertain variables directly affects the optimization results of the model. Often we want to make a trade-off between robustness and each physical realization of the uncertain variable and the size of the uncertainty set. Common uncertainty sets mainly fall into the following classes as shown in Figure 2.6.

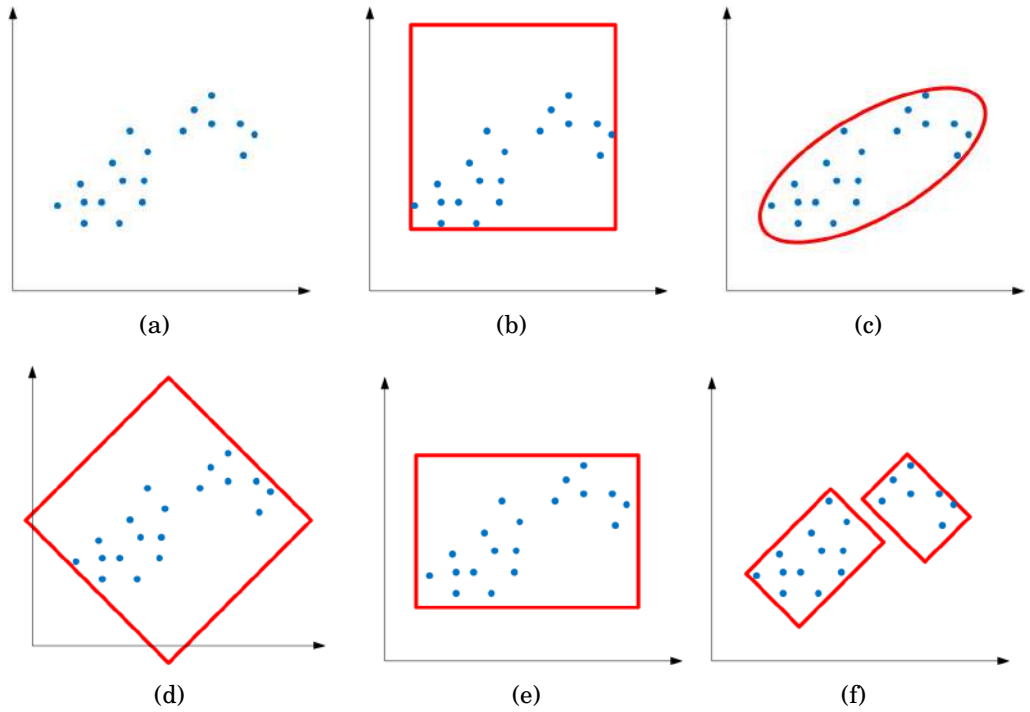

Figure 2.6: (a) Scatter plot of uncertainty variables (b) Box uncertainty set (c) Ellipsoidal uncertainty set (d) Polyhedral uncertainty set (e) Budget uncertainty set (f) Data-driven uncertainty set

1. Box uncertainty set

$$\mathbb{U}_{\infty} = \left\{\xi : \|\xi\|_{\infty} \leqslant \tau\right\} \tag{2.42}$$

The box uncertainty set is the simplest uncertainty set. As for the RO, the worst case in which uncertain variables fall in the upper and lower bounds of the interval set will be considered. However, in practice, the probability of this situation may be very low or will not occur. Therefore, it is easy to be overly conservative.

2. Ellipsoidal uncertainty set

$$\mathbb{U}_{2} = \left\{\xi : \|\xi\|_{2} \leqslant \Omega\right\} \tag{2.43}$$

Although ellipsoidal uncertainty sets can represent many types of sets and reflect the correlation among uncertain variables to a certain extent, they are not widely used due to the increased complexity of the resultant solving problems.

3. Polyhedral uncertainty set

$$\mathbb{U}_{1} = \left\{\xi : \|\xi\|_{1} \leqslant \Gamma\right\} \tag{2.44}$$

Compared with box uncertainty sets, polyhedral uncertainty sets are inferior to describe the correlation between uncertain variables. But they are widely adopted in practical engineering problems because of their linear structure and easy control of uncertainty.

4. Budget uncertainty set

$$\mathbb{U} = \left\{\xi : \sum \left|\frac{\xi_i - \hat{\xi}_i}{\overline{\xi_i} - \underline{\xi_i}}\right| \leqslant \Gamma\right\} \tag{2.45}$$

where $\overline{\xi_i}$ and $\underline{\xi_i}$ are upper and lower boundary of the uncertain parameters and $\hat{\xi}_i$ is the estimation value. This kind of uncertainty set can show the fluctuation of variables. But it needs additional effort to find out appropriate boundary.

5. Data-driven uncertainty set

In order to solve the over-conservatism of above uncertainty sets, data-drive uncertainty set based on historical data has been proposed in recent years. The construction uses confidence intervals of statistical hypothesis testing to accurately

depict the distribution of uncertain variables. As shown in Figure 2.6(f), a data-driven mixture model is tighter than the other uncertainty sets. It captures the correlated, asymmetric characteristics of the underlying 2-dimensional data.

2.4.4 Simulation Tools and Software

A general process to be used to efficiently solve the optimization problem in power system is shown in Figure 2.7. There are a wide variety of simulation tools and commercial software available to assist the formulation of the problem and optimization algorithms. In this section, some of the most popular tools are reviewed.

Figure 2.7: Simulation process of optimization problems in power system

Programming languages and software packages - The choice of programming languages usually follows academic conventions in the field of power system. Due to the computational advantages of matrices, MATLAB is a high-performance programming languages suitable for mathematical and computational projects developed by MathWorks [131]. Although it is not developed specifically to optimization problems, there is a built-in optomization toolbox that can solve simple LP and MILP problems. In addition, it has an active group of users who create functional toolboxes. For example, MATPOWER [132] is an open-source MATLAB software package that includes functions of power flow and OPF. Yalmip is a MATLAB toolbox for modeling optimization problems [133]. It can call built-in optomization toolbox as well as commercial optimization solvers, such as CPLEX [134], MOSEK [135] and GUROBI [136]. These kind of commercial solvers are compatible with not only MATLAB but also other programming languages including Python, C, C++, Java and the software GAMS which will introduced later.

Another promising high-level programming language is Python because of its enormous open-source packages, especially for machine learning and AI-based applications such as data processing in the power system. It should be noted that there is also an

optimization modeling software package available in Python language - Pyomo - which works well with commercial optimization solvers. .

Algebraic modeling language - The algebraic modeling language is used for solving high complexity problems with large-scale computation requirements. For instance, GAMS representing general algebraic modeling system is an alternative high-level modeling software that is designed for mathematical optimization [137]. It can solve LP, MIP and also nonlinear optimization problems and can be implemented on various computer platforms. It supports a group of optimization solvers. Different solver is capable of solving different problems. For instance, CPLEX is a competitive LP/MIP solver. The details of genral information of solvers used in GAMS can be found at [138]. GAMS is popular because it is the first algebraic modeling language for large-scale optimization problems. Although the use of GAMS in academics is not as much as other languages nowadays, it is still prevailing in industry.

Independent software - HOMER, which stands for Hybrid Optimization of Multiple Energy Resources, is a software dedicated for accurate, flexible and robust techno-economic solutions of hybrid power systems [139]. The software can simulate real-word performance for grid-connected and islanded microgrids and consider fuel price changes, load growth and also battery degradation.

CHAPTER 3

DISTRIBUTED GENERATION PLANNING IN MICROGRIDS

Distributed generation (DG) is one of the most important elements in microgrids. It can generate energy on-site, rather than transmitting bulky energy from centralized power plants [140]. Therefore, it brings significant techno-economical benefits to the power system such as the reduction of grid energy loss [141], the improvement of system efficiency [142] as well as the power supply flexibility [143], etc. These advantages make DG a catalyst for the rapid development of microgrids, such as the network expansion in remote areas and the rural electrification in developing countries.

An important task in microgrid application is the DG planning, which aims to determine the optimal sizing and locating of multiple DG units in a microgrid in order to meet the demand they serve. In recent years, the development of RESs tops the priority agenda in many countries and regions along with their decarbonization commitments [144–146]. However, RESs such as wind and solar energy are naturally intermittent and variable due to geographical restrictions. It is very challenging to predict their generations. For instance, the generation of solar panels depends not only on the location, temperature and time but also the cloud cover impact. The short-term variability of clouds will strongly affect the power production, which makes it complex to control the device setting and keep the system frequency stable. The accumulated prediction

deviations will also make a difference on long-term planning as the size of the generators could be easily overestimated or underestimated due to inaccurate generation figures. Moreover, the planning is also affected by a range of issues, such as the fluctuations of load demand, electricity market prices, environmental and socio-political factors [147], which makes the problem harder in order to maintain the balance of electricity supply and demand for a long period.

The researches in the literature to address the impacts of the uncertainties arising from the variable renewable generations and loads over the past few years can be categorized as two popular optimization modelling techniques: stochastic optimization (SO) and robust optimization (RO). SO techniques model the uncertainties by a statistical model. To reflect the probability distribution of uncertainty accurately, methods such as scenario-based modeling, Monte Carlo simulation and point estimation have been widely used. In [148], the RES and load uncertainties have been divided into 16 sampled scenarios for a joint planning of the distribution network and renewable energy expansion. The same techniques have been adopted by [149]. A two-stage stochastic programming is developed to replace the full representation of the uncertainties of the hydro production with a subset of scenarios. Although the model adequately represents the time-dependent quantities, it incurs a considerably heavy computational burden while it can not guarantee that the construction of scenario samples is accurate enough to represent the future trends.

Recent studies [150–152] have shown that RO approaches could be successful applied to the power system operation and planning problems by improving the operation robustness against the uncertainties. Compared with SO, RO modelling method has several prominent advantages. First, RO can obtain an optimal solution against uncertainty that is deterministically formulated by uncertainty sets, which do not need accurate probability distribution in advance. Second, unlike the SO using probabilistic assumptions, the worst scenario reaches the top of the queue in RO.

In this Chapter, a two-stage data-driven adaptive robust distributed generation planning (DDARDGP) framework for microgrids is proposed. The overall framework

will encompass DG system configuration design, analysis of renewable energy resource availability and load profile, objective and constraints formulation of RO, optimisation solving techniques and the uncertainty processing technique. Particularly, a novel data-driven method based on a Bayesian nonparametric approach will be introduced for forming the uncertainty set.

3.1 Distributed Generation Planning Model

Generally speaking, a DG planning design aims to find the best combinations from possible generation technologies, such as biomass generation, wind turbine (WT), solar photovoltaic (PV) panels, diesel engine, gas turbine, etc.. In general, the DG units can be classified as dispatchable units, e.g., microturbine (MT) and diesel engine that converts fossil fuels to the electricity or non-dispatchable units which are mostly based on renewable energy sources (RESs), e.g., WT and PV panels. High-efficiency WT and PV are considered as non-dispatchable DGs, which means that all the energy they produce will be fully utilized. Recently, wind and solar generations have been widely deployed in microgrids, especially for rural areas and islands with rich natural resources.

A WT is a device that converts the kinetic energy of wind into electrical energy. The blades of a turbine are turned around a rotor by the wind. The generation which is connected to the spinning rotor either directly or through a shaft and a gear box produce the electricity. The capacity of WT is in directly proportion to the height of the hub and length of blades. The world's largest WT provides a capacity of 15 MW which stands over 260 m and will sweep over 43,000 m^2 [153]. As the installation of WT requires large space, the large-scale of WT or wind farms are often deployed in rural areas or offshore areas.

PV devices convert sunlight intro electrical energy based on photovoltaic effect of semiconductor materials. A single PV cell typically produces about 1 or 2 W. The cells are connected in chains to form a larger panel. The panels can be used individually or be connected to boost the power output. The capacity of a single PV panel varies by the

manufacturers and materials, which can be as low as several W or as high as hundreds of w [154]. It can be easily mounted and the most common location for the installation is the roof.

MT devices are gas turbines that produce the electricity on a small scale. The capacity of commercial machines ranges from 30 kW to 500 kW [155]. MTs have capabilities such as full controllability, high response speed and low emission, which are popular in commercial applications such as office buildings, hotels, hospitals and industrial applications like manufacturing plants. Through suitable power electronic devices, i.e., inverter interfaces, these DG units could be connected to the microgrids.

3.1.1 Objective Function

The optimal integration of DGs into a microgrid has many benefits from the operational, environmental and techno-economical aspects. Each category of DG i.e. WT, PV and MT) has several different performance parameters to choose from. For example, if three types of WTs can be possibly installed at the same location, they can produce three different power generation profiles based on their design parameters. The objective is to determine the optimal locations, sizes and mixtures of DGs with the purpose to maximize the long-term economic profits. Assume that the utility of the microgrid owns all infrastructure and services, including the DG units deployment and operation, energy transactions with the main grid and regional customers, the total cost of the utility can be formulated as follows:

$$\min_{f,P,Q,V} C^{INV} + C^{OM} + C^{FC} + C^{EMI} - C^{REV} \tag{3.1}$$

where

$$C^{INV} = \sum_i \sum_j \sum_l inv^{MT} f^{MT}_{i,j,l} C^{MT}_j + \sum_i \sum_j \sum_l inv^{WT} f^{WT}_{i,j,l} C^{WT}_j + \sum_i \sum_j \sum_l inv^{PV} f^{PV}_{i,j,l} C^{PV}_j \tag{3.2}$$

$$C^{OM} = \sum_t \left[\sum_i \sum_j \sum_l om^{MT}_t f^{MT}_{i,j,l} C^{MT}_j + \sum_i \sum_j \sum_l om^{WT}_t f^{WT}_{i,j,l} C^{WT}_j + \sum_i \sum_j \sum_l om^{PV}_t f^{PV}_{i,j,l} C^{PV}_j \right] \tag{3.3}$$

$$C^{FC} = \alpha^{FC} \sum_{t} \sum_{i} P_{i,t}^{MT} \tag{3.4}$$

$$C^{EMI} = \alpha^{EMI} \sigma \sum_{t} \sum_{i} P_{i,t}^{MT} \tag{3.5}$$

$$C^{REV} = \rho^{C} \sum_{t} \sum_{i} P_{i,t}^{C} \Delta t + \rho^{S} \sum_{t} P_{1,t}^{+} \Delta t - \rho^{B} \sum_{t} P_{1,t}^{-} \Delta t \tag{3.6}$$

$$P_{1,t} = P_{1,t}^{-} - P_{1,t}^{+}, \forall P_{1,t}^{+}, P_{1,t}^{-} \geqslant 0 \tag{3.7}$$

The objective function (3.1) consists of five parts: investment cost (C^{INV}), operation and maintenance (O&M) cost of DGs (C^{OM}), fuel cost (C^{FC}) and emission penalty cost of fossil fuel sourced MTs (C^{EMI}) and the total revenue of the microgrid (C^{REV}). Equation (3.2) is the investment cost that represents the amortized one-time up-front costs of all categories and types of DGs, where inv^{MT}, inv^{WT} and inv^{PV} are capital investments for MT, WT and PV (\$/kW), respectively. C^{MT}, C^{WT} and C^{PV} are one discrete increment of capacity (kW) of MT, WT and PV, respectively. O&M cost in Equation (3.3) represents costs of operation and maintenance, consumables and replacement elements of all DGs during the planning horizon. om_t^{MT}, om_t^{WT} and om_t^{PV} are O&M costs for certain types of DG (\$/kWh) at time t. Fuel cost and emission penalty cost of MTs are described in Equation (3.4) and (3.5) where α^{FC}, α^{EMI} and σ are fuel price (\$/kWh), emission price (\$/kWh) and emission factor of MT. Equation (3.6) describes the total revenues that are achieved by selling the electricity to customers in the microgrid at price ρ^{C} (\$/kWh) and profits through the energy transactions with the main grid. The price ρ^{B} (\$/kWh) is the sale price at which the mail grid sells electricity to the microgrid, and ρ^{S} (\$/kWh) is called the feed-in tariff at which microgrid sells electricity back to the main grid. The electricity transaction is defined by Equation (3.7). $P_{1,t}^{+}$ and $P_{1,t}^{-}$ are power surplus and deficiency of the microgrid at time t respectively.

The binary indicators $f_{i,j,l}^{MT}$, $f_{i,j,l}^{WT}$ and $f_{i,j,l}^{PV}$ are decision variables that represent whether the kth increment of jth type of DG (including microturbine, wind turbine, and PV unit) is deployed at bus i. The other continuous variables P, Q, V introduced in the following section will make the problem a mixed-integer linear programming (MILP) formulation.

3.1.2 Constraints

3.1.2.1 Power Flow Model

A simple radial network with DG is shown in Figure 3.1. The DG could be either MT, WT or PV.

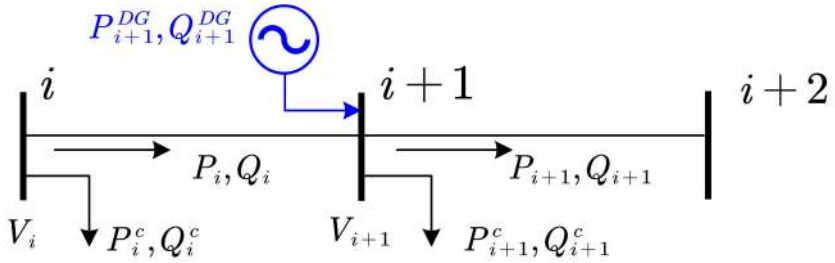

Figure 3.1: Schematic diagram of radial network

LinDistFlow is used for the power flow calculation. As introduced in Section 2.2.3. It is a linearized formulation of power flow that overcomes the complexity of quadratic equations and the non-convex feature of conventional DistFlow formulation. In the microgrid, LinDistFlow formulations among bus bars [93] are guaranteed by Constraints (3.8) - (3.10). The active and reactive load $P^C_{i,t}$, $Q^C_{i,t}$ are uncertain variables which are assumed to belong to uncertainty set $\mathbb{U}$.

$$P_{i+1,t} = P_{i,t} - P^C_{i+1,t} + P^{MT}_{i+1,t} + P^{WT}_{i+1,t} + P^{PV}_{i+1,t}, \quad \forall P^C_{i,t} \in \mathbb{U} \tag{3.8}$$

$$Q_{i+1,t} = Q_{i,t} - Q^C_{i+1,t} + Q^{MT}_{i+1,t} + Q^{WT}_{i+1,t} + Q^{PV}_{i+1,t}, \quad \forall Q^C_{i,t} \in \mathbb{U} \tag{3.9}$$

$$V_{i+1,t} = V_{i,t} - \frac{r_i P_{i,t} + x_i Q_{i,t}}{V_0} \tag{3.10}$$

The voltage at each bus should be within the utility's permissible limit, which is usually ±5% deviation from reference bus voltage V_0

$$V_{min} \leqslant V_{i,t} \leqslant V_{max} \tag{3.11}$$

The current of each line $I_{i,t}$ is maintained within the limit

$$-I_{max} \leqslant I_{i,t} \leqslant I_{max} \tag{3.12}$$

3.1.2.2 Operating Constraints

To achieve robust operation, operating constraints of each time segment must be taken into account in the planning horizon. We will have

$$0 \leq P_{i,t}^{MT} \leq \sum_{j}\sum_{l} f_{i,j,l}^{MT} C_{j}^{MT} \tag{3.13}$$

$$P_{i,t}^{WT} = \sum_{j}\sum_{l} f_{i,j,l}^{WT} \omega_{i,j,l,t}^{WT}, \quad \forall \omega_{i,j,l,t}^{WT} \in \mathbb{U} \tag{3.14}$$

$$P_{i,t}^{PV} = \sum_{j}\sum_{l} f_{i,j,l}^{PV} \omega_{i,j,l,t}^{PV}, \quad \forall \omega_{i,j,l,t}^{PV} \in \mathbb{U} \tag{3.15}$$

Constraints (3.16) - (3.18) represent the active power production requirements for all DGs. MT is a dispatchable generation while WT and PV are non-dispatchable units. It is assumed that every lth incremental active power produced by jth type WT ($\omega_{i,j,l,t}^{WT}$) is an uncertain variable and they will be restricted by the uncertainty set $\mathbb{U}$ during the planning horizon. The same assumption holds for PV ($\omega_{i,j,l,t}^{PV}$). To determine the uncertainty set $\mathbb{U}$, a specific technique based on historical weather information will be introduced in the next section.

$$pf_{min}^{MT} \leqslant pf^{MT} \leqslant 1 \tag{3.16}$$

$$pf_{min}^{WT} \leqslant pf^{WT} \leqslant 1 \tag{3.17}$$

$$pf_{min}^{PV} \leqslant pf^{PV} \leqslant 1 \tag{3.18}$$

$$Q^{MT} = \pm P^{MT} \cdot tan\left(cos^{-1}(pf^{MT})\right) \tag{3.19}$$

$$Q^{WT} = \pm P^{WT} \cdot tan\left(cos^{-1}(pf^{WT})\right) \tag{3.20}$$

$$Q^{PV} = \pm P^{PV} \cdot tan\left(cos^{-1}(pf^{PV})\right) \tag{3.21}$$

Constraints (3.19) - (3.24) represent the requirements for inverter-based DGs. The reactive power Q^{MT},Q^{WT} and Q^{PV} are adjustable based on the power factor pf^{MT},pf^{WT} and pf^{PV} required by the utility.

Constraint (3.25) is the operational requirement for the microgrid at the islanded mode [151]. The installed capacity of DG units should be higher than or equal to a

certain percentage of load within the microgrid. Therefore, τ represents the minimum requirement for DG capacity.

$$\tau \sum_{t}\sum_{i} P_{i,t}^{c} <= \sum_{t}\sum_{i}\sum_{j}\sum_{l} f_{i,j,l}^{MT} C_{j}^{MT} + \sum_{i}\sum_{j}\sum_{l} f_{i,j,l}^{WT} C_{j}^{WT} + \sum_{i}\sum_{j}\sum_{l} f_{i,j,l}^{PV} C_{j}^{PV} \tag{3.22}$$

3.2 Data-driven Based Forecasting Model for Uncertainties

3.2.1 Renewable Energy Resource Availability

Suppose the utility and related authorities have access to the empirical database that stores meteorological data from on-site measurements, i.e. solar irradiance and wind speed. One of the major work prior to the DG planing is the thorough assessment of the RES availability because of the intermittent nature of RES-based DGs.

3.2.1.1 Wind Turbine Output Power Model

Wind power generation models can be classified into three categories. The first one comprises of fluid dynamics that considers air density, swept area of wind turbine rotor and power coefficient, wind speed and electro-mechanical conversion efficiency. The second category is a non-liner model based on wind speed on-the-spot. The third category is the regression model or AI-based model developed from the average normalised power curve of historical data, which is not available for a new area without commercial MTs.

In the study, the second type is used. Compared with the first one, the complexity of the model is simpler with fewer parameters at the cost of slightly reduced model accuracy. The output power of a wind turbine is dependent on the average wind speed $v_{av,t}$ at the site as well as the parameters of the power performance curve. Therefore, once the speed data is gathered for a specific time segment t, the output power of each

WT type is calculated according to its corresponding characteristics:

$$\omega_t^{WT} = \begin{cases} 0 & 0 \leq v_{av,t} < v_{ci} \\ \frac{(v_{av,t} - v_{ci})}{(v_r - v_{ci})} * P_r^{wt} & v_{ci} \leq v_{av,t} < v_r \\ P_r^{wt} & v_r \leq v_{av,t} < v_{co} \\ 0 & v_{co} \leq v_{av,t} \end{cases} \tag{3.23}$$

where P_r^{WT} is the rated power generation of one wind turbine, and v_{ci}, v_{co}, v_r are the wind turbine cut-in, cut-off and rated wind speeds respectively.

3.2.1.2 PV Module Output Power Model

Similar to WT, there are also several popular generation models, such as the model related to solar irradiance, solar PV array area, and solar PV system efficiency and empirical regression models. Here, we will use a simplified model based on the current-voltage (I-V) relationship [156]. The output power of the PV module is assumed to be working under maximum power point tracking (MPPT) which is usually the case when they are connected to an inverter. The output power is dependent on the solar irradiance and ambient temperature on the site as well as the characteristics of the module itself. Therefore, once the solar irradiance and ambient temperature data is collected for a specific time period, the output power for different type of solar cells could be calculated using the following equation:

$$\omega_t^{PV} = FF * V * I \tag{3.24}$$

$$FF = \frac{V_{MPP} * I_{MPP}}{V_{oc} * I_{sc}} \tag{3.25}$$

$$T_c = T_a, t + s_{av,t}\left(\frac{T_{no} - 20}{0.8}\right) \tag{3.26}$$

$$V = V_{oc} - K_v * T_c \tag{3.27}$$

$$I = s_{av}\left[I_{sc} + K_i\left(T_c - 25\right)\right] \tag{3.28}$$

where FF is the fill factor of solar cell. T_c is the cell temperature ($^\circ C$). T_a is the ambient temperature ($^\circ C$). s_{av} is the average solar irradiance (kW/m^2). K_v and K_i represent voltage temperature coefficient ($V/^\circ C$) and current temperature coefficient ($A/^\circ C$). T_{no}

is the nominal operating temperature of cell ($°C$). I_{sc} and V_{oc} are short circuit current (A) and open-circuit voltage (V). I_{MPP} and V_{MPP} are current (A) and voltage (V) at the maximum power point.

3.2.2 Load Profile Analysis

Load profile analysis is another important prerequisites for DG planning. In order to satisfy the stable operation of the microgrid, the power generation must be matched with the load from hour to hour. Thanks to the smart meter technology, for the network expansion nowadays, it is more common for the utility companies to get access to the records of customers' load profiles. For instance, there will be a dataset shown as Figure 1. $D = \{D^1, D^2, ..., D^t\}$ is a vector of measurements of demand at different load points at time slot t. We will have $D^t = \{d_1^t, d_2^t, ..., d_i^t\}$ where d_i^t is the demand at ith location at time slot t. The temporal-spatial data is shown in Figure 3.2. The whole database will continuously store the data collected from n different locations for a period of time and mark them with specific location labels. Each day the smart meter will automatically record the power consumption where it is installed at reprogrammed time interval. Therefore, each day there will be nt sample loads in the database.

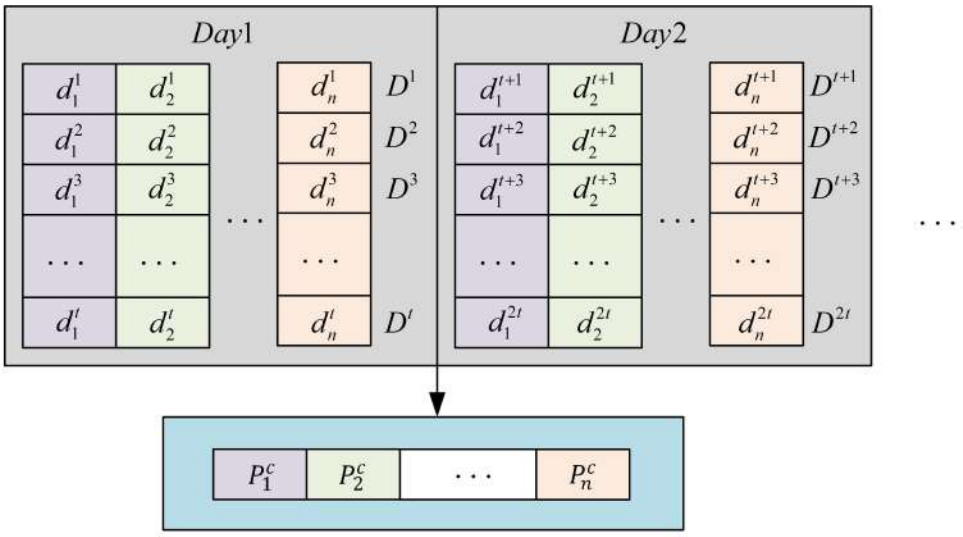

Figure 3.2: Schematic diagram of the database of a load profile.

The time span of the database determines the reliability and accuracy of the un-

certainty set of demand $P^c = \{P_1^c, P_2^c, ..., P_n^c\}$ where $P_i^c = \{d_i^1, d_i^2, ..., d_i^{t+1}, d_i^{t+2}, ...\}$. For instance, on the one-day basis, there would be t elements in the P_i^c vector. It is assumed that there is no variation of the load profile from season to season, and from weekday to weekend. For a long time span, there is no doubt more information like daily variations of load demand will remain. If database has several years of load profile, it is attractive to find out an effective machine-learning method to cope with large amounts of high-dimensional data.

3.2.3 Data-driven Uncertainty Set

Under the framework of proposed DDARDGP, uncertainty set refers to the region where uncertain variables or called uncertain parameters reside. It guarantees all the constraints are satisfied for all points within the uncertainty set. In the previous section, four variables are indicated as uncertain variables, which are active and reactive load $P_{i,t}^C$, $Q_{i,t}^C$, lth incremental active power produced by jth type WT ($\omega_{i,j,l,t}^{WT}$) and lth incremental active power produced by jth type PV ($\omega_{i,j,l,t}^{PV}$). To accurately describe the boundaries and capture the correlated information of the high dimension data, data-driven uncertainty set is used. Compared with other uncertainty sets introduced in Section 2.4.3.2, like box uncertainty set and budget uncertainty set, the data-driven one finds the better trade-off between tractability and conservativeness for RO problem because the set in the function space is tighter.

3.2.3.1 Dirichlet Process Mixture Model

Probabilistic models have been widely used in machine learning to model distributions over observed data. Traditional parametric models using a fixed and finite number of parameters can suffer from over- or under-fitting of data when there is a misfit between the complexity of the model and the amount of data available. As a result, the guess of a single distribution function, or model selection with the right complexity, is often an important issue in parametric modeling. For instance, the wind speed characteristics is often described by using the Weibull distribution [157]. However, in the same predefined

time period, solar irradiation is defined based on Beta distribution, which might not be suitable for describing its stochastic nature. It is because the solar irradiation has unique daily pattern. The Beta distribution used in [157] only works on specific dataset.

The Bayesian nonparametric approach is an alternative approach to parametric modeling and selection. It defines prior and posterior distributions on a single fixed parameter space. As opposed to the parametric models, the dimension of the parameter space is adaptive to data size. By using a model with an unbounded complexity, the underfitting issue is mitigated.

The Dirichlet process mixture model (DPMM) is a popular clustering implementation of Bayesian nonparamatirc models. Compared with other machine-learning algorithms, i.e. K-means and Gaussian mixture model, it can naturally adapt the number of clusters to the complexity of the data to avoid overfitting.

The Dirichlet process is the fundamental prior on probability distributions for DPMM. It is a distribution over distributions, i.e. each draw from a Dirichlet process is itself a distribution. Let G_0 be a base measure, and α be a positive scalar. A random measure G can be generated as a Dirichlet process $G \sim DP(\alpha, G_0)$. For any partition $\{A_1, ..., A_k\}$, it fits the Dirichlet distribution.

$$(G(A_1), ..., G(A_k)) \sim Dir(\alpha G_0(A_1), ..., \alpha G_0(A_k)) \tag{3.29}$$

The construction of measure G follows the stick-breaking procedures [158]. Let $\eta_k \sim G_0$ for $k = \{1, 2, ...\}$ and δ_{η_k} denotes the Dirac delta indicator function at η_k. G is given by the expression

$$\pi_k(v) = v_k \prod_{j=1}^{k-1} (1 - v_j) \tag{3.30}$$

$$G = \sum_{k=1}^{\infty} \pi_k(v) \delta_{\eta_k} \tag{3.31}$$

where the stick lengths $\pi_k(v)$ are given by repeatedly breaking a stick of initial length 1 at points η_k. The length v_k draws from a beta distribution $Beta(a_k, b_k) \in (0, 1)$. Therefore, the stick could be broken into infinite number of pieces. Analogously, G is a mixture of infinite discrete components δ_{η_k} with proportions $\pi_k(v)$ as shown in Figure 3.3.

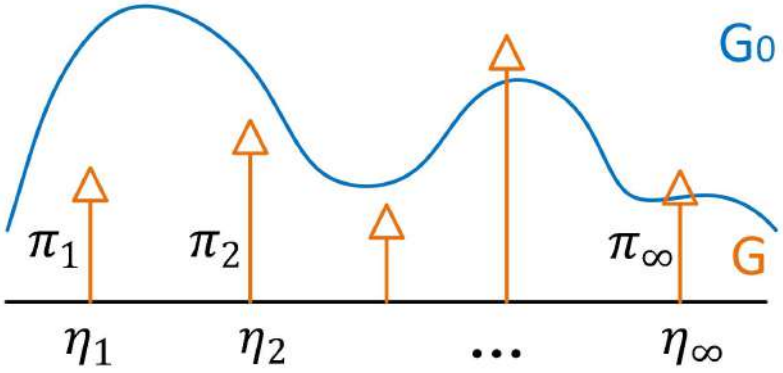

Figure 3.3: Construction of random measure G for DPMM

A generalization DPMM for observed data $Xn = \{x_1, x_2, ..., x_n\}$ can be written as

$$\begin{aligned} G|\{\alpha, G_0\} &\sim DP(\alpha, G_0) \\ \eta_k|G &\sim G \\ X_n|\eta_k &\sim p(x_n|\eta_k) \end{aligned} \tag{3.32}$$

Suppose each sampled data x_n is generated from a different distribution η_k with its own parameters. In the study, we choose a multivariate probability distribution - normal Wishart distribution $NW(\mu_k, \kappa_k, \nu_k, \Psi_k)$ - as the conjugate prior of η_k. The distribution over distribution η_k follows G which is generated based on the length $v_k \sim Beta(a_k, b_k)$. Due to its computational efficiency and deterministic nature, variational inference has been used to approximate the likelihood and posterior distributions in DPMM from observed data. Refer to Appendix A, a detailed derivation will be provided for parameter setting of $\Xi = argmax\ p(a_k, b_k, \mu_k, \kappa_k, \nu_k, \Psi_k|X_n)$.

3.2.3.2 Formulation of Data-driven Uncertainty Set

The construction of the Bayesian nonparametric uncertainty set based on DPMM is to find out the most valuable mixtures that represent the posterior predictive distribution of $p(x_{n+1}|X_n, \Xi)$. Because of the nature of conjugate distribution, the posterior distribution is in the same probability distribution family as the NW prior. The posterior predictive distribution of NW distribution follows Student's t-distribution with $\nu_k + 1 - dim(X_k)$

degrees of freedom [159]. It can be written as

$$p(x_{n+1}|X_n,\Xi) \sim \sum_k \lambda_k \mathbf{St}_{\nu'_k+1-dim(X_k)}\left(\mu'_k, \frac{\kappa'_k+1}{\kappa'_k(\nu'_k+1-dim(X_k))}\Psi'^{-1}_k\right) \tag{3.33}$$

$$\lambda_k = \begin{cases} \dfrac{a_k}{a_k+b_k}\displaystyle\prod_{j=1}^{k-1}\frac{b_j}{a_j+b_j}, & k=1...,T-1 \\ 1-\displaystyle\sum_{j=1}^{T-1}\lambda_k, & k=T \end{cases} \tag{3.34}$$

$$\mu'_k = \frac{\kappa_k\mu_k + n_k\overline{x_k}}{\kappa_k+n_k} \tag{3.35}$$

$$\kappa'_k = \kappa_k + n_k \tag{3.36}$$

$$\nu'_k = \nu_k + n_k \tag{3.37}$$

$$\Psi'^{-1}_k = \Psi^{-1}_k + S_k + \frac{\kappa_k n_k}{\kappa_k+n_k}(\mu_k-\overline{x_k})(\mu_k-\overline{x_k})^T \tag{3.38}$$

$$S_k = \sum_{i=1}^{n}(x_i-\overline{x_k})(x_i-\overline{x_k})^T \tag{3.39}$$

where λ_k is the weight of kth mixture component of DPMM. The weight is calculated based on the stick length in Equation (3.34), indicating the importance of the kth mixture component. $\mu'_k, \kappa'_k, \nu'_k, \Psi'_k$ are the parameters of NW posterior distribution. n_k and $\overline{x_k}$ are the data size and the mean value belongs to mixture component k.

Suggest a λ_{th} as the truncation threshold value, only mixture components with weights larger than λ_{th} will be considered. Therefore, the Bayesian nonparametric uncertainty set $\mathbb{U}$ is an union of T basic uncertainty sets as follows

$$\mathbb{U} = \mathbb{U}_1 \cup \mathbb{U}_2 ... \cup \mathbb{U}_T \tag{3.40}$$

The method determines the number of clusters systematically and automatically rather than specifying this number as a priori. Each basic uncertainty set $\mathbb{U}_k$ for component k is defined based on t value

$$\mathbb{U}_k = \left\{x_{n+1}|x_{n+1} = \mu'_k + \zeta l_k \Lambda, \qquad \|\Lambda\|_n \le 1\right\} \tag{3.41}$$

where $l_k = \sqrt{\frac{\kappa'_k+1}{\kappa'_k(\nu'_k+1-dim(X_k))}}\Psi'^{-1/2}_k$. Λ is the latent uncertainty and can choose norm 1,2 or ∞. ζ is a scaling factor that adjusts the confidence interval of the uncertainty set.

The proposed construction method of the uncertainty set is cast as a union of multiple basic uncertainty sets. Its geometric shape is flexible enough to capture the distribution of high-dimensional uncertain data. Outliers will be removed through a self-adaptive truncation process without additional computation complexity. One of the significant highlights is that the proposed uncertainty sets are suitable for multi-dimensional data processing. As the latent uncertainty Λ establishes the underlying relationship between multidimensional data, a polyhedral set is devised for each basic uncertainty set, which benefits the resulting DDARDGP problem with enormous computational efficiency.

3.3 Solution Methodologies

3.3.1 Adaptive Robust MG Planning Model

The solution of a single-stage RO is always criticized to be over conservative. To address the issue, Equation (3.1) is reformulated into a two-stage adaptive robust optimization modelling framework as shown below in Equation (3.42). The adaptive robust optimization framework has already been widely used in power system applications, such as unit commitment [160], economic dispatch [161] , reactive power optimization [162], etc., to immunize against the uncertainties in RES generation and load demand. The first-stage cost only covers the investment cost, O&M cost of DG units, and the second-stage costs will include the remaining fuel cost, emission penalty cost and electricity cost exchanged with the main grid and regional customers. Therefore, the first-stage forms the here-and-now part, which only includes the binary decision variables that indicate whether or not a certain type of DG should be installed. The second-stage called wait-and see decision. It includes all the other costs relating to the daily schedule of the system once DGs are installed.

The DDARDGP problem can be generalized as:

$$\min_{\mathbf{f}\in\mathbb{F}} \mathbf{A}^T\mathbf{f} + \max_{\mathbf{u}\in\mathbb{U}} \min_{\mathbf{y}\in\mathbb{Y}(\mathbf{f},\mathbf{u})} \mathbf{B}^T\mathbf{y} + \mathbf{C}^T\mathbf{u} \tag{3.42}$$

s.t.

$$\mathbf{Dy} + \mathbf{Eu} = \mathbf{m} \tag{3.43}$$

$$\mathbf{Jf} + \mathbf{Gy} + \mathbf{Hu} \leq \mathbf{n} \tag{3.44}$$

where $\mathbf{f}$ denotes the vector of all first-stage decisions including $\mathbf{f}^{MT} = [f^{MT}_{i,j,l}]$, $\mathbf{f}^{WT} = [f^{WT}_{i,j,l}]$ and $\mathbf{f}^{PV} = [f^{PV}_{i,j,l}]$ $\forall i,j,l$. The binary set $\mathbb{F} = \{0,1\}^{3*I_b*J_g*L_i}$ imposes constraints on L_i increments of J_g types of MT, WT and PV in a microgrid with I_b candidate buses. $\mathbf{A}$ and $\mathbf{J}$ are corresponding parameter matrices for the binary variables $\mathbf{f}$. Meanwhile in the second stage, $\mathbb{U}$ represents the uncertainty set for the vector $\mathbf{u}$ that includes the wind and solar power output $\omega^{WT} = [\omega^{WT}_{i,j,l,t}]$, $\omega^{PV} = [\omega^{PV}_{i,j,l,t}]$ $\forall i,j,l,t$, and the active & reactive load demand $P^C = [P^C_{i,t}]$, $Q^C = [Q^C_{i,t}]$ $\forall i,t$. $\mathbf{C}$, $\mathbf{E}$ and $\mathbf{H}$ are parameter matrices for the uncertain variables $\mathbf{u}$. $\mathbb{Y}(f,u) = \{(f,u)|Eqns(3.43,3.44)\}$ represents the feasible region for the vector of other continuous variables $\mathbf{y} = [P^{MT};P^{WT};P^{PV};Q^{MT};Q^{WT};Q^{PV};P;Q;V]$ where $P^{MT} = [P^{MT}_{i,t}]$, $P^{WT} = [P^{WT}_{i,t}]$, $P^{PV} = [P^{PV}_{i,t}]$, $Q^{MT} = [Q^{MT}_{i,t}]$, $Q^{WT} = [Q^{WT}_{i,t}]$, $Q^{PV} = [Q^{PV}_{i,t}]$, $Q = [Q_{i,t}]$, $V = [V_{i,t}]$ $\forall i,t$ and $P = [P^+_{1,t},P^-_{1,t},P_{i,t}]$ $\forall i,t,i \neq 1$. The corresponding parameter matrices in the objective function and inequality constraints are represented by $\mathbf{B}$ and $\mathbf{G}$. $\mathbf{m}$ and $\mathbf{n}$ are the vectors for the remaining scalars in equality constraints and inequality constraints, respectively.

3.3.2 Solution Algorithm

The proposed two-stage DDARDGP model (3.42)-(3.44) is very difficult to compute. In [163], two kinds of solving methods have been discussed. One is the Benders decomposition (BD) technique and the other is the CC&G algorithm. Compared with the Benders-style cutting plane methods, the CC&G algorithm is a general procedure with a unified approach to deal with optimality and feasibility. It is proved that the latter performs an order of magnitude faster on a two-stage robust problem [163].

To apply the CC&G in the proposed linear formulation model, the uncertainty is chosen to be a polyhedron. The optimal solution for the maximization problem over u is an extreme point of one of the basic polyhedral uncertainty set $\mathbb{U}_k$. In view of this, we can solve the optimization problem by enumerating all the extreme points. However from the aspect of computational efficiency, just think about the master problem will generate 2^{n_f} possibilities where n_f is the number of first-stage variables. It is prohibitively challenging to solve such a problem with external enumeration of uncertain variables. Therefore, the problem is spilt to two stages. In the first-stage, the master problem (MP) is formulated to generate significant scenarios.

(MP)

$$\min_{\mathbf{f}\in\mathbb{F}} \mathbf{A}^T\mathbf{f}+\xi \tag{3.45}$$

s.t.

$$\xi \geq \mathbf{B}^T\mathbf{f}+\mathbf{C}^T\mathbf{u} \tag{3.46}$$

$$\mathbf{Dy}+\mathbf{Eu}=\mathbf{m} \tag{3.47}$$

$$\mathbf{Jf}+\mathbf{Gy}+\mathbf{Hu}\leq\mathbf{n} \tag{3.48}$$

The result of the master problem is a relaxation of the original one as the constraints of continuous and uncertain variables are not defined. Thus, it yields a lower bound LB and the result of the master problem is recorded as $\hat{\mathbf{f}}$. Further in the second-stage, the remaining part that does not involve binary variables is decomposed into a set of subproblems ($SP_k, k = 1,...,T$) for later stage. Each subproblem SP_k corresponds to a basic uncertainty set $\mathbb{U}_k$ as introduced in Equation (3.41). The subproblem can be defined as:

(SP_k)

$$\max_{\mathbf{u}\in\mathbb{U}_k} \min_{\mathbf{y}\in\mathbb{Y}\{\mathbf{f},\mathbf{u}\}} \mathbf{B}^T\mathbf{y}+\mathbf{C}^T\mathbf{u} \tag{3.49}$$

s.t.

$$\mathbf{Dy}+\mathbf{Eu}=\mathbf{m} \tag{3.50}$$

$$\mathbf{Jf}+\mathbf{Gy}+\mathbf{Hu}\leq\mathbf{n} \tag{3.51}$$

The subproblem leads to a series of upper bound UB_k to identify the worst-case scenario of uncertainties. The optimality cuts which is associated with worst-case uncertain variables are then added to the master problem. To solve the bi-level "max-min" subproblem which is difficult to be solved with open-shelf solvers, KKT optimality conditions [163] of the problem is formulated as follows:

$$\mathbf{Dy} + \mathbf{Eu} = \mathbf{m} \tag{3.52}$$

$$\mathbf{B}^T + \gamma^T \mathbf{G} + \delta^T \mathbf{D} = 0 \tag{3.53}$$

$$\mathbf{Jf} + \mathbf{Gy} + \mathbf{Hu} \leq \mathbf{n} \tag{3.54}$$

$$\gamma^T (\mathbf{n} - \mathbf{Jf} - \mathbf{Gy} - \mathbf{Hu}) = 0 \tag{3.55}$$

Constraint (3.55) is the complementary slackness condition, which means only one of γ and $\mathbf{n} - \mathbf{Jf} - \mathbf{Gy} - \mathbf{Hu}$ is 0. It can be transformed together with Constraint (3.54) by the Big-M method [151] and yields

$$0 \leq \mathbf{n} - \mathbf{Jf} - \mathbf{Gy} - \mathbf{Hu} \leq M\sigma \tag{3.56}$$

$$0 \leq \gamma \leq M(1 - \sigma) \tag{3.57}$$

where M is a large value and σ is a binary variable. KKT condition is sufficient when the subproblem problem is convex. The constraints become (3.52), (3.53), (3.56) and (3.57).

Unlike the conventional RO problem, the proposed DDARDGP model has combined multiple basic uncertainty sets, which cannot be solved by the original CC&G algorithm. The flow chart of a modified CC&G [150] algorithm for DDARDGP is shown in Figure 3.4. In each SP, the corresponding extreme points are solved iteratively for a certain MP result, which generates optimality cuts. In the case where SP is an infeasible problem, the infeasible cuts will be generated. Both infeasible cuts and worse-case optimality cuts will be added to the master problem.

The comprehensive procedures of the solving method can be summarized as follows:

Step 0: Initialization. Set the lower bound $LB = -\infty$, the upper bound $UB = +\infty$, the tolerance of the optimality gap ϵ and iteration number $g = 1$.

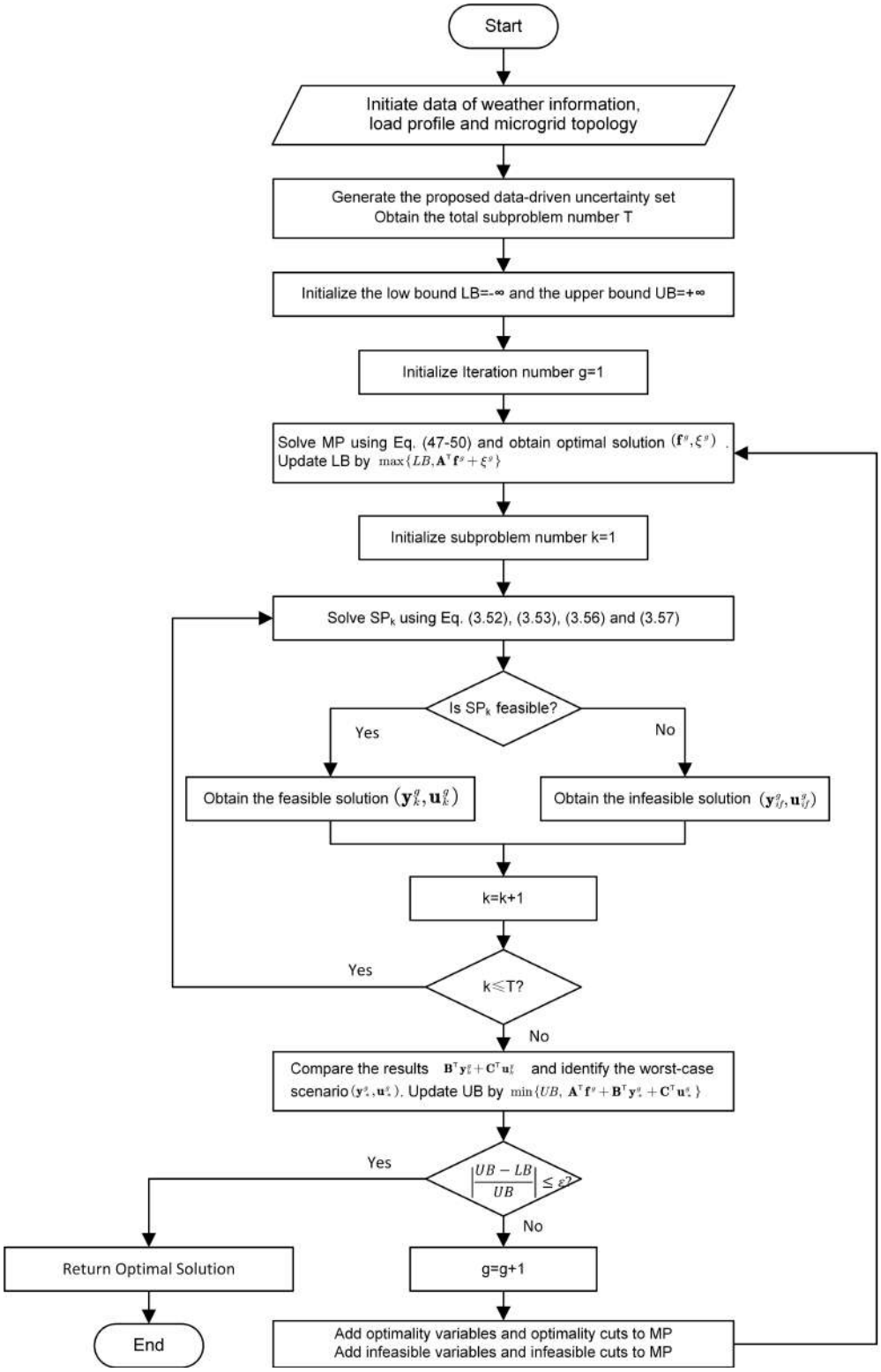

Figure 3.4: Flowchart of the solution algorithm for DDARDGP framework.

Step 1: Solve the master problem (MP) and obtain the optimal solution $(\mathbf{f}^g, \xi^g)$. Update the lower bound $LB = max\{LB, \mathbf{A}^T\mathbf{f}^g + \xi^g\}$.

Step 2: Solve all the subproblems SP_k^g using $\mathbf{f}^g$ and obtain the optimal solution $\mathbf{Q}_k^g = (\mathbf{y}_k^g, \mathbf{u}_k^g)$.

Step 3: Compare $\mathbf{Q}_k^i$ for all $k = 1, 2, ...T$ and identify the worst-case scenario $\mathbf{Q}_*^g = (\mathbf{y}_*^g, \mathbf{u}_*^g)$ and infeasible scenario set $\mathbf{Q}_{if}^g = (\mathbf{y}_{if}^g, \mathbf{u}_{if}^g)$. Update the upper bound $UB = min\{UB, \mathbf{A}^T\mathbf{f}^g + \mathbf{B}^T\mathbf{y}_*^g + \mathbf{C}^T\mathbf{u}_*^g\}$.

Step 4: Denote the optimality gap as $Gap = \left|\frac{UB-LB}{UB}\right|$. If the $Gap < \epsilon$, the algorithm terminates and output the optimal decision. Otherwise update the MP by adding new variables $\mathbf{y}_*^g, \mathbf{y}_{if}^g$ and corresponding optimality cuts ($\mathbf{D}\mathbf{y}_*^g + \mathbf{E}\mathbf{u}_*^g = \mathbf{m}$ and $\mathbf{F}\mathbf{f} + \mathbf{G}\mathbf{y}_*^g + \mathbf{H}\mathbf{u}_*^g \leq \mathbf{n}$) and infeasible cuts ($\mathbf{D}\mathbf{y}_{if}^g + \mathbf{E}\mathbf{u}_{if}^g = \mathbf{m}$ and $\mathbf{F}\mathbf{f} + \mathbf{G}\mathbf{y}_{if*}^g + \mathbf{H}\mathbf{u}_{if}^g \leq \mathbf{n}$). Update $g = g + 1$ and go back to Step 1.

3.4 Case Study: Distributed Generation Planning in a Microgrid

In the section, a modified IEEE 33-bus 12.66 kV distribution system is used as the test microgrid to validate the DG planning design with the DDARDGP framework. To find the optimal DG mix, the proposed methodologies will be analysed under various conditions.

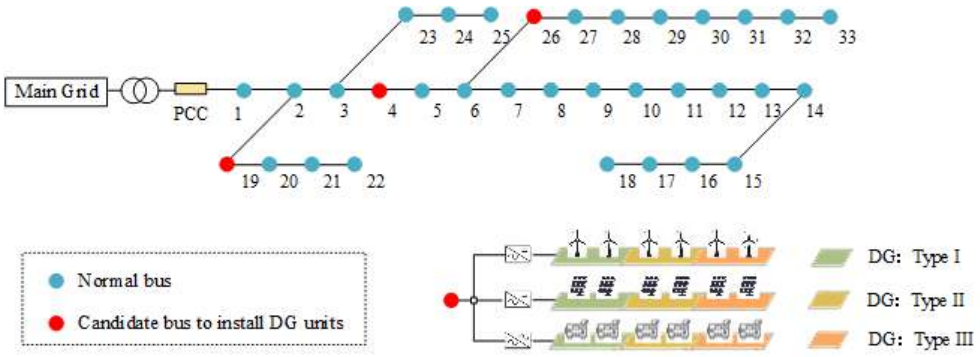

Figure 3.5: The schematic microgrid test system

3.4.1 System Under Study

The single line topology of the system is shown in Figure 3.5 and line data can be found in [164]. The total basic load is 3715 kW and 2300 kVAR. In the figure, the blue nodes are denoted as normal buses where load demands are connected. The red nodes are three possible sites (bus 4, 19 and 26) that not only have load demands connected but also can be chosen to install DG units due to its geographic advantages. Each possible site could install either wind generation, PV panels or fuel-based generation. The capital costs for MT, WT and PV generations are $2293/kVA, $1882/kVA and $4004/kVA, respectively, while the O&M costs of the three DG units are $0.012/kWh, $0.01/kWh and $0.01/kWh, respectively. For MT, the fuel cost and emission penalty cost are $0.63/kWh and $0.02kg/kWh, respectively. The emission factor is $0.003 kg/kWh. All the aforementioned parameters are taken from [151].

The planning horizon of the DG units in the microgrid is 15 years and the time resolution of the load and DG units is one hour. For each different category of DG units, there are three different types. The related parameters and characteristics for WT and PV modules to calculate the hourly power generation are listed in Table 3.1. It is noted that the PV modules are working in a 15,000-series configuration, thus the peak power output of the three type are 750kW, 795kW and 900kW, respectively. Meanwhile, 10 same type MTs work together to meet the demand, which can output the peak power of 1000kW, 1500kW and 2000kW, respectively.

All DG units are assumed to work with 0.95 power factor according to the grid code. The voltage range for all buses are set to [0.95, 1.05]. More than one type of individual DG categories are available, but there is an upper limit, for instance 2 in the case, because of land limitations.

3.4.2 Performance Comparison of DG Units

As defined in the previous section, fuel-based MT generations will operate as dispatchable units. Their performance is only related to their rated power outputs. In the meanwhile,

Table 3.1: Characteristics of available microturbines, wind turbines and PV modules.

Micro-turbine Parameters			
Parameters	Type I	Type II	Type III
Rated Power (kW)	100	150	200
Wind Turbine Parameters			
Parameters	Type I	Type II	Type III
Rated Power(kW)	850	1100	2000
Cut-in speed (m/s)	4	3.5	4
Rated speed (m/s)	10	12	11.5
Cut-out speed (m/s)	25	24	25
PV Module Parameters [156]			
Parameters	Type I	Type II	Type III
Peak Power (W)	50	53	60
Open circuit voltage (V)	55.50	21.70	21.10
Short circuit current(A)	1.80	3.40	3.80
Voltage at maximum power point (V)	38.00	17.40	17.10
Current at maximum power point (A)	1.32	3.05	3.50
Voltage temperature coefficient ($mV/°C$)	194.00	88.00	75.00
Current temperature coefficient ($mA/°C$)	1.40	1.50	3.10
Nominal cell operating temperature ($°C$)	43.00	43.00	43.00

all the power generated by WT and PV panels will be consumed by the microgrid, which will strongly be influenced by the weather condition (i.e. wind speed, solar irradiance and ambient condition) and unit parameters. Figure 3.6 illustrates the power generation profiles of the 6 type renewable generations of a typical day in the winter time. The fluctuation of the results reveals that no certain category of generation outperforms the others in all weather conditions, which proves the importance of DG mix selection, despite its sizing and location.

The fluctuation of the results shows that no certain type of generation outperforms the others in all weather conditions, which proves the importance of DG mix selection, despite its sizing and location.

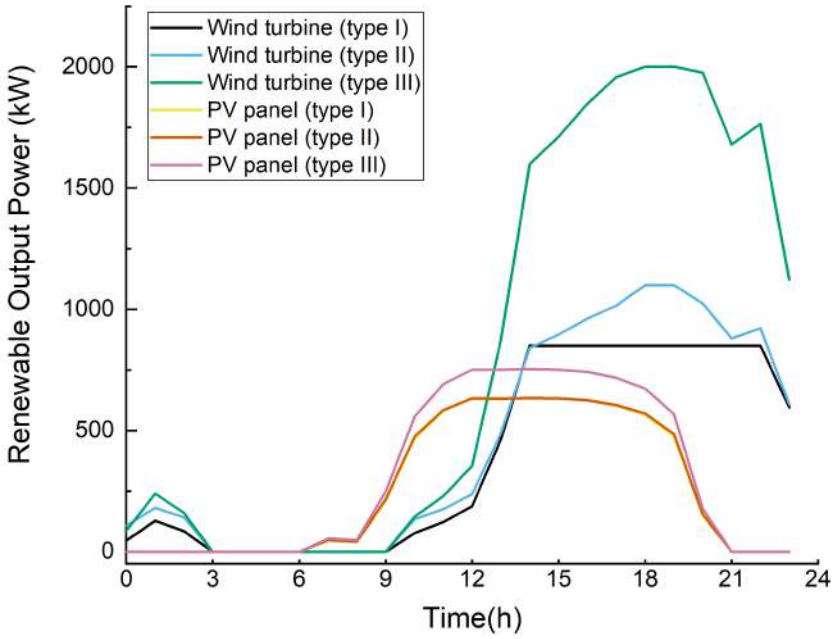

Figure 3.6: Output power of different types of renewable generations.

3.4.3 Evaluation of Uncertainty Set

The uncertainties in the proposed DDARDGP problem come from three factors: the power outputs of WT, PV and load demend of the microgrid. To predict the hourly renewable generation output, solar irradiance, ambient temperature and wind speed figures are needed according to models discussed in Section 3.2.1. Here, one year data at three weather stations obtained from SAURN (Southern African Universities Radiometric Network) [165] is used for three candidate buses 4, 19 and 26 respectively. The load profile is obtained from NYISO for all connected loads. Although in practice every consumer has its own energy usage preference, the analysis of the topic is beyond the scope of work here. The planner can easily change the setting if there are other load profiles. Therefore, the dimension of the corresponding uncertainties is $N_{bus} * TYPE_{WT} + N_{bus} * TYPE_{PV} + TYPE_{load} = 3 * 3 + 3 * 3 + 1 = 19$.

The DPMM-based uncertainty sets are a combination of infinite sets. It is adaptive to data size with a predefined truncation threshold value ω_{th}, which is the minimal weight of mixture components. Table 3.2 shows the results of set number and data coverage under different threshold values. It is noted that the rate of data coverage is negative

correlated with the threshold. Although a smaller number of sets will decrease the computational complexity in DDARDGP framework for planning, the data distribution is not fully captured. To find the balance between computational complexity and set accuracy, ω_{th} is set to be 0.02 in the case study.

Table 3.2: Uncertainty sets under different truncation threshold value ω_{th}

ω_{th}	Set number of uncertainties	Data coverage rate (%)
0.006	11	99.45
0.007	11	99.27
0.008	11	98.78
0.009	10	98.76
0.01	9	97.77
0.02	9	97.18
0.03	8	93.61
0.04	7	93.13
0.05	7	89.53
0.06	6	83.86
0.07	5	77.05
0.08	4	72.34

The set-up of the polyhedron for each uncertainty set is based on Equation (3.49). The scaling factor ζ for confidence level is determined by looking up the t-distribution table shown in Figure 3.7. The degrees of each uncertainty set will vary from several hundred to more than two thousand. As the t value does not change much for degrees over 100, we could choose the value with the infinite degree for convenience.

3.4.4 Numerical Results of DG Planning for the Microgrid

Once the uncertainty sets are ready, the proposed modified CC&G algorithm will be used to solve DDARDGP problem. All the simulation results are implemented with CPLEX 12.8.0 using a computer with an Inter(R) Core(TM) i5-6400 CPU at 2.7 GHz.

3.4.4.1 Comparisons under Different Confidence Levels

Figure 3.8 illustrates the results of cost of the utility which is responsible for the DG planning and 15-year operation of the microgrid under different confidence level. As

cum. prob	$t_{.50}$	$t_{.75}$	$t_{.80}$	$t_{.85}$	$t_{.90}$	$t_{.95}$	$t_{.975}$	$t_{.99}$	$t_{.995}$	$t_{.999}$	$t_{.9995}$
one-tail	0.50	0.25	0.20	0.15	0.10	0.05	0.025	0.01	0.005	0.001	0.0005
two-tails	1.00	0.50	0.40	0.30	0.20	0.10	0.05	0.02	0.01	0.002	0.001
df											
1	0.000	1.000	1.376	1.963	3.078	6.314	12.71	31.82	63.66	318.31	636.62
2	0.000	0.816	1.061	1.386	1.886	2.920	4.303	6.965	9.925	22.327	31.599
3	0.000	0.765	0.978	1.250	1.638	2.353	3.182	4.541	5.841	10.215	12.924
4	0.000	0.741	0.941	1.190	1.533	2.132	2.776	3.747	4.604	7.173	8.610
5	0.000	0.727	0.920	1.156	1.476	2.015	2.571	3.365	4.032	5.893	6.869
6	0.000	0.718	0.906	1.134	1.440	1.943	2.447	3.143	3.707	5.208	5.959
7	0.000	0.711	0.896	1.119	1.415	1.895	2.365	2.998	3.499	4.785	5.408
8	0.000	0.706	0.889	1.108	1.397	1.860	2.306	2.896	3.355	4.501	5.041
9	0.000	0.703	0.883	1.100	1.383	1.833	2.262	2.821	3.250	4.297	4.781
10	0.000	0.700	0.879	1.093	1.372	1.812	2.228	2.764	3.169	4.144	4.587
11	0.000	0.697	0.876	1.088	1.363	1.796	2.201	2.718	3.106	4.025	4.437
12	0.000	0.695	0.873	1.083	1.356	1.782	2.179	2.681	3.055	3.930	4.318
13	0.000	0.694	0.870	1.079	1.350	1.771	2.160	2.650	3.012	3.852	4.221
14	0.000	0.692	0.868	1.076	1.345	1.761	2.145	2.624	2.977	3.787	4.140
15	0.000	0.691	0.866	1.074	1.341	1.753	2.131	2.602	2.947	3.733	4.073
16	0.000	0.690	0.865	1.071	1.337	1.746	2.120	2.583	2.921	3.686	4.015
17	0.000	0.689	0.863	1.069	1.333	1.740	2.110	2.567	2.898	3.646	3.965
18	0.000	0.688	0.862	1.067	1.330	1.734	2.101	2.552	2.878	3.610	3.922
19	0.000	0.688	0.861	1.066	1.328	1.729	2.093	2.539	2.861	3.579	3.883
20	0.000	0.687	0.860	1.064	1.325	1.725	2.086	2.528	2.845	3.552	3.850
21	0.000	0.686	0.859	1.063	1.323	1.721	2.080	2.518	2.831	3.527	3.819
22	0.000	0.686	0.858	1.061	1.321	1.717	2.074	2.508	2.819	3.505	3.792
23	0.000	0.685	0.858	1.060	1.319	1.714	2.069	2.500	2.807	3.485	3.768
24	0.000	0.685	0.857	1.059	1.318	1.711	2.064	2.492	2.797	3.467	3.745
25	0.000	0.684	0.856	1.058	1.316	1.708	2.060	2.485	2.787	3.450	3.725
26	0.000	0.684	0.856	1.058	1.315	1.706	2.056	2.479	2.779	3.435	3.707
27	0.000	0.684	0.855	1.057	1.314	1.703	2.052	2.473	2.771	3.421	3.690
28	0.000	0.683	0.855	1.056	1.313	1.701	2.048	2.467	2.763	3.408	3.674
29	0.000	0.683	0.854	1.055	1.311	1.699	2.045	2.462	2.756	3.396	3.659
30	0.000	0.683	0.854	1.055	1.310	1.697	2.042	2.457	2.750	3.385	3.646
40	0.000	0.681	0.851	1.050	1.303	1.684	2.021	2.423	2.704	3.307	3.551
60	0.000	0.679	0.848	1.045	1.296	1.671	2.000	2.390	2.660	3.232	3.460
80	0.000	0.678	0.846	1.043	1.292	1.664	1.990	2.374	2.639	3.195	3.416
100	0.000	0.677	0.845	1.042	1.290	1.660	1.984	2.364	2.626	3.174	3.390
1000	0.000	0.675	0.842	1.037	1.282	1.646	1.962	2.330	2.581	3.098	3.300
z	0.000	0.674	0.842	1.036	1.282	1.645	1.960	2.326	2.576	3.090	3.291
	0%	50%	60%	70%	80%	90%	95%	98%	99%	99.8%	99.9%
	Confidence Level										

Figure 3.7: Two-tails t-distribution value table

shown from the bar chart, the red bar is the total cost and the blue bar represents the first-stage cost which includes investment and O&M costs of installed DG units. The first-stage cost of DDARDGP goes up with the increase of the confidence level of uncertainty set. The decision is made to deploy more DG units and import a large amount of electricity from the main grid in order to maintain the safety operation of the microgrid in island mode.

The gap between the total cost and first stage cost for all instances are negative, which is the second-stage cost. It implies that the proposed DG deployment plan can gain positive profits through electricity arbitrage with the main grid and its consumer demand. The gaps shrink moderately with the increase of confidence level. This is due to the reason that wider confidence intervals lead to more conservative results. For confidence level over 90%, the cost hardly grows, which implies that the boundary reaches

the maximum range. This phenomenon represents no "worse" case will be discovered, and it might lead to the trap of over-conservatism. Therefore, prior to the planning, confidence level should be carefully selected to balance between the model accuracy and conservatism. In the case study, the confidence level is set to 80%.

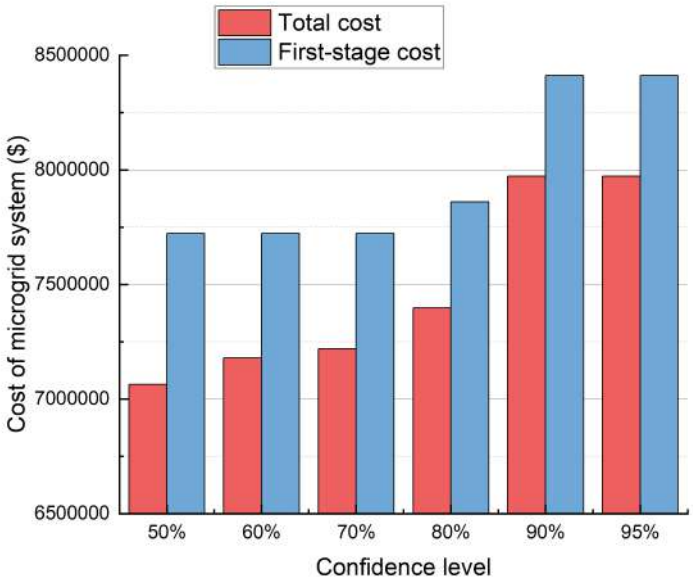

Figure 3.8: The cost of DDARDGP framework under different confidence levels

The deployment results under different confidence levels of the uncertainty set are listed in Table 3.3. It can be seen that the category of installed DG units are the same in all instances, which is WT. It is understandable that WT is the most cost-effective one based on its low capital cost and O&M cost. In instances 1, 2 and 3, the total installed capacity is 2800kW with two type I WT and one type II WT installed. The highest capacity 3050 kW appears in instances 5 and 6. The chosen locations are different in the same system topology under various confidence levels. This is because the first-stage decision is made based on the worst-case scenario generated in the second-stage of the DDARDGP framework.

Table 3.4 shows the computational results in each iteration of the modified CC&G algorithm. In all instances, the optimality gap converges in three iterations. It is noticeable that the gap narrows to less than 1% at the second iteration, which verifies

Table 3.3: DG deployment under different confidence levels

Instance	Confidence level	Location	Category	Capacity (kW)	Number	Total Capacity (kW)
1	50%	26	WT	850 1100	2 1	2800
2	60%	19	WT	850 1100	2 1	2800
3	70%	19	WT	850 1100	2 1	2800
4	80%	4 26	WT	850 2000	1 1	2850
5	90%	19	WT	850 1100	1 2	3050
6	95%	19 26	WT	850 1100	1 2	3050

the effectiveness of the proposed algorithm. For a large-scale system, the algorithm is guaranteed to work within a reasonable amount of time.

Table 3.4: Bounds and gaps under different confidence levels under different confidence levels

Instance	Confidence level	Iteration	LB	UB	Optimality Gap
		1	-42,075,758	56,140,273	174.95%
1	50%	2	7,047,322	7,064,629	0.24%
		3	7,064,629	7,064,629	0.00%
		1	-42,075,758	56,135,575	174.95%
2	60%	2	7,071,359	7,179,857	1.51%
		3	7,179,857	7,179,857	0.00%
		1	-42,075,758	56,293,283	174.74%
3	70%	2	7,200,853	7,218,691	0.25%
		3	7,218,691	7,218,691	0.00%
		1	-42,075,758	56,294,637	174.74%
4	80%	2	7,336,441	7,397,419	0.92%
		3	7,397,419	7,397,419	0.00%
		1	-42,075,758	56,301,486	174.73%
5	90%	2	7,898,586	7,972,174	0.92%
		3	7,972,174	7,972,174	0.00%
		1	-42,075,758	56,299,217	174.74%
6	95%	2	7,896,317	7,972,174	0.95%
		3	7,972,174	7,972,174	0.00%

3.4.5 Comparisons with Budget Uncertainty Set

Budget uncertainty set is widely used in the literature because of its simple structure. However the method is not adaptive to data distribution as a certain budget interval should be set prior to the calculation. Table 3.5 lists the results of deployment plan under the same weather condition and load demand. Set the range of the box uncertainty set to be 1. In the extreme situation, the budget uncertainty set degenerates to the box uncertainty set. There will be one type III WT installed at bus 4 and one type I WT installed at bus 19. The deployment is different from the previous plan shown in Table 3.3. However, the total installed capacity is the same as the plan with 80% confidence level.

Table 3.5: DG deployment under budget uncertainty set

Uncertainty set type	Location	Category	Capacity (kW)	Number	Total Capacity (kW)
Budget uncertainty set	4 19	WT	2000 850	1 1	2850

Table 3.6 shows the computational results of DDARDGP frame with budget uncertainty set and the proposed data-driven uncertainty set. The result indicates that the data-driven uncertainty set is 34.14% less conservative than the conventional one as the ranges of the budget uncertainty set and the data-driven uncertainty set are 0.6622 and 0.4361, respectively. The second-stage cost with budget uncertainty set is $-439,696 which is $23,185 larger than that with data-driven uncertainty set i.e. $-462,881. Hence, the proposed approach has achieved 0.3% reduction of the total cost than the budget uncertainty. Besides, it is also worth pointing out that the proposed data-driven uncertainty set can avoid constraint violation i.e. voltage violation while the occasions appear substantially as an infeasible problem at the second-stage subproblem solving phase. Although the construction of data-driven uncertainty set takes more time, the computational time for both uncertainty sets are small using the modified CC&G algorithm. The algorithm converges quickly, which means that it can work efficiently with the proposed DDARDGP framework.

Table 3.6: Comparison of computation results between budget uncertainty set and data-driven uncertainty set

Uncertainty set type	Budget uncertainty set	Data-driven uncertainty set
Range	0.6622	0.4361
Total cost ($)	7,420,604	7,397,419
First-stage cost ($)	7,860,300	7,860,300
Second-stage cost ($)	-439,696	-462,881
Binary variables	54	54
Continuous variables	115	1035
Uncertain variables	64	576
Constraints	311	2799
CPU time	11.66s	112.56s

3.4.6 Comparisons under Different Cost Weights

Compared with the first-stage cost, the effects of the second-stage cost are not significant. It is difficult for a system operator to recover the spend at the operation stage once the DG units are installed. To better understand the framework, we will compare the results of DDARDGP by adding a new cost weight factor θ as follows:

$$\min_{\mathbf{f}\in\mathbb{F}}(\theta\mathbf{A}^T\mathbf{f}) + \max_{\mathbf{u}\in\mathbb{U}} \min_{\mathbf{y}\in\mathbb{Y}(\mathbf{f},\mathbf{u})} \mathbf{B}^T\mathbf{y} + \mathbf{C}^T\mathbf{u} \tag{3.58}$$

The cost weight factor in the objective will influence the deployment plan. Table 3.7 shows the deployment plan with different weight factors ranging from 0.00001 to 1 using the same data-driven uncertainty set. It is observed that the identified worst case is the same. If the planner concerns more on the one-time investment cost, larger θ should be used. Otherwise, more RES-based DG units will be installed. This is because small θ in the objective will put more weights on the fuel cost and emission cost at the second-stage.

3.5 Chapter Summary

The DG planning for a long term such as decades has been an attractive research area in power system planning. In recent years, the demand for decarbonization transformation and electrification progress in both developed and developing countries and network

Table 3.7: DG deployment under different cost weight factor.

θ	Location	Category	Capacity (kW)	Number	Total Capacity (kW)
1	4	WT	850	1	2850
	26		2000	1	
0.1	4	WT	850	1	2850
	26		2000	1	
0.01	4	WT	850	1	2850
	26		2000	1	
0.001	4	WT	1100	1	3050
	19		850	1	
	26		1100	2	
0.0001	19	WT	850	1	3050
			1100	2	
0.00001	19	WT	850	1	3050
			1100	2	

expansion in rural areas has called for more research and development efforts in microgrids which could be an effective and flexible supplement to the traditional power grid.

In this Chapter, a two-stage adaptive robust optimization framework namely DDARDGP has been proposed for microgrid utility to investigate the DG planing strategy including category, type, number and location decisions. A novel data-driven based uncertainty set construction method has been used to handle the uncertainty of renewable power generations and load demand. As an independent step of the system planning, the construction of uncertainty sets incorporates spatio-temporal information from weather stations and smart meters, making the framework adaptive to new data sets. A modified CC&G algorithm is presented to solve the two-stage optimization problem within a reasonable computational time.

Experiments were conducted using a modified IEEE 33-bus system. Both dispatchable fuel-based microturbines and on-dispatchable RES-based DG units are considered. Through the analysis of the impact of under different truncation threshold values and confidence levels of data-driven uncertainty sets, the system planner could find the trade-off between the conservatism and robustness of the framework. The effectiveness

of the proposed DDARDGP framework has been verified by the comparisons with the budget uncertainty set and under different cost weights of the objective. The simulation results show that the data distribution is well captured by a combination of 9 polyhedral sets, resulting 0.3% reduction of the total cost and 34.14% reduction on uncertainty estimation. The problem of over-conservatism is avoided. In addition, the total installed RES capacity will increase 200kW when cost weight changes from 0.01 to 0.001. Therefore, the proposed DDARDGP is suitable for the system planner to accommodate more renewable DG units due to public policy initiatives in practice.

One way to reduce the problem conservativeness is to construct additional uncertainty sets for different time intervals, for instance from hour to hour or from season to season. This adds more difficulty and complexity to the DG planning decision-makers. In the next chapter, energy storage units will be introduced in an alternative solution.

CHAPTER 4

ENERGY STORAGE PLANNING IN MICROGRIDS

To tackle the global challenge of climate change and reduce the green-house gas emissions from thermal power generation plants, governments worldwide are advancing the development of environmentally friendly power projects such as renewable distributed generations i.e. wind farms and solar panels in residential areas [166, 167]. With generous incentives and subsides [168], the installed capacity of renewable generation worldwide has experienced a major expansion in recent years with a remarkable annual growth rate of 15% from 2015-2020 [169], resulting in significant changes on the power flow in terms of direction and magnitude [170]. The emergence of large-scale and distributed energy resources imposes new challenges to the system operator that the strategy to maintain the power quality [171] as well as the protection settings [170] should be reconsidered. In addition, in the new electricity market reform, more types of market entities are allowed to participate [172]. However, the research on energy storage system (ESS) planning model for microgrids participation in the spot market is limited.

In this chapter, a novel two-stage stochastic ESS planning with low energy procurement risks (EPLEPR) model will be proposed for microgrids. The uncertainties of renewable energy and price variability are considered. An optimal sizing and location of single and multiple ESSs will be obtained through a cost-benefit analysis.

4.1 Market Operation Strategy

The prosumer indicates the individual who can purchase and sell the same commodity. Along with the progress of electricity market deregulation, microgrids and large-scale ESSs are allowed to purchase and sell electricity as energy prosumers in the spot market. According to different time scales, the spot market, known as the “pool”, is divided into the day-ahead market and the intraday market. In this study, the intraday market is not considered due to its small trading scale [173] and unawareness of strategies from other market participants. In the rest of this section , the "ESS" is particularly referred to as the battery energy storage system.

4.1.1 Energy Procurement in the Day-ahead Market

In the day-ahead market, the producers and purchasers bid for the delivery of electricity the next day based on the day-ahead generation, load and market price forecast. Usually, all figures are on an hourly basis. For a microgrid with distributed generations, the expected energy procurement at each time interval can be expressed as the net load $P_t^{NET\_DA}$ as follows:

$$P_t^{NET\_DA} = P_t^{D\_DA} - P_t^{G\_DA} \tag{4.1}$$

where $P_t^{D\_DA}$ and $P_t^{G\_DA}$ are the forecasted day-ahead power consumption and production of the microgrid at time t.

Due to the fluctuations of predicted hourly prices, ESS is incorporated into an adjustment strategy of the energy procurement for arbitrage opportunities. An illustration is shown in Figure 4.1 where the capacity of the ESS is 2000kW. The data used to draw the figure is randomly chosen from the yearly predicted load and wind generation of Elia Grid [174] and electricity market price of Nord Pool [175]. When the prices are higher than the predefined upper bound (the blue line), a signal of reduction in energy procurement, which could be compensated by ESS, is triggered. On the contrary, ESS is supposed to be charged with an incremental energy procurement signal during the

period of low prices. The adjustment amount of energy procurement in the day-ahead market is related to the energy capacity of ESS as follows [176]:

$$\Delta P_t^{NET\_DA} = \begin{cases} \frac{\rho_t^{DA} - \beta_{min}\bar{\rho}^{DA}}{\sum_{\rho_t^{DA} < \beta_{min}\bar{\rho}^{DA}} (\rho_t^{DA} - \beta_{min}\bar{\rho}^{DA})} D^{AR} C^{ESS}; & \rho_t^{DA} < \beta_{min}\bar{\rho}^{DA} \\ 0; & \beta_{min}\bar{\rho}^{DA} < \rho_t^{DA} < \beta_{max}\bar{\rho}^{DA} \\ -\frac{\rho_t^{DA} - \beta_{max}\bar{\rho}^{DA}}{\sum_{\rho_t^{DA} > \beta_{max}\bar{\rho}^{DA}} (\rho_t^{DA} - \beta_{max}\bar{\rho}^{DA})} D^{AR} C^{ESS}; & \rho_t^{DA} > \beta_{max}\bar{\rho}^{DA} \end{cases} \tag{4.2}$$

where ρ_t^{DA} is the forecasted day-ahead electricity price ($/kWh). $\bar{\rho}^{DA}$ is the average day-ahead electricity price ($/kWh). β_{max} and β_{min} are the upper and lower price boundary indexes, respectively. D^{AR} is the allowed depth (%) of ESS for arbitrage in day-ahead market. C^{ESS} is the energy capacity (kWh) of ESS.

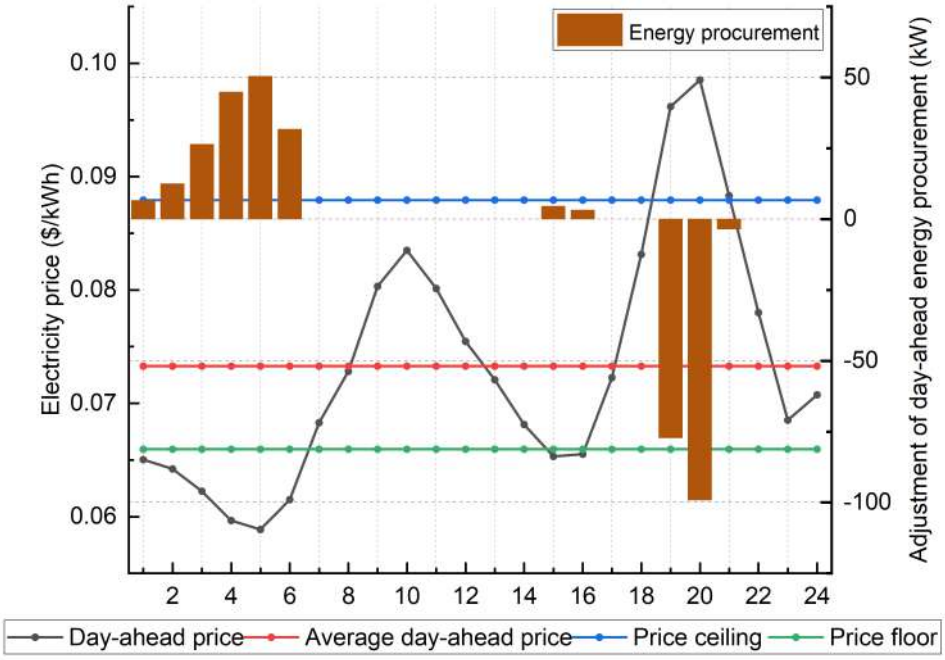

Figure 4.1: Adjustment strategy of the energy procurement of microgrids

Once the adjustment is settled, the final energy procurement will become

$$P_t'^{NET\_DA} = P_t^{NET\_DA} + \Delta P_t^{NET\_DA} \tag{4.3}$$

In equation (4.3), $P_t^{\prime NET\_DA}$ is the energy procurement decision of the microgrid in the day-ahead market. The day-ahead energy procurement cost at time interval t is

$$C_t^{DA} = \rho_t^{DA} P_t^{\prime NET\_DA} \tag{4.4}$$

It should noted that the decision-making is on daily basis. Therefore, the total day-ahead energy procurement cost becomes

$$C_d^{DA} = \sum_{t=1}^{24} C_t^{DA} \tag{4.5}$$

4.1.2 Trading Risk of Energy Procurement

The actual power dispatch takes place in the following day. There are always prediction errors due to the intermittent nature of renewable energy resources and load variations. However, the actual real-time measured data of load and generation are usually unavailable for the system operator, which needs to be checked and verified by other authorities for up to several months. Therefore, the actual load and generation are approximated with the most recent estimations. The actual real-time net load of a microgrid without ESS is

$$P_t^{NET\_RT} = P_t^{D\_RT} - P_t^{G\_RT} \tag{4.6}$$

where $P_t^{D\_RT}$ and $P_t^{G\_RT}$ are the actual real-time values of load demand and generation within the microgrid at time t, respectively.

The difference between day-ahead energy procurement and real-time decision is called trading risk of energy procurement. An intuitive idea is to set $P_t^{NET\_RT} - P_t^{\prime NET\_DA}$ as a charging/discharging signal for ESS: charge ESS when the signal is positive and discharge ESS when the signal is negative. Figure 4.2 illustrates an example of the operation of ESS in a day using the proposed strategy. The data used for the actual load and wind generation is the same day as that in Figure 4.1. During 1 am to 6 am, the day-ahead energy procurement exceeds the real-time net load. ESS is charged by the redundant energy. At the rest time of the day, ESS discharges to fill the gap between the day-ahead energy procurement and real-time demands. In the case shown in Figure 4.2, the ESS is fully discharged at 16:00 and remains empty for the rest of the day.

If the energy capacity of ESS is sufficiently large, the trading risk of day-ahead energy procurement will be 0. However, the trading risk is not the only criterion to be considered in the model as it may lead to an inefficient utilization of ESS.

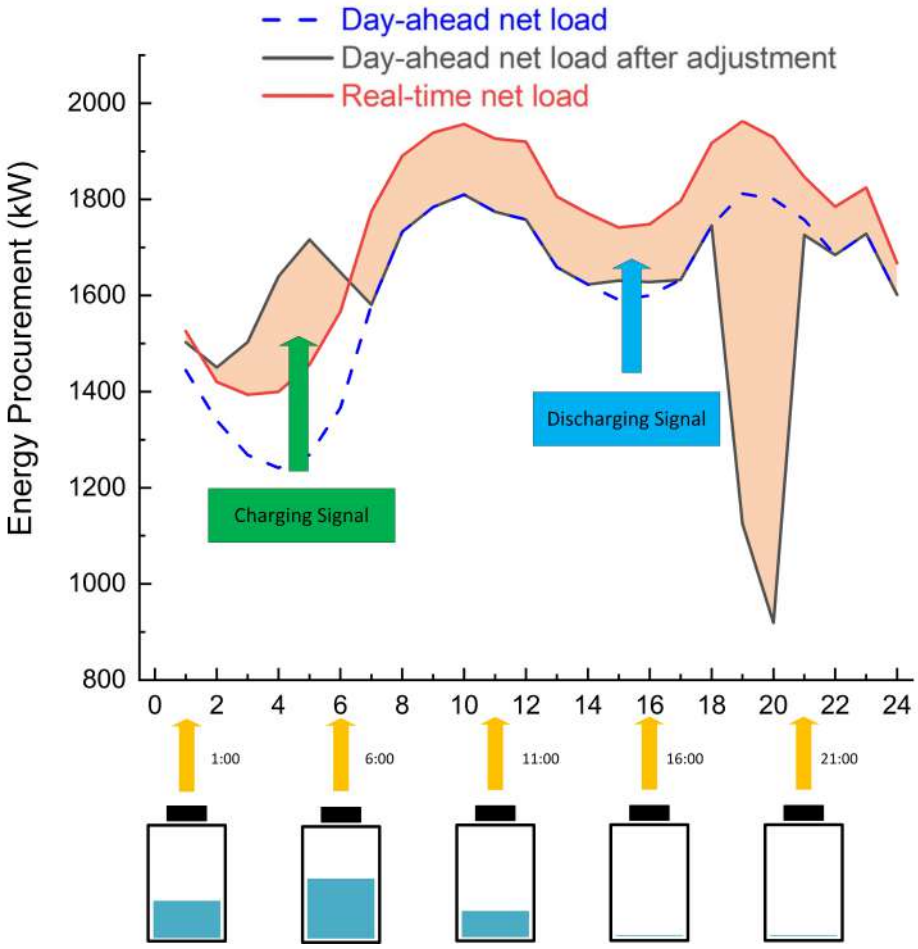

Figure 4.2: Operation strategy of ESS

4.2 System Operation Strategy

In this section, the system operation strategy is proposed. Specifically, a ESS operation strategy in microgrid will be developed. First, the fundamental charging and discharging principle of an individual ESS connected to the grid is investigated. Generally speaking, the energy stored in the ESS during each time interval E_t^{ESS} is defined by (4.7),

incorporating the charging efficiency η_c and discharge efficiency η_d, respectively.

$$E_t^{ESS} = E_{t-1}^{ESS} + \eta_c P_t^{ch} \Delta t - \frac{P_t^{dis}}{\eta_d} \Delta t \tag{4.7}$$

where Δt is the duration time of each interval. It is worth noting that P_t^{ch} and P_t^{dis} are the charging and discharging power from the grid side. The ESS could only be charged or discharged at each time interval, so that $P_t^{ch} P_t^{dis} = 0$.

The state-of-charge (SOC) is used to express the level of charge in ESS relative to its capacity as a percentage (0% = empty; 100% = full) as follows

$$SOC_t = \frac{E_t^{ESS}}{C^{ESS}} \tag{4.8}$$

where C^{ESS} is the nominal energy capacity of ESS.

The operation of normal ESS is subject to the following constraints

$$SOC_{min} \leqslant SOC_t \leqslant SOC_{max} \tag{4.9}$$

$$0 \leqslant \eta_c P_t^{ch} \leqslant P_{max}^{ch} \tag{4.10}$$

$$0 \leqslant \frac{P_t^{dis}}{\eta_d} \leqslant P_{max}^{dis} \tag{4.11}$$

In Equation (4.9), the upper bound SOC_{max} and the lower bound SOC_{max} are recommendations from the manufacturer's technical sheet by considering the life-cycle performance such as degradation of ESS. The charge and discharge power of ESS are constrained in Equation (4.10) and (4.11) respectively. The maximum charge power (P_{max}^{ch}) and discharge power (P_{max}^{dis}) power are related to the battery's C-rates, a terminology to measure the charge/discharge rate. For instance, the discharge C-Rate 2 is the discharging current that a fully-charged battery will be fully discharged in half an hour.

4.2.1 Single ESS Operation Strategy

In pursuit of maximal revenues under physical and market-based constraints, the optimal operation strategy of ESS in a microgrid should reduce the trading risk of energy procurement and benefit the balance of generation and consumption in real time. An ESS-based business model is proposed in the following section.

Reserve - Apart from the arbitrage benefit introduced in the day-ahead market, ESS is able to provide ancillary services such as fast reserve to maintain operational security and reliability. In the UK, fast reserve is procured by the electricity system operation as a part of balancing mechanisms during the daytime, typically between 06:00-23:00 [177] to meet the requirement of total fast reserve volume. Discharge power in Constraint (4.11) will be replaced as follows:

$$0 \leqslant \frac{P_t^{dis}}{\eta_d} \leqslant P_{max}^{dis} - \frac{P_{max}^{dis\_fr}}{\eta_d} \tag{4.12}$$

$$\frac{P_{max}^{dis\_fr}}{\eta_d} = 0.5 P_{max}^{dis} \tag{4.13}$$

where $P_{max}^{dis\_fr}$ is a fixed discharge power allocated for FR according to a pre-defined ratio of maximum discharge power. In Equation (4.12), we choose it to be 50% of maximum discharge power based on [178].

The SOC of ESS that provides fast reserve service is expressed as follows:

$$SOC_{min} + D^{FR} C^{ESS} \leqslant SOC_t \leqslant SOC_{max} \tag{4.14}$$

where D^{FR} is the assigned depth (%) of ESS for FR.

The total revenue R^{FR} of ESS for fast reserve is as follows:

$$R_d^{FR} = \rho^{fr} D^{FR} C^{ESS} \tag{4.15}$$

where ρ^{fr} is the average price ($\$/kWh$) of FR service.

Combing the reserve and arbitrage services together, the total charge/discharge capability of ESS is required to remain within a reasonable depth of discharge (DOD) based on the battery's lifetime.

$$D^{FR} + D^{AR} = DOD \tag{4.16}$$

Balancing - Another important role that the ESS plays in the model is related to trading risk of day-ahead energy procurement. Electricity market participants have the

financial responsibility for imbalances between day-ahead contracted volume and actual metered volume of energy. The real-time net load in a microgrid with a ESS is as follows

$$P_t^{\prime NET\_RT} = P_t^{NET\_RT} + P_t^{ch} - P_t^{dis} \tag{4.17}$$

The power deviation from day-ahead energy procurement to real-time net load will be penalized for each settlement period as follows:

$$C_t^{IB} = \begin{cases} \rho_t^{sell}\left(P_t^{\prime NET\_DA} - P_t^{\prime NET\_RT}\right); & P_t^{\prime NET\_DA} \geqslant P_t^{\prime NET\_RT} \\ \rho_t^{buy}\left(P_t^{\prime NET\_RT} - P_t^{\prime NET\_DA}\right); & P_t^{\prime NET\_DA} < P_t^{\prime NET\_RT} \end{cases} \tag{4.18}$$

C_t^{IB} is the imbalance charges ($) of the risk of energy procurement at time t . ρ_t^{sell} and ρ_t^{buy} indicate system sell price and system buy price ($/$kWh$) to cover the system energy imbalance. The total daily imbalance charge therefore becomes as follows:

$$C_d^{IB} = \sum_{t=1}^{24} C_t^{IB} \tag{4.19}$$

4.2.2 Multiple ESS Operation Strategy

Multiple ESS operation strategy is similar to single ESS one. The adjustment amount of energy procurement in the day-ahead spot market can be expressed as follow:.

$$\Delta P_t^{NET\_DA} = \begin{cases} \frac{\rho_t^{DA} - \beta_{min}\bar{\rho}^{DA}}{\sum_{\rho_t^{DA} < \beta_{min}\bar{\rho}^{DA}}\left(\rho_t^{DA} - \beta_{min}\bar{\rho}^{DA}\right)} D_s^{AR} \sum_{s=1}^{n} C_s^{ESS}; & \rho_t^{DA} < \beta_{min}\bar{\rho}^{DA} \\ 0 & \beta_{min}\bar{\rho}^{DA} < \rho_t^{DA} < \beta_{max}\bar{\rho}^{DA} \\ -\frac{\rho_t^{DA} - \beta_{max}\bar{\rho}^{DA}}{\sum_{\rho_t^{DA} > \beta_{max}\bar{\rho}^{DA}}\left(\rho_t^{DA} - \beta_{max}\bar{\rho}^{DA}\right)} D_s^{AR} \sum_{s=1}^{n} C_s^{ESS}; & \rho_t^{DA} > \beta_{max}\bar{\rho}^{DA} \end{cases} \tag{4.20}$$

where s is the index of ESSs.

Each ESS could adopt different battery types. The DOD of each ESS should be chosen based on their battery type as well. The constraints of SOC are described below:

$$SOC_{s,min} + D_s^{FR} C_s^{ESS} \leqslant SOC_{s,t} \leqslant SOC_{s,max}, \forall s \tag{4.21}$$

$$D_s^{FR} + D_s^{AR} = DOD_s, \forall s \tag{4.22}$$

The optimal depths for reserve and arbitrage services will be obtained in the model.

The proposed operation strategy aims to make full use of the ESS by tracking the day-ahead forecast and near real-time forecast, except for providing balancing services at the system operator's requests. Through carefully selected location and size in the microgrid, ESS is capable of minimizing the regulation cost and energy procurement cost at a considerable amount.

Compared with the existing conventional strategies, the advantages of the proposed strategy are remarkable. Firstly, it considers both the day-ahead procurement energy and the capacity of ESS, eliminating the limitations of existing strategies proposed in the literature which only consider the market price fluctuations in day-ahead market, while the impact of ESS capacity is not considered. In addition to arbitrage, the cost of energy procurement can be further reduced. Secondly, instead of moving load peaks to valleys, the proposed strategy focuses on the forecast errors at different time intervals which are always small. The corresponding required energy capacity of ESS will become more economically viable. Thirdly, by jointly optimizing the charging/discharging power for arbitrage and regulation purposes, the potential of ESS in providing the ancillary services can be achieved, leveraging additional revenues which are often ignored in existing approaches in the literature.

4.3 Energy Storage System Planning Model

4.3.1 Objective Function

An important task in planning the installation of an ESS in a microgrid is to find its optimal sizing and sitting to minimize the total costs over the whole planning horizon. Thus, the objective function can be formulated as follows

$$\min_{C_s^{ESS}, L_s^{ESS}, E_{s,t}^{ESS}, D_s^{AR}} C^{INV} + C^{OM} + C^{UoS} + C^{DA} + C^{IB} - R^{RV} - R^{FR} \tag{4.23}$$

$$C^{INV} = \sum_s inv_s^{ESS} C_s^{ESS} \tag{4.24}$$

$$C^{OM} = \sum_{y} \gamma_y \left(\sum_{t=1}^{8760} \sum_{s} om_{s,y,t}^{ESS} C_s^{ESS} \right) \tag{4.25}$$

$$C^{UoS} = \sum_{y} \gamma_y \left(\sum_{t=1}^{8760} \rho_{y,t}^{UoS} \left(I_{l_{i\to j},y,t} \right)^2 r_{l_{i\to j}} \right) \tag{4.26}$$

$$C^{DA} = \sum_{y} \gamma_y \left(\sum_{d=1}^{365} C_d^{DA} \right) \tag{4.27}$$

$$C^{IB} = \sum_{y} \gamma_y \left(\sum_{d=1}^{365} C_d^{IB} \right) \tag{4.28}$$

$$R^{RV} = \gamma_y \sum_{s} inv_s^{ESS} C_s^{ESS} LC_s^R \tag{4.29}$$

$$R^{FR} = \sum_{y} \gamma_y \left(\sum_{d=1}^{365} R_d^{FR} \right) \tag{4.30}$$

$$LC_s^R = \frac{LC_s - \frac{\sum_t E_{s,t}^{ESS\_total}}{C_s^{ESS}}}{LC_s} \tag{4.31}$$

$$E_{s,t}^{ESS\_total} = \left(\eta_c P_{s,t}^{ch} + \frac{P_{s,t}^{dis} + P_{s,t}^{dis\_fr}}{\eta_d} \right) \Delta t \tag{4.32}$$

$$\gamma_y = \frac{1}{(1+dr)^y} \tag{4.33}$$

The whole objective function (4.23) consists of seven parts: investment cost, operation and maintenance (O&M) cost of ESSs, use of system (UoS) cost, cost of day-ahead energy procurement and real-time imbalance charges, residual values of ESSs and revenues of fast reserve service. Equation (4.24) and (4.25) represent the total capital cost and O&M cost that depends on the battery type and its sizing. inv_s^{ESS} is the investment cost of sth ESS ($/kWh$). $om_{s,y,t}^{ESS}$ is the O&M cost of ESS s ($/kWh$) at time t of year y. The UoS cost or called distribution charge in (4.26) cover the expenses of the use of the distribution system to deliver the electricity from generation to consumers, where $\rho_{y,t}^{UoS}$ is a fixed rate electricity price ($/kW$) that is used to recover the costs of power losses. $I_{l_{i\to j},y,t}$ is the line current flowing from bus i to j at time t of year y. The total cost of day-ahead energy procurement and real-time regulation cost is shown in Equation (4.27) and (4.28), respectively. The daily energy procurement C_d^{DA} and daily imbalance charges C_d^{IB} is given in Equation (4.5) and (4.19).

The residual value of ESS after y years' operation is given in Equation (4.29). It is determined by the investment cost and the remaining life cycles LC_s^R. LC_s^R is a fraction of total life cycles LC_s of the sth ESS at a predetermined DOD. $E_{s,t}^{ESS\_total}$ is the total charging and discharging energy of the sth ESS at time interval t. The total revenue for participating the fast reserve service R^{FR} given in Equation (4.30) is based on daily fast reserve profit R_d^{FR} defined in (4.15). All the costs and revenues except for investment cost are converted to yearly values and represented in net present value (NPV) with NPV factor γ_y shown in (4.33) where dr is the annual discount rate.

There are two type of decision variables. L_s^{ESS} is an integer variable that indicates the location of sth ESS which is within the full set of all candidate buses. The continues decision variables consist C_s^{ESS}, $E_{s,t}^{ESS}$ and D_s^{AR} which are energy capacity, stored energy at time t and assigned depth for arbitrage, respectively. The corresponding $P_{L_s^{ESS},t}^{ch}$ or $P_{L_s^{ESS},t}^{dis}$ are calculated according to the operation strategy of ESS. Due to the non-linear formulation of the market operation strategy, the model is clearly a MINLP (Mixed-integer Nonlinear Programming) problem.

4.3.2 Constraints

4.3.2.1 Power Flow Constraint

Instead of using the simplified LinDistFlow formulation adopted in the previous chapter, DistFlow will be used in this study as it will improve the accuracy of the power flow analysis. It simply follows the original definition of Ohm's law and power balance. For a radial network, the active/reactive power satisfies branch flow equations as follows:

$$\sum_{l_{d_i} \in \mathbb{D}_i} P_{l_{d_i}} = P_{l_{u_i}} + P_i^{DG} - P_i^{ch} + P_i^{dis} - r_{l_{u_i}} \frac{P_{l_{u_i}}^2 + Q_{l_{u_i}}^2}{V_i^2} - P_i^C \tag{4.34}$$

$$\sum_{l_{d_i} \in \mathbb{D}_i} Q_{l_{d_i}} = Q_{l_{u_i}} - x_{l_{u_i}} \frac{P_{l_{u_i}}^2 + Q_{l_{u_i}}^2}{V_i^2} - Q_i^C \tag{4.35}$$

$$V_j^2 = V_i^2 - 2(r_{l_{i\to j}} P_{l_{i\to j}} + x_{l_{i\to j}} Q_{l_{i\to j}}) + (r_{l_{i\to j}}^2 + x_{l_{i\to j}}^2) \frac{P_{l_{i\to j}}^2 + Q_{l_{i\to j}}^2}{V_i^2} \tag{4.36}$$

where P_i^{DG} and Q_i^{DG} are active/reactive power generations of distributed generators. $P_{i,t}^{ch}$ and $P_{i,t}^{dis}$ are the power charged and discharged to the grid from ESS. Note that the part $\frac{P_{l_{i\to j}}^2+Q_{l_{i\to j}}^2}{V_{i,t}^2}$ is the square of the line current $\left(I_{l_{i\to j}}\right)^2$ which is used to calculate the power loss.

4.3.2.2 Voltage Constraint

The voltage at each bus should be within the utility's permissible limits

$$V_{min} \leqslant V_{i,t} \leqslant V_{max} \tag{4.37}$$

4.3.2.3 Branch Capacity Constraint

The branch capacity of each line $S_{l_{i\to j},t}$ is maintained within the limits

$$0 \leqslant S_{l_{i\to j},t} \leqslant S_{max} \tag{4.38}$$

4.3.2.4 ESS Operation Constraint

The technical and operation constraints of ESS are subject to Equation (4.7)-(4.8), (4.10), (4.12)-(4.13) and (4.14),(4.16).

4.4 Solution Methodologies

4.4.1 Probability-weighted ESS Planning Model

To achieve the optimal planning of ESS in microgrid over the planning horizon, scenarios are generated based on the input data which includes the day-ahead and most recent forecasted intermittent renewable generation output $P_t^{G\_DA}$ and $P_t^{G\_RT}$, the day-ahead predicted load demand $P_t^{D\_DA}$ and most recent predicted load demand $P_t^{D\_RT}$, day-ahead forecast electricity price ρ_t^{DA} and system sell/buy price ρ_t^{sell} and ρ_t^{buy}. The high-dimensional data will be modeled in probability-weighted form of several scenarios to represent future events.

Figure 4.3(b) shows an example of a daily load forecast. Unlike a single hourly prediction generated based on the same dataset shown as Figure 4.3(a) from Section 3.2.2, it can be seen that the result is a t-hour array at location i for any $i = 1,2,3,....n$. The daily forecast is more precise than hourly forecast with details of load fluctuations at each hour. A daily load difference can attain more than 20% between peak hours and off-peak hours.

In Section 3.2.3, a self-adaptive data-driven nonparametric approach is introduced for clustering high-dimension high-volume datasets based on DPMM. In this section, the same approach is used to generate scenarios. It should be noted that the expression of uncertainties in previous section is conceptually identical to scenario variations discussed in this section. Recall the expression of basic uncertainty set Γ_k

$$\Gamma_k = \left\{x_{t+1} | x_{t+1} = \mu_k + \zeta l_k \Lambda, \qquad \|\Lambda\|_{norm} \leq 1\right\}, \forall k \tag{4.39}$$

where μ_k and l_k are the mean value and the standard variance, respectively. Λ and ζ are hyper-parameters that are used to adjust the confidence interval of the uncertainty set.

Compared with the robust programming used for DG planning, stochastic programming is another type of decision making optimization techniques for probability-weighted objective function with uncertainties. Robust optimization mainly considers worst-case scenarios. For DG units, they only produce and do not consume electricity. Worst-case scenarios in which wind or solar resources are insufficient to meet the needs of high demand will determine the decisions of sitting and sizing. However, ESS works as prosumers in the electricity grid that both produce and consume electricity. The robust programming based models are not suitable in such cases which will lead to a bias of over-charge or over-discharge. Instead, objective function (4.23) is converted to a two-stage stochastic programming model for ESS planning with low energy procurement risks (EPLEPR) in a microgrid as shown below in Equation (4.40) - (4.42). The first-stage formulation makes the here-and-now decision. It covers the investment cost, O&M cost of ESSs, and the residual values of ESSs, which only includes the decision variables that indicate the sitting and sizing of ESSs. The remaining use of system (UoS) cost, day-ahead energy procurement cost, real-time imbalance charges and revenues of fast reserve services

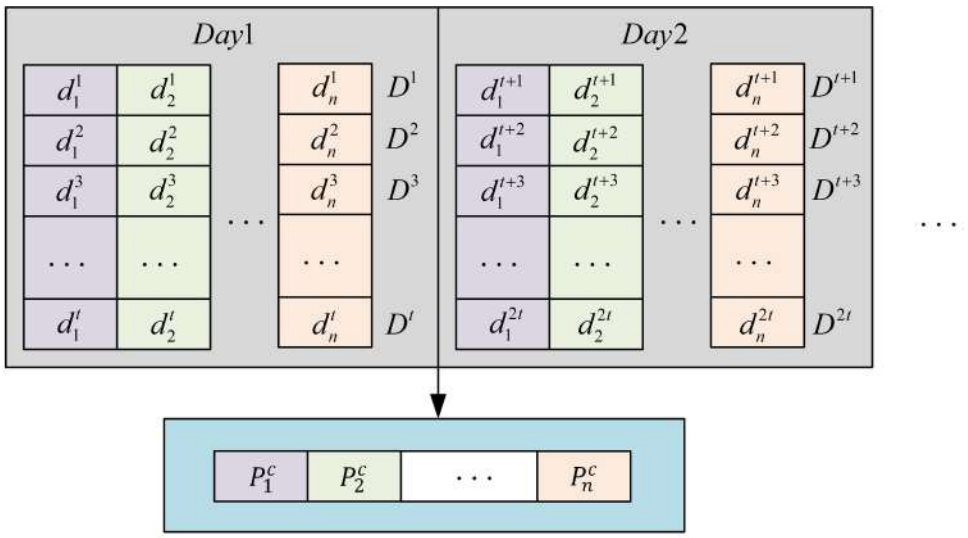

(a)

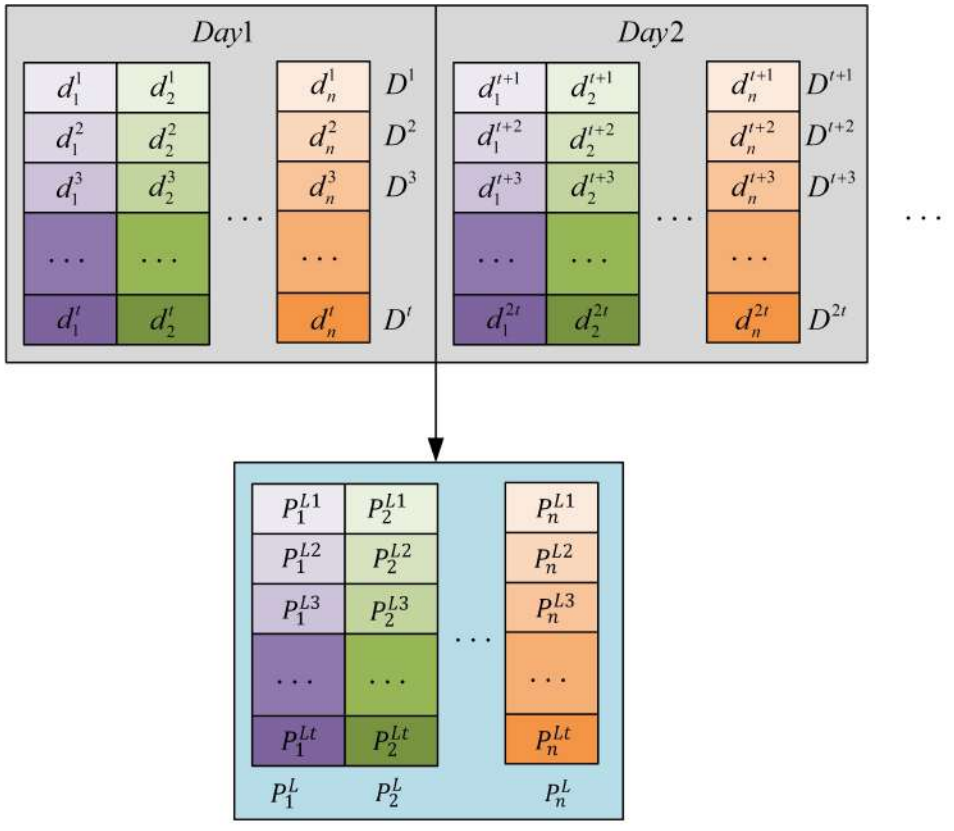

(b)

Figure 4.3: Schematic diagram of the database of load profile for (a) the hourly forecast (b) the daily forecast at different locations

form the second-stage costs. Therefore, the second-stage is called wait-and see decision. It includes all the other costs relating to the daily schedule of the system once ESSs are installed.

(First-stage formulation)

$$\underset{\mathbf{x}\in\mathbb{X}}{minf}(\mathbf{x}) + Q \tag{4.40}$$

(Second-stage formulation)

$$Q = \sum_{k\in\mathbb{K}} \lambda_k g_k(\mathbf{x},\mathbf{y}) \tag{4.41}$$

s.t.

$$h_k(\mathbf{x},\mathbf{y}) = 0, \forall k \tag{4.42}$$

$\mathbf{x}$ is the vector of first-stage decision variables that includes C_s^{ESS} and L_s^{ESS}. $\mathbf{y}$ denotes the second-stage decision vector of stored energy $E_{s,t}^{ESS}$ and assigned depth for arbitrage D_s^{AR} in scenario k. λ_k is the weight of kth scenario. The mean value used in the probability-weighted model is μ_k given in Equation (4.39). Constraint (4.42) guarantees that the optimal solution is valid in all scenarios. The proposed probability-weighted EPLEPR framework is generic and can fully capture the spectrum of data inputs, which shows the potential of the model to be used for the network upgrade and reconfiguration.

4.4.2 Solving Algorithm

4.4.2.1 Overview of CMA-ES algorithm

As discussed earlier, a number of meta-heuristic algorithms have been proposed for solving complex nonlinear mixed-integer optimization problems, such as GA, PSO, DE, etc. However, little has been done so far to design suitable meta-heuristic approaches to solve such complex optimization problems considering a range of uncertainties as discussed in this thesis. In this chapter, we will focus on a fairly new meta-heuristic approach, namely Covariance Matrix Adaptation Evolution Strategy (CMA-ES) which has a great potential for solving the problems under investigation in this thesis.

CMA-ES was first proposed by Hansen and Ostermeier in 2010 [179]. It inherits the merits of Evolution Strategy (ES) that uses weighted recombination of μ parents

through adaptive covariance matrix to generate λ offsprings. A comparison of different recombination methods of ES is given in Appendix B. The core idea of CMA-ES or called $(\mu/\mu_W, \lambda)$-ES algorithm is to learn the dependencies and relative ratios along different directions of a multivariate normal distribution $N(m, \sigma^2 C)$, which improves the defect of fixed covariance matrix in all iteration steps of ES. Here, a detailed introduction of the algorithm will be given below.

Sampling Similar to other ES variants, the CMA-ES algorithm begins a new search with a population of λ individual searching points (or called offsprings). The initial sampling points is based on a multivariate normal distribution. For each generation $g = 0, 1, 2, ...$, the expression of offsprings will become as follows:

$$x_{h,g+1} \sim m_g + \sigma_g N(0, C_g) \qquad for \quad h = 1, ..., \lambda \tag{4.43}$$

where $x_{h,g+1}$ is hth offspring at $(g+1)$th generation. m_g is the mean value of all offsprings at gth generation. σ_g is the standard deviation at gth generation, which controls the scale of the distribution of all offsprings. The larger σ_g is, the better searching space we will have. $N(0, C_g)$ is a multivariate normal distribution with zero mean value and C_g covariance matrix which is always positive semi-definite. As mentioned earlier, λ here denotes the number of offsprings in a population.

Once the initialization of offsprings is completed, the next key steps are to develop an adaptive strategy for mean value m_{g+1}, standard deviation σ_{g+1} and covariance matrix C_{g+1} which will be iterated during the whole evolution process.

Selection and Recombination The update strategy for mean value m_{g+1} at the next generation can be summarized as three steps. First, sort the objective function evaluations of offsprings at $(g+1)$th generation from the smallest to the largest for a minimization problem, denoting as $x'_{1,g+1}, x'_{2,g+1}, ...x'_{\lambda,g+1}$. Second, select the best μ offsprings $x'_{1,g+1}, x'_{2,g+1}, ...x'_{\mu,g+1}$. Third, update the mean value with the weighted average of the selected values. It could be expressed as:

$$m_{g+1} = \sum_{h=1}^{\mu} w_p x'_{h,g+1} \tag{4.44}$$

$$\sum_{h=1}^{\mu} w_h = 1 \qquad w_1 \geqslant w_2 \geqslant ...w_\mu > 0 \tag{4.45}$$

A more generalized update strategy of mean value m_{g+1} is

$$m_{g+1} = m_g + c_m \sum_{h=1}^{\mu} w_h (x'_{h,g+1} - m_g) \tag{4.46}$$

where $c_m \leqslant 1$ is a learning rate that controls the update rate of mean value m_{g+1}. The default value of c_m is 1. In the case $c_m = 1$, Equation (4.46) is the same as (4.44).

Adapting the Covariance Matrix - The covariance matrix C_{g+1} is estimated by C^{μ}_{g+1} based on the same μ best offsprings $x'_{1,g+1}, x'_{2,g+1}, ...x'_{\mu,g+1}$ in the weighted selection mechanism in Equation(4.46).

$$C^{\mu}_{g+1} = \sum_{h=1}^{\mu} w_s \left(x'_{h,g+1} - m_g\right)\left(x'_{h,g+1} - m_g\right)^T \tag{4.47}$$

C^{μ}_{g+1} is reliable to reproduce the offsprings only when the selected population is large enough. For small population which will be executed fast in each iteration step, two independent routes have been involved.

- Rank-μ-Update: uses C^{μ}_{g} $(g = 0, 1, 2, ...)$ in previous steps to make the estimator C_{g+1} more reliable. If we consider only the most recent information and choose C_0 to be the unity matrix I, we have

$$\begin{aligned} C_{g+1} &= \left(1 - c_\mu\right) C_g + c_\mu \frac{1}{\sigma_g^2} C^{\mu}_{g+1} \\ &= \left(1 - c_\mu\right) C_g + c_\mu \sum_{h=1}^{\mu} w_p \frac{\left(x'_{h,g+1} - m_g\right)}{\sigma_g} \frac{\left(x'_{h,g+1} - m_g\right)^T}{\sigma_g} \\ &= \left(1 - c_\mu\right) C_g + c_\mu \sum_{h=1}^{\mu} w_p \left(y_{h,g+1}\right)\left(y_{h,g+1}\right)^T \\ &= C_g^{1/2}\left(I + c_\mu \sum_{h=1}^{\mu} w_h \left(z_{h,g+1} z^T_{h,g+1} - I\right)\right) C_g^{1/2} \end{aligned} \tag{4.48}$$

  where c_μ is a learning rate for updating the covariance matrix $(0 < c_\mu \leqslant 1)$. When $c_\mu = 1$, the evolution all depends on prior information. When $c_\mu = 0$, $C_{g+1} = C_0 = I$ that there is no learning from previous steps. An appropriate choice is $c_\mu \approx \frac{\mu_{eff}}{n^2}$

where μ_{eff} is variance effectuve selection mass $\mu_{eff} = \frac{1}{\sum_{h=1}^{\mu} w_h^2}$. $y_{h,g+1} = \frac{x'_{h,g+1} - m_g}{\sigma_g} \sim N(0, C_g)$ and $z_{h,g+1} = C_{g+1}^{-1/2} y_{h,g+1} \sim N(0, I)$ are used here to simplify the expression.

- Rank-One-Update: estimates the lost sign information that is correlations between consecutive steps from the history $y_{h,g+1} y_{h,g+1}^T = (-y_{h,g+1})(-y_{h,g+1})^T$. To reproduce it, an evolution path p_c is constructed with the average of moving step $y_{h,g+1}$. $p_\sigma \sim N(0, C)$ is conjugate before and after an update and $p_{c,0} = 0$. The details of construction of evolution path p_c could be found in Appendix C.1.

$$p_{c,g+1} = (1 - c_c) p_{c,g} + \sqrt{c_c (2 - c_c) \mu_{eff}} \frac{m_{g+1} - m_g}{\sigma_g} \tag{4.49}$$

where $c_c \leqslant 1$ is the learning rate for the evolution path. The factor $\sqrt{c_c (2 - c_c) \mu_{eff}}$ is normalization constant for p_c. Rank-one update of covariance matrix is as follows:

$$C_{g+1} = (1 - c_1) C_g + c_1 p_{c,g+1} p_{c,g+1}^T \tag{4.50}$$

The overall adaptive strategy for conariance matrix combing rank-one and rank-μ update is

$$C_{g+1} = \left(1 - c_1 - c_\mu \sum w_p\right) C_g + c_1 p_{c,g+1} p_{c,g+1}^T + c_\mu \sum_{h=1}^{\mu} w_p \left(y_{h,g+1}\right) \left(y_{h,g+1}\right)^T \tag{4.51}$$

Step-size Control - The step-size or called standard deviation controls the scale of the distribution. Another evaluation path p_σ is constructed to evaluate whether current step size is appropriate. Here, $p_\sigma \sim N(0, I)$ is conjugate and starts with $p_{\sigma,0} = 0$.

$$p_{\sigma,g+1} = (1 - c_\sigma) p_{\sigma,g} + \sqrt{c_\sigma (2 - c_\sigma) \mu_{eff}} C_g^{-1/2} \frac{m_{g+1} - m_g}{\sigma_g} \tag{4.52}$$

where $c_\sigma \leqslant 1$ is the learning rate for the conjugate evolution path. The factor $\sqrt{c_\sigma (2 - c_\sigma) \mu_{eff}}$ is normalization constant for p_σ. The construction of evolution path p_σ is similar to that of p_c. The details could be found in Appendix C.2. The expected length of p_σ under random selection is $\mathbb{E} \|N(0, I)\|$. The update of σ_g is as follows:

$$\sigma_{g+1} = \sigma_g \cdot exp\left(\frac{c_\sigma}{d_\sigma} \left(\frac{\|p_{\sigma,g+1}\|}{\mathbb{E} \|N(0, I)\|} - 1\right)\right) \tag{4.53}$$

Algorithm 1 CMA-ES algorithm

Set λ, $w_{h=1...\lambda}$, c_σ,d_σ, c_c, c_1 and c_μ
Initialize m, σ, $p_\sigma = 0$, $p_c = 0$, $C = I$ and $g = 0$
while not terminate **do**
    eigenvalue decomposition $C_g = BD^2B^T$
    for $k = 1$ to λ **do**
        $z_k \sim N(0,I)$
        $y_k = BDz_k \sim N(0,C_g)$
        $x_k = m_g + \sigma_g y_k \sim N(m_g, \sigma_g^2 C_g)$
    end for
    sort $f(x'_1) \leqslant f(x'_2) \leqslant ... \leqslant f(x'_\lambda)$ // sort fitness
    $m_{g+1} \leftarrow \sum_{h=1}^{\mu} w_h x'_{k,g+1}$ // selection and recombination
    $p_{c,g+1} \leftarrow (1-c_c)p_{c,g} + \sqrt{c_c(2-c_c)\mu_{eff}}\frac{m_{g+1}-m_g}{\sigma_g}$
    $C_{g+1} \leftarrow (1-c_1-c_\mu\sum w_p)C_g + c_1 p_{c,g+1}p_{c,g+1}^T + c_\mu \sum_{k=1}^{\lambda} w_k (y_{k,g+1})(y_{k,g+1})^T$ // covariance matrix adaptation
    $p_{\sigma,g+1} \leftarrow (1-c_\sigma)p_{\sigma,g} + \sqrt{c_\sigma(2-c_\sigma)\mu_{eff}}C_g^{-1/2}\frac{m_{g+1}-m_g}{\sigma_g}$
    $\sigma_{g+1} \leftarrow \sigma_g \cdot exp\left(\frac{c_\sigma}{d_\sigma}\left(\frac{\|p_{\sigma,g+1}\|}{\mathbb{E}\|N(0,I)\|} - 1\right)\right)$ // step-size control
    $g \leftarrow g+1$
end while

where $d_d \approx 1$ is the damping parameter which scales the change of σ_g.

The pseudocode of the algorithm can be found below.

$$C_{g+1} = \left(1 - c_1 - c_\mu \sum w_s\right) C_g + c_1 p_{c,g+1} p_{c,g+1}^T + c_\mu \sum_{h=1}^{\mu} w_h \left(y_{h,g+1}\right)\left(y_{h,g+1}\right)^T \tag{4.54}$$

The default parameters of CMA-ES can be found in Appendix C.3.

4.4.3 Fast IPOP-CMA-ES Algorithm

In order to improve the computational efficiency for a global minimization problem, a new start drive signal for CMA-ES with increasing population size (IPOP) is introduced. The IPOP-CMA-ES algorithm is proven to be a simple and effective strategy [180]. By comparing the iterating CMA-ES solutions, the best one in the loop is chosen to be the algorithm result. In each iteration, the calculation stops when convergence is observed or its parameters do not indicate further improvement [181]. A new start is then launched by increasing the population size with a factor of 2.

Learning faster - So far the rank-one update guarantees the direction of the best solution appears with the maximum likelihood in the next generation. The $(\mu+\lambda)$-selection mechanism results in an optimal moving in different generations. In order to speed up the learning efficiency in the iterative process, in this study a $(\mu+\lambda)$-selection is combined with IPOP-CMA-ES algorithm by adding the historical best candidate $x_{best,g-1}$ to be part of the offsprings if it is superior to the current best one as below:

$$x_{best,g} = \begin{cases} x_{best,g-1} & f(x'_{1,g}) \geqslant f(x_{best,g-1}) \\ x'_{1,g} & f(x'_{1,g}) < f(x_{best,g-1}) \end{cases} \tag{4.55}$$

$$z_{best,g} = \begin{cases} z_{best,g-1} & f(x'_{1,g}) \geqslant f(x_{best,g-1}) \\ (BD)^{-1}\frac{x_{best,g}-m_g}{\sigma_g} & f(x'_{1,g}) < f(x_{best,g-1}) \end{cases} \tag{4.56}$$

where BD is derived from the eigenvalue decomposition of covariance matrix C_g in the current iteration. The proposed algorithm is named Fast IPOP-CMA-ES algorithm, aiming at improvement of computational efficiency as well as the preservation of existing exploration ability of IPOP method.

4.4.4 Solution of EPLEPR Problem Using Fast IPOP-CMA-ES Algorithm

To implement the Fast IPOP-CMA-ES algorithm, it should follow processes of the sampling, selection and recombination, adaptation of the covariance matrix and step-size control with appropriate static and dynamic parameters. It should be noted that before the sampling, a two-stage initialization of mean value vector is needed for the proposed two-stage stochastic EPLEPR problem. The details of the implementation steps are as follows:

Step 1: Generate scenarios using DPMM based on the long-term generation profile, load profile and price profile for the microgrid.

Step 2: Initialize a restart counter r to be 1 and set the stopping criterion R.

Step 3: Initialize the parameters for the fast IPOP-CMA-ES algorithm. The static parameters consist of λ, $w_{1...\lambda}$, $\boldsymbol{c_\sigma}$,d_σ, $\boldsymbol{c_c}$, $\boldsymbol{c_1}$ and $\boldsymbol{c_\mu}$ which stay the same during the iteration. The dynamic parameters are $\mathbf{m}$, $\boldsymbol{\sigma}$, $\boldsymbol{p_\sigma}$, $\boldsymbol{p_c}$ and $\mathbf{C}$. These parameters are updated for sampling during the iteration in the next step. The process to generate initial mean value vector $\mathbf{m}$ is split into two stages as shown in Figure 4.4. $\mathbf{m}$ consists of L_s^{ESS}, C_s^{ESS}, $E_{s,t}^{ESS}$ and D_s^{AR}. In the first-stage, the location L_s^{ESS} and sizing C_s^{ESS} of sth ESS are chosen within the lower and upper limit. The stored energy of the sth ESS at any time t $E_{s,t}^{ESS}$ will be created in the second-stage and it is smaller than the upper limit of the capacity C_s^{ESS}. Meanwhile the assigned depth for arbitrage D_s^{AR} are chosen between 0 and 1.

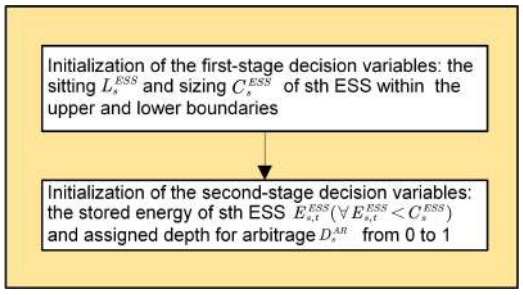

Figure 4.4: Initialization of two-stage stochastic optimization by using the fast IPOP-CMA-ES algorithm

Step 4: Initialize the evaluation counter c to be 1 and set the stopping criterion SC. The counter is used to count the number of fitness calculations. If the stopping counter number SC is large, the computation of the algorithm can be extremely time-consuming.

Step 5: Sample the population of λ parents using Equation (4.43).

Step 6: Solve power flow equations for all parents. Check the physical constraints such as nodal voltage constraint, branch capacity constraint and ESS operation constraint. If all physical constraints are satisfied, go to step 7. Otherwise, generate new searching points by using the same two-stage initialization technique in Step 3 and make sure they are feasible. Here, the Backward/Forward Sweep (BFS) method is used for power flow calculation in the study. It is an efficient method that has

been widely used for power system operation, control and planning [182], especially the radical network topology based on Kirchhoff's laws. The method consists of two step: backward sweep and forward sweep. First in the backward sweep, the branch current and power injection at each bus are calculated from farthest node to the sending end by Kirchhoff's Current Law and Kirchhoff's Voltage Law. Second in forward sweep, downstream nodal bus voltage are updated based on the bus voltage in the sending node and corresponding branch current. The power mismatches are used as the convergence criterion of the method.

Step 7: Evaluate all parents using the objective function (4.40)-(4.41).

Step 8: Select best μ offsprings based on the evaluation values.

Step 9: Update dynamic parameters for the next iteration.

Step 10: Update evaluation counter and check if it is smaller than the stopping counter number SC. Yes, go back to step 5 and start a new iteration. Otherwise, go to step 11.

Step 11: Update the restart counter by adding 1 and check if it meets the stopping criterion R. Yes, return the optimal solution. Otherwise, go back to step 3 and reinitialize the static and dynamic parameters.

The flow chart of the proposed solution is given in Figure 4.5.

4.5 Case Study: Energy Storage Planning in a Microgrid

4.5.1 System Under Study

In the section, we will implement the energy storage system based on the topology from the result of Chapter 3. As examined in the Chapter, only the cost-effective renewable WTs are installed. There are one 850kW type I WT installed at bus 4 and one 2000kW

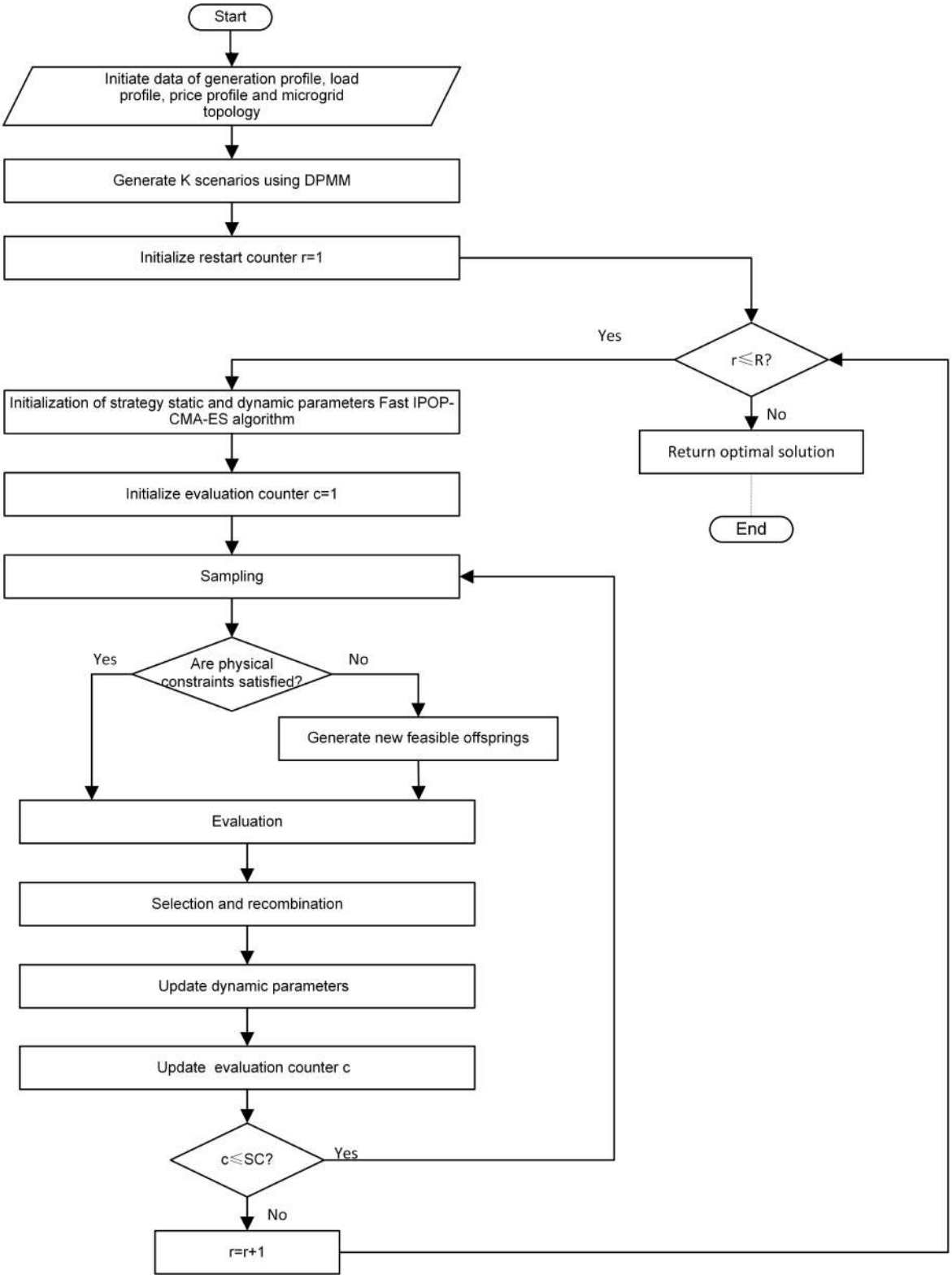

Figure 4.5: Flow chart of fast IPOP-CMA-ES algorithm for EPLEPR problem

type III WT installed at bus 26. The total WT capacity is 2850kW. The total basic load demand of the 33-bus microgrid is 3715 kW and 2300 kVAR, respectively. The single line diagram is shown in Figure 4.6.

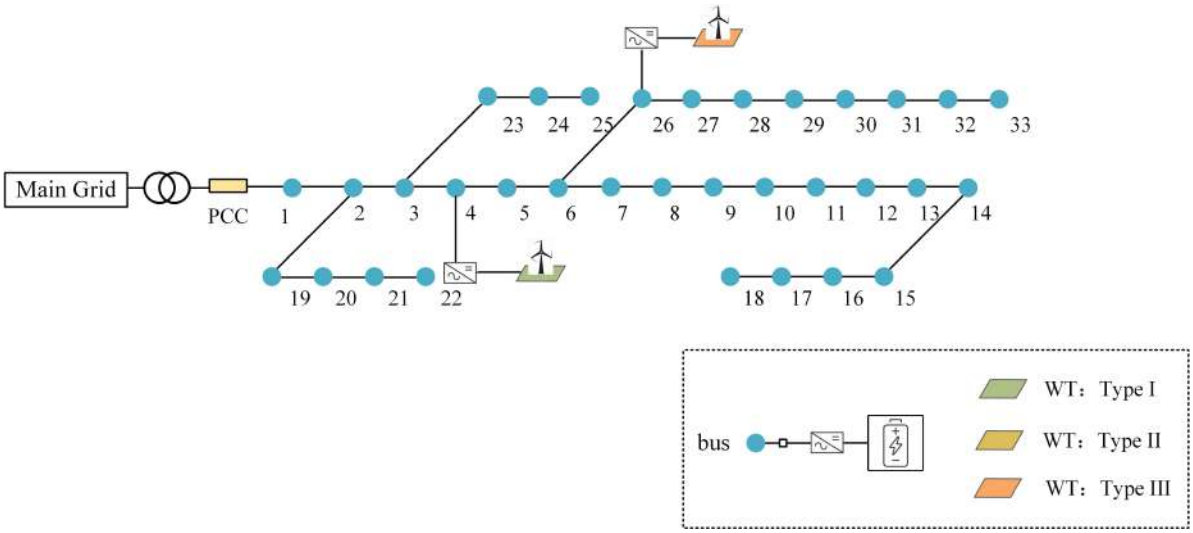

Figure 4.6: The schematic microgrid test system with wind turbines

The data of yearly predicted and actual load and wind generation from Elia Grid [174] is used for analyses of load and renewable generation fluctuations. Meanwhile, the day-ahead electricity market price data are taken from the Nord Pool [175]. The system sell price and system buy price is a single price from Elecxon [183]. After scenario reduction by using the same self-adaptive data-driven nonparametric approach for the data-driven generating uncertainty set in Chapter 3, there are two representative scenarios with shares of 94.72% and 5.28% respectively. The results as shown in Figure 4.7 and Figure 4.8 indicate that in almost all cases the predicted values are larger than the actual values. It reflects the bias of the prediction algorithms chosen by Elia Grid and Nord Pool, which is beyond the scope of this chapter. The major difference of the two scenarios falls in the daily wind power generation. As can be observed from Figure 4.7(a) and Figure 4.7(b), the range of wind generation varies from 813kW to 1001 kW and from 172kW to 455kW. V_0 is set to 1 p.u. V_{min} and V_{max} are 0.9 p.u. and 1.1 p.u., respectively. The branch capacity limit is 4 MVA.

The estimated planning time horizon of the ESS is 10 years. To find out the optimal

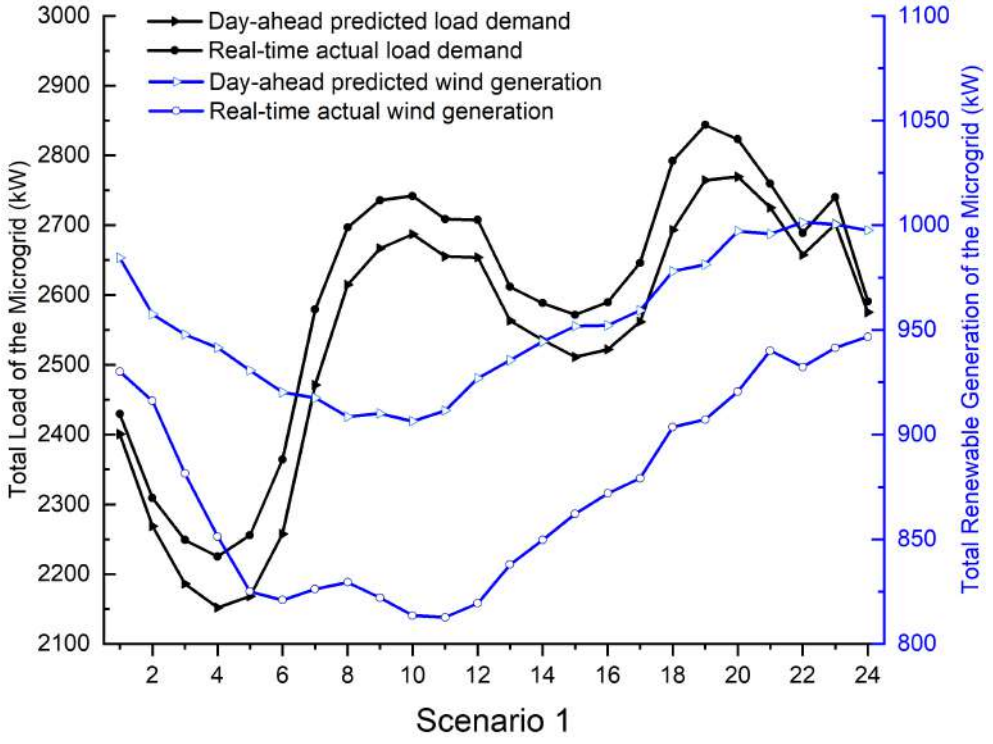

(a)

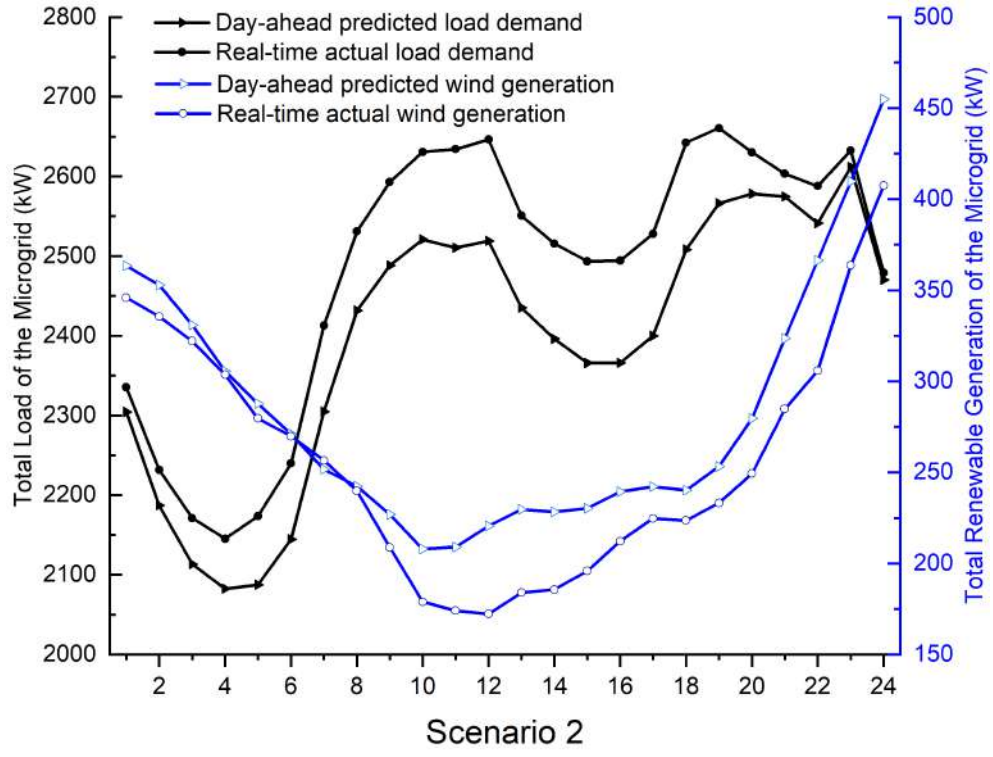

(b)

Figure 4.7: Total load demand and wind generation of the microgrid in (a) Scenario 1 (b) Scenario 2

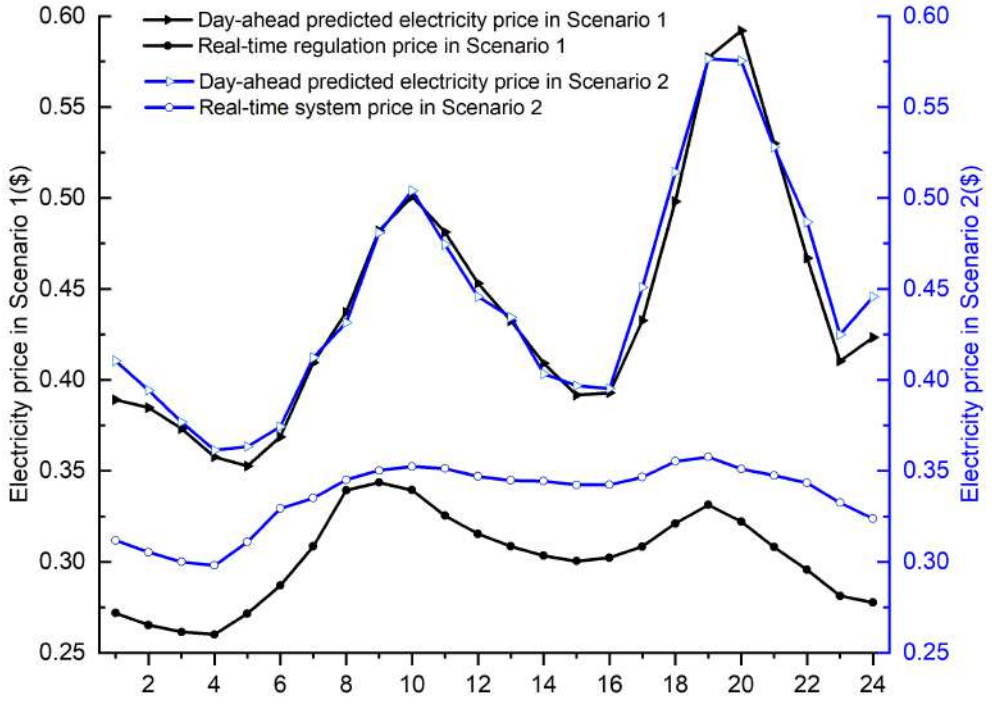

Figure 4.8: Day-ahead predicted electricity price and system price in Scenario 1 and 2

size and location of ESS that suit both scenarios, three types of battery - Advanced Lead-Acid (ALA), Lithium-Ion (Li-ion) and Lithium-titanate (LT) - are investigated under various conditions. All the simulation results are implemented using a computer with an Inter(R) Core(TM) i7-7560U CPU at 2.40 GHz. Table 4.1 shows the parameters of the three aforementioned types of ESSs [97, 176, 184]. The discharge C-Rate 2 in the table indicates that the discharge power $\frac{P_t^{dis}}{\eta_d}$ should not exceed the capacity of the battery when a fixed 50% discharge power is allocated for fast reserve. LT battery has the maximal the charge C-Rate and life cycles. However, the investment cost is much higher than the other types of batteries.

Other key parameters for the simulation could be found in Table 4.2. The average price used for the service of fast reserve is from [97] based on the balancing mechanisms in the UK. It can be seen that the price is far lower than the electricity price in the spot market.

Table 4.1: Battery parameters

Item	Advanced Lead-Acid	Lithium-Ion	Lithium-Titanate
Investment Cost ($/$kWh$)	137	296	773
O&M Cost ($/$kW-yr$)	20	20	20
Charge efficiency (%)	95	99	96
Discharge efficiency (%)	86	92	99
Charge C-Rate	0.33	1	3.5
Discharge C-Rate	2	2	2
Life cycles at 90% DOD (times)	1000	1500	5000

Table 4.2: Parameters for simulation

Item	Value
Discount rate (%)	5
Price upper boundary β_{max}	1.2
Price lower boundary β_{min}	0.9
DOD of ESS (%)	90
Average price of fast reserve service ($/$kWh$)	0.01

4.5.2 Simulation Results

4.5.2.1 Assessments of Algorithms

The simulation is carried out for the proposed EPLEPR problem with three types of ESS, namely ALA, Li-ion and LT, and the problem is solved by three different optimization algorithms, namely $(\mu + \lambda)$-ES, CMA-ES and fast IPOP-CMA-ES. The optimal results are shown in Table 4.3. Here, all the results show the average values after 10 runs of corresponding algorithm. The obtained locations and capacities of the three algorithms are different from each other because of the inherent characteristic of meta-heuristic algorithms, that is they do not guarantee a globally optimum. This kind of methods are likely to terminate when one of the local optimums is found. One algorithm may perform slightly better than the other in a particular problem. Therefore, a comparison is always performed among different meta-heuristic algorithms for a particular problem. Here it is evident that the proposed fast IPOP-CMA-ES algorithm outperforms other algorithms in finding the optimum with minimum computation time for all three types of ESSs. The optimal result is achieved by installing a Li-ion type ESS at bus 3 with storage capacity

of 459.37 kWh. The optimal assigned depth for arbitrage is 78.90%. The total cost in the situation is $ 53,167,141 which is $82,878 lower than the total cost solved by CMA-ES algorithm. The cost saving is not very significant because the generation is lower than the load in both scenarios. As the planning horizon of the ESS is 10 years, the day-ahead energy procurement cost dominates the total cost, which is over $ 48,000000 in all cases.

Table 4.3: Simulation results of single ESS planning

Battery type	Algorithm	Location	Capacity (kWh)	Assigned depth for arbitrage (%)	Total cost ($)	Computation time (s)
ALA	$(\mu+\lambda)$-ES	7	2.88	16.48	53,190,468	1558.26
	CMA-ES	33	2.10	90	53,198,301	1045.98
	fast IPOP-CMA-ES	32	702.35	50.12	53,176,638	682.47
Li-ion	$(\mu+\lambda)$-ES	9	0.06	28.74	53,198,762	1165.17
	CMA-ES	25	1314.14	53.70	53,250,019	892.90
	fast IPOP-CMA-ES	3	459.37	78.90	53,167,141	729.26
LT	$(\mu+\lambda)$-ES	10	1.50	49.36	53,198,946	1281.29
	CMA-ES	2	0.38	90	53,199,844	1581.03
	fast IPOP-CMA-ES	23	28.58	73.33	53,198,719	609.65

Figure 4.9 illustrates the convergence of the three algorithms. $(\mu+\lambda)$-ES algorithm converges within a small number of iterations as shown in Figure 4.9(a). However, the computation cost in each iteration is higher. This is because the recombination and mutation processes are likely to generate infeasible offsprings which have to be discarded. The simulation results also interestingly reveal that the resultant ESS capacity solved by $(\mu+\lambda)$-ES algorithm is rather small. For this kind of multi-modal optimization problems, the $(\mu+\lambda)$-ES algorithm is unable to find a good trade-off between the exploration and exploitation in finding the optimum.

The CMA-ES algorithm adopts (μ,λ)-selection method. As shown in Figure 4.9(b), the fitness value varies dramatically during iterations. Although it needs more iterations to converge than the $(\mu+\lambda)$-ES, the computation effort in each iteration is much smaller. The obtained planning result by the CMA-ES algorithm is however the worst among the three algorithms. Therefore, it is also not the most suitable algorithm for the proposed problem.

10 colored lines in Figure 4.9(c) represent the convergence of the fast-IPOP-CMA-ES

algorithm which is implemented for 10 runs of the single CMA-ES algorithm. Each line converges quickly as a response to the $(\mu + \lambda)$-selection method. The computation time verifies the effectiveness of the proposed fast IPOP-CMA-ES algorithm. For instance, the computation time for Li-ion type ESS is 729.26s, which is 37.41% and 18.33% faster than the $(\mu + \lambda)$-ES and CMA-ES algorithm. This advantage guarantees the validity of the proposed algorithm for solving large-scale optimization problems.

Figure 4.10 shows the results of nodal voltage in two generated scenarios. With the same ESS charging/discharging scheme, the lowest voltages appear at the same terminal end - bus 18 - in both scenarios, which are 0.95 p.u. at 19:00 in Scenario 1 and 0.93 p.u. at 12:00 in Scenario 2. The branch apparent power (in MVA) in the two scenarios are shown in Figure 4.11. The largest power occurs at the branch connecting bus 2 and bus 3 at 11:00 in both scenarios. The evaluation of the resultant voltage and current profiles confirms that the planning result is within the system's limits.

4.5.2.2 Assessments of ESS types

Table 4.4 shows the cost breakdown of investment cost (C^{INV}), operation and maintenance cost (C^{OM}), use of system cost (C^{UoS}), day-ahead energy procurement cost (C^{DA}), real-time imbalance charge (C^{IB}), residual value (R^{RV}), and revenue of the fast reserve service (R^{FR}) of the three ESS types. The minimal values of these costs achieved by the fast-IPOP-CMA-ES algorithm are $ 53,188,238, $ 53,167,141 and $ 53,198,771, respectively. The most suitable battery type for ESS implementation is Li-ion. The results in the table are consistent with the recent widespread development of Li-ion type ESSs. Although ALA battery has the lowest capital cost, the disadvantage of short life cycles leads to a limited residual value after ten-year operation. The highest capital cost per unit of LT battery hinders its development. It can be seen from the table that the installed capacity of LT-type ESS is so small that it could be ignored. Along with the development of battery technologies, the investment cost and OM cost will become much less in the future.

The ten-year-time energy procurement cost C^{DA} accounts for the lion's share (90.93%)

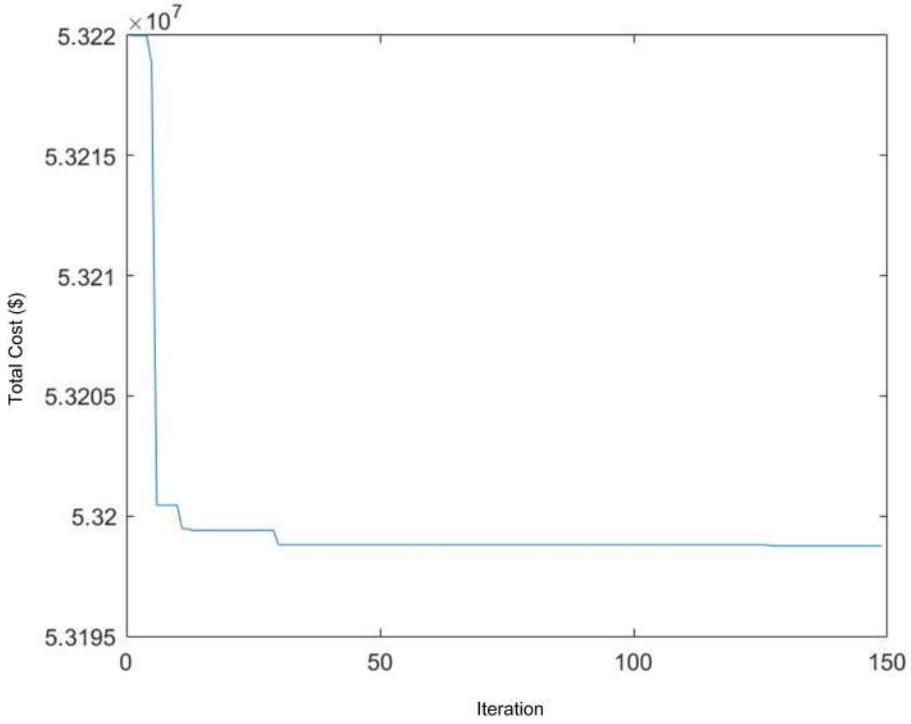
×10^7
5.322
5.3215
5.321
5.3205
5.32
5.3195
Total Cost ($)
0
50
100
150
Iteration

(a)

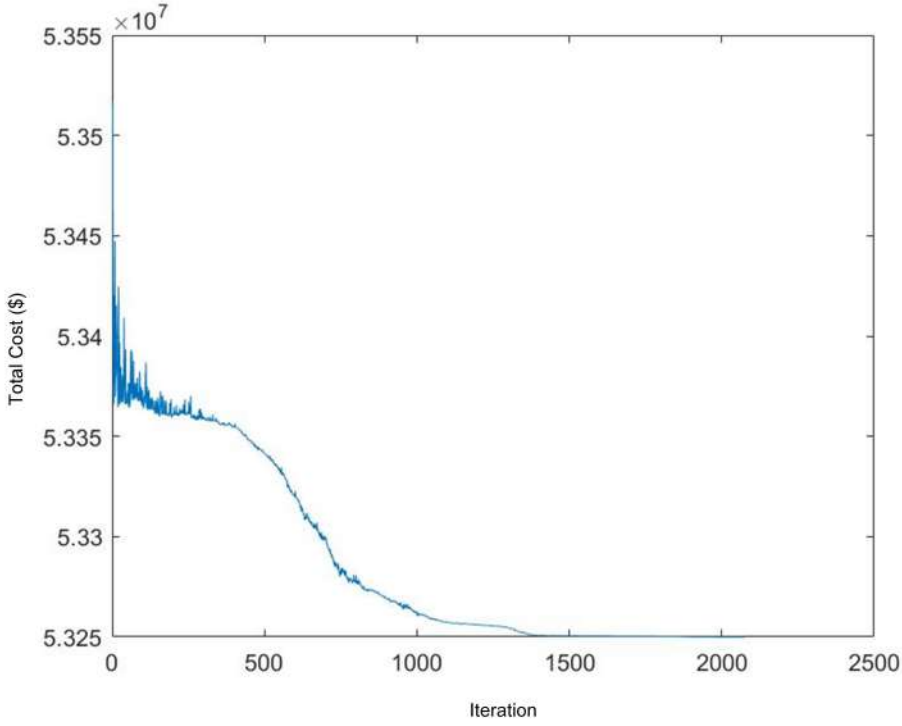
×10^7
5.355
5.35
5.345
5.34
5.335
5.33
5.325
Total Cost ($)
0
500
1000
1500
2000
2500
Iteration

(b)

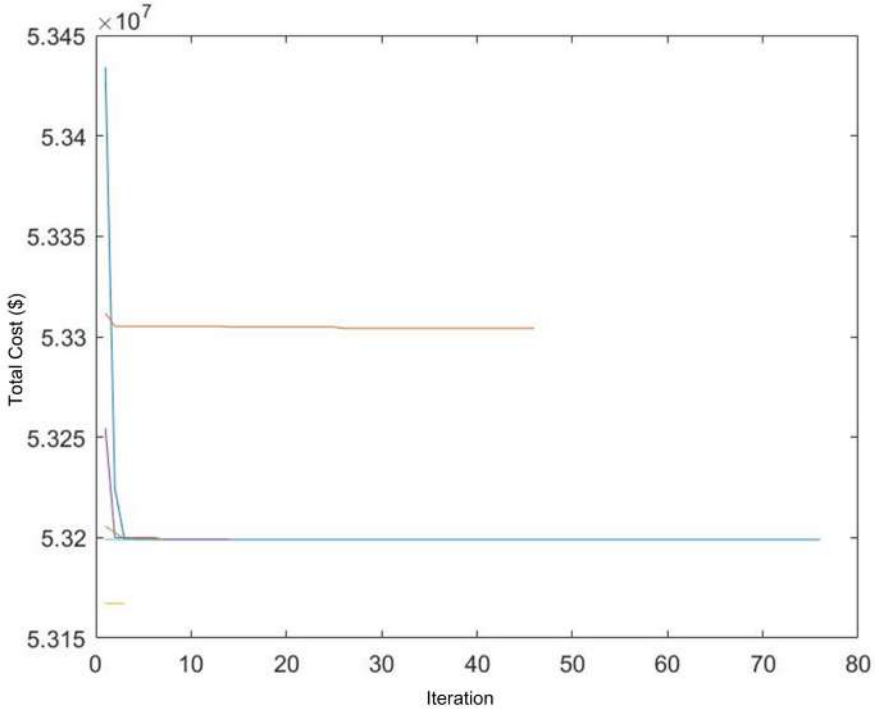

(c)

Figure 4.9: Iterative process of simulation solved by the algorithm of (a) $(\mu + \lambda)$-ES (b) CMA-ES and (c) fast IPOP-CMA-ES

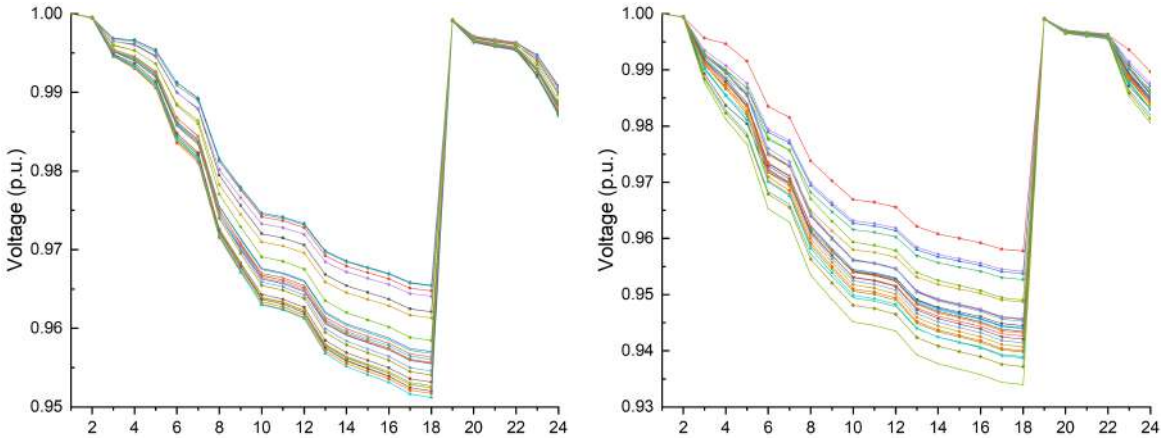

(a) (b)

Figure 4.10: Nodal voltage in (a) Scenario 1 (b) Scenario 2

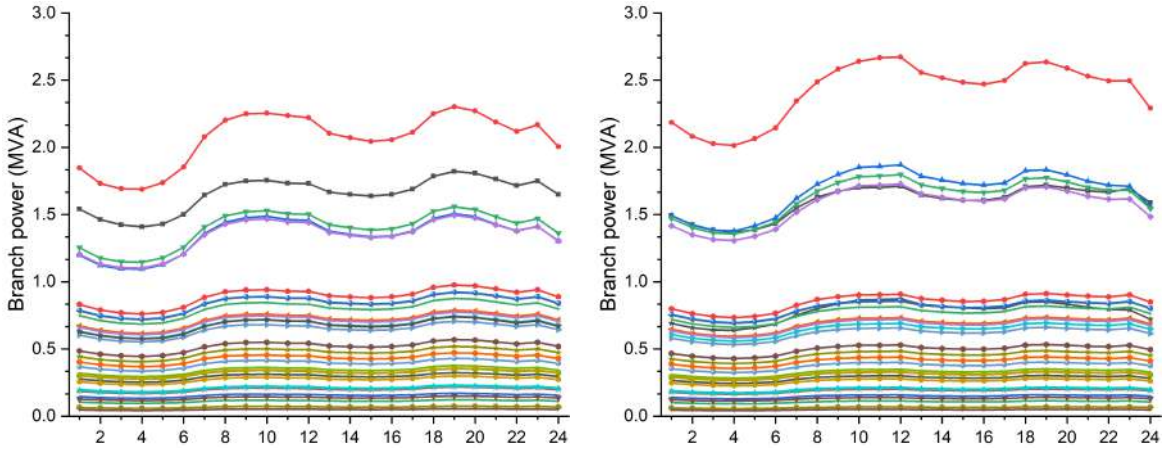

(a) (b)

Figure 4.11: Branch power in (a) Scenario 1 (b) Scenario 2

Table 4.4: Cost breakdown of three types of ESS

Battery type	ALA	LI	LT
C^{INV} ($)	96,222	135,974	85
C^{OM} ($)	108,467	70,943	44
C^{UoS} ($)	1,838,842	1,838,855	1,838,842
C^{DA} ($)	48,247,163	48,240,749	48,463,868
C^{IB} ($)	2,952,910	2,954,553	2,895,933
R^{RV} ($)	59,072	72,496	52
R^{FR} ($)	7,894	1,437	1
Total cost ($)	53,176,638	53,167,141	53,198,719

of the total costs for Li-ion type ESS. This huge expense is due to the gap between the renewable generation and consumption as shown in Figure 4.7, especially when the wind turbine fails to deliver the required power. The adjustment of day-ahead energy procurement in spot market is related to the capacity of ESS. If the capacity is large, the ability of ESS for arbitrage will reduce the cost of energy procurement. However, large capacity of ESS will increase the cost of investment and O&M at the same time. The proposed EPLEPR model is therefore able to find a good trade-off of these contradicting objectives.

The total capacity of Li-ion type ESS that is assigned for arbitrage is 362.46 kWh. Figure 4.12 shows the SOC curve of the ESS during a day. It is the result of the optimal

decision of ESS charging/discharging plan. During 9:00-10:00, the ESS discharges 12.42 kWh while during 10:00-11:00 the ESS is recharged with the same amount of energy. The decision influences the regulation cost associated with trading risk of energy procurement and UoS cost regarding to power loss. The two items consist of 9.02% of the total cost.

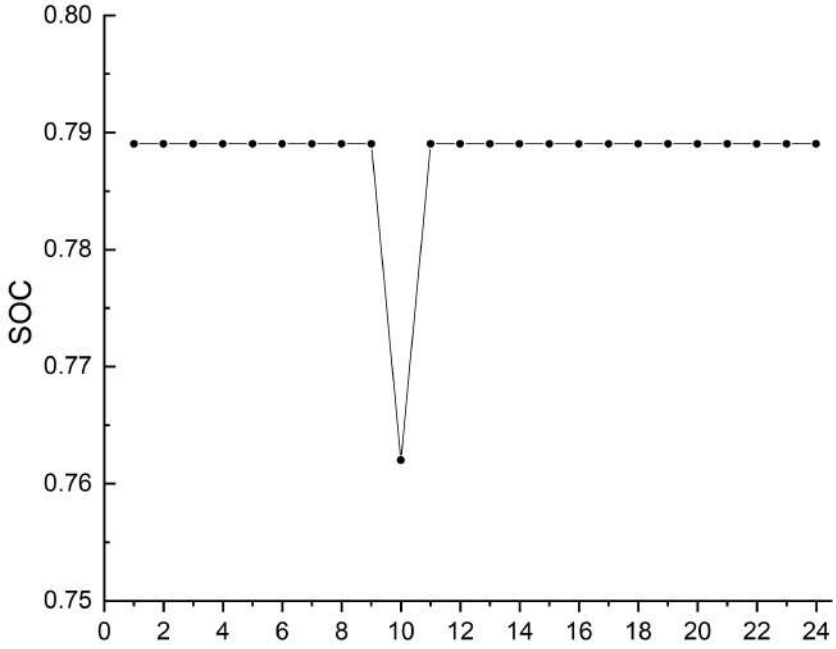

Figure 4.12: SOC of the ESS

4.6 Chapter Summary

With the rapid development of deregulated electricity market, private investors such as generation companies have actively invested in renewable energy to seek profit maximisation. ESS is endeared to system operators and regulators as a promising solution to tackle the reliability and security issues arisen from the integration of renewable energies.

This chapter proposes a two-stage stochastic ESS planning with low energy procurement risks (EPLEPR) model for investors to develop BESS projects in the microgrid with high penetration of renewable energy. The optimal sizing and location needs to consider different financial costs and benefits, incorporating arbitrage, regulation and fast reserve

services for electricity market. The future development of new battery technology and more flexible energy aggregation method, such as virtual power plant in electricity market could be easily merged with the proposed framework. Scenarios of the probabilistic model are generated using a Bayesian nonparametric approach that can fully capture the uncertainty spectrum of high-dimensional data.

A novel algorithm namely the fast IPOP-CMA-ES is proposed to solve the non-convex optimization problem for three battery ESS types, and is compared with two popular optimization algorithms $(\mu+\lambda)$-ES and CMA-ES. The optimal cost \$ 53,167,141 is achieved when installing a Li-ion type ESS at bus 3 with storage capacity of 459.37 kWh and the optimal assigned depth for arbitrage is 78.90% by using the proposed fast IPOP-CMA-ES algorithm, which is \$31,621 lower than the cost solved by $(\mu+\lambda)$-ES algorithm and \$82,878 lower than the cost solved by CMA-ES algorithm. Simulation results also confirm that the proposed algorithm inherits the advantages of fast convergence from $(\mu+\lambda)$-selection of $(\mu+\lambda)$-ES which is 37.41% and 18.33% faster than the $(\mu+\lambda)$-ES and CMA-ES algorithm and great exploration ability from CMA-ES. By tracking the forecasting errors, the investment cost of ESS is offset by the residual value over 10-year operation. By subtracting the residual value from the investment cost, the actual ageing cost of the ESS is \$ 63,478, which is 46.68% smaller than the original investment cost. It implies the life of the ESS is more than 20 years. Meanwhile, a reasonable day-ahead energy procurement is planned by adopting the method. The ten-year-time energy procurement cost accounts for 90.93% of the total costs for the Li-ion ESS because there is not enough renewable generation compared to consumption in the microgrid.

So far, the time scale of planning discussed in the previous two chapters is on a yearly basis. In the next chapter, a smaller time scale- daily basis - will be introduced to validate the resilience of the proposed microgrid planning and operation methods.

CHAPTER 5

RESILIENT OPERATION AND POST-DISASTER RESTORATION SCHEME WITH TESS AND SOP

The traditional design of power systems is based on limited number of known threats to guarantee reliable and secure operations under interruptions. However, the increasing frequency of extreme events due to climate change,e.g. earthquakes, storms and hurricanes, as well as man-made events such as cyber attacks imposes severe challenges to the traditional power systems, demanding resilience-oriented methods to cope with major failures. In 2002, the big Hurricane Sandy destroyed over 100 thousand electrical wires and several substations, which result in a power outage affected around 7 million people in the US [185]. The next decade from 2003 to 2012 witnessed a tremendous increase of weather-related outages, disconnecting more than 10 million customers from power supply [186]. The term "resilience" has different definitions that involve multi-disciplinary knowledge. It covers the ability of a power system to prepare for and adapt to changing conditions, the manners and capacity of a system to "resist" and "recover" from a disturbance [187].

It is a common sense now that one of the important roles that microgrids play is to enhance the power system resilience given the local resources such as DGs when

the microgrid operates on an islanded mode. In addition, a microgrid can be split into multiple segmented microgrids powered by a stationary DG in each island after the network reconfiguration. To mitigate the influence of potential power outages caused by extreme weather events, in this chapter, the transportable energy storage system (TESS) and a D-FACTS device, namely soft-open point (SOP) are introduced. The TESS is a new technology adopted as a post-disaster restoration measure due to its flexibility and mobility. A TESS with pre-stored energy are utilized to restore the areas with power shortage. Additionally, it has the potential to mitigate the renewable power curtailment for a system with high penetration of renewable generation in normal conditions. While SOP can provide both active and reactive power to support the integration of DGs and TESSs. In this Chapter, a multi-objective techno-economic evaluation will be carried out to find out the optimal joint scheme of resilient operation and post-disaster restoration for a microgrid.

5.1 Network Reconfiguration

In Graph Theory, an undirected tree $\mathbb{G} = (\mathbb{N}, \mathbb{E})$ guarantees that two nodes are connected by exactly one branch. This is assumed to be the most popular network structure in power syste, distribution networks due to its simplicity and cost-efficiency. In extreme weather conditions or under man-made cyber-attacks, one or multiple parts of the power system might be damaged, and part of the feeders may lose connection to power supply. During the period, the system can be reconfigured to operate as several islanded microgrids by switching on/off tie switches that connect two feeders. An ideal system after reconfiguration should still retain the radial topology and restore as much loads as possible. Therefore, some of the islanded loads might be restored from another feeder where the remaining isolated area have to wait until the damaged lines are repaired.

Figure 5.1 shows a system with two distributed generators, four feeders and five normally open tie switches. When line faults occurs, the system lose the connection with the main grid, resulting in a microgrid operating in the islanded mode. As the number of

branches in a connected graph with N vertices is $N-1$, the system remain the radical topology.

Now, consider the situation when another line fault occurs after disastrous events. Two possible fault scenarios arise as follows:

(1) The new line fault occurs at $\alpha_{(4,5)}$, $\alpha_{(5,6)}$ or $\alpha_{(6,26)}$.

(2) The new line fault occurs at the other lines different from (1).

Here $\alpha_{(i,j)}$ is a binary variable that represents the line state between bus i and bus j. If $\alpha_{(i,j)}$ is 0, it implies a line fault occurs between bus i and bus j. The first scenario separates the two generators. Each DG will then form a microgrid with radical topology without tie-switches closed. In scenario 2, the two generators are connected together. In order to maintain the radical topology, a tie-switch is closed and the system will operate as one normal islanded microgrid.

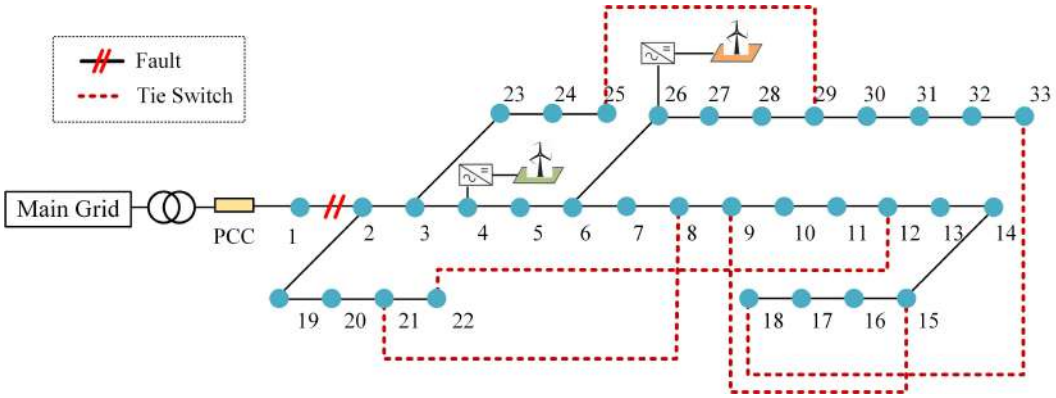

Figure 5.1: The schematic power grid with multiple switches

In this study, a more complicated scenario is considered where three line faults occur, and more than one microgrids are formed after reconfiguration. The reconfiguration follows the principle that each generator operates as a root bus of a microgrid.

$$\sum_{(i,j)\in\mathbb{S}} \eta_{(i,j)} = N_{LF} - N_{MG} \tag{5.1}$$

where N_{LF} and N_{MG} are the number of line faults and microgrid, respectively. $\mathbb{S}$ represents the set of tie switches. $\eta_{i,j}$ is a binary variable that represents the state of tie

switch between bus i and j. If $\eta_{i,j} = 1$, it implies the switch is closed. Otherwise, it is open. For instance, Figure 5.2 shows the N-3 contingency of a system after extreme weather conditions. The system is disconnected from the main grid. In addition, two other line faults occur, resulting in an isolated area in the feeder from bus 11 to bus 18. Equation (5.1) indicates that one switch should be turned off to maintain the radial network configuration. There are several possible network reconfiguration topologies $\mathbb{P} = \{\mathbf{P}_1, \mathbf{P}_2, ..., \mathbf{P}_k\}$ where $\mathbf{P}_k = [\eta_{(i,j)} | \forall (i,j) \in \mathbb{S}]$. In order to restore as much loads as possible, one optimal reconfiguration network should be selected based on a certain criterion.

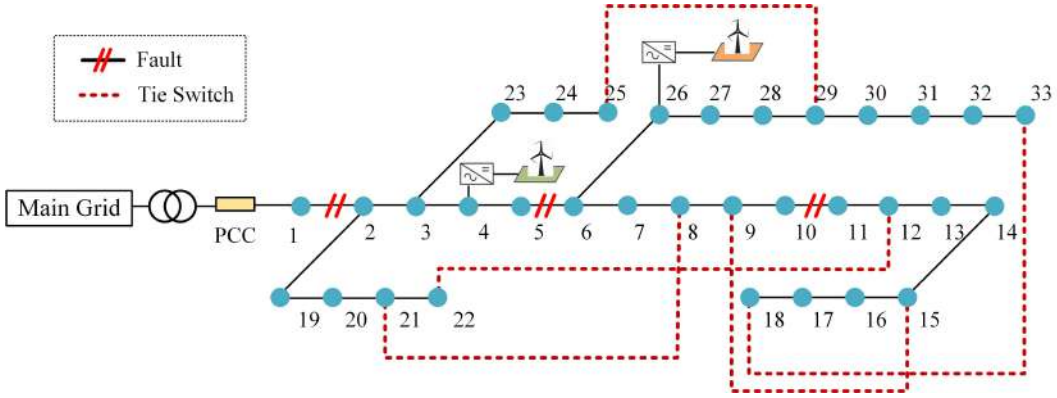

Figure 5.2: The schematic power grid with N-3 contingency

5.2 Modelling of Soft Open Point

A soft open point (SOP) is a new type of power electronic equipment that is considered to replace traditional tie switches [188]. Figure 5.3 shows a back-to-back voltage source converter (VSC) based SOP that connects two feeders at the terminal bus m and n. In the power flow control mode, VSC1 works on the P–Q control scheme whilst VSC2 operates on the $V_{dc} - Q$ control scheme. It provides decoupled active power and reactive power control at both terminals. If a fault occurs on the VSC2 side, loads at the feeder are lost. In addition, the frequency and voltage of VSC2 are decoupled from the grid. In this case, VSC2 is switched to the $V_{ac} - \theta$ control scheme, acting as a voltage source and providing frequency support to the outage area. VSC1 acts as a current source and operates with

the $V_{dc}-Q$ control scheme. The control mode of SOP in both power flow condition and supply restoration condition are summarized in Table 5.1. The transient response can be found in [189]. Simulation results show that SOP can successfully switch among different modes within seconds. The problems of current offset and inrush are solved in the process of mode transition, which reduces unexpected protection operations.

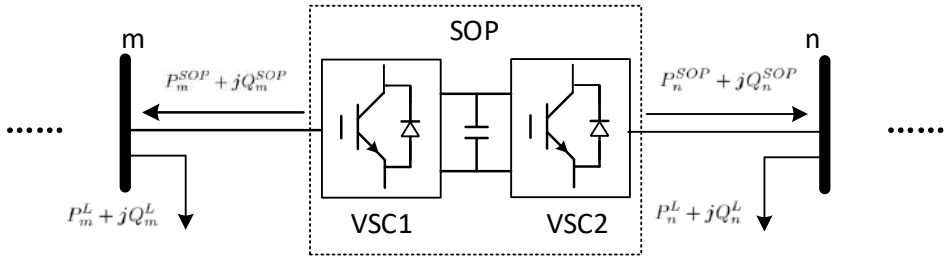

Figure 5.3: Power injection model of SOP

Table 5.1: SOP control mode

Condition	VSC1	VSC2
Nomal power flow condition	$P-Q$	$V_{dc}-Q$
Supply restoration condition (fault connects to VSC2)	$V_{dc}-Q$	$V_{ac}-\theta$

The active power constraint of SOP to be considered is as follows:

$$P_m^{SOP}+P_n^{SOP}+P_{loss}^{SOP}=0 \tag{5.2}$$

where P_m^{SOP} and P_n^{SOP} denote the active power of SOP entering feeder ends at bus m and n, respectively. P_{loss}^{SOP} is the internal power loss of the SOP. As to a high efficiency SOP, P_{loss}^{SOP} is very small and can be neglectable. It becomes

$$P_m^{SOP}+P_n^{SOP}=0 \tag{5.3}$$

The reactive power outputs of SOP are independent, which implies both power compensation and absorption are available. The operational limits of power entering the feeders are constrained by the capacities of the two symmetrical VSCs, it follows

$$(P_m^{SOP})^2+(Q_m^{SOP})^2\leqslant(S_m^{SOP})^2 \tag{5.4}$$

$$(P_n^{SOP})^2 + (Q_n^{SOP})^2 \leqslant (S_n^{SOP})^2 \tag{5.5}$$

where S_m^{SOP} and S_n^{SOP} are the rating power of VSC1 and VSC2. The steady-state model represents the capability of SOP to control the active/reactive power flow, as well as the volt/VAr control of the joint feeders.

Constraints (5.4) and (5.5) are quadratic circular constraints. The feasible region can be expressed by the circle in Figure 5.4. To simplify the calculation, the circular constraints are converted to several square constraints instead [190]. More square constraints will improve the accuracy of the approximation. In the study, two square constraints are used to approximate one circular constraint due to the symmetric nature. Constraints (5.4) and (5.5) are therefore converted as follows:

$$-cos(\pi/8)S_m^{SOP} \leqslant P_m^{SOP} \leqslant cos(\pi/8)S_m^{SOP} \tag{5.6}$$

$$-cos(\pi/8)S_m^{SOP} \leqslant Q_m^{SOP} \leqslant cos(\pi/8)S_m^{SOP} \tag{5.7}$$

$$-cos(\pi/8)S_m^{SOP} \leqslant P_m^{SOP} + Q_m^{SOP} \leqslant cos(\pi/8)S_m^{SOP} \tag{5.8}$$

$$-cos(\pi/8)S_m^{SOP} \leqslant P_m^{SOP} - Q_m^{SOP} \leqslant cos(\pi/8)S_m^{SOP} \tag{5.9}$$

$$-cos(\pi/8)S_n^{SOP} \leqslant P_n^{SOP} \leqslant cos(\pi/8)S_n^{SOP} \tag{5.10}$$

$$-cos(\pi/8)S_nSOP \leqslant Q_n^{SOP} \leqslant cos(\pi/8)S_n^{SOP} \tag{5.11}$$

$$-cos(\pi/8)S_n^{SOP} \leqslant P_n^{SOP} + Q_n^{SOP} \leqslant cos(\pi/8)S_n^{SOP} \tag{5.12}$$

$$-cos(\pi/8)S_n^{SOP} \leqslant P_n^{SOP} - Q_n^{SOP} \leqslant cos(\pi/8)S_n^{SOP} \tag{5.13}$$

It is worth noting that the polyhedron shown as the grey area in Figure 5.4 is slightly smaller than the original circular area. Therefore, it is possible that the obtained result may be slightly bigger for a minimization problem.

5.3 Modelling of Transportable Energy Storage System

The dynamics of the transportable energy storage system (TESS) will increase the resilience of the power system operation. A TESS refers to a compact system that

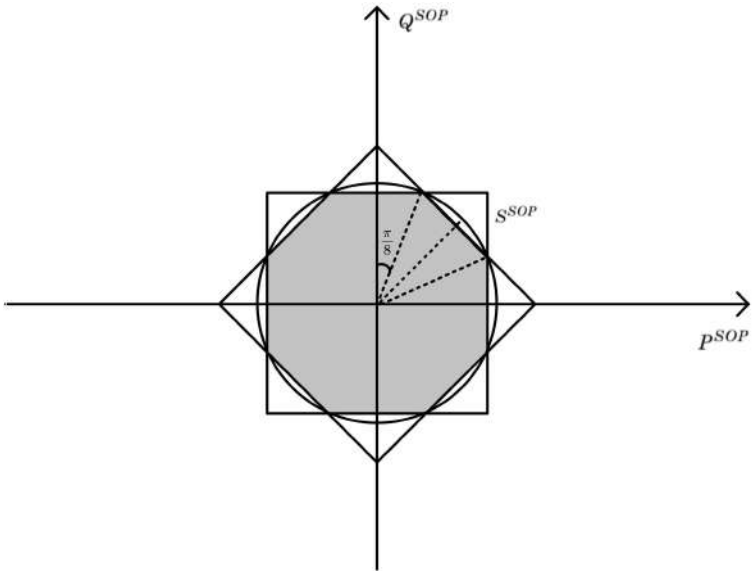

Figure 5.4: Linearization of circular constraint

consists of battery cells and a bidirectional power converter [191]. Unlike the stationary ESS described in Chapter 4, the system is installed in a container which is mounted either on a truck or in a railway carriage to achieve mobility. The charging/discharging schedule of the TESS is therefore combined with the routing problem.

5.3.1 TSN-based Repositioning of TESS

Time-space network (TSN) is an approach that is widely used for modeling the routing schedule of vehicles [192] and railways [193]. It is suitable to demonstrate the variations of spatial components as well as temporal intervals. Figure 5.5 illustrates a simple road grid of a TESS. The transportation network has three real stations and one virtual station. A virtual station is an imaginary station which is proposed to standardize the traveling time among any two connected stations. As shown in Figure 5.5, the travailing time interval between any two stations (whether they are real stations or virtual stations) is one unit time. For instance, the time spent to travel from station 2 to station 3 is twice as from station 1 to station 2. When an extreme weather condition occurs, the TESS is likely to move to the outage area and restore as much loads as possible.

The routes of the TESS are rearranged in terms of time span as shown in Figure 5.6.

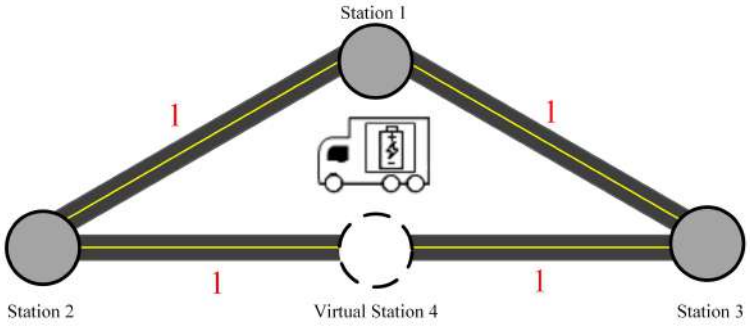

Figure 5.5: The schematic road grid of a TESS

The sold arrow between two adjacent points in time indicates a park arc while the dotted arrow represents a transit arc. The TESS has two possible transit paths at each station, whether it is real station or virtual station. For virtual station only, there is no park. The pattern of park arcs and transit arcs remains the same at all time intervals.

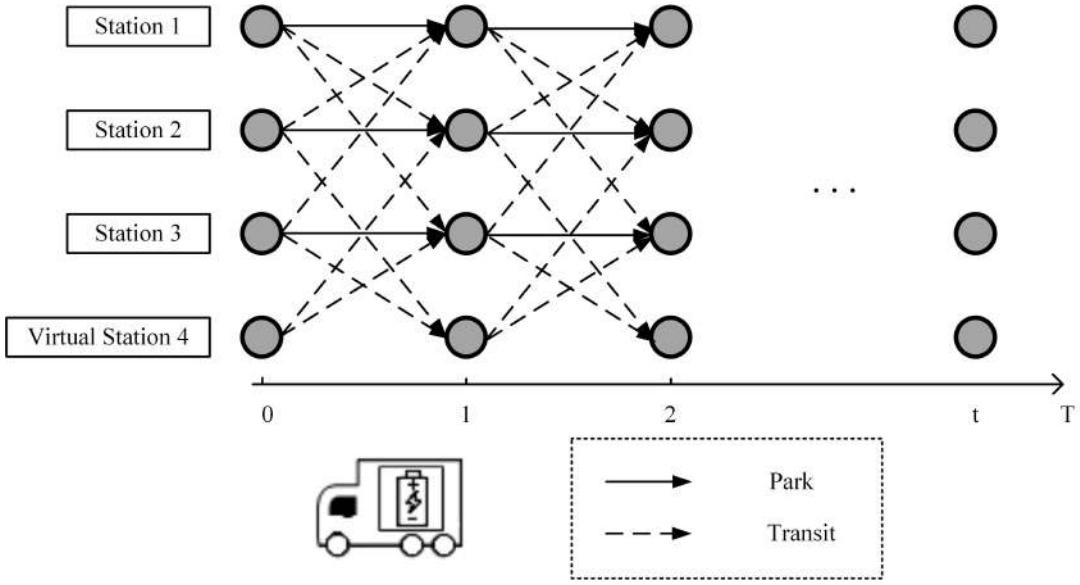

Figure 5.6: TSN model for the schematic road grid of the TESS

The TSN-based repositioning model is formulated as follows:

$$\sum_{(p,q)\in\mathbb{Q}} \gamma_{b,(p,q),t} = 1, \forall b \in \mathbb{B}, t \in \mathbb{T} \tag{5.14}$$

$$\sum_{p\in\mathbb{Y}^+} \delta_{b,p,0} = 1, \forall b \in \mathbb{B} \tag{5.15}$$

$$\sum_{(p,q)\in\mathbb{Q}_p^+} \gamma_{b,(p,q),t+1} = \sum_{(p,q)\in\mathbb{Q}_p^-} \gamma_{b,(p,q),t}, \forall b \in \mathbb{B}, p \in \mathbb{Y}, t \in \mathbb{T} \setminus \{0\} \tag{5.16}$$

$$\sum_{(p,q)\in\mathbb{Q}_p^+} \gamma_{b,(p,q),1} = \delta_{b,p,0}, \forall b \in \mathbb{B}, p \in \mathbb{Y}^+ \tag{5.17}$$

$$\gamma_{b,(p,q),t} + \gamma_{b,(q,p),t+1} \leqslant 1, \forall b \in \mathbb{B}, (p,q) \in \mathbb{Q}, p \neq q \tag{5.18}$$

Constraint (5.14) defines the state of TESS b at time interval t by binary variable $\gamma_{b,(p,q),t}$. $\mathbb{B}$ is the set of TESSs. $\mathbb{T}$ is the set of time spans where $\mathbb{T} = \{0, 1, ..., t\}$. In any time span, TESS b either transits from station p to station q or stays still. (p,q) represents the transit arc/park arc. If p is the same as q, it is a park arc. Otherwise, it is a transit arc. $\mathbb{Q}$ is set of arcs. For instance, there are total 11 arcs (including both park arcs and transit arcs) in a specified time interval for the road grid in Figure 5.6. Constraint (5.15) defines the initial position of TESS b at time interval 0. If TESS b locates at station p, the binary variable $\delta_{b,p,0}$ is 1. Otherwise, it is 0. $\mathbb{Y}^+$ is set of real stations. Constraint (5.16) states that if the TESS b is at the station p at the end of time interval t, it must be in the arc that starts from the station p at the next time interval $t+1$. $\mathbb{Q}_p^+$ is the set of arcs starting from the station p and $\mathbb{Q}_p^-$ is the set of arcs ending at the station p. $\mathbb{Y}$ is the set of stations including both real stations and virtual stations. The initial repositioning state of TESS b is declared in constraint (5.17), which is related to its initial position. Constraint (5.18) states no TESS will return immediately to the station where it travels from at the previous time interval because there is no point in doing so.

5.3.2 Operation of TESS

When considering spatial displacement, only on park arcs can TESS charge from or discharge to the grid. Therefore, we will have

$$0 \leqslant \eta_b^{ch} P_{b,p,t}^{ch} \leqslant \gamma_{b,(p,p),t} P_{max}^{ch}, \forall b \in \mathbb{B}, p \in \mathbb{Y}^+, t \in \mathbb{T} \tag{5.19}$$

$$0 \leqslant \frac{P_{b,p,t}^{dis}}{\eta_b^{dis}} \leqslant \gamma_{b,(p,p),t} P_{max}^{dis}, \forall b \in \mathbb{B}, p \in \mathbb{Y}^+, t \in \mathbb{T} \tag{5.20}$$

$$0 \leqslant \eta_b^{ch} \sum_{p\in\mathbb{Y}^+} P_{b,p,t}^{ch} \leqslant \varphi_{b,t}^{ch} P_{max}^{ch}, \forall b \in \mathbb{B}, t \in \mathbb{T} \tag{5.21}$$

$$0 \leqslant \frac{\sum_{p\in\mathbb{Y}^+} P_{b,p,t}^{dis}}{\eta_b^{dis}} \leqslant \varphi_{b,t}^{dis} P_{max}^{dis}, \forall b \in \mathbb{B}, t \in \mathbb{T} \tag{5.22}$$

where $P^{ch}_{b,p,t}$ and $P^{dis}_{b,p,t}$ are charging and discharging power from the grid to TESS b in the station p at time interval t, respectively. η^{dis}_b is charging efficiency of TESS b and η^{dis}_b is corresponding discharge efficiency. $\varphi^{ch}_{b,t}$ and $\varphi^{dis}_{b,t}$ are binary variable that states the charging/discharging state of TESS b at time interval t. Based on the TSN model, $\sum_{p\in\mathbb{Y}^+}\gamma_{b,(p,p),t}$ is 1 when there exists park arc at time interval t. In this case, there are three possible operation modes of the TESS b: charging, discharging and idle mode. However, when TESS b is on transit arc, the TESS neither charge nor discharge. $\sum_{p\in\mathbb{Y}^+}\gamma_{b,(p,p),t}=0$. The constraints of operation modes of TESS are given below:

$$\varphi^{ch}_{b,t}+\varphi^{dis}_{b,t}\leqslant\sum_{p\in\mathbb{Y}^+}\gamma_{b,(p,p),t},\forall b\in\mathbb{B},t\in\mathbb{T} \tag{5.23}$$

The other technical principles of charging and discharging operation of TESS is similar to the stationary ESS as defined in Section 4.1.3.

$$E^{TESS}_{b,t+1}=E^{TESS}_{b,t}+\eta^{ch}_b\sum_{p\in\mathbb{Y}^+}P^{ch}_{b,p,t}\Delta t-\frac{\sum_{p\in\mathbb{Y}^+}P^{dis}_{b,p,t}}{\eta^{dis}_b}\Delta t,\forall b\in\mathbb{B},t\in\mathbb{T}\setminus\{0\} \tag{5.24}$$

$$SOC_{b,t}=\frac{E^{TESS}_{b,t}}{C^{TESS}_b},\forall b\in\mathbb{B},t\in\mathbb{T} \tag{5.25}$$

$$SOC_{min}\leqslant SOC_{b,t}\leqslant SOC_{max},\forall b\in\mathbb{B},t\in\mathbb{T} \tag{5.26}$$

The energy stored at each time interval t is described in constraint (5.24). Constraints (5.25) and (5.26) define the state-of-charge (SOC) of TESS b and its boundaries where C^{TESS}_b is the energy capacity of TESS b.

5.4 Problem Formulation

5.4.1 Objective Function

Different working conditions for the microgrid are considered below. The first one is the normal resilient operation condition. The objective function Ob_{Q1} in normal condition aims to minimize the total cost that consists of operation and maintenance (O&M) cost of DGs and TESS ($C^{OM_{Q1}}$), wind curtailment cost ($C^{WC_{Q1}}$) , repositioning cost of TESS

($C^{POS_{Q1}}$) and maximize the total revenue of the system ($C^{REV_{Q1}}$).

$$Ob_{Q1} = \min_{\gamma,\varphi,\delta,P,Q,V,P^{DG},Q^{DG},P^{ch},P^{dis},SOC} C^{OM_{Q1}} + C^{WC_{Q1}} + C^{POS_{Q1}} - C^{REV_{Q1}} \tag{5.27}$$

where

$$C^{OM_{Q1}} = \sum_t \left(om^{DG} \sum_l C_l^{DG} + om^{TESS} \sum_b C_b^{TESS} \right) \tag{5.28}$$

$$C^{WC_{Q1}} = \rho^{WC} \sum_t \sum_l \left(P_{max,l,t}^{DG} - P_{l,t}^{DG} \right) \Delta t \tag{5.29}$$

$$C^{POS_{Q1}} = \sum_t \sum_b pos_b \sum_{(p,q)\in\mathbb{Q}, p\neq q} \gamma_{b,(p,q),t} \tag{5.30}$$

$$C^{REV_{Q1}} = \rho^c \sum_t \sum_i P_{i,t}^c \Delta t - \sum_t \rho_t^b P_{1,t} \Delta t \tag{5.31}$$

The first term $C^{OM_{Q1}}$ in Equation (5.28) represents the operation and maintenance costs of all DGs and TESSs during the operating horizon. Here in the study, we only consider the location of the TESS in the operating time horizon. The total number of b and sizing C_b^{TESS} of TESS is predetermined. om^{DG} and om^{TESS} are O&M costs for DG and TESS ($/$kWh$) in the time span t. The second term $C^{WC_{Q1}}$ is wind curtailment cost. $P_{max,l,t}^{DG}$ and $P_{l,t}^{DG}$ are maximal and actual dispatched wind generation of WT l at time interval t, respectively. ρ^{WC} is the price of wind curtailment ($/$kWh$). The third term $C^{POS_{Q1}}$ is regarding the repositioning cost of TESS. If TESS is on the transit arc that $(p,q) \in \mathbb{Q}, p \neq q$, then $\gamma_{b,(p,q),t} = 1$. $pos_{b,t}$ is the cost per unit of time ($) to transport the TESS b. The last term $C^{REV_{Q1}}$ describes the total revenues that are achieved by selling the electricity its customers at price ρ^c ($/$kWh$) and profits through the energy transactions with the main grid. The price ρ_t^b ($/$kWh$) is the sale price at which the main grid sells electricity to the microgrid in the spot market.

The second operation condition considered here is the post-disaster restoration. Under this circumstance, the utility company aims to restore as much load as possible caused by the power outages by choosing the best network reconfiguration topology $\mathbf{P}_k$. Apart from the three cost terms in the objective function Ob_{Q1}, another cost, namely the interruption cost $C^{INT_{Q2}}$ are included in the objective function Ob_{Q1}. In Equation (5.33), int_i is the unit interruption cost for the load at bus i ($/$kWh$). The interruption cost of critical loads is much higher than normal loads in order to guarantee the priority of restoration order.

$$Ob_{Q2} = min\ F(\mathbf{P}_k) = \min_{\gamma,\varphi,\delta,P,Q,V,P^{DG},Q^{DG},P^{ch},P^{dis},SOC,P^{rc}} C^{INT_{Q2}} + C^{OM_{Q2}} + C^{WC_{Q2}} + C^{POS_{Q2}} - C^{REV_{Q2}} \tag{5.32}$$

where

$$C^{INT_{Q2}} = \sum_t \left[\sum_i int_i \left(P^c_{i,t} - P^{rc}_{i,t} \right) \Delta t \right] \tag{5.33}$$

$$C^{OM_{Q2}} = \sum_t \left(om^{DG} \sum_l C^{DG}_l + om^{TESS} \sum_b C^{TESS}_b \right) \tag{5.34}$$

$$C^{WC_{Q2}} = \rho^{WC} \sum_t \sum_l \left(P^{DG}_{max,l,t} - P^{DG}_{l,t} \right) \Delta t \tag{5.35}$$

$$C^{POS_{Q2}} = \sum_t \sum_b pos_b \sum_{(p,q)\in\mathbb{Q},p\neq q} \gamma_{b,(p,q),t} \tag{5.36}$$

$$C^{REV_{Q2}} = \rho^c \sum_t \sum_i P^{rc}_{i,t} \Delta t \tag{5.37}$$

The terms of O&M cost ($C^{OM_{Q2}}$), wind curtailment cost ($C^{WC_{Q2}}$) and repositioning cost of TESS ($C^{POS_{Q2}}$) are the same as Ob_{Q1}. In Equation (5.37), the total revenue $C^{REV_{Q2}}$ does not include the energy transaction with the main grid because of the line fault after extreme weather conditions.

The two objective functions Ob_{Q1} and Ob_{Q2} are coupled in the positioning of TESS, thus the problem in the study is a multi-objective function. We will use the weighted sum model (WSM) to evaluate the decision making results. The WSM score of joint scheme of resilient operation and post-disaster restoration is formulated as follows:

$$Ob = \sum_\omega \omega_1 Ob_{Q1} + \omega_2 Ob_{Q2} \tag{5.38}$$

where ω_1 denotes the weight factor of importance of the normal condition Ob_{Q1} and ω_2 denotes the weight of importance of the post-disaster condition Ob_{Q1}. If all the combinations of ω_1 and ω_2 where $\omega_1 + \omega_2 = 1$ are gone through, a Pareto-optimal front will be generated. In the study, we only consider the simplest multi-criteria decision-making method WSM by assigning a few special combinations of ω_1 and ω_2.

5.4.2 Power Flow Constraints

Resilient Operation Condition LinDistFlow in Equations (5.39)-(5.41) is adopted here as the power flow models. In normal conditions, the load is $P^C_{i,t}$ and $Q^C_{i,t}$ at bus i in the time interval t.

$$\sum_{(i,j)\in\mathbb{E}} P_{(i,j),t} = P_{(h,i),t} - P^C_{i,t} + P^{DG}_{i,t} + P^{SOP}_{i,t} - P^{ch}_{i,t} + P^{dis}_{i,t}, \forall i \in \mathbb{N}, t \in \mathbb{T} \tag{5.39}$$

$$\sum_{(i,j)\in\mathbb{E}} Q_{(i,j),t} = Q_{(h,i),t} - Q^C_{i,t} + Q^{DG}_{i,t} + Q^{SOP}_{i,t}, \forall i \in \mathbb{N}, t \in \mathbb{T} \tag{5.40}$$

$$V_{j,t} = V_{i,t} - \frac{r_{(i,j)}P_{(i,j),t} + x_{(i,j)}Q_{(i,j),t}}{V_0}, \forall (i,j) \in \mathbb{E}, t \in \mathbb{T} \tag{5.41}$$

$$V_{min} \leqslant V_{i,t} \leqslant V_{max}, \forall i \in \mathbb{N}, t \in \mathbb{T} \tag{5.42}$$

where $P_{(i,j),t}$ and $Q_{(i,j),t}$ are active and reactive power flows from bus i to bus j respectively. $r_{(i,j)}$ and $x_{(i,j)}$ are resistance and reactance between bus i and bus j. $P^{DG}_{i,t}$ and $Q^{DG}_{i,t}$ are corresponding active/reactive power generations of DG at bus i. $V_{i,t}$ is the voltage at bus i and V_0 is the reference voltage. Equation (5.42) is the operation limits of voltage magnitude. $\mathbb{E}$ is the set of all branches and $\mathbb{N}$ is the set of all buses.

The branch capacity limit in Equation (5.41) is a circular constraint.

$$P^2_{(i,j),t} + Q^2_{(i,j),t} \leqslant S^2_{(i,j),t}, \forall (i,j) \in \mathbb{E} \tag{5.43}$$

To convert it into a linear constraint, two square constraints as introduced in 5.1.2 are adopted.

$$-cos(\pi/8)S_{(i,j),t} \leqslant P_{(i,j),t} \leqslant cos(\pi/8)S_{(i,j),t}, \forall (i,j) \in \mathbb{E} \tag{5.44}$$

$$-cos(\pi/8)S_{(i,j),t} \leqslant Q_{(i,j),t} \leqslant cos(\pi/8)S_{(i,j),t}, \forall (i,j) \in \mathbb{E} \tag{5.45}$$

$$-cos(\pi/8)S_{(i,j),t} \leqslant P_{(i,j),t} + Q_{(i,j),t} \leqslant cos(\pi/8)S_{(i,j),t}, \forall (i,j) \in \mathbb{E} \tag{5.46}$$

$$-cos(\pi/8)S_{(i,j),t} \leqslant P_{(i,j),t} - Q_{(i,j),t} \leqslant cos(\pi/8)S_{(i,j),t}, \forall (i,j) \in \mathbb{E} \tag{5.47}$$

Post-disaster Restoration Condition When an extreme weather event occurs, the microgrid may suffer several line faults. After reconfiguration, the power flow model for each new microgrid a to restore loads $P^{rc}_{i,t}$ and $Q^{rc}_{i,t}$ is given as follows:

$$\sum_{(i,j)\in\mathbb{E}_a} P_{(i,j),t} = \sum_{(h,i)\in\mathbb{E}_a} P_{(h,i),t} - P^{rc}_{i+1,t} + P^{DG}_{i+1,t} - P^{ch}_{i,t} + P^{dis}_{i,t}, \forall i \in \mathbb{N}_a, t \in \mathbb{T} \tag{5.48}$$

$$\sum_{(i,j)\in\mathbb{E}} Q_{(i,j),t} = \sum_{(h,i)\in\mathbb{E}} Q_{(h,i),t} - Q^{rc}_{i+1,t} + Q^{DG}_{i+1,t}, \forall i \in \mathbb{N}_a, t \in \mathbb{T} \tag{5.49}$$

$$V_{i+1,t} = V_{i,t} - (r_i P_{i,t} + x_i Q_{i,t})/V_0, \forall i \in \mathbb{N}_a, t \in \mathbb{T} \tag{5.50}$$

where $\mathbb{E}_a$ and $\mathbb{N}_a$ are branch and bus sets of microgrid a.

5.4.3 Other Operation Constraints

The charging/discharging power to the grid at bus i is dependant on the status of TESS. If the station p is located at bus i, it is represented by the symbol $p \downarrow i$. When TESS b parks at station p, then the following equations hold:

$$P^{ch}_{i,t} = \sum_b P^{ch}_{b,p,t}, \forall i \in \mathbb{N}, t \in \mathbb{T}, p \downarrow i \tag{5.51}$$

$$P^{dis}_{i,t} = \sum_b P^{dis}_{b,p,t}, \forall i \in \mathbb{N}, t \in \mathbb{T}, p \downarrow i \tag{5.52}$$

The maximal active power generated by DG, denoted as $P^{DG}_{max,i,t}$ will be injected to the grid depends on weather condition. However, the line fault will cause grid congest or over-voltage issues in the post-disaster condition. In the case, DG should curtail the output as follows:

$$0 \leqslant P^{DG}_{i,t} \leqslant P^{DG}_{max,i,t} \tag{5.53}$$

Through the power electronic device, i.e. inverter interface, DG unit is capable to adjust its reactive power to satisfy the power factor pf^{DG}_i required by the system operator. The operation constraints of the adjustable inverter-interfaced DG are mathematically formulated as:

$$-P^{DG}_{i,t} \cdot tan\left[cos^{-1}(pf^{DG}_i)\right] \leqslant Q^{DG}_{i,t} \leqslant P^{DG}_{i,t} \cdot tan\left[cos^{-1}(pf^{DG}_i)\right], \forall i \in \mathbb{N}, t \in \mathbb{T} \tag{5.54}$$

where pf enforces the power factor of each generator.

$$0 \leqslant P^{rc}_{i,t} \leqslant P^{c}_{i,t}, \forall i \in \mathbb{N}, t \in \mathbb{T} \tag{5.55}$$

$$Q^{rc}_{i,t} = P^{c}_{i,t} tan\left[cos^{-1}(pf^{c}_{i})\right], \forall i \in \mathbb{N}, t \in \mathbb{T} \tag{5.56}$$

The Constraint (5.55) enforces the upper and lower boundary on restored active load $P^{rc}_{i,t}$. The reactive load is required by the load power factor pf^{c}_{i} of each bus i in Constraint (5.56).

5.5 Case Study: Resilient Operation of Multiple Microgrids

The case study of the resilient operation will be implemented on a modified IEEE 33-bus system as shown in Figure 5.7. The initial configuration has five tie switches, two WT generators, 33 load buses, 32 transmission lines and one TESS. The tie switches plays an important role in system reconfiguration when line faults occur. In the case study, we also consider the situation when the tie switch is replaced by a SOP.

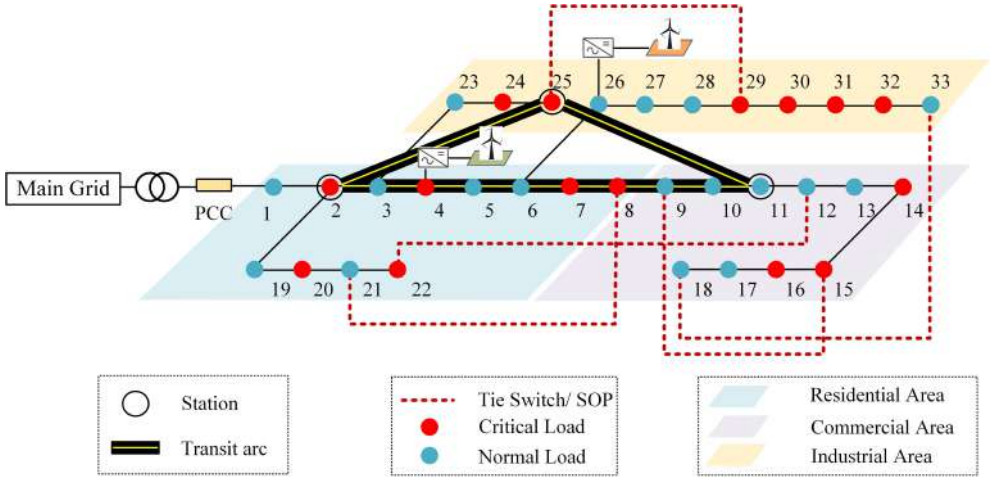

Figure 5.7: The schematic test system

5.5.1 System Under Study

Different from Chapter 3 and Chapter 4, the time scale in this study is one day and the time resolution of load, renewable generation and electricity price is one hour. The location and capacity of WT is taken from the result of Chapter 3. There are one 850kW WT installed at bus 4 and one 2000kW WT installed at bus 26. The total WT capacity is 2850kW. The black dotted curve in Figure 5.8 (a) shows the total generation profile of the two WTs, while the blue one shows the electricity sale price for transactions between the main grid and the microgrid. The variation tendency of the plot is taken from the result of Chapter 4. The original data for clustering of wind generation and electricity price are from Elia Grid [174] and Nord Pool [175]. The O&M cost of WT is 0.01 $/kW.

As shown in Figure 5.8(b), the loads in the study are categorized into three types, namely residential, commercial and industrial customers. The 24-hour load profile is taken from [182]. The total load profile is accumulated shown as the black curve with triangular symbols in Figure 5.8(a). The total load is larger than the total generation at peak hours which are from 11:00 to 13:00 and from 19:00 to 22:00. Other periods are non-peak. The power factor for each type is 0.96, 0.94 and 0.9, respectively. Among the 33 loads, there are 15 critical loads which have a higher restoration priority in the event of a power outage. The interruption costs of critical loads and normal loads are 10 $/kWh and 2 $/kWh, respectively. The tariffs in residential, commercial and industrial area is 0.33 $/kWh, 0.26 $/kWh and 0.24$/kWh, respectively.

The ESS can charge/discharge energy to the power system att three stations. Station 1 is located at bus 25, Station 2 is located at bus 2 while station 3 is at bus 11. The distance between Station 2 and Station 3 is 2 unit length, which is twice the length between Station 1 and 2 and between Station 1 and 3. The repositioning cost per unit length is $ 80. The TESS is Li-ion type with 459.37 kWh energy capacity taken from the result of Chapter 4. The parameters of the TESS can be found below in Table 5.2.

The SOP considered in the study is based on the result of [29]. It replaces the tie switch between bus 18 and bus 33. The capacity of the SOP is 600 kVA. All the simulation results in the remaing sections are implemented with CPLEX 12.8.0 using computer

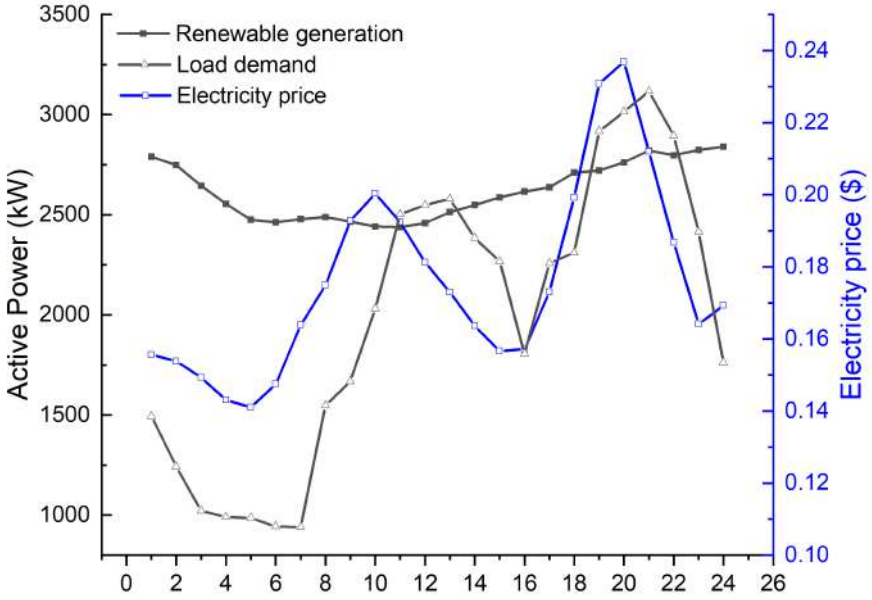

(a)

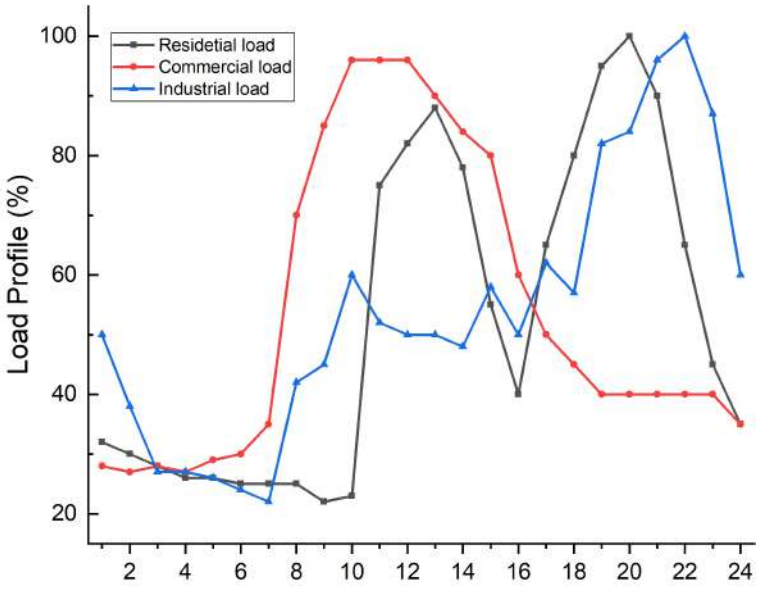

(b)

Figure 5.8: (a) Total generation, load and price profile (b) Load profiles for residential, commercial and industrial area

Table 5.2: TESS parameters

Item	Lithium-ion
O&M Cost ($/$kWh$)	0.02
Charge efficiency (%)	99
Discharge efficiency (%)	92
Charge C-Rate	1
Discharge C-Rate	2
Initial SOC	0.79
SOC_{min}	0
SOC_{max}	0.9

with an Inter(R) Core(TM) i5-6400 CPU at 2.7 GHz.

5.5.2 Case 1: Microgrid in Resilient Operation Condition

In this section, the operation of one day in the test system under normal operation condition is considered. It is regarded as the base case for the post-disaster schedule in the Case 2 and Case 3 of the study. The objective function is Q_1 in the Equation (5.27) which includes O&M cost of DGs and TESS ($C^{OM_{Q1}}$), wind curtailment cost ($C^{WC_{Q1}}$), repositioning cost of TESS ($C^{POS_{Q1}}$) and the revenue of the system ($C^{REV_{Q1}}$) are adopted as the objectives.

Two scenarios are investigated in the remaining section to show the optimal schedules of DG and TESS as follows:

- Scenario 1: Mircrogrid without SOP
- Scenario 2: Mircrogrid with SOP connecting bus 18 and bus 33

Simulation results are listed in Table 5.3. The total cost and breakdown are the same in both scenarios. The total cost is $ -14501.81. The negative value indicates that the total revenue in the system is higher than the total cost. The O&M cost is a fixed expense once the capacity of DG and TESS are decided, which is $ 904.50 per day. The repositioning cost is zero. It means that the optimal option for the TESS is to park at the station 2 during the scheduling horizon in order to minimize the total cost. The wind

curtailment cost is also zero. Therefore, all the power generated by distributed WTs are injected into the grid. The total revenue of the system is $ 15,405.31, which consists of two parts. The first part $ 12952.77 is the revenue from selling electricity to three types of served customers: residential, commercial and industrial loads. The second part $ 2452.54 is the revenue gained from the transactions with the main grid.

Table 5.3: Simulation results of Case 1

	Scenario 1	Scenario 2
Objective ($)	-14501.81	–14501.81
O&M cost ($)	904.50	904.50
Wind curtailment cost ($)	0	0
TESS repositioning cost ($)	0	0
Total revenue ($)	15405.31	15405.31

Figure 5.9 illustrates the optimal wind generation profiles of WT1 and WT2 in both scenarios. The fluctuations of the two WTs are the same. The generated power of WT2 is 2.35 times of the power generated by WT1 due to the capacity limit. The power factor of the two WTs remains at 0.95 to maintain the reliability of the system over the time span. Figure 5.10 (a) illustrates the resultant SOC curves of the TESS in both scenarios. It discharges 333.46 kWh from 1:00 to 2:00, 380.36 kWh from 10:00 to 11:00 and 380.36 kWh from 20:00 to 21:00 to the grid and charges 417.61 kWh from 5:00 to 6:00 and 417.61 kWh from 15:00 to 16:00 from the grid. The active power surplus and shortage of the microgrid is shown in Figure 5.10 (b). The negative power in the figure indicates that the WT generation and TESS are not sufficient to serve all the load demands in 11:00-13:00, 15:00, 19:00 and 21:00-22:00. The duration of power shortage within the microgrid is identical to Figure 5.8 (a), which is 7 hours in the scheduling planning horizon. However, the time segment is different. The power gap is filled by the TESS with energy charged and discharged from the main grid due to the price factor.

The active and reactive power of SOP are demonstrated in Figure 5.11. It is evident that the active power is moving from the feeder where high capacity WT is located to the other feeder with heavy load demands except for 8:00 hr and 18:00 hr. The reactive power works for three hours for voltage control. Figure 5.12 shows the nodal voltages

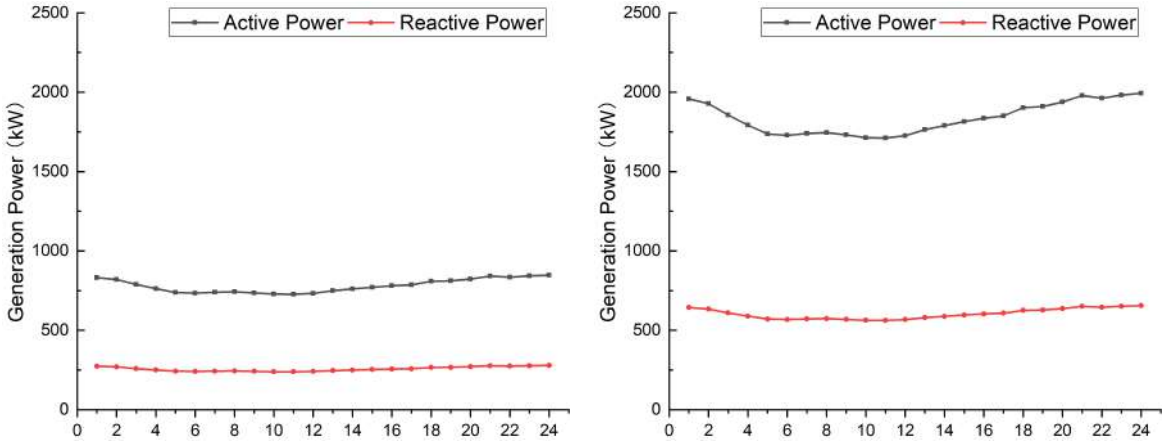

Figure 5.9: (a) Generation profiles of WT1 in Case 1 (b) Generation profiles of WT2 Case 1

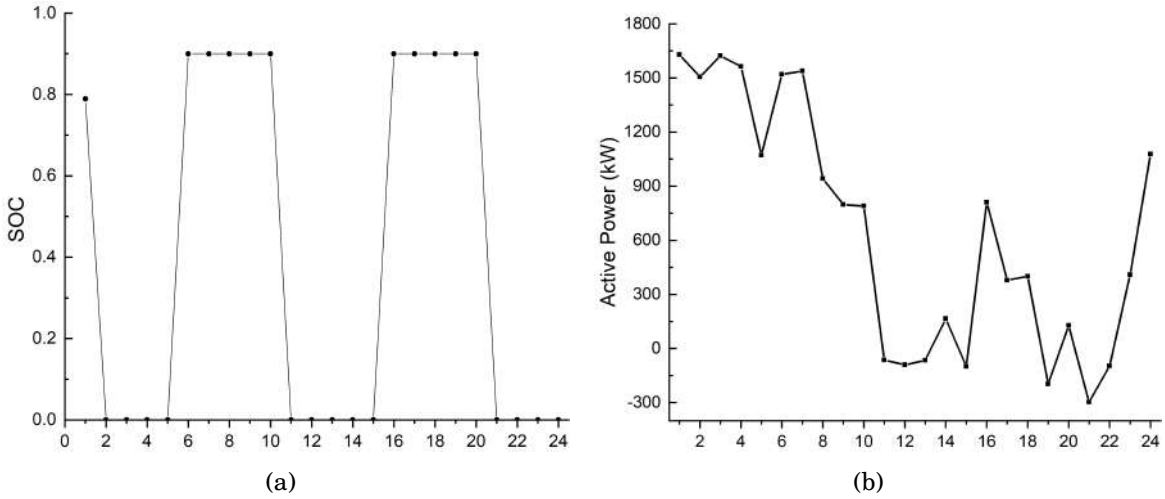

Figure 5.10: (a) SOC of TESS in Case 1 (b) Active power flowing from the microgrid to the main grid in Case 1

which are within permissible limits. The power losses shown in Figure 5.13 also display a critical role that SOP plays in terms of energy efficiency. The total power loss of all branches within a day is 1309.40 kW in Scenario 1, while the figure drops to 1269.00 kW in Scenario 2. Generally speaking, the branch power losses at peak hours are lower than the non-peak hours. It reveals the advantages of the microgrid that consumes energy on-site. The biggest power loss is found at 2:00 hr in Scenario 1 and 3:00 hr in Scenario 2 when the biggest power surplus occurs in the microgrid. In addition, line congestion is relieved with the lower branch current in Scenario 2.

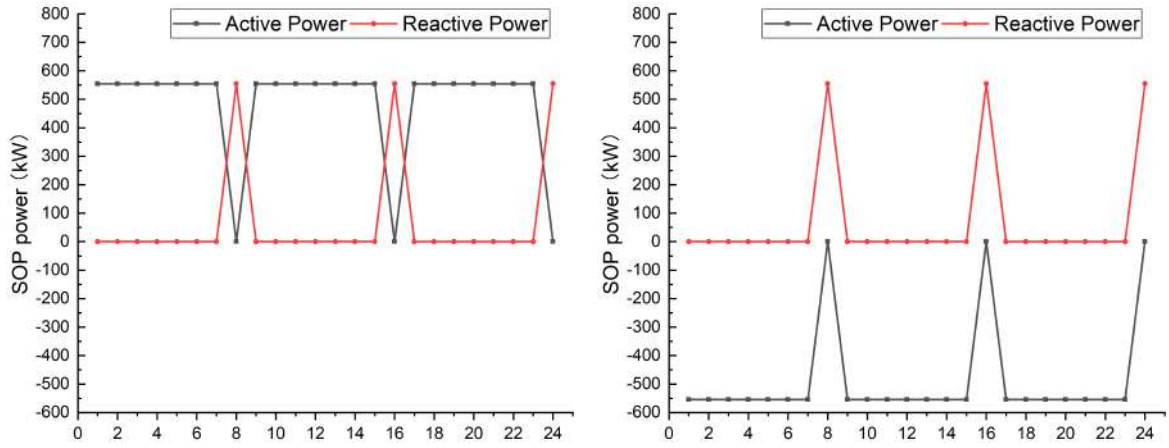

Figure 5.11: (a) SOP power connecting bus 18 in Case 1 (b) SOP power connecting bus 33 in Case 1

The results in normal operation condition show that the TESS work the same as stationary ESS installed at bus 2. Same results of total cost can be achieved when a stationary ESS is placed at bus 11 and 25. It indicates that the location of ESS does not affect the revenues of the test system.

5.5.3 Case 2: Multiple Microgrids with Tie Switches in Post-disaster Condition

The operation in normal condition is regarded as the base case. The results provide prerequisites for a restoration plan, for instance SOC and position of the TESS. In this

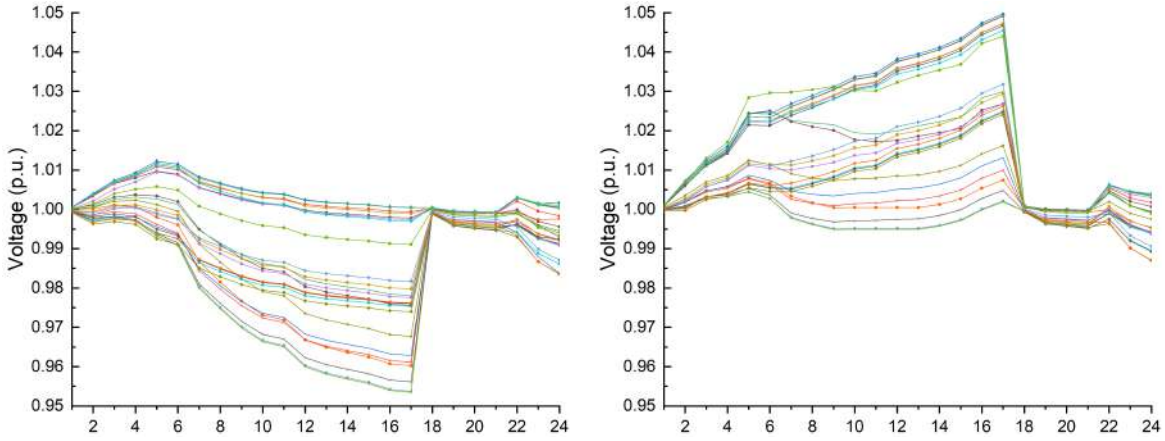

(a) (b)

Figure 5.12: (a) Voltage profile in Scenario 1 of Case 1 (b) Voltage profile in Scenario 2 of Case 1

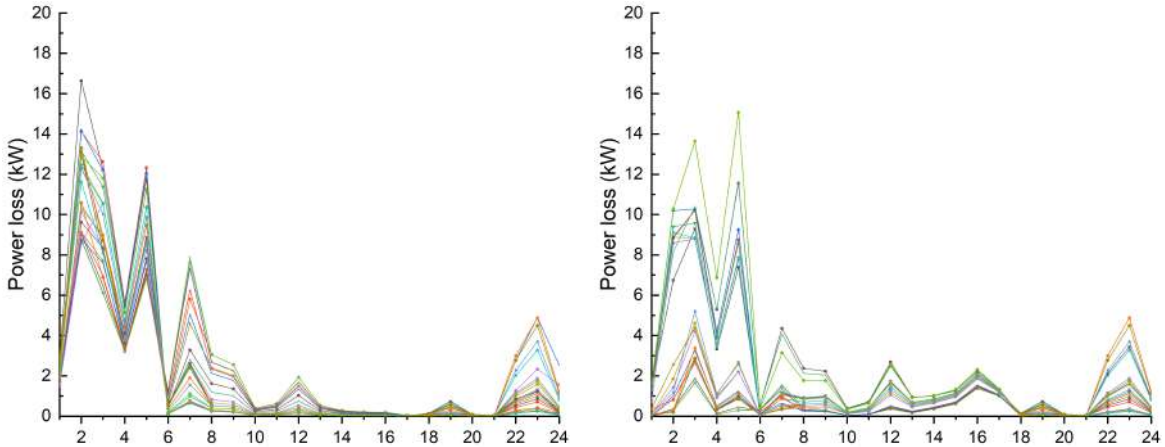

(a) (b)

Figure 5.13: (a) Power loss in Scenario 1 of Case 1 (b) Power loss in Scenario 2 of Case 1

case, line faults as shown in Figure 5.14 are considered. The test system disconnects the main grid and loses the loads between bus 11 to bus 18. Two islanded microgrids powered by WTs are formed without network reconfiguration.

Following the sysmbols and formulation in Section 5.1.1, there are three possible reconfiguration topology which could be represented as $\mathbb{P} = \{\mathbf{P}_1, \mathbf{P}_2, \mathbf{P}_3\}$. $\mathbf{P}_k = [\eta_{(8,21)}; \eta_{(9,15)}; \eta_{(12,22)}; \eta_{(18,33)}; \eta_{(25,29)}]$ where $k = 1, 2, 3$ indicates the states of five tie switches. $\mathbf{P}_1 = [0; 0; 1; 0; 0]$ is the topology with closing switch $\eta_{(12,22)}$. $\mathbf{P}_2 = [0; 1; 0; 0; 0]$ is to close switch $\eta_{(9,15)}$ and $\mathbf{P}_3 = [0; 0; 0; 1; 0]$ is to close switch $\eta_{(18,33)}$.

Incorporating TESS into the system operation leads to a more resilient restoration schedule in the post-disaster condition. In the following section, it assumes that four hours are taken to repair all line faults back to normal operation condition. Three scenarios are simulated to show the generality and particularity of network reconfiguration as follows:

- Power surplus over the restoration period
- Both power surplus and shortage over the restoration period
- Power shortage over the restoration period

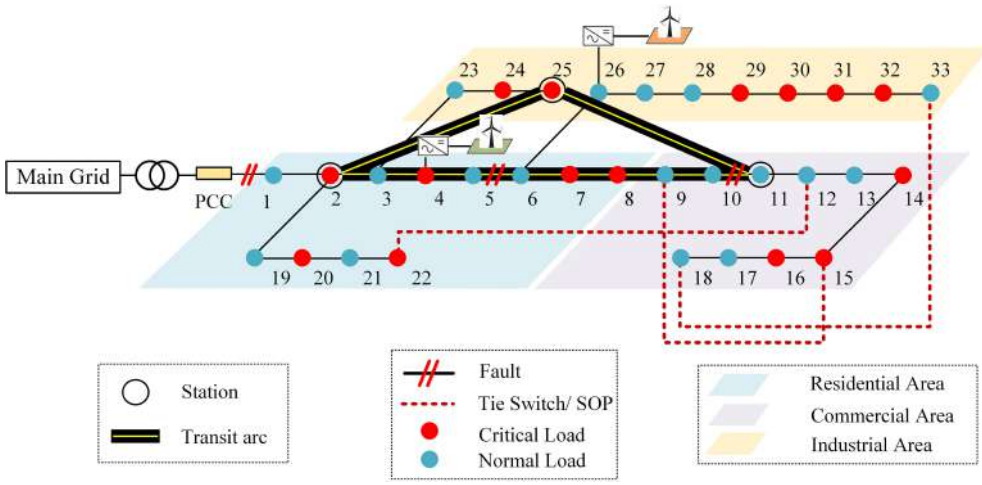

Figure 5.14: The schematic test system with line faults

5.5.3.1 Scenario 1: Power Surplus over the Restoration Period

In this scenario, line faults occur and the topology is reconfigured at 4:00 hr. The restoration takes place from 4:00 - 8:00. Afterwards the tie switch is open, making the system return to work in its normal condition.

The two-objective optimization problems with different objective weight vectors are solved. Simulation results are shown in Table 5.4. In the first three columns, the largest weight is assigned for Ob_{Q2} with no consideration of the objective Ob_{Q1}. It provides the best solution in terms of reducing total power loss (TPL). The second weight vector shown in columns 4-6 is a fair decision in terms of economic aspects. Both objective Ob_{Q1} in resilient operation condition and Ob_{Q2} in post-disaster condition have been equally treated. The first and second weight vectors provide the same restoration schedules, resulting in a 68.19%, 62.60% and 62.50% load restoration rate in reconfiguration topology $\mathbf{P}_2$, $\mathbf{P}_2$ and $\mathbf{P}_3$ reconfiguration, respectively. The last weight vector shows the results when the objective Ob_{Q2} is overlooked. It is not attractive as the load restoration rate is relatively low.

Among the three reconfiguration topology, $\mathbf{P}_1$ is the best reconfiguration topology, which has the lowest interruption cost and wind curtailment cost. For instance, the total interruption cost and wind curtailment cost is $ 9734.16 in $\mathbf{P}_1$ with the first weight vector, which is 9.54% less than the figures in $\mathbf{P}_2$ and $\mathbf{P}_3$. The schedule results of $\mathbf{P}_2$ and $\mathbf{P}_3$ are the same. However, loads cannot be restored as much as the reconfiguration topology $\mathbf{P}_1$. Meanwhile, less renewable resources are utilized to maintain the reliability and security of the system during the restoration period.

Generally speaking, both the first and second weight vectors could provide optimal reconfiguration topology for load restoration. However, in terms of WT generation schedule and TESS charging/discharging decision-making in normal resilient operation condition, simulation results are very different. TPL is recognised as as a technical criterion. As shown in Table 5.4, TPLs in topology $\mathbf{P}_1$, $\mathbf{P}_2$ and $\mathbf{P}_3$ with the first weight vector are 553.69 kW, 532.83 and 532.40 kW, respectively, and they become 960.99 kW, 954.30 kW and 953.87 kW with the second weight vector. Therefore, it can be concluded that the

first weight vector tends to find the results with lower power losses, while the second vector makes it easier to find out the most economically feasible outcome.

Reconfiguration	$\mathbf{P}_1$	$\mathbf{P}_2$	$\mathbf{P}_3$	$\mathbf{P}_1$	$\mathbf{P}_2$	$\mathbf{P}_3$	$\mathbf{P}_1$	$\mathbf{P}_2$	$\mathbf{P}_3$
Ob_{Q1} weight ω_1		0			0.5			1	
Ob_{Q2} weight ω_2		1			0.5			0	
$C^{OM_{Q1}}$($)	603.00	603.00	603.00	603.00	603.00	603.00	603.00	603.00	603.00
$C^{WC_{Q1}}$($)	1299.89	1299.89	1299.89	0	0	0	0	0	0
$C^{POS_{Q1}}$($)	480.00	480.00	480.00	0	0	0	0	0	0
$C^{REV_{Q1}}$($)	8536.22	8544.17	8544.17	10646.47	10646.47	10646.47	10646.47	10646.47	10646.47
$C^{INT_{Q2}}$($)	8966.25	9865.42	9865.42	8966.25	9865.42	9865.42	23027.59	21493.60	21493.60
$C^{OM_{Q2}}$($)	150.75	150.75	150.75	150.75	150.75	150.75	150.75	150.75	150.75
$C^{WC_{Q2}}$($)	767.91	797.75	797.75	767.91	797.75	797.75	977.19	977.87	977.87
$C^{POS_{Q2}}$($)	0	0	0	0	0	0	0	0	0
$C^{REV_{Q2}}$($)	845.43	780.87	780.87	845.43	780.87	780.87	365.55	356.39	356.39
Ob	9039.48	10033.05	10033.05	-502	-5.21	-5.21	-10043.47	-10043.47	-10043.47
Ob_{Q1}	-6153.33	-6161.29	-6161.29	-10043.47	-10043.47	-10043.47	-10043.47	-10043.47	-10043.47
Ob_{Q2}	9039.48	10033.05	10033.05	9039.48	10033.05	10033.05	22265.83	22265.83	22265.83
TPL (kW)	553.69	532.83	532.40	960.99	954.30	953.87	954.79	948.79	948.79
Critical load restoration rate (%)	73.78	72.09	72.09	73.78	72.09	72.09	28.91	35.50	35.50
Normal load restoration rate (%)	57.15	43.52	43.52	57.15	43.52	43.52	26.94	13.53	13.53
Total load restoration rate (%)	68.19	62.50	62.50	68.19	62.50	62.50	28.25	28.12	28.12

Table 5.4: Simulation results in Scenario 1 of Case 2

Figure 5.15(a)-(d) shows the generation profiles of WT1 and WT2 in $\mathbf{P}_1$, while generation profiles which are identical in $\mathbf{P}_2$ and $\mathbf{P}_3$ are illustrated in Figure 5.15 (e)-(h). In contrast to results in Case 1, the wind generation of WT2 is not proportional to WT1 during the restoration horizon. The active power generation of WT2 from 5:00 to 8:00 with first and second weight vectors are not the maximum. This is because reactive consumption, especially heavy industrial loads which locate at the microgrid powered by WT2 are not restored. Considering the 0.95 power factor of WT2, wind curtailment cost is therefore high to maintain the power quality during the restoration period.

Figure 5.17 depicts the SOC and repositioning schedules of TESS in $\mathbf{P}_1$, $\mathbf{P}_2$ and $\mathbf{P}_3$. The initial SOC at 5:00 is 0 based on the result of Case 1. It can be seen that the TESS is charged by the WT on-site during the restoration period in the scenario when the total renewable generation is larger than the total consumption. However, the charging speed of TESS is much slower than that in the normal condition to avoid violation of voltage constraints. The optimal schedule of TESS with the first weight vector is shown

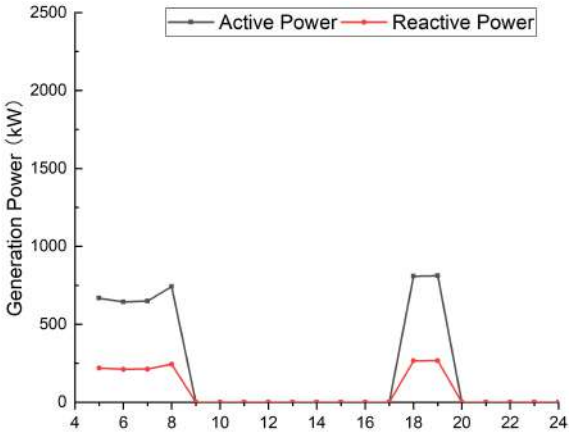

(a) WT1 in $\mathbf{P}_1$ with first weight vector

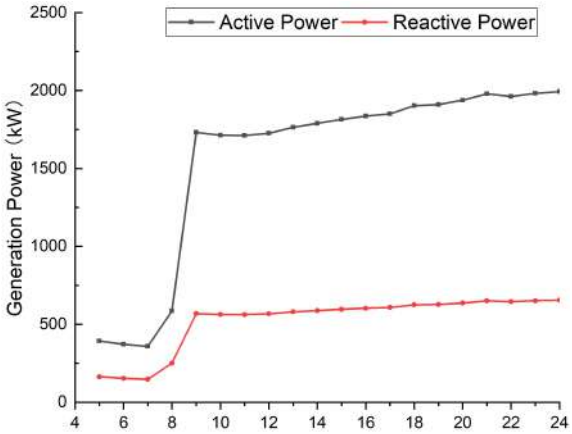

(b) WT2 in $\mathbf{P}_1$ with first weight vector

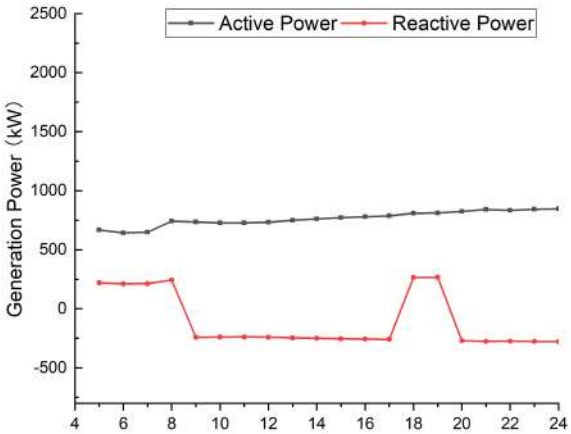

(c) WT1 in $\mathbf{P}_1$ with second weight vector

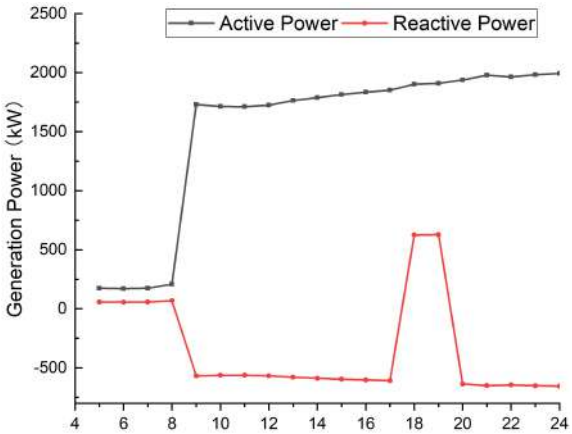

(d) WT2 in $\mathbf{P}_1$ with second weight vector

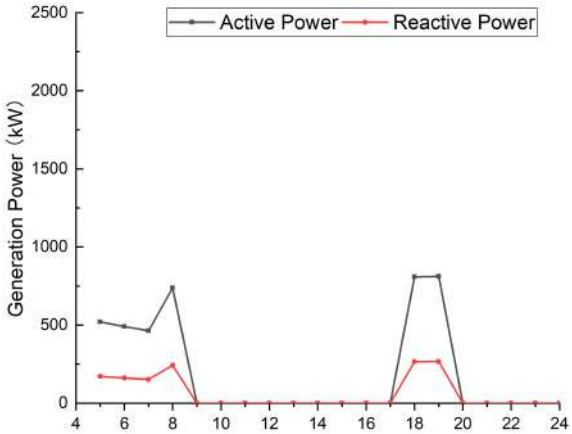

(e) WT1 in $\mathbf{P}_2$ and $\mathbf{P}_3$ with first weight vector

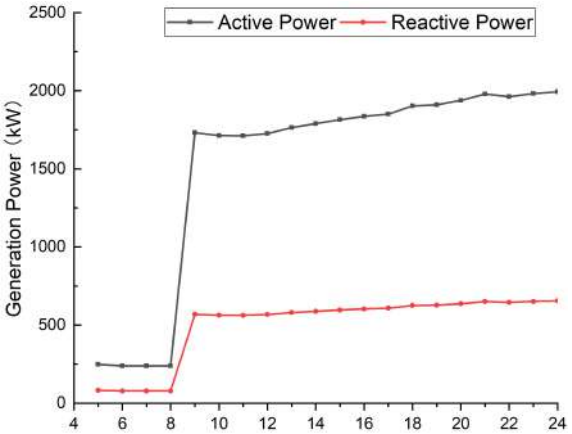

(f) WT2 in $\mathbf{P}_2$ and $\mathbf{P}_3$ with first weight vector

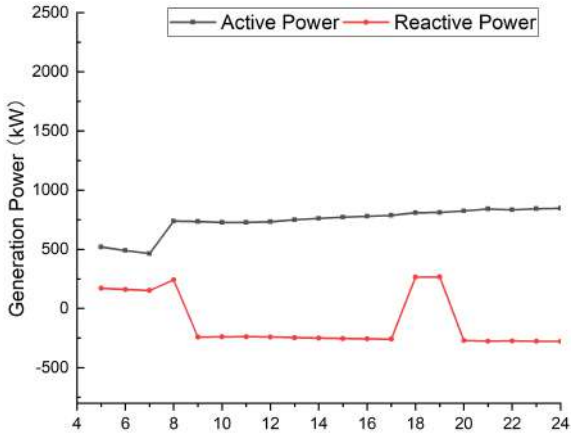

(g) WT1 in $\mathbf{P}_2$ and $\mathbf{P}_3$ with second weight vector

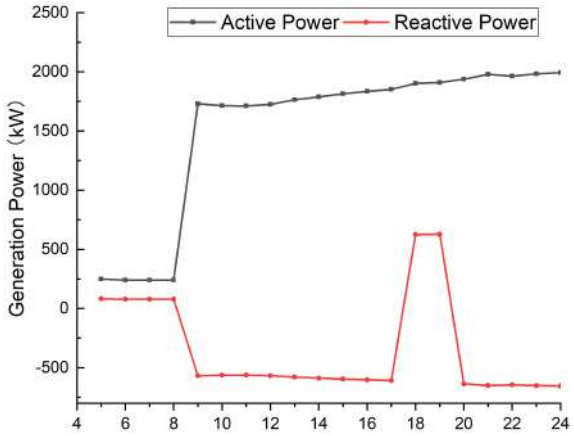

(h) WT2 in $\mathbf{P}_2$ and $\mathbf{P}_3$ with second weight vector

Figure 5.15: Generation profiles in Scenario 1 of Case 2

in Figure 5.16(a) and Figure 5.16(c). The position of TESS indicates low power loss can be achieved by transferring energy among stations 1 to 3. In terms of economic optimal schedule, the TESS remains at station 2 as shown in Figure 5.16(b) and (d) with the second weight vector.

5.5.3.2 Scenario 2: Both Power Surplus and Shortage over the Restoration Period

In scenario 2, the restoration scheme is assumed to begin at 11:00 and end at 15:00. The situation involves both power surplus and shortage during the restoration period. The total generation of the scheduled system is insufficient during 12:00 to 14:00 and becomes power surplus from 14:00 to 16:00.

Table 5.5 shows the simulation results. The third objective weight vector that results in a low load restoration is clearly not a good choice as indicated in Scenario 1. Therefore, in the following, only the fist two weight vectors are discussed. In contrast to scenario 1, the optimal objective values are obtained in $\mathbf{P}_2$ and $\mathbf{P}_3$. With the first weight vector, the total cost for restoration has reduced by 26.77% when changing from reconfiguration $\mathbf{P}_1$ to $\mathbf{P}_2$ or $\mathbf{P}_3$. TPL in $\mathbf{P}_2$ is 337.75 kW with the first weight vector and 627.51 kW with the second weight vector, which are 4.25% and 2.33% less than the TPL in $\mathbf{P}_3$. Therefore,

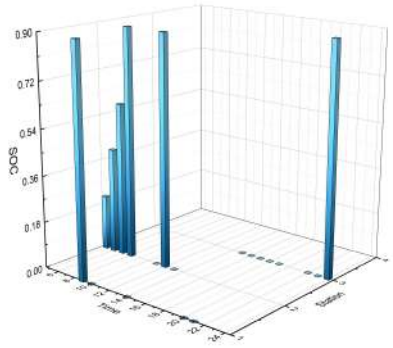

(a) TESS in $\mathbf{P}_1$ with first weight vector

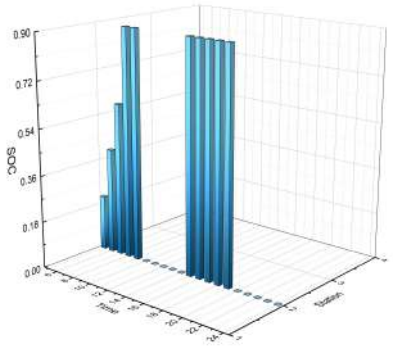

(b) TESS in $\mathbf{P}_1$ with second weight vector

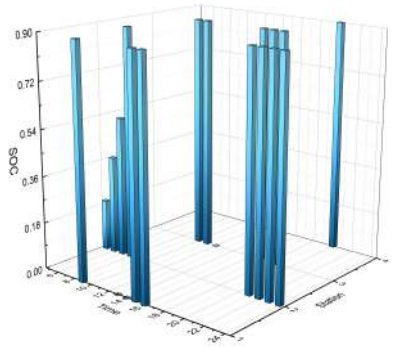

(c) TESS in $\mathbf{P}_2$ and $\mathbf{P}_3$ with first weight vector

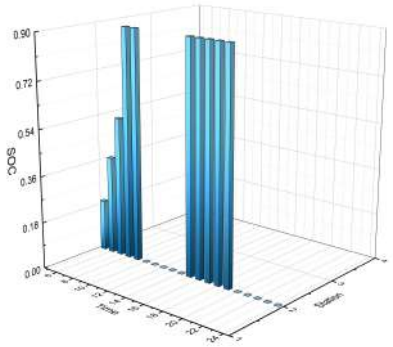

(d) TESS in $\mathbf{P}_2$ and $\mathbf{P}_3$ with second weight vector

Figure 5.16: TESS schedules in Scenario 1 of Case 2

Table 5.5: Simulation results in Scenario 2 of Case 2

Reconfiguration	$\mathbf{P}_1$	$\mathbf{P}_2$	$\mathbf{P}_3$	$\mathbf{P}_1$	$\mathbf{P}_2$	$\mathbf{P}_3$	$\mathbf{P}_1$	$\mathbf{P}_2$	$\mathbf{P}_3$
Ob_{Q1} weight ω_1		0			0.5			1	
Ob_{Q2} weight ω_2		1			0.5			0	
$C^{OM_{Q1}}$($)	339.19	339.19	339.19	339.19	339.19	339.19	339.19	339.19	339.19
$C^{WC_{Q1}}$($)	874.69	874.69	874.69	0	0	0	0	0	0
$C^{POS_{Q1}}$($)	320.00	0	0	0	0	0	0	0	0
$C^{REV_{Q1}}$($)	4841.75	4865.71	4865.71	6351.56	6373.80	6373.80	6373.80	6373.80	6373.80
$C^{INT_{Q2}}$($)	27622.09	21086.74	21086.74	27622.09	21086.74	21086.74	58236.40	53393.92	53393.92
$C^{OM_{Q2}}$($)	150.75	150.75	150.75	150.75	150.75	150.75	150.75	150.75	150.75
$C^{WC_{Q2}}$($)	597.76	341.07	341.07	597.76	341.07	341.07	983.91	921.87	921.87
$C^{POS_{Q2}}$($)	0	160.00	160.00	0	160.00	160.00	80	0	0
$C^{REV_{Q2}}$($)	1409.62	1995.04	1995.04	1409.62	1995.04	1995.04	459.95	553.21	553.21
Ob	26960.97	19743.52	19743.52	10474.30	6854.45	6854.45	-6034.62	-6034.62	-6034.62
Ob_{Q1}	-3307.87	-3651.83	-3651.83	-6034.62	-6034.62	-6034.62	-6034.62	-6034.62	-6034.62
Ob_{Q2}	26960.97	19743.52	19743.52	26960.97	19743.52	19743.52	58991.10	53913.32	53913.32
TPL (kW)	286.35	337.75	352.76	576.49	627.51	642.52	549.06	555.95	555.95
Critical load restoration rate (%)	65.51	70.38	70.38	65.51	70.38	70.38	18.95	26.37	26.37
Normal load restoration rate (%)	17.78	68.36	68.36	17.78	68.36	68.36	5.37	6.81	6.81
Total load restoration rate (%)	48.99	69.68	69.68	48.99	69.68	69.68	14.25	19.60	19.60

reconfiguration topology $\mathbf{P}_2$ is the optimal topology during the restoration period under the circumstance when both technical and economic aspects are investigated.

The optimal total load restoration rate in Scenario 2 is 69.68 % which is slightly higher than the optimal result 68.19% in Scenario 1. However, the critical load restoration rate drops from 73.78% in Scenario 1 to 70.38% in Scenario 2 when power supply is insufficient.

The corresponding WT generation dispatch is shown in Figure 5.17. The generation profiles in Scenario 2 show a smaller amount of wind curtailment in $\mathbf{P}_1$, $\mathbf{P}_2$ and $\mathbf{P}_3$ compared with Scenario 1. The difference originates from the power shortage of wind generation during the restoration period. When the wind generation is small, the additional wind curtailment due to reactive power consumption is also reduced. The power factor for WT1 and WT2 are 0.95 in all simulations.

The joint charging/discharging and routing schedules of TESS are shown in Figure 5.18. The initial SOC at 11:00 is 0 based on Case 1. Intuitively, when line faults occur, the TESS should neither discharge or charge the grid at the first two hours according to the power shortage. It is shown in Figure 5.18(c) and Figure 5.18(d) that TESS moves from station 1 to station 3 and is not charged until two hours after the restoration. However, simulation results as shown in Figure 5.18(a) and Figure 5.18(b) depicts a different situation. For instance, as shown in Figure 5.18(a), the SOC of TESS increases from 0 to 0.20 from 11:00 to 13:00. To further investigate this phenomena, the topology $\mathbf{P}_1$ is analyzed. The resulting generation of WT1 during 11:00-15:00 indicates that it os working at the maximum power. It is regarded as root bus of a microgrid that serves 20 loads. However, the power factor of WT1 is 0.95. The generation of reactive power is not comparable with the commercial and industrial loads whose power factor is 0.94 and 0.9, respectively. By charging extra active power to TESS, the proposed formulation therefore provides a good trade-off between load interruption and wind curtailment.

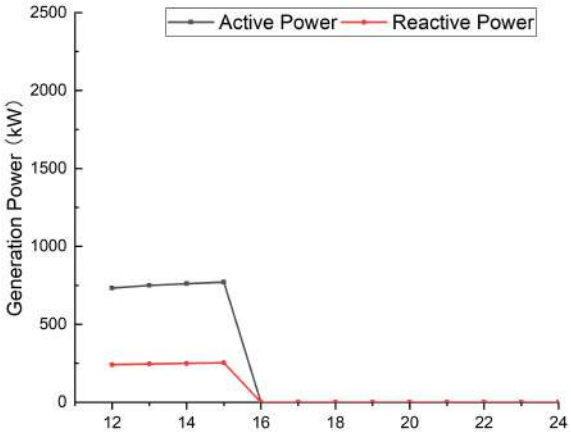

(a) WT1 in $\mathbf{P}_1$ with first weight vector

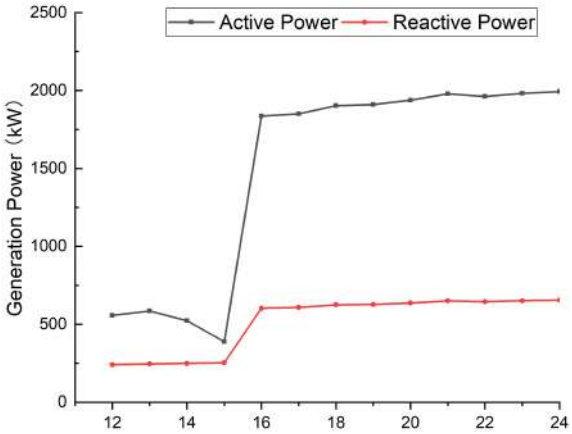

(b) WT2 in $\mathbf{P}_1$ with first weight vector

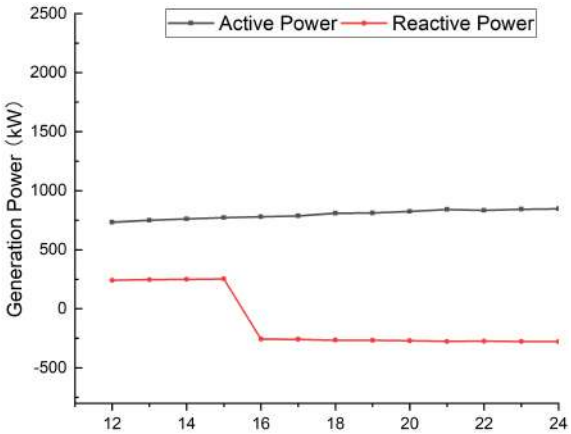

(c) WT1 in $\mathbf{P}_1$ with second weight vector

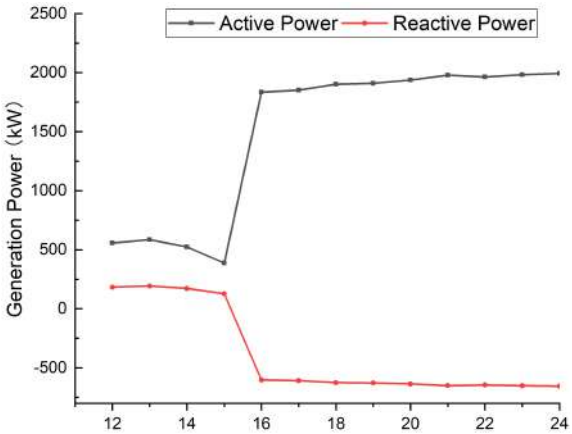

(d) WT2 in $\mathbf{P}_1$ with second weight vector

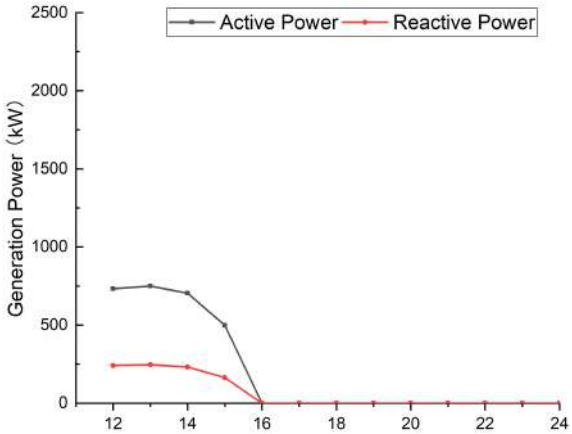

(e) WT1 in $\mathbf{P}_2$ and $\mathbf{P}_3$ with first weight vector

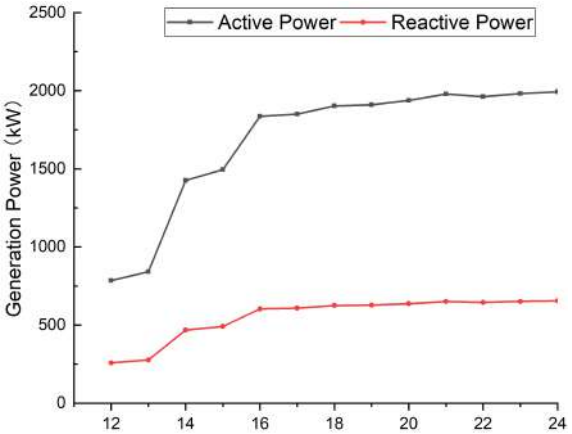

(f) WT2 in $\mathbf{P}_2$ and $\mathbf{P}_3$ with first weight vector

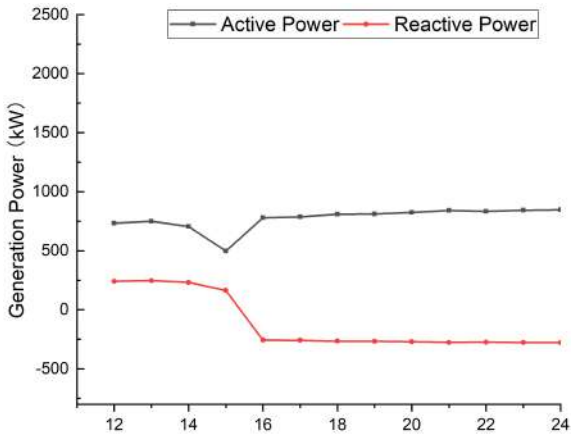

(g) WT1 in $\mathbf{P}_2$ and $\mathbf{P}_3$ with second weight vector

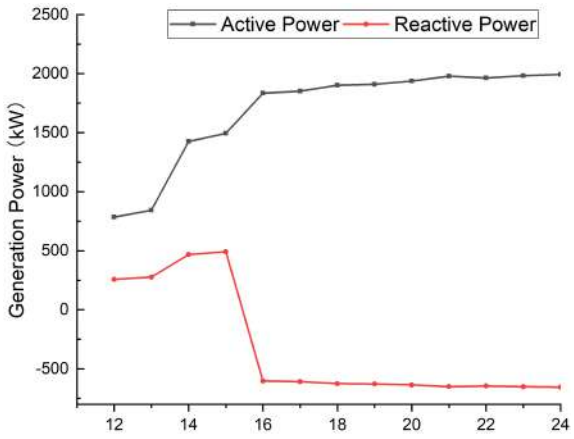

(h) WT2 in $\mathbf{P}_2$ and $\mathbf{P}_3$ with second weight vector

Figure 5.17: Generation profiles in Scenario 2 of Case 2

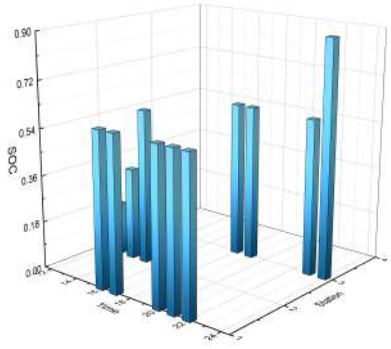

(a) TESS in $\mathbf{P}_1$ with first weight vector

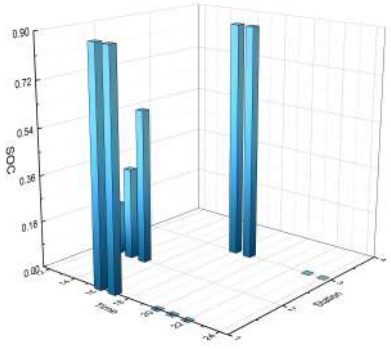

(b) TESS in $\mathbf{P}_1$ with second weight vector

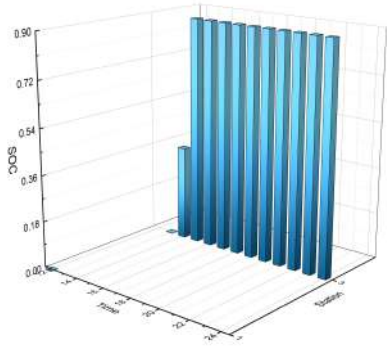

(c) TESS in $\mathbf{P}_2$ and $\mathbf{P}_3$ with first weight vector

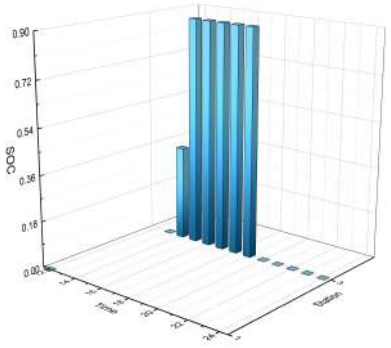

(d) TESS in $\mathbf{P}_2$ and $\mathbf{P}_3$ with second weight vector

Figure 5.18: TESS schedules in Scenario 2 of Case 2

5.5.3.3 Scenario 3: Power shortage over the Restoration period

The third scenario considered is the power shortage from 18:00 to 22:00. The generation is less than the consumption, leading to an exceptional power outage at peak hours.

Table 5.6: Simulation results in Scenario 3 of Case 2

Reconfiguration	$\mathbf{P}_1$	$\mathbf{P}_2$	$\mathbf{P}_3$	$\mathbf{P}_1$	$\mathbf{P}_2$	$\mathbf{P}_3$	$\mathbf{P}_1$	$\mathbf{P}_2$	$\mathbf{P}_3$
Ob_{Q1} weight ω_1		0			0.5			1	
Ob_{Q2} weight ω_2		1			0.5			0	
$C^{OM_{Q1}}$($)	75.37	75.37	75.37	75.37	75.37	75.37	75.37	75.37	75.37
$C^{WC_{Q1}}$($)	200.36	200.36	200.36	0	0	0	0	0	0
$C^{POS_{Q1}}$($)	160.00	160.00	160.00	0	0	0	0	0	0
$C^{REV_{Q1}}$($)	1067.27	1067.27	1067.27	1413.33	1413.33	1413.33	1413.33	1413.33	1413.33
$C^{INT_{Q2}}$($)	50216.45	49718.65	49718.65	50216.45	49718.65	49718.65	78955.20	78955.20	78955.20
$C^{OM_{Q2}}$($)	150.75	150.75	150.75	150.75	150.75	150.75	150.75	150.75	150.75
$C^{WC_{Q2}}$($)	669.72	602.23	602.23	669.72	602.23	602.23	1125.53	1125.53	1125.53
$C^{POS_{Q2}}$($)	0	0	0	0	0	0	NaN	NaN	NaN
$C^{REV_{Q2}}$($)	1679.37	1839.92	1839.92	1679.37	1839.92	1839.92	531.30	531.30	531.30
Ob	49357.55	48631.71	48631.71	24009.80	23646.88	23646.88	-1337.96	-1337.96	-1337.96
Ob_{Q1}	-631.54	-631.54	-631.54	-1337.96	-1337.96	-1337.96	-1337.96	-1337.96	-1337.96
Ob_{Q2}	49357.55	48631.71	48631.71	49357.55	48631.71	48631.71	NaN	NaN	NaN
TPL (kW)	75.09	84.15	79.64	143.60	152.66	148.15	124.32	124.32	124.32
Critical load restoration rate (%)	46.44	45.51	45.51	46.44	45.51	45.51	16.12	16.12	16.12
Normal load restoration rate (%)	43.28	63.31	63.31	43.28	63.31	63.31	6.45	6.45	6.45
Total load restoration rate (%)	45.58	50.36	50.36	45.58	50.36	50.36	13.48	13.48	13.48

Simulation results of resilient operation and post-disaster restoration scheme in three reconfiguration topologies $\mathbf{P}_1$, $\mathbf{P}_2$ and $\mathbf{P}_3$ are compared and shown in Table 5.6. The same results are achieved in $\mathbf{P}_2$ and $\mathbf{P}_3$, which are the economically optimal reconfiguration topology. As shown in the table, the objective values in $\mathbf{P}_2$ and $\mathbf{P}_3$ are $ 48631.71 with the first weight vector and $ 23646.88 with the second weight vector. Meanwhile, the TPL in $\mathbf{P}_3$ is 79.64 kW with the first weight vector and 148.15 kW with the second weight vector, which are 4.51 kW and 4.51 kW smaller than TPL in $\mathbf{P}_2$ with first and second weight vector, respectively. Overall, the reconfiguration topology $\mathbf{P}_3$ is the optimal topology from the techno-economic aspects. The load restoration rate in Scenario 3 is the worst compared to Scenario 1 and 2. Only 45.51% of critical loads and 63.31% of normal loads are restored due to power shortage.

The generation profiles are shown in Figure 5.19. During the restoration period, wind curtailment is less in $\mathbf{P}_2$ and $\mathbf{P}_3$ than that in $\mathbf{P}_1$. Based on the 0.95 power factor limit of

WT, the microgrid powered by WT2 serves more loads in $\mathbf{P}_2$ and $\mathbf{P}_3$. At the peak hour from 20:00 to 21:00, both WT1 and WT2 do not operate at the maximum power in $\mathbf{P}_2$ and $\mathbf{P}_3$. During other restoration periods, only the generation of WT2 is curtailed.

Figure 20 demonstrates the SOC and routing schedule of the TESS. The initial SOC is 0.9 when line faults occur. In $\mathbf{P}_2$ and $\mathbf{P}_3$, the TESS should discharge 15.03 kW in 18:00-19:00 and 65.35 kW in 19:00-20:00. In addition, it is re-charged by 8.95 kW in 20:00-21:00 and 79.31 kW in 21:00-22:00. Overall, the SOC decreases from 0.9 to 0.73 during the power shortage restoration period.

5.5.4 Case 3: Multiple Microgrids with SOP in Post-disaster Condition

The Scenario 2 in Case 1 is used as the base case to provide the initial position and SOC of TESS once the restoration scheme begins. When the same line faults shown in Figure 5.14 occur, two islanded microgrids are naturally formed. The lost loads at bus 11 to 18 are restored by SOP by shifting from power flow control mode to restoration control mode in seconds. The techno-economic results are shown in Table 5.7 in the following three scenarios :

1 Power surplus during the restoration period (4:00-8:00)

2 Both power surplus and shortage occurs during the restoration period (11:00-15:00)

3 Power shortage during the restoration period (18:00-22:00)

The results in the three scenarios with reconfiguration topology $\mathbf{P}_3$ in Case 2 are summarised in Table 5.8. It is worth noting that the closing tie switch for reconfiguration locates at the same tie-line where SOP is placed in this case. From Tables 5.7 and 5.8, it is clear that the results of Ob_{Q2} are the same with either the first or second weight vector. Compared with Case 2, the objective values deceases significantly in Case 3. Load restoration rates have also improved with SOP. As shown in the table, the total load

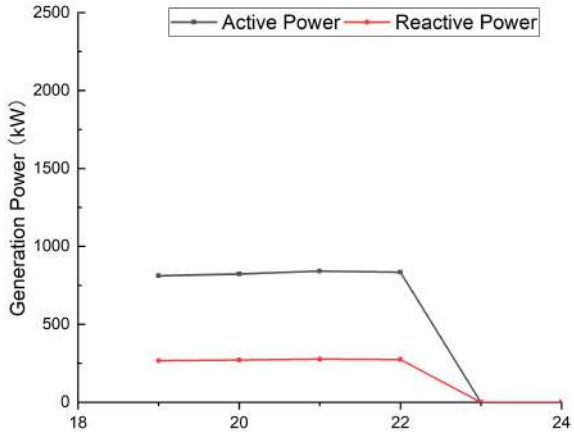

(a) WT1 in $\mathbf{P}_1$ with first weight factor

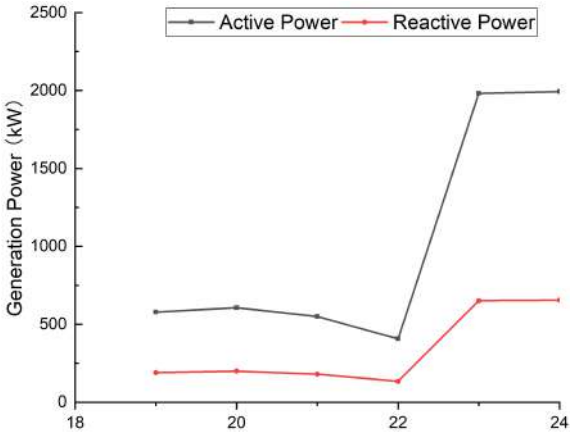

(b) WT2 in $\mathbf{P}_1$ with first weight factor

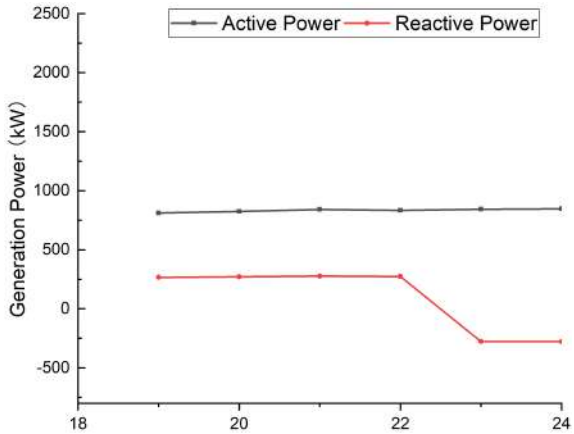

(c) WT1 in $\mathbf{P}_1$ with second weight factor

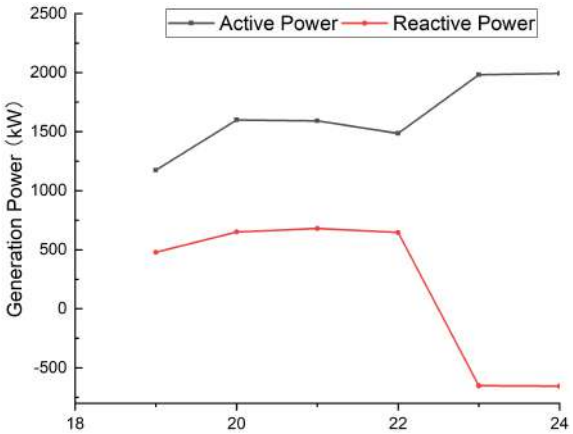

(d) WT2 in $\mathbf{P}_1$ with second weight factor

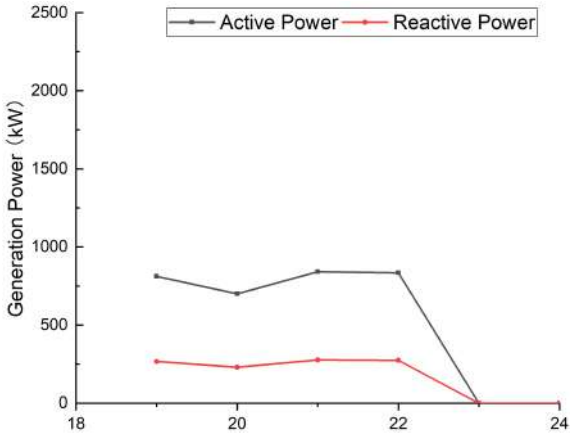

(e) WT1 in $\mathbf{P}_2$ and $\mathbf{P}_3$ with first weight factor

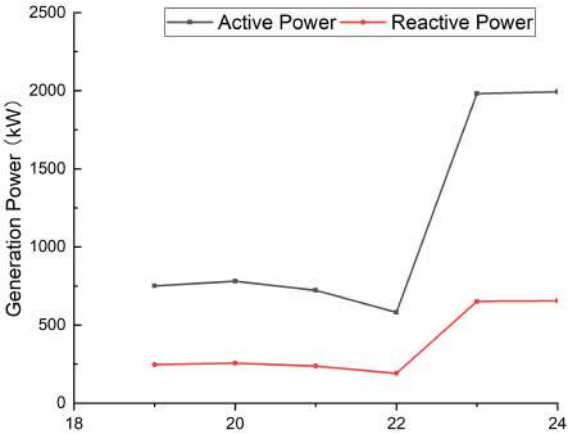

(f) WT2 in $\mathbf{P}_2$ and $\mathbf{P}_3$ with first weight factor

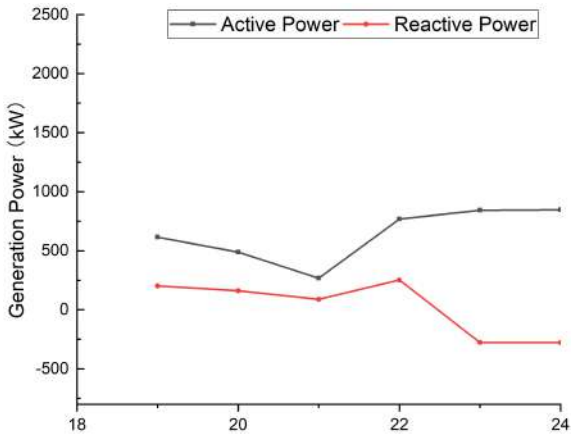

(g) WT1 in $\mathbf{P}_2$ and $\mathbf{P}_3$ with second weight factor

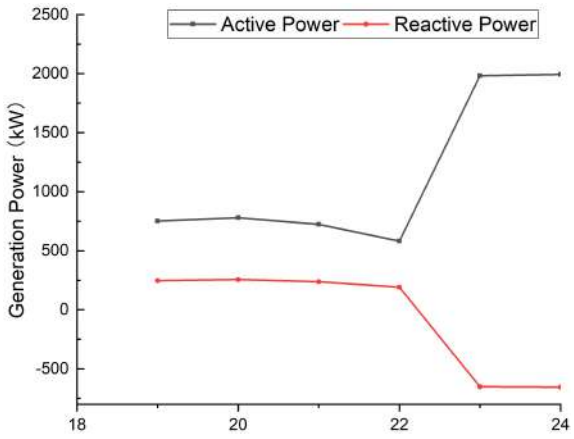

(h) WT2 in $\mathbf{P}_2$ and $\mathbf{P}_3$ with second weight factor

Figure 5.19: Generation profiles in Scenario 3 of Case 2

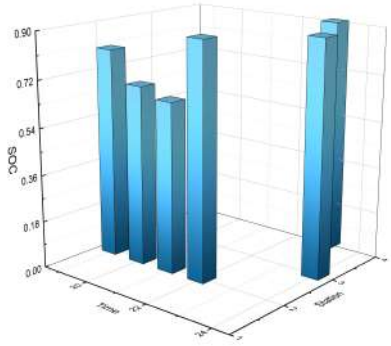

(a) TESS in $\mathbf{P}_1$ with first weight factor

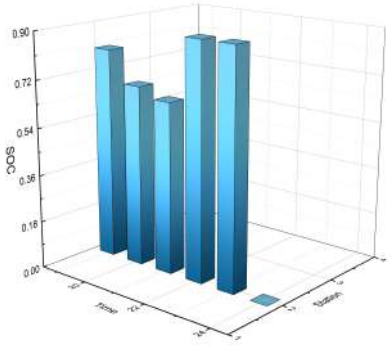

(b) TESS in $\mathbf{P}_1$ with second weight factor

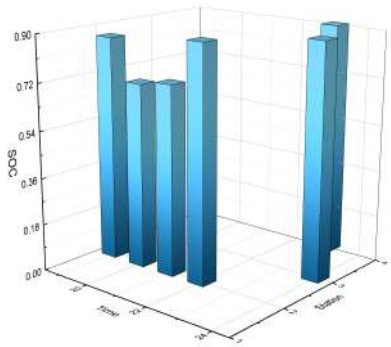

(c) TESS in $\mathbf{P}_2$ and $\mathbf{P}_3$ with first weight factor

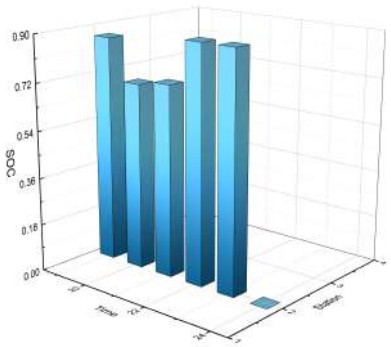

(d) TESS in $\mathbf{P}_2$ and $\mathbf{P}_3$ with second weight factor

Figure 5.20: TESS schedules in Scenario 3 of Case 2

Table 5.7: Simulation results in Case 3

Scenario	1		2		3	
Ob_{Q1} weight ω_1	0	0.5	0	0.5	0	0.5
Ob_{Q2} weight ω_2	1	0.5	1	0.5	1	0.5
$C^{OM_{Q1}}$($)	603.00	603.00	339.19	339.19	75.37	75.37
$C^{WC_{Q1}}$($)	1492.03	0.00	874.69	0.00	200.36	0.00
$C^{POS_{Q1}}$($)	960.00	0.00	480.00	0.00	160.00	0.00
$C^{REV_{Q1}}$($)	8597.28	11051.54	4926.82	6434.91	1051.14	1397.21
$C^{INT_{Q2}}$($)	77.56	77.56	7718.13	7718.13	25449.20	25449.20
$C^{OM_{Q2}}$($)	150.75	150.75	150.75	150.75	150.75	150.75
$C^{WC_{Q2}}$($)	603.18	603.18	209.66	209.66	253.81	253.81
$C^{POS_{Q2}}$($)	0	0	0	0	0	0
$C^{REV_{Q2}}$($)	1181.30	1181.30	2242.83	2242.83	2584.11	2584.11
Ob	-349.81	-5399.18	5835.70	-130.0110	23269.66	10973.91
Ob_{Q1}	-5542.25	-10448.54	-3232.94	-6095.72	-615.41	-1321.83
Ob_{Q2}	-349.81	-349.81	5835.70	5835.70	23269.66	23269.66
TPL (kW)	468.41	950.71	326.36	622.98	136.74	206.11
Critical load restoration rate (%)	100.00		91.59		71.51	
Normal load restoration rate (%)	97.39		65.39		89.26	
Total load restoration rate (%)	99.12		82.53		76.35	

restoration rates in the three scenarios increase from 62.50%, 69.68% and 50.36% to 99.12%, 82.53% and 76.35%, respectively.

Figure 5.21 demonstrates the generation profiles in Case 3. The power factors of both WT1 and WT2 are 0.95 over the time span. More wind curtailments are observed with the second weight vector than the first one in all scenarios. In addition, the obtained wind curtailment costs are also less than that in Case 2.

The SOC profile and spatio-temporal schedule of TESS are provided in Figure 5.22. In Scenario 1 and 2 with the first weight vector, the TESS is fully charged from 0 to 0.9 during the restoration period. In Scenario 3, the TESS discharges 78.19 kW from 18:00 to 19:00 and 47.34 kW from 19:00 to 20:00. It is recharged to full capacity in the following two hours. The spatial dynamics of TESS reduces the power losses of the system. TPL with the first weight vector decreases 50.73%, 47.61% and 33.66% respectively in three scenarios compared to the second weight vector.

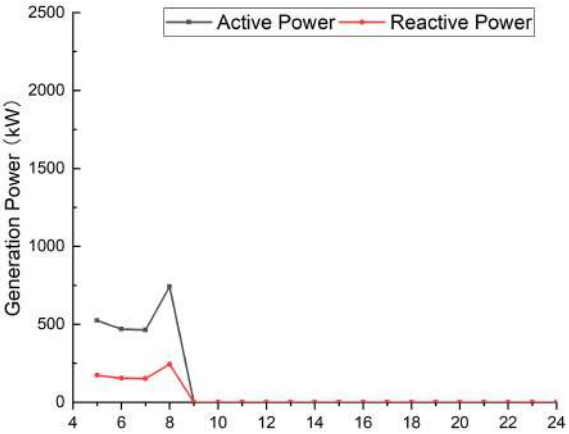

(a) WT1 in Scenario 1 with first weight vector

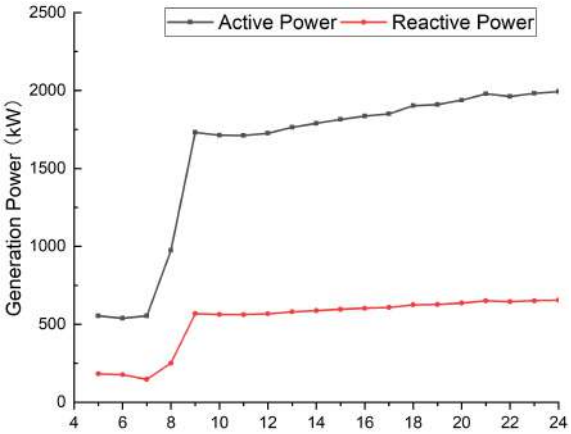

(b) WT2 in Scenario 1 with first weight vector

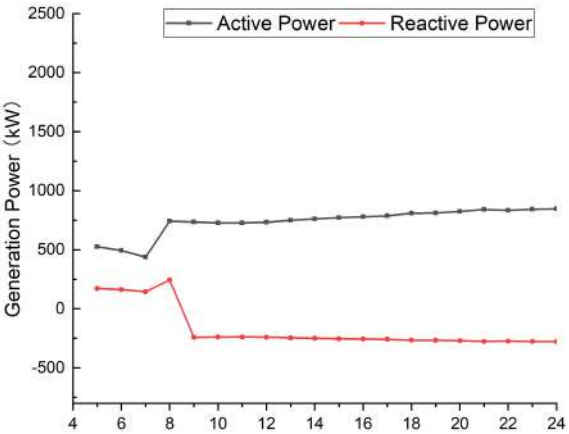

(c) WT1 in Scenario 1 with second weight vector

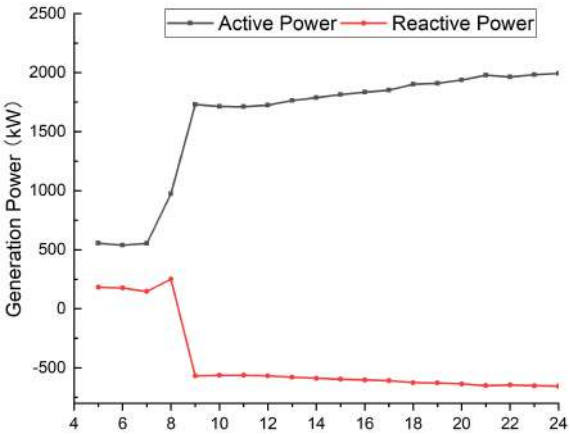

(d) WT2 in Scenario 1 with second weight vector

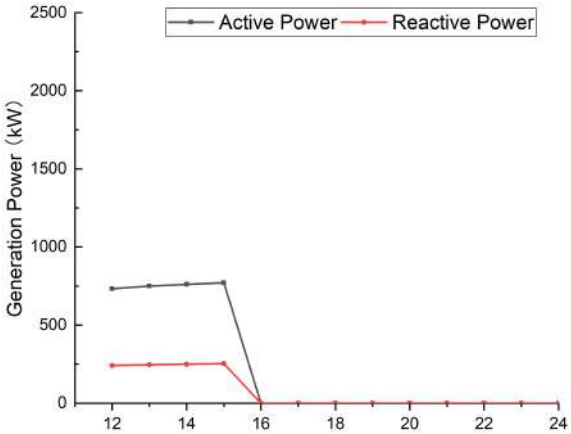

(e) WT1 in Scenario 2 with first weight vector

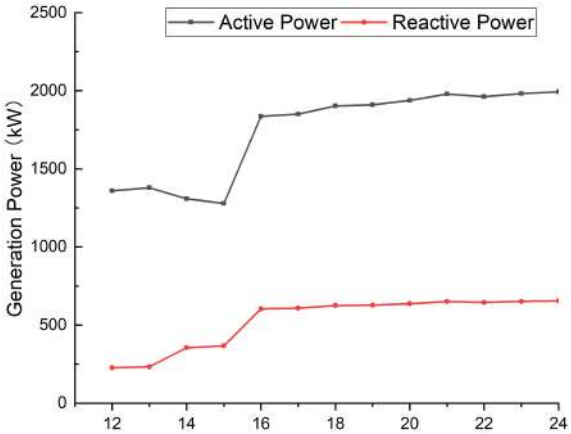

(f) WT2 in Scenario 2 with first weight vector

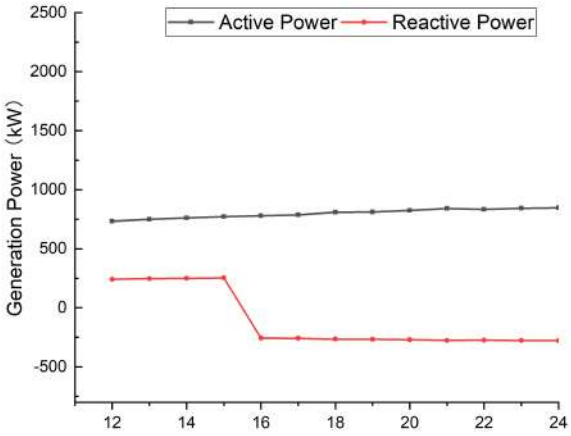

(g) WT1 in Scenario 2 with second weight vector

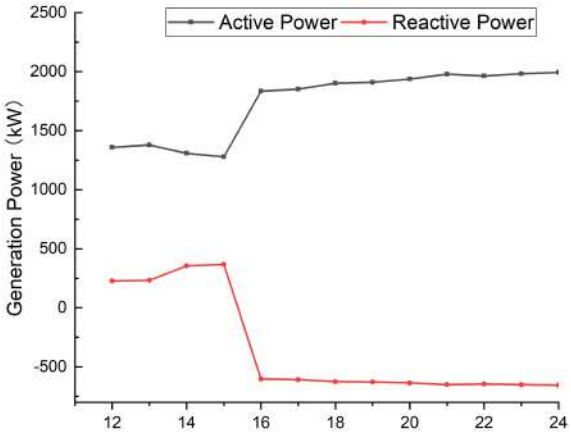

(h) WT2 in Scenario 2 with second weight vector

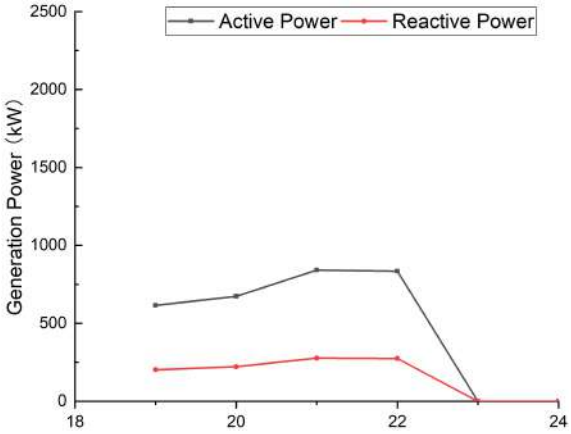

(i) WT2 in Scenario 3 with second weight vector

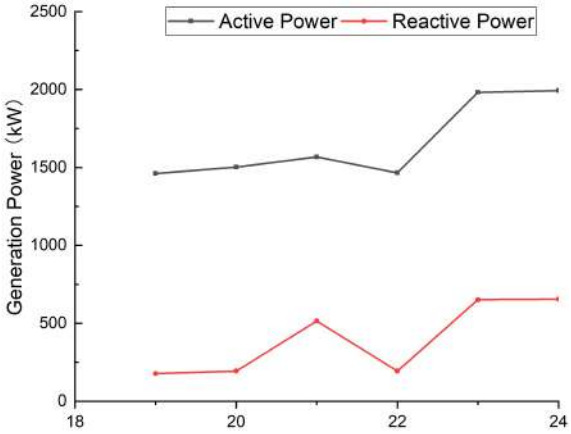

(j) WT2 in Scenario 3 with second weight vector

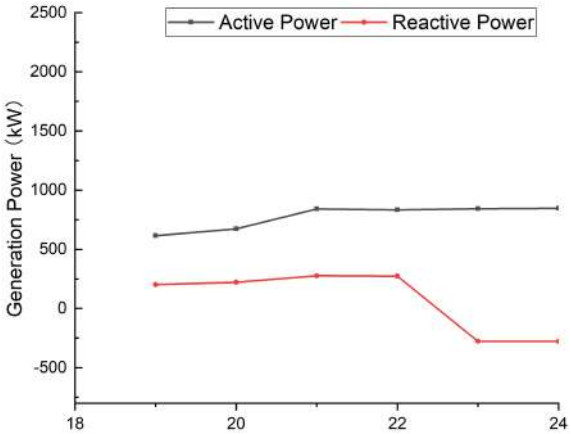

(k) WT2 in Scenario 3 with second weight vector

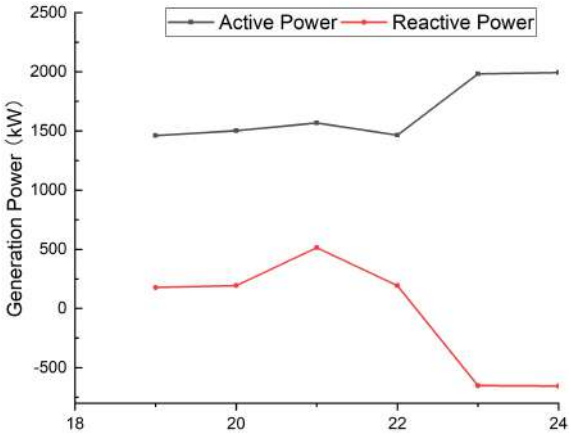

(l) WT2 in Scenario 3 with second weight vector

Figure 5.21: Generation profiles in Case 3

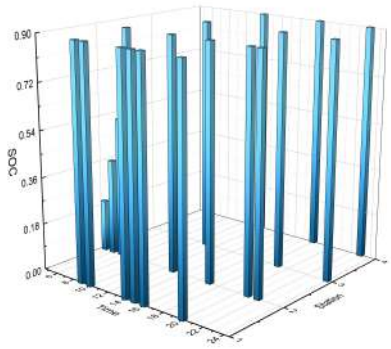

(a) TESS in Scenario 1 with first weight vector

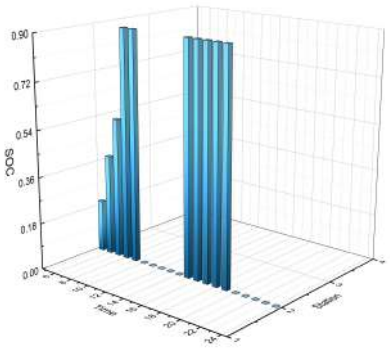

(b) TESS in Scenario 1 with second weight vector

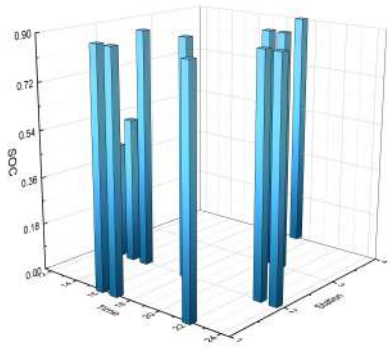

(c) TESS in Scenario 2 and $\mathbf{P}_3$ with first weight vector

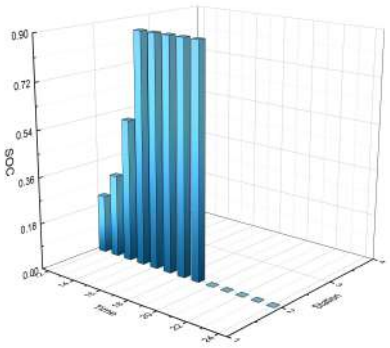

(d) TESS in Scenario 2 and $\mathbf{P}_3$ with second weight vector

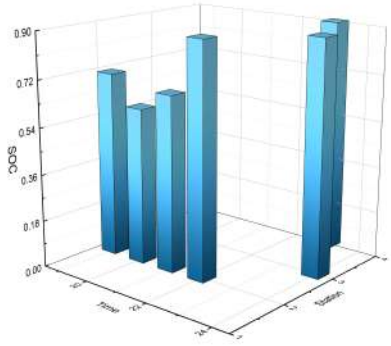

(e) TESS in Scenario 3 and $\mathbf{P}_3$ with second weight vector

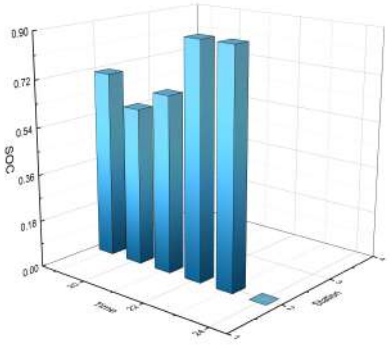

(f) TESS in Scenario 3 with second weight vector

Figure 5.22: TESS schedule in Case 3

Table 5.8: Simulation results in Case 2

Scenario	1		2		3	
Ob_{Q1} weight ω_1	0	0.5	0	0.5	0	0.5
Ob_{Q2} weight ω_2	1	0.5	1	0.5	1	0.5
$C^{OM_{Q1}}$($)	603.00	603.00	339.19	339.19	75.37	75.37
$C^{WC_{Q1}}$($)	1299.89	0.00	874.69	0.00	200.36	0.00
$C^{POS_{Q1}}$($)	480.00	0.00	0.00	0.00	160.00	0.00
$C^{REV_{Q1}}$($)	8544.17	10646.47	4865.71	6373.80	1067.27	1413.33
$C^{INT_{Q2}}$($)	9865.42	9865.42	21086.74	21086.74	49718.65	49718.65
$C^{OM_{Q2}}$($)	150.75	150.75	150.75	150.75	150.75	150.75
$C^{WC_{Q2}}$($)	797.75	797.75	341.07	341.07	602.23	602.23
$C^{POS_{Q2}}$($)	0.00	0.00	160.00	160.00	0.00	0.00
$C^{REV_{Q2}}$($)	780.87	780.87	1995.04	1995.04	1839.92	1839.92
Ob	10033.05	-5.21	19743.52	6854.45	48631.71	23646.88
Ob_{Q1}	-6161.29	-10043.47	-3651.83	-6034.62	-631.54	-1337.96
Ob_{Q2}	10033.05	10033.05	19743.52	19743.52	48631.71	48631.71
TPL (kW)	532.3966	953.87	352.76	642.52	79.64	148.15
Critical load restoration rate (%)	72.09		70.38		45.51	
Normal load restoration rate (%)	43.52		68.36		63.31	
Total load restoration rate (%)	62.50		69.68		50.36	

The SOP power injection profile to the system is shown in Figure 5.23. From the figure, it can be observed that the feeder of bus 18 are restored by the SOP by transferring the active power from the feeder of bus 33.

5.6 Chapter Summary

In this chapter, a joint scheme of resilient operation and post-disaster restoration with TESS and SOP is formulated, which simultaneously minimizes the O&M cost, wind curtailment cost, repositioning cost of TESS, and load interruption cost and maximizes the total revenues. A TSN model is generated for simulating the mobility of TESS on a N-3 contingency-constrained 33-bus system. The results are compared between network reconfiguration using tie switches and SOP with power flow capability in three conditions: power surplus, power shortage and both power surplus and shortage. The numerical results reveal the following findings:

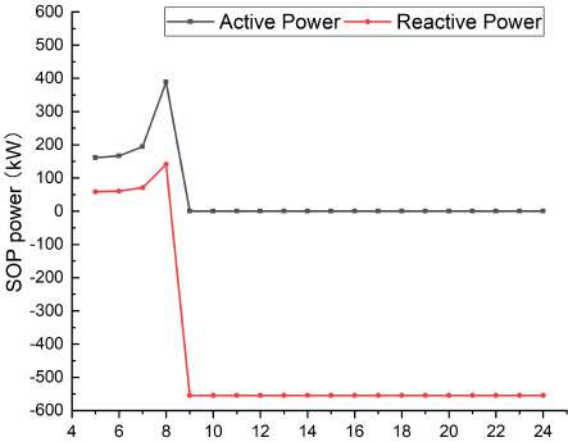

(a) SOP power connecting bus 18 in Scenario 1

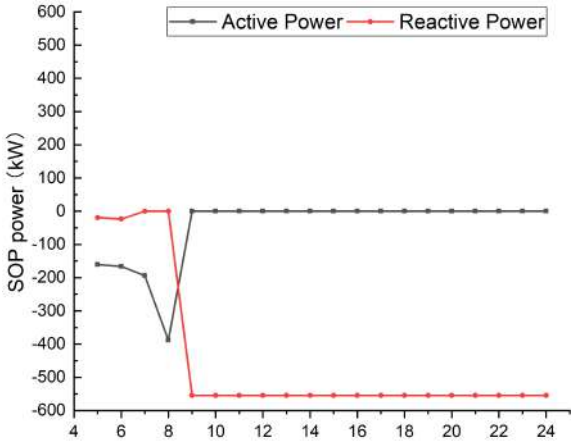

(b) SOP power connecting bus 33 in Scenario 1

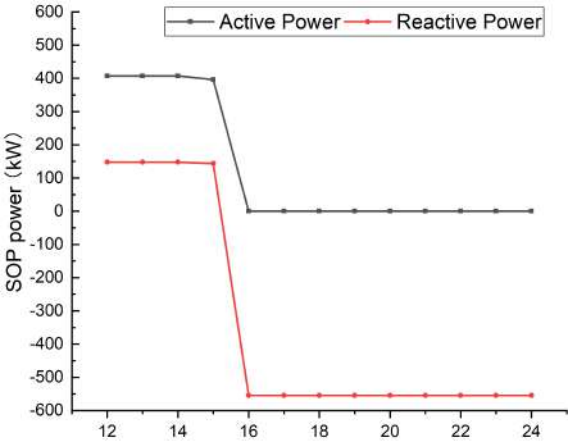

(c) SOP power connecting bus 18 in Scenario 2

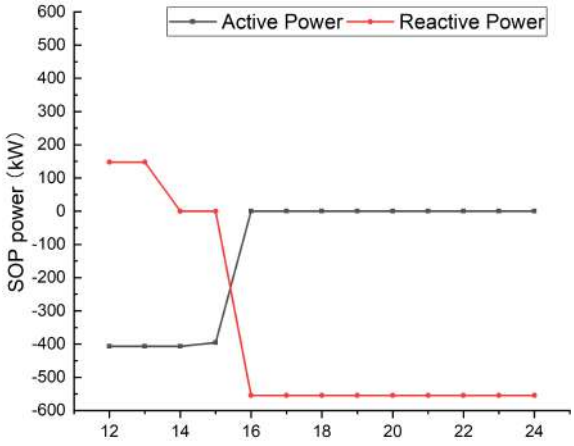

(d) SOP power connecting bus 33 in Scenario 2

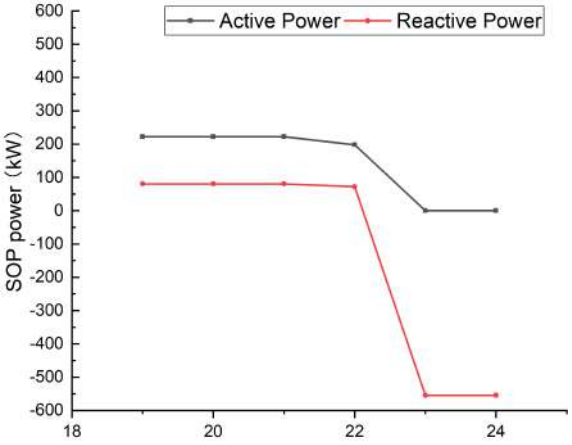

(e) SOP power connecting bus 18 in Scenario 3

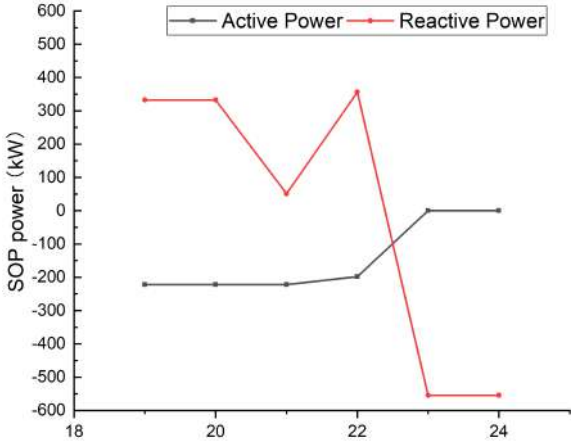

(f) SOP power connecting bus 18 in Scenario 3

Figure 5.23: SOP power in Case 3

- The utilization of TESS can not only enhance the system resilience by providing or absorbing power where it is needed, but also improve the system operation in terms of wind curtailment and power loss reduction through power exchange among multiple microgrids.
- Total power losses drop significantly by 50.73%, 47.61% and 33.66%, respectively in three scenarios with SOP.
- The load restoration rate depends on the network topology and power factor of the loads. If reactive power generation is insufficient, extra active power generation will be curtailed to maintain the security of the system.

CHAPTER 6

CONCLUSION AND FUTURE WORK

The thesis is focusing on one of the recurring and most important themes in electric power systems, namely the optimal planning and resilient operation of microgrids, which occupies a very important place in the power industry and also faces some significant new challenges in recent years with the integration of RES. On the other hand, it also offers great opportunities for the system operators and market operators to evolve current planning and scheduling methods to achieve a more reliable, cost effective and environmental friendly system.

6.1 Concluding Summary

The discussion of the thesis revolves around three main topics presented in Section 1.2, that is, uncertainties, smart grid and energy management. As illustrated in Figure 6.1, the methodology proposed in the thesis takes into account all three aspects. In Chapter 3, a data-driven clustering approach based on DPMM is developed. Uncertainties arising from wind speed, solar irradiance, temperature and load profile are grouped to formulate the uncertainty set. The same approach is used in Chapter 4 for a probabilistic model. The analysis covers comparisons between stochastic model and robust model in dealing

with uncertainties.

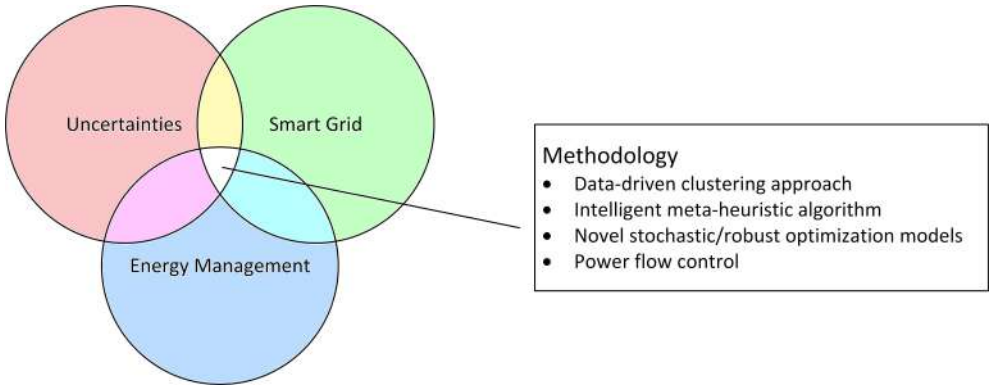

Figure 6.1: The correlation of chapters

To optimally solve the ESS planning problem when considering a complex market model, an efficient meta-heuristic algorithm, fast IPOP-CMA-ES, is proposed. The advantages of conventional method lie on their good solving speed and global optimal value of specific formulation, where meta-heuristic methods are more flexible and can solve high-dimensional non-linear non-convex problems which are more common in practice.

Power flow analysis is a supporting method to the operation of microgrid involving the calculation of power flows through each line and voltage at each bus. The integration of SOP will significantly improve the utilization of energy by reducing the power losses. Meanwhile, ESS is a helpful complement to the high penetration of RES. DistFlow and its linearized formulation LinDistFlow are discussed throughout the thesis. Different power flow methods have different rate of convergence which is at the cost of simplification of system parameters.

In summary, this thesis is featured with the following main contributions:

(1) A novel data-driven framework for DG planning considering both grid-connected and islanded modes of microgrids has been developed, which makes good use of spatio-temporal data of historical weather and grid information based on Bayesian nonparametric method. Compared with existing work, the total cost of the utility is decreased by 0.3% while the microgrid is capable to accommodate more renewable energy.

(2) A multi-objective stochastic two-stage stochastic energy storage system planning has been proposed, which integrates energy procurement risk into the optimal sizing and location problem. It emphasizes on the economic potential of ESS in the day-ahead and balancing market, resulting in an optimal solution with $1437 revenue for participating the fast reserve service and $48,240,749 cost for ten-year energy procurement in the day-ahead market.

(3) To solve the energy storage system planning problem when considering a complex market model, a fast IPOP-CMA-ES method has been proposed to solve the non-convex optimization problems in the micorgrid planning. Extensive simulation studies confirm the efficiency of fast IPOP-CMA-ES approach in both the convergence speed and solution accuracy in comparison with other intelligent optimization methods. For instance, the proposed fast IPOP-CMA-ES method algorithm is 37.41% and 18.33% faster than the $(\mu+\lambda)$-ES and CMA-ES algorithm. The optimal cost $ 53,167,141 achieved by the proposed fast IPOP-CMA-ES algorithm is $31,621 lower than the cost solved by $(\mu+\lambda)$-ES algorithm and $82,878 lower than the cost solved by CMA-ES algorithm.

(4) A joint scheme of resilient operation and post-disaster restoration of a microgrid is formulated. The system under study include one transportable energy storage system (TESS) and a novel power electronic device, namely soft open point (SOP) with active and reactive power flow capabilities. Simulation studies have confirmed that the utilization of transportable energy storage systems not only enhances the system resilience but also improves the system operation in terms of wind curtailment and power loss reduction. The total load restoration rates in the three scenarios of the study rises from 62.50%, 69.68% and 50.36% to 99.12%, 82.53% and 76.35%, respectively while the total power losses of the system decrease by 50.73%, 47.61% and 33.66%, respectively by utilizing the SOP.

However, there are still remaining limitations of the work need to consider. First, the proposed two-stage data-driven adaptive robust distributed generation planning

(DDARDGP) framework in Chapter 3 does not consider the economic potential in electricity market. Second, in Chapter 4, although the data used to cluster the generation and load are real data from industry [174, 175], the scaled generation is still smaller than the corresponding load due to the development lag of renewable generation. Other cases such as energy surplus of the microgrid are not discussed. Third, Chapter 5 is an attempt to evaluate the joint performance of TESS and SOP. The multi-objective formulation in the study is still too basic to analyse the resilience of the single microgrid and multiple microgrids and the post-disaster restoration entirely. Otherwise, advanced multi-objective techniques such as intelligent optimization algorithms or hybrid methods are needed for the particular problem.

6.2 Suggestions for Future Work

In this thesis, the analysis mainly focuses on the single microgrid design and its operation. When shifting to multi-microgrid system, the interaction among adjacent networks and non-adjacent networks will face scenarios with increasing complexity. The following two research directions are worthy further study in the future. The first topic is the joint spatio-temporal scheduling of microgrid system and transportable system. Aggregated or dispersive transportable energy resources like electric vehicles and TESS can provide various services to the grid, such as the mitigation of the network congestion, reduction of wind curtailment and power restoration. With the further development of electrification, it requires much more complicated control and management schemes to deal with increasing transportable energy resources at various energy levels and moving capabilities. Secondly, the arrangement of energy transactions between two or more microgrids should evolve with the deregulation of electricity market. As a potential market participant, DG will compete with utilities over customers. Although the prosumer nature gives the microgrid large degree of freedom in scheduling, the resulting uncertain pricing strategy will have a great impact on customers' consumption choices.

APPENDIX A

VARIATIONAL INFERENCE FOR DPMM

In the DPMM model, following the stick-breaking procedure, each stick length $\pi(v_k)$ is determined from a random drawn from a Beta distribution, alongside the atom η_k is taken from G_0. We assign a new variable Z_n for corresponding nth sampled data x_n to identify the mixture component from a multinomial distribution. The process of data generation can be summarized as follows:

1. For each mixture component
   (a) Draw $v_k|(a_k,b_k) \sim Beta(a_k,b_k)$ for $k = \{1,2,...\}$
   (b) Draw $\eta_k|G_0 \sim G_0$ for $k = \{1,2,...\}$

2. For each data point
   (a) Draw $Z_n|\{v_1,v_2,...\} \sim Mult(\pi(v))$
   (b) Draw $X_n|z_n \sim p(x_n|\eta_{z_n})$

The graphical model representation is shown in Figure 1.3 where the latent parameter sets $W = \{Z,V,\eta\}$. However, there is no direct way to calculate the posterior distribution based on data $\mathrm{x} = \{x_1,x_2,...x_n\}$ as the posterior distribution

$$p(W|\mathrm{x},\alpha,\lambda) = \exp\{\log p(\mathrm{x},W|\alpha,\lambda) - \log p(\mathrm{x}|\alpha,\lambda)\} \tag{A.1}$$

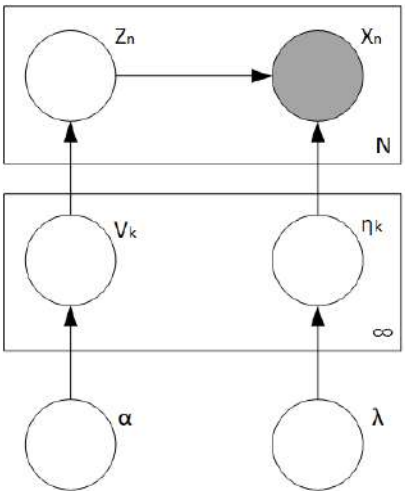

Figure A.1: Schematic diagram of DPMM

is depend on a intractable marginal likelihood $p(x|\alpha,\lambda)$. Variational inference can approximate the latent variables W through a predefined simpler distribution $q_v(W)$ where v is a variational distribution. By minimizing the Kullback-Leibler (KL) divergence between $q_v(W)$ and wanted posterior, the parameter is achieved.

$$\mathrm{KL}(q_v(W)||p(W|\mathrm{x},\alpha,\lambda)) = \mathrm{E}_q[\log q_v(W)] - \mathrm{E}_q[\log p(\mathrm{x},W|\alpha,\lambda)] + \log p(\mathrm{x}|\alpha,\lambda) \tag{A.2}$$

Since the KL is a non-negative value, the rigt hand side term is

$$\log p(\mathrm{x}|\alpha,\lambda) \geqslant \mathrm{E}_q[\log p(\mathrm{x},W|\alpha,\lambda)] - \mathrm{E}_q[\log q_v(W)] \tag{A.3}$$

By substituting our model $W = \{Z,V,\eta\}$ into (A.3), we can get

$$\begin{aligned}\log p(\mathrm{x}|\alpha,\lambda) \geqslant & \mathrm{E}_q[\log p(V|\alpha)] + \mathrm{E}_q\left[\log p(\eta|\lambda)\right] \\ & + \sum_{n=1}^{N}(\mathrm{E}_q[\log p(Z_n|V)] + \mathrm{E}_q[\log p(X_n|Z_n)]) \\ & - \mathrm{E}_q\left[\log q_v(V,\eta,Z)\right]\end{aligned} \tag{A.4}$$

In the context, we propose a truncated factorized variational distributions for q_v as follows

$$q_v(v,\eta,z) = \prod_{t=1}^{T-1} q_{\gamma_t}(v_t) \prod_{t=1}^{T} q_{\tau_t}(\eta_t) \prod_{n=1}^{N} q_{\phi_n}(z_n) \tag{A.5}$$

where variational parameters are $v = \{\gamma_1,\ldots\gamma_{T-1},\tau_1,\ldots\tau_T,\phi_1,\ldots\phi_N\}$. $q_{\gamma_t}(v_t)$ are beta distributions, $q_{\tau_t}(\eta_t)$ are inverse Wishart distributions and $q_{\phi_n}(z_n)$ are multinomial distributions. Note that here T denotes a truncation level by constraining finite stick-breaking

times. It means that T mixture components are possible to represent all data. The update rule is then achieved by computing the gradient of the right hand side term of (A.4) on each parameter [158] as shown:

$$\gamma_{t,1} = 1 + \sum_{n} \phi_{n,t} \tag{A.6}$$

$$\gamma_{t,2} = \alpha + \sum_{n} \sum_{j=t+1}^{T} \phi_{n,j} \tag{A.7}$$

$$\tau_{t,1} = \lambda_1 + \sum_{n} \phi_{n,t} x_n \tag{A.8}$$

$$\tau_{t,2} = \lambda_2 + \sum_{n} \phi_{n,t} \tag{A.9}$$

$$\phi_{n,t} \propto (S_{n,t}) \tag{A.10}$$

$$S_{n,t} = \Psi(\gamma_{t,1}) - \Psi(\gamma_{t,1}+\gamma_{t,2}) + \sum_{i=1}^{T-1} x_n(\Psi(\gamma_{t,2}) - \Psi(\gamma_{t,1}+\gamma_{t,2})) + \mathrm{E}_q\left[\eta^*\right]^T x_n - \mathrm{E}_q\left[a(\eta^*)\right] \tag{A.11}$$

where $\phi_{n,t}$ are normalized according to $\sum_t \phi_{n,t} = 1$ and Ψ is the digamma function to derive the log normalizer for the beta distribution.

APPENDIX B

EVOLUTION STRATEGY

An evolution strategy (ES) is a method of optimization based on evolutionary principles which consists of mutation, recombination, and selection steps. The early version using a simple selection mechanism termed (1+1)-ES was proposed by Schwefel [194] to solve a numerical optimization problem. In the algorithm, mutations with identical standard deviations are applied to two individuals and the resulting better offsprings survive in the next generation. Later version incorporating the principle of a population is called (μ+1)-ES where $\mu > 1$. In a (μ+1)-ES algorithm, μ parents recombine according to a certain recombination mechanism, forming offsprings with better fitness values after mutation. Some of the common recombination mechanisms are as follows:

$$x_i' = \begin{cases} x_{S,i} & no\ recombination \\ x_{S_i}\ or\ x_{T,i} & discrete \\ x_{S_i}\ or\ x_{T_i,i} & panmictic\ discrete \\ \frac{x_{S_i}+x_{T,i}}{2} & intermediate \\ \frac{x_{S_i}+x_{T_i,i}}{2} & panmictic\ intermediate \\ \omega x_{S_i}+(1-\omega)x_{T,i} & generalized\ intermediate \\ \omega_i x_{S_i}+(1-\omega_i)x_{T,i} & panmictic\ generalized\ intermediate \end{cases} \tag{B.1}$$

where the index i represents the ith dimension or called component of the objective variables. $x_{S,i}$ and $x_{T,i}$ are two randomly picked parents from the population. $\omega \in [0,1]$ is a weight factor. The recombinations with panmictic indicate one of the two parents in each component is sampled anew from the population while the two others don't exclude two identical parents.

The selection operation falls into two groups: $(\mu+\lambda)$-selection and (μ,λ)-selection. In [194], Schwefe indicated that the former mechanism selects the μ best individuals for the next generation from all current parents and offsprings while the latter only consider the union of offsprings. The performance of the two selection approaches is widely divided on different applications. The $(\mu+\lambda)$-selection preserves the historical best solution and is intuitively more computational effective. The (μ,λ)-selection with moving optimum is more likely to escape from local optima and therefore has advantageous for multimodal problems.

The utilization of independent recombination on objective variables and strategy parameters (standard deviations and rotation angles) is justified by experimental observations concerning the performance of the resulting variants of ES. Theoretical investigations of this topic are still an open field of research.

APPENDIX C

CMA-ES

C.1 Evolution Path p_c for Rank-one-update of Covariance Matrix

The update rule of evolution path for rank-one-update of covariance matrix is based on the average of all $y_{s,g+1}$ at the generation $g+1$. Suppose the weighted selection mechanism is adopted, we will have

$$\sum_{s=1}^{\mu} w_s y_{s,g+1} = \sum_{s=1}^{\mu} w_s \frac{x'_{s,g+1} - m_g}{\sigma_g} = \frac{m_{g+1} - m_g}{\sigma_g} \tag{C.1}$$

As we know that $y_{s,g+1} = \frac{x'_{s,g+1} - m_g}{\sigma_g} \sim N(0, C_g)$

$$\sum_{s=1}^{\mu} w_s y_{s,g+1} \sim \frac{1}{\sqrt{\mu_{eff}}} N(0, C_g) \tag{C.2}$$

Therefore, we will have

$$\sqrt{\mu_{eff}} \frac{m_{g+1} - m_g}{\sigma_g} \sim N(0, C_g) \tag{C.3}$$

Remark that $(1-c_c)^2 + \sqrt{c_c(2-c_c)}^2 = 1$. The evaluation path is balanced between recent evolation path $p_{c,g}$ and the average of moving step $y_{s,g+1}$ in the same generation

$$p_{c,g+1} = (1-c_c) p_{c,g} + \sqrt{c_c(2-c_c)\mu_{eff}} \frac{m_{g+1} - m_g}{\sigma_g} \tag{C.4}$$

C.2 Evolution Path p_σ for Step-size Control

The update rule of evolution path for step-size control is similar to the update of rank-one-update of covariance matrix. The moving step of $y_{s,g+1}$ at the generation $g+1$ could be further written as:

$$\sum_{s=1}^{\mu} w_s y_{s,g+1} \sim N(0, C_g) \sim \frac{1}{\sqrt{\mu_{eff}}} C_g^{1/2} N(0, I) \tag{C.5}$$

$$\sqrt{\mu_{eff}}\, C_g^{-1/2} \frac{m_{g+1} - m_g}{\sigma_g} \sim N(0, I) \tag{C.6}$$

Use the normalized constant $\sqrt{c_\sigma(2-c_\sigma)}$ where $(1-c_\sigma)^2 + \sqrt{c_\sigma(2-c_\sigma)}^2 = 1$. The evaluation path is

$$p_{\sigma,g+1} = (1-c_\sigma) p_{\sigma,g} + \sqrt{c_\sigma(2-c_\sigma)\mu_{eff}}\, C_g^{-1/2} \frac{m_{g+1} - m_g}{\sigma_g} \tag{C.7}$$

C.3 Default Parameters

All parameters are taken from [195].

Selection and Recombination

$$\lambda = 4 + \lfloor 3 \ln n \rfloor \tag{C.8}$$

$$\mu = \left\lfloor \frac{\lambda}{2} \right\rfloor \tag{C.9}$$

$$w_i' = \ln \frac{\lambda+1}{2} - \ln i \quad i = 1, 2, ..., \lambda \tag{C.10}$$

$$\mu_{eff} = \frac{(\sum_{i=1}^{\mu} w_i')^2}{\sum_{i=1}^{\mu} w_i'^2} \tag{C.11}$$

$$\mu_{eff}^- = \frac{(\sum_{i=\mu+1}^{\lambda} w_i')^2}{\sum_{i=\mu+1}^{\lambda} w_i'^2} \tag{C.12}$$

$$w_i = \begin{cases} \frac{1}{\sum |w_j'|^+} w_i' & if \quad w_i' \geqslant 0 \\ \frac{min\left(\alpha_\mu^-, \alpha_{eff}^-, \alpha_{posdef}^-\right)}{\sum |w_j'|^-} w_i' & if \quad w_i' \leqslant 0 \end{cases} \tag{C.13}$$

where

$$\alpha_{\mu}^{-} = 1 + \frac{c_1}{c_{\mu}} \tag{C.14}$$

$$\alpha_{eff}^{-} = 1 + \frac{2\mu_{eff}^{-}}{\mu_{eff} + 2} \tag{C.15}$$

$$\alpha_{posdef}^{-} = \frac{1 - c_1 - c_{\mu}}{n c_{\mu}} \tag{C.16}$$

Step-size control

$$c_{\sigma} = \frac{\mu_{eff} + 2}{n + \mu_{eff} + 5} \tag{C.17}$$

$$d_{\sigma} = 1 + 2max\left(0, \sqrt{\frac{\mu_{eff} - 1}{n + 1}} - 1\right) + c_{\sigma} \tag{C.18}$$

Covariance matrix adaptation

$$c_c = \frac{4 + \frac{\mu_{eff}}{n}}{n + 4 + 2\frac{\mu_{eff}}{n}} \tag{C.19}$$

$$c_1 = \frac{\alpha_{cov}}{(n + 1.3)^2 + \mu_{eff}} \quad \alpha_{cov} = 2 \tag{C.20}$$

$$c_{\mu} = min\left(1 - c_1, \alpha_{cov}\frac{\mu_{eff} - 2 + \frac{1}{\mu_{eff}}}{(n+2)^2 + \frac{\alpha_{cov}\mu_{eff}}{2}}\right) \quad \alpha_{cov} = 2 \tag{C.21}$$

BIBLIOGRAPHY

[1] A. Ajanovic and R. Haas, "The impact of energy policies in scenarios on ghg emission reduction in passenger car mobility in the eu-15," *Renewable and Sustainable Energy Reviews*, vol. 68, pp. 1088–1096, 2017.

[2] Guidehouse Insights, "Microgrid deployment tracker 3q21," 2021. [Online]. Available: https://guidehouseinsights.com/reports/microgrid-deployment-tracker-3q21

[3] W. Feng, M. Jin, X. Liu, Y. Bao, C. Marnay, C. Yao, and J. Yu, "A review of microgrid development in the united states – a decade of progress on policies, demonstrations, controls, and software tools," *Applied Energy*, vol. 228, pp. 1656–1668, 2018. [Online]. Available: https://www.sciencedirect.com/science/article/pii/S0306261918309644

[4] O. Palizban and K. Kauhaniemi, "Energy storage systems in modern grids—matrix of technologies and applications," *Journal of Energy Storage*, vol. 6, pp. 248–259, 2016.

[5] ETRM Systems, "Power markets in europe," 2021. [Online]. Available: http://www.etrmsystems.com/markets-EUpower.htm

[6] Statista, "Net consumption of electricity worldwide in select years from 1980 to 2018," 2021. [Online]. Available: https://www.statista.com/statistics/280704/world-power-consumption/

[7] International Energy Agency, "Electricity market report - january 2022," 2022. [Online]. Available: https://www.iea.org/reports/electricity-market-report-january-2022

[8] D. T. Ton and M. A. Smith, "The u.s. department of energy's microgrid initiative," *The Electricity Journal*, vol. 25, no. 8, pp. 84–94, 2012. [Online]. Available: https://www.sciencedirect.com/science/article/pii/S1040619012002254

[9] K. Hirose, "Behavior of the sendai microgrid during and after the 311 great east japan disaster," in *Intelec 2013; 35th International Telecommunications Energy Conference, SMART POWER AND EFFICIENCY*, 2013, pp. 1–6.

[10] International Energy Agency, "Shares of different generation technologies in energy, 2018, iea, paris," 2020. [Online]. Available: https://www.iea.org/data-and-statistics/charts/asean-shares-of-different-generation-technologies-in-energy-2018

[11] D. Bodansky, "The paris climate change agreement: A new hope?" *American Journal of International Law*, vol. 110, no. 2, p. 288–319, 2016.

[12] Department for Business, Energy Industrial Strategy, "Energy trends," 2021. [Online]. Available: https://assets.publishing.service.gov.uk/government/uploads/system/uploads/attachment_data/file/1021989/Energy_Trends_September_2021.pdf

[13] J. Yu, C. Marnay, M. Jin, C. Yao, X. Liu, and W. Feng, "Review of microgrid development in the united states and china and lessons learned for china," *Energy Procedia*, vol. 145, pp. 217–222, 2018.

[14] U.S. Department of Energy Combined Heat and Power and Microgrid Installation Databases, "Microgrid Installations," Accessed Dec. 13, 2021 [Online]. [Online]. Available: https://doe.icfwebservices.com/microgrid

[15] R. Lasseter, A. Akhil, C. Marnay, J. Stephens, J. Dagle, R. Guttromson, A. Meliopoulous, R. Yinger, and J. Eto, "The certs microgrid concept," *White paper for Transmission Reliability Program, Office of Power Technologies, US Department of Energy*, vol. 2, no. 3, p. 30, 2002.

[16] A. Khodaei, S. Bahramirad, and M. Shahidehpour, "Microgrid planning under uncertainty," *IEEE Transactions on Power Systems*, vol. 30, no. 5, pp. 2417–2425, 2014.

[17] A. Agüera-Pérez, J. C. Palomares-Salas, J. J. G. De La Rosa, and O. Florencias-Oliveros, "Weather forecasts for microgrid energy management: Review, discussion and recommendations," *Applied energy*, vol. 228, pp. 265–278, 2018.

[18] D. Neves, M. C. Brito, and C. A. Silva, "Impact of solar and wind forecast uncertainties on demand response of isolated microgrids," *Renewable energy*, vol. 87, pp. 1003–1015, 2016.

[19] A. Nikoobakht, J. Aghaei, M. Shafie-khah, and J. P. S. Catalão, "Assessing increased flexibility of energy storage and demand response to accommodate a high penetration of renewable energy sources," *IEEE Transactions on Sustainable Energy*, pp. 1–1, 2018.

[20] P. Denholm, M. O'Connell, G. Brinkman, and J. Jorgenson, "Overgeneration from solar energy in california. a field guide to the duck chart," National Renewable Energy Lab.(NREL), Golden, CO (United States), Tech. Rep., 2015.

[21] E. Kuznetsova, C. Ruiz, Y.-F. Li, and E. Zio, "Analysis of robust optimization for decentralized microgrid energy management under uncertainty," *International Journal of Electrical Power & Energy Systems*, vol. 64, pp. 815–832, 2015.

[22] K. Moharm, "State of the art in big data applications in microgrid: A review," *Advanced Engineering Informatics*, vol. 42, p. 100945, 2019.

[23] J. Zhan, J. Huang, L. Niu, X. Peng, D. Deng, and S. Cheng, "Study of the key technologies of electric power big data and its application prospects in smart grid," in *2014 IEEE PES Asia-Pacific Power and Energy Engineering Conference (APPEEC)*. IEEE, 2014, pp. 1–4.

[24] P. Kundur, *Power system stability and control*. McGraw-hill, 1994.

[25] M. Yin, K. Li, and Y. James, "A data-driven approach for microgrid distributed generation planning under uncertainties," *Applied energy*, in press.

[26] M. Yin, K. Li, and X. Cheng, "A review on artificial intelligence in high-speed rail," *Transportation Safety and Environment*, vol. 2, no. 4, pp. 247–259, 2020.

[27] Y. Li, K. Li, M. Yin, and X. Cheng, "Advances in fault diagnosis for high-speed railway: A review," in *2019 6th International Conference on Frontiers of Industrial Engineering (ICFIE)*. IEEE, 2019, pp. 67–72.

[28] H. Zhang, D. Yue, W. Yue, K. Li, and M. Yin, "Moea/d-based probabilistic pbi approach for risk-based optimal operation of hybrid energy system with intermittent power uncertainty," *IEEE Transactions on Systems, Man, and Cybernetics: Systems*, 2019.

[29] M. Yin and K. Li, "Optimal allocation of distributed generations with sop in distribution systems," in *2020 IEEE Power & Energy Society General Meeting (PESGM)*. IEEE, 2020, pp. 1–5.

[30] M. Yin, K. Li, and M. Zheng, "Spectrum utilization of cognitive radio in industrial wireless sensor networks-a review," *Intelligent Computing and Internet of Things*, pp. 419–428, 2018.

[31] S. Krishnamurthy, T. M. Jahns, and R. H. Lasseter, "The operation of diesel gensets in a certs microgrid," in *2008 IEEE Power and Energy Society General Meeting - Conversion and Delivery of Electrical Energy in the 21st Century*, 2008, pp. 1–8.

[32] S. Mishra, D. Ramasubramanian, and P. C. Sekhar, "A seamless control methodology for a grid connected and isolated pv-diesel microgrid," *IEEE Transactions on Power Systems*, vol. 28, no. 4, pp. 4393–4404, 2013.

[33] F. Katiraei and C. Abbey, "Diesel plant sizing and performance analysis of a remote wind-diesel microgrid," in *2007 IEEE Power Engineering Society General Meeting*, 2007, pp. 1–8.

[34] 2003.

[35] P. Breeze, "Natural gas-fired gas turbines and combined cycle power plants," *Power Generation Technologies*, pp. 67–92, 2014.

[36] J. Romankiewicz, C. Marnay, N. Zhou, and M. Qu, "Lessons from international experience for china's microgrid demonstration program," *Energy Policy*, vol. 67, pp. 198–208, 2014.

[37] H. Wei, W. Ziping, N. Ming, Z. Jianhua, G. Yuanbo, and W. Chong, "Dynamic modelling and simulation of microturbine generation system for the parallel operation of microgrid," in *2009 International Conference on Sustainable Power Generation and Supply*, 2009, pp. 1–8.

[38] M. Zachar and P. Daoutidis, "Scheduling and supervisory control for cost effective load shaping of microgrids with flexible demands," *Journal of Process Control*, vol. 74, pp. 202–214, 2019.

[39] 2021.

[40] S.-H. Huang, J. Schmall, J. Conto, J. Adams, Y. Zhang, and C. Carter, "Voltage control challenges on weak grids with high penetration of wind generation: Ercot experience," in *2012 IEEE Power and Energy Society General Meeting*. IEEE, 2012, pp. 1–7.

[41] P. Sreedharan, J. Farbes, E. Cutter, C.-K. Woo, and J. Wang, "Microgrid and renewable generation integration: University of california, san diego," *Applied energy*, vol. 169, pp. 709–720, 2016.

[42] M. Nthontho, S. Chowdhury, S. Winberg, and S. Chowdhury, "Protection of domestic solar photovoltaic based microgrid," 2012.

[43] R. B. Hytowitz and K. W. Hedman, "Managing solar uncertainty in microgrid systems with stochastic unit commitment," *Electric Power Systems Research*, vol. 119, pp. 111–118, 2015.

[44] L. Bird, D. Lew, M. Milligan, E. M. Carlini, A. Estanqueiro, D. Flynn, E. Gomez-Lazaro, H. Holttinen, N. Menemenlis, A. Orths *et al.*, "Wind and solar energy curtailment: A review of international experience," *Renewable and Sustainable Energy Reviews*, vol. 65, pp. 577–586, 2016.

[45] D. Akinyele, E. Olabode, and A. Amole, "Review of fuel cell technologies and applications for sustainable microgrid systems," *Inventions*, vol. 5, no. 3, p. 42, 2020.

[46] M. Gabbasa, K. Sopian, A. Fudholi, and N. Asim, "A review of unitized regenerative fuel cell stack: Material, design and research achievements," *International journal of hydrogen energy*, vol. 39, no. 31, pp. 17 765–17 778, 2014.

[47] O. Z. Sharaf and M. F. Orhan, "An overview of fuel cell technology: Fundamentals and applications," *Renewable and sustainable energy reviews*, vol. 32, pp. 810–853, 2014.

[48] G. Han, Y. Kwon, J. B. Kim, S. Lee, J. Bae, E. Cho, B. J. Lee, S. Cho, and J. Park, "Development of a high-energy-density portable/mobile hydrogen energy storage system incorporating an electrolyzer, a metal hydride and a fuel cell," *Applied Energy*, vol. 259, p. 114175, 2020.

[49] L. Wang, D.-J. Lee, L.-Y. Chen, J.-Y. Yu, S.-R. Jan, S.-J. Chen, W.-J. Lee, M.-H. Tsai, W.-T. Lin, Y.-C. Li, and B. K. Blyden, "A micro hydro power generation system for sustainable microgrid development in rural electrification of africa," in *2009 IEEE Power Energy Society General Meeting*, 2009, pp. 1–8.

[50] W. Gil-González, O. D. Montoya, and A. Garces, "Modeling and control of a small hydro-power plant for a dc microgrid," *Electric Power Systems Research*, vol. 180, p. 106104, 2020.

[51] Y. Xu, C. Li, Z. Wang, N. Zhang, and B. Peng, "Load frequency control of a novel renewable energy integrated micro-grid containing pumped hydropower energy storage," *IEEE Access*, vol. 6, pp. 29 067–29 077, 2018.

[52] A. Rathore and N. Patidar, "Reliability assessment using probabilistic modelling of pumped storage hydro plant with pv-wind based standalone microgrid," *International Journal of Electrical Power & Energy Systems*, vol. 106, pp. 17–32, 2019.

[53] G. Pathak, B. Singh, and B. K. Panigrahi, "Wind–hydro microgrid and its control for rural energy system," *IEEE Transactions on Industry Applications*, vol. 55, no. 3, pp. 3037–3045, 2019.

[54] Y. Guan, J. C. Vasquez, J. M. Guerrero, Y. Wang, and W. Feng, "Frequency stability of hierarchically controlled hybrid photovoltaic-battery-hydropower microgrids," *IEEE Transactions on Industry Applications*, vol. 51, no. 6, pp. 4729–4742, 2015.

[55] P. Vadana, S. K. Kottayil *et al.*, "Dynamic energy management on a hydro-powered smart microgrid," in *Proceedings of the International Conference on Soft Computing Systems*. Springer, 2016, pp. 627–635.

[56] T. Mahlia, T. Saktisahdan, A. Jannifar, M. Hasan, and H. Matseelar, "A review of available methods and development on energy storage; technology update," *Renewable and sustainable energy reviews*, vol. 33, pp. 532–545, 2014.

[57] H. Yan, D. Zhang, X. Duo, X. Sheng *et al.*, "A review of spinel lithium titanate (li4ti5o12) as electrode material for advanced energy storage devices," *Ceramics International*, vol. 47, no. 5, pp. 5870–5895, 2021.

[58] M. Faisal, M. A. Hannan, P. J. Ker, A. Hussain, M. B. Mansor, and F. Blaabjerg, "Review of energy storage system technologies in microgrid applications: Issues and challenges," *Ieee Access*, vol. 6, pp. 35 143–35 164, 2018.

[59] T. A. Nguyen, M. L. Crow, and A. C. Elmore, "Optimal sizing of a vanadium redox battery system for microgrid systems," *IEEE transactions on sustainable energy*, vol. 6, no. 3, pp. 729–737, 2015.

[60] H. Qian, J. Zhang, J.-S. Lai, and W. Yu, "A high-efficiency grid-tie battery energy storage system," *IEEE transactions on power electronics*, vol. 26, no. 3, pp. 886–896, 2010.

[61] A.-I. Stroe, M. Swierczynski, D.-I. Stroe, and R. Teodorescu, "Performance model for high-power lithium titanate oxide batteries based on extended characterization tests," in *2015 IEEE Energy Conversion Congress and Exposition (ECCE)*, 2015, pp. 6191–6198.

[62] M. A. Mirzaei, M. Hemmati, K. Zare, B. Mohammadi-Ivatloo, M. Abapour, M. Marzband, and A. Farzamnia, "Two-stage robust-stochastic electricity market clearing considering mobile energy storage in rail transportation," *IEEE Access*, vol. 8, pp. 121 780–121 794, 2020.

[63] M. Rahmani-Andebili, "Vehicle-for-grid (vfg): A mobile energy storage in smart grid," *IET Generation, Transmission & Distribution*, vol. 13, no. 8, pp. 1358–1368, 2019.

[64] J. Kim and Y. Dvorkin, "Enhancing distribution system resilience with mobile energy storage and microgrids," *IEEE Transactions on Smart Grid*, vol. 10, no. 5, pp. 4996–5006, 2019.

[65] Y. Song, Y. Liu, R. Wang, and M. Ming, "Multi-objective configuration optimization for isolated microgrid with shiftable loads and mobile energy storage," *IEEE Access*, vol. 7, pp. 95 248–95 263, 2019.

[66] K. Lee, E. Miguel, and C. Wolfram, "Does household electrification supercharge economic development?" *Journal of Economic Perspectives*, vol. 34, no. 1, pp. 122–44, 2020.

[67] B. Dalla Chiara, F. Deflorio, M. Pellicelli, L. Castello, and M. Eid, "Perspectives on electrification for the automotive sector: A critical review of average daily distances by light-duty vehicles, required range, and economic outcomes," *Sustainability*, vol. 11, no. 20, p. 5784, 2019.

[68] G. Liu, B. Xiao, M. Starke, O. Ceylan, and K. Tomsovic, "A robust load shedding strategy for microgrid islanding transition," in *2016 IEEE/PES Transmission and Distribution Conference and Exposition (T&D)*. IEEE, 2016, pp. 1–5.

[69] M. Q. Ahsan, A. H. Chowdhury, S. S. Ahmed, I. H. Bhuyan, M. A. Haque, and H. Rahman, "Technique to develop auto load shedding and islanding scheme to prevent power system blackout," *IEEE transactions on Power Systems*, vol. 27, no. 1, pp. 198–205, 2011.

[70] M. Marzband, M. M. Moghaddam, M. F. Akorede, and G. Khomeyrani, "Adaptive load shedding scheme for frequency stability enhancement in microgrids," *Electric Power Systems Research*, vol. 140, pp. 78–86, 2016.

[71] M. H. Albadi and E. F. El-Saadany, "A summary of demand response in electricity markets," *Electric power systems research*, vol. 78, no. 11, pp. 1989–1996, 2008.

[72] N. N. A. Bakar, M. Y. Hassan, M. F. Sulaima, M. Na'im Mohd Nasir, and A. Khamis, "Microgrid and load shedding scheme during islanded mode: A review," *Renewable and Sustainable Energy Reviews*, vol. 71, pp. 161–169, 2017.

[73] S. Golshannavaz, S. Afsharnia, and F. Aminifar, "Smart distribution grid: Optimal day-ahead scheduling with reconfigurable topology," *IEEE Transactions on Smart Grid*, vol. 5, no. 5, pp. 2402–2411, Sep. 2014.

[74] M. Mazidi, H. Monsef, and P. Siano, "Incorporating price-responsive customers in day-ahead scheduling of smart distribution networks," *Energy Conversion and Management*, vol. 115, pp. 103 – 116, 2016. [Online]. Available: http://www.sciencedirect.com/science/article/pii/S0196890416300541

[75] A. Zakariazadeh, O. Homaee, S. Jadid, and P. Siano, "A new approach for real time voltage control using demand response in an automated distribution system," *Applied Energy*, vol. 117, pp. 157 – 166, 2014. [Online]. Available: http://www.sciencedirect.com/science/article/pii/S0306261913009884

[76] C. Sahin, M. Shahidehpour, and I. Erkmen, "Allocation of hourly reserve versus demand response for security-constrained scheduling of stochastic wind energy," *IEEE Transactions on Sustainable Energy*, vol. 4, no. 1, pp. 219–228, Jan 2013.

[77] M. Jamil, B. Hussain, M. Abu-Sara, R. Boltryk, and S. Sharkh, "Microgrid power electronic converters: State of the art and future challenges," in *2009 44th International Universities Power Engineering Conference (UPEC)*. IEEE, 2009, pp. 1–5.

[78] R. Bayindir, E. Hossain, E. Kabalci, and R. Perez, "A comprehensive study on microgrid technology," *International Journal of Renewable Energy Research (IJRER)*, vol. 4, no. 4, pp. 1094–1107, 2014.

[79] S. Peyghami, P. Palensky, and F. Blaabjerg, "An overview on the reliability of modern power electronic based power systems," *IEEE Open Journal of Power Electronics*, vol. 1, pp. 34–50, 2020.

[80] K. S. Ratnam, K. Palanisamy, and G. Yang, "Future low-inertia power systems: Requirements, issues, and solutions-a review," *Renewable and Sustainable Energy Reviews*, vol. 124, p. 109773, 2020.

[81] T. Kerdphol, F. S. Rahman, M. Watanabe, and Y. Mitani, "Robust virtual inertia control of a low inertia microgrid considering frequency measurement effects," *IEEE Access*, vol. 7, pp. 57 550–57 560, 2019.

[82] J. Wang, Z. Wang, L. Xu, and Z. Wang, "A summary of applications of d-facts on microgrid," in *2012 Asia-Pacific Power and Energy Engineering Conference*, 2012, pp. 1–6.

[83] W. Rohouma, R. S. Balog, A. A. Peerzada, and M. M. Begovic, "D-statcom for harmonic mitigation in low voltage distribution network with high penetration of nonlinear loads," *Renewable Energy*, vol. 145, pp. 1449–1464, 2020.

[84] Z. Liu, M. Su, Y. Sun, L. Li, H. Han, X. Zhang, and M. Zheng, "Optimal criterion and global/sub-optimal control schemes of decentralized economical dispatch for ac microgrid," *International Journal of Electrical Power & Energy Systems*, vol. 104, pp. 38–42, 2019.

[85] T. Ding, Z. Wang, W. Jia, B. Chen, C. Chen, and M. Shahidehpour, "Multiperiod distribution system restoration with routing repair crews, mobile electric vehicles, and soft-open-point networked microgrids," *IEEE Transactions on Smart Grid*, vol. 11, no. 6, pp. 4795–4808, 2020.

[86] J. Li, M. E. Khodayar, J. Wang, and B. Zhou, "Data-driven distributionally robust co-optimization of p2p energy trading and network operation for interconnected microgrids," *IEEE Transactions on Smart Grid*, vol. 12, no. 6, pp. 5172–5184, 2021.

[87] P. Kundur, N. J. Balu, and M. G. Lauby, *Power system stability and control*. McGraw-hill New York, 1994, vol. 7.

[88] J. Carpentier, "Contribution to the economic dispatch problem," *Bulletin de la Societe Francoise des Electriciens*, vol. 3, no. 8, pp. 431–447, 1962.

[89] J. Zhu, *Optimization of power system operation*. John Wiley & Sons, 2015, vol. 47.

[90] B. Stott, "Review of load-flow calculation methods," *Proceedings of the IEEE*, vol. 62, no. 7, pp. 916–929, July 1974.

[91] M. E. Baran and F. F. Wu, "Optimal capacitor placement on radial distribution systems," *IEEE Transactions on Power Delivery*, vol. 4, no. 1, pp. 725–734, 1989.

[92] K. Turitsyn, P. Šulc, S. Backhaus, and M. Chertkov, "Distributed control of reactive power flow in a radial distribution circuit with high photovoltaic penetration," in *IEEE PES General Meeting*, 2010, pp. 1–6.

[93] M. E. Baran and F. F. Wu, "Network reconfiguration in distribution systems for loss reduction and load balancing," *IEEE Transactions on Power Delivery*, vol. 4, no. 2, pp. 1401–1407, 1989.

[94] A. Gholami, T. Shekari, F. Aminifar, and M. Shahidehpour, "Microgrid scheduling with uncertainty: The quest for resilience," *IEEE Transactions on Smart Grid*, vol. 7, no. 6, pp. 2849–2858, 2016.

[95] K. Gong, X. Wang, C. Jiang, M. Shahidehpour, X. Liu, and Z. Zhu, "Security-constrained optimal sizing and siting of bess in hybrid ac/dc microgrid considering post-contingency corrective rescheduling," *IEEE Transactions on Sustainable Energy*, 2021.

[96] Y. Parag and B. K. Sovacool, "Electricity market design for the prosumer era," *Nature energy*, vol. 1, no. 4, pp. 1–6, 2016.

[97] J. Martins and J. Miles, "A techno-economic assessment of battery business models in the uk electricity market," *Energy Policy*, vol. 148, p. 111938, 2021.

[98] J. Newman and P. MacDougall, "Increasing der integration through discrete intraday settlements," *The Electricity Journal*, vol. 34, no. 4, p. 106932, 2021.

[99] Nord Pool, "Intraday trading," 2021. [Online]. Available: https://www.nordpoolgroup.com/trading/

[100] P. Shinde and M. Amelin, "A literature review of intraday electricity markets and prices," in *2019 IEEE Milan PowerTech*. IEEE, 2019, pp. 1–6.

[101] National grid ESO, "Balancing services," 2021. [Online]. Available: https://www.nationalgrideso.com/industry-information/balancing-services

[102] G. Dantzig, *Linear programming and extensions*. Princeton university press, 2016.

[103] B. Stott and J. L. Marinho, "Linear programming for power-system network security applications," *IEEE Transactions on Power Apparatus and Systems*, vol. PAS-98, no. 3, pp. 837–848, May 1979.

[104] A. Farag, S. Al-Baiyat, and T. C. Cheng, "Economic load dispatch multiobjective optimization procedures using linear programming techniques," *IEEE Transactions on Power Systems*, vol. 10, no. 2, pp. 731–738, May 1995.

[105] S. Granville, J. C. O. Mello, and A. C. G. Melo, "Application of interior point methods to power flow unsolvability," *IEEE Transactions on Power Systems*, vol. 11, no. 2, pp. 1096–1103, May 1996.

[106] Z. Jizhong and X. Guoyu, "A new economic power dispatch method with security," *Electric power systems research*, vol. 25, no. 1, pp. 9–15, 1992.

[107] B. Stott and J. Marinho, "Linear programming for power-system network security applications," *IEEE Transactions on Power Apparatus and Systems*, no. 3, pp. 837–848, 1979.

[108] O. Alsac and B. Stott, "Optimal load flow with steady-state security," *IEEE transactions on power apparatus and systems*, no. 3, pp. 745–751, 1974.

[109] J. Zhu, "Application of network flow techniques to power systems. wa," 2005.

[110] J.-Y. Fan and L. Zhang, "Real-time economic dispatch with line flow and emission constraints using quadratic programming," *IEEE Transactions on Power Systems*, vol. 13, no. 2, pp. 320–325, May 1998.

[111] J. A. Momoh, S. X. Guo, E. C. Ogbuobiri, and R. Adapa, "The quadratic interior point method solving power system optimization problems," *IEEE Transactions on Power Systems*, vol. 9, no. 3, pp. 1327–1336, 1994.

[112] J. A. Momoh and J. Z. Zhu, "Improved interior point method for opf problems," *IEEE Transactions on Power Systems*, vol. 14, no. 3, pp. 1114–1120, Aug 1999.

[113] N. Grudinin, "Reactive power optimization using successive quadratic programming method," *IEEE Transactions on Power Systems*, vol. 13, no. 4, pp. 1219–1225, 1998.

[114] J. Lavaei, A. Rantzer, and S. Low, "Power flow optimization using positive quadratic programming," *Proc. 18th IFAC World Congr*, pp. 10 481–10 486, 2011.

[115] I. M. Nejdawi, K. A. Clements, and P. W. Davis, "An efficient interior point method for sequential quadratic programming based optimal power flow," *IEEE Transactions on Power Systems*, vol. 15, no. 4, pp. 1179–1183, 2000.

[116] S. Binato, M. V. F. Pereira, and S. Granville, "A new benders decomposition approach to solve power transmission network design problems," *IEEE Transactions on Power Systems*, vol. 16, no. 2, pp. 235–240, 2001.

[117] H. Shuai, J. Fang, X. Ai, Y. Tang, J. Wen, and H. He, "Stochastic optimization of economic dispatch for microgrid based on approximate dynamic programming," *IEEE Transactions on Smart Grid*, vol. 10, no. 3, pp. 2440–2452, 2018.

[118] Y. Zhu, D. Zhao, X. Li, and D. Wang, "Control-limited adaptive dynamic programming for multi-battery energy storage systems," *IEEE Transactions on Smart Grid*, vol. 10, no. 4, pp. 4235–4244, 2018.

[119] L. N. An and T. Quoc-Tuan, "Optimal energy management for grid connected microgrid by using dynamic programming method," in *2015 IEEE Power & Energy Society General Meeting*. IEEE, 2015, pp. 1–5.

[120] Q. P. Zheng, J. Wang, and A. L. Liu, "Stochastic optimization for unit commitment—a review," *IEEE Trans. Power Syst*, vol. 30, no. 4, pp. 1913–1924, 2015.

[121] H. Kanchev, B. Francois, and V. Lazarov, "Unit commitment by dynamic programming for microgrid operational planning optimization and emission reduction," in *International Aegean Conference on Electrical Machines and Power Electronics and Electromotion, Joint Conference*. IEEE, 2011, pp. 502–507.

[122] C.-P. Cheng, C.-W. Liu, and C.-C. Liu, "Unit commitment by lagrangian relaxation and genetic algorithms," *IEEE transactions on power systems*, vol. 15, no. 2, pp. 707–714, 2000.

[123] W. L. Peterson and S. R. Brammer, "A capacity based lagrangian relaxation unit commitment with ramp rate constraints," *IEEE Transactions on Power Systems*, vol. 10, no. 2, pp. 1077–1084, 1995.

[124] W. Ongsakul and N. Petcharaks, "Unit commitment by enhanced adaptive lagrangian relaxation," *IEEE Transactions on Power Systems*, vol. 19, no. 1, pp. 620–628, 2004.

[125] Warsono, D. J. King, C. S. Ozveren, and D. A. Bradley, "Economic load dispatch optimization of renewable energy in power system using genetic algorithm," in *2007 IEEE Lausanne Power Tech*, July 2007, pp. 2174–2179.

[126] D. C. Walters and G. B. Sheble, "Genetic algorithm solution of economic dispatch with valve point loading," *IEEE Transactions on Power Systems*, vol. 8, no. 3, pp. 1325–1332, Aug 1993.

[127] Y. L. Abdel-Magid and M. A. Abido, "Optimal multiobjective design of robust power system stabilizers using genetic algorithms," *IEEE Transactions on Power Systems*, vol. 18, no. 3, pp. 1125–1132, Aug 2003.

[128] A. Charnes and W. W. Cooper, "Chance-constrained programming," *Management science*, vol. 6, no. 1, pp. 73–79, 1959.

[129] R. E. Bellman and L. A. Zadeh, "Decision-making in a fuzzy environment," *Management science*, vol. 17, no. 4, pp. B–141, 1970.

[130] S. Peng, "Chance constrained problem and its applications," Ph.D. dissertation, Université Paris Saclay (COmUE); Xi'an Jiaotong University, 2019.

[131] MATLAB, *version 7.10.0 (R2010a)*. Natick, Massachusetts: The MathWorks Inc., 2010.

[132] R. D. Zimmerman, C. E. Murillo-Sanchez, and R. J. Thomas, "Matpower: Steady-state operations, planning, and analysis tools for power systems research and education," *IEEE Transactions on Power Systems*, vol. 26, no. 1, pp. 12–19, Feb 2011.

[133] J. Lofberg, "Yalmip: A toolbox for modeling and optimization in matlab," in *2004 IEEE international conference on robotics and automation (IEEE Cat. No. 04CH37508)*. IEEE, 2004, pp. 284–289.

[134] C. Bliek1ú, P. Bonami, and A. Lodi, "Solving mixed-integer quadratic programming problems with ibm-cplex: a progress report," in *Proceedings of the twenty-sixth RAMP symposium*, 2014, pp. 16–17.

[135] M. ApS, "Mosek optimization toolbox for matlab," *User's Guide and Reference Manual, Version*, vol. 4, 2019.

[136] B. Bixby, "The gurobi optimizer," *Transp. Re-search Part B*, vol. 41, no. 2, pp. 159–178, 2007.

[137] M. R. Bussieck and A. Meeraus, "General algebraic modeling system (gams)," in *Modeling languages in mathematical optimization*. Springer, 2004, pp. 137–157.

[138] "Solver manuals." [Online]. Available: https://www.gams.com/35/docs/S_MAIN.html

[139] T. Lambert, P. Gilman, and P. Lilienthal, "Micropower system modeling with homer," *Integration of alternative sources of energy*, vol. 1, no. 1, pp. 379–385, 2006.

[140] F. Katiraei and M. Iravani, "Power management strategies for a microgrid with multiple distributed generation units," *IEEE Transactions on Power Systems*, vol. 21, no. 4, pp. 1821–1831, 2006.

[141] E. Karunarathne, J. Pasupuleti, J. Ekanayake, and D. Almeida, "The optimal placement and sizing of distributed generation in an active distribution network with several soft open points," *Energies*, vol. 14, no. 4, 2021. [Online]. Available: https://www.mdpi.com/1996-1073/14/4/1084

[142] S. Karki, M. Kulkarni, M. D. Mann, and H. Salehfar, "Efficiency improvements through combined heat and power for on-site distributed generation technologies," *Cogeneration and distributed generation journal*, vol. 22, no. 3, pp. 19–34, 2007.

[143] M. A. Hossain, H. R. Pota, W. Issa, and M. J. Hossain, "Overview of ac microgrid controls with inverter-interfaced generations," *Energies*, vol. 10, no. 9, 2017. [Online]. Available: https://www.mdpi.com/1996-1073/10/9/1300

[144] X. Xu, X. Jin, H. Jia, X. Yu, and K. Li, "Hierarchical management for integrated community energy systems," *Applied Energy*, vol. 160, pp. 231–243, 2015.

[145] X. Tang, B. Fox, and K. Li, "Reserve from wind power potential in system economic loading," *IET Renewable Power Generation*, vol. 8, no. 5, pp. 558–568, 2014.

[146] Y. Li, B. Feng, G. Li, J. Qi, D. Zhao, and Y. Mu, "Optimal distributed generation planning in active distribution networks considering integration of energy storage," *Applied energy*, vol. 210, pp. 1073–1081, 2018.

[147] W. L. Theo, J. S. Lim, W. S. Ho, H. Hashim, and C. T. Lee, "Review of distributed generation (dg) system planning and optimisation techniques: Comparison of

numerical and mathematical modelling methods," *Renewable and Sustainable Energy Reviews*, vol. 67, pp. 531–573, 2017.

[148] M. Asensio, P. Meneses de Quevedo, G. Muñoz-Delgado, and J. Contreras, "Joint distribution network and renewable energy expansion planning considering demand response and energy storage—part i: Stochastic programming model," *IEEE Transactions on Smart Grid*, vol. 9, no. 2, pp. 655–666, 2018.

[149] E. Gil, I. Aravena, and R. Cárdenas, "Generation capacity expansion planning under hydro uncertainty using stochastic mixed integer programming and scenario reduction," *IEEE Transactions on Power Systems*, vol. 30, no. 4, pp. 1838–1847, 2014.

[150] C. Zhang, Y. Xu, and Z. Y. Dong, "Probability-weighted robust optimization for distributed generation planning in microgrids," *IEEE Transactions on Power Systems*, vol. 33, no. 6, pp. 7042–7051, 2018.

[151] Z. Wang, B. Chen, J. Wang, J. Kim, and M. M. Begovic, "Robust optimization based optimal dg placement in microgrids," *IEEE Transactions on Smart Grid*, vol. 5, no. 5, pp. 2173–2182, 2014.

[152] B. Jeddi, V. Vahidinasab, P. Ramezanpour, J. Aghaei, M. Shafie-khah, and J. P. Catalão, "Robust optimization framework for dynamic distributed energy resources planning in distribution networks," *International Journal of Electrical Power & Energy Systems*, vol. 110, pp. 419–433, 2019.

[153] "New world's largest wind turbine as offshore wind scale-up continues." [Online]. Available: https://www.maritime-executive.com/article/new-world-s-largest-wind-turbine-as-offshore-wind-scale-up-continues

[154] G. Notton, V. Lazarov, and L. Stoyanov, "Optimal sizing of a grid-connected pv system for various pv module technologies and inclinations, inverter efficiency characteristics and locations," *Renewable Energy*, vol. 35, no. 2, pp. 541–554, 2010.

[155] P. Breeze, *Gas-Turbine power generation*. Academic Press, 2016.

[156] Y. Atwa, E. El-Saadany, M. Salama, and R. Seethapathy, "Optimal renewable resources mix for distribution system energy loss minimization," *IEEE Transactions on Power Systems*, vol. 25, no. 1, pp. 360–370, 2009.

[157] K. Zou, A. P. Agalgaonkar, K. M. Muttaqi, and S. Perera, "Distribution system planning with incorporating dg reactive capability and system uncertainties," *IEEE Transactions on Sustainable Energy*, vol. 3, no. 1, pp. 112–123, 2011.

[158] D. M. Blei, M. I. Jordan *et al.*, "Variational inference for dirichlet process mixtures," *Bayesian analysis*, vol. 1, no. 1, pp. 121–143, 2006.

[159] K. P. Murphy, "Conjugate bayesian analysis of the gaussian distribution," *def*, vol. 1, no. $2\sigma 2$, p. 16, 2007.

[160] D. Bertsimas, E. Litvinov, X. A. Sun, J. Zhao, and T. Zheng, "Adaptive robust optimization for the security constrained unit commitment problem," *IEEE transactions on power systems*, vol. 28, no. 1, pp. 52–63, 2012.

[161] A. Lorca and X. A. Sun, "Adaptive robust optimization with dynamic uncertainty sets for multi-period economic dispatch under significant wind," *IEEE Transactions on Power Systems*, vol. 30, no. 4, pp. 1702–1713, 2014.

[162] T. Ding, S. Liu, W. Yuan, Z. Bie, and B. Zeng, "A two-stage robust reactive power optimization considering uncertain wind power integration in active distribution networks," *IEEE Transactions on Sustainable Energy*, vol. 7, no. 1, pp. 301–311, 2015.

[163] B. Zeng and L. Zhao, "Solving two-stage robust optimization problems using a column-and-constraint generation method," *Operations Research Letters*, vol. 41, no. 5, pp. 457–461, 2013.

[164] M. E. Baran and F. F. Wu, "Network reconfiguration in distribution systems for loss reduction and load balancing," *IEEE Power Engineering Review*, vol. 9, no. 4, pp. 101–102, 1989.

[165] M. J. Brooks, S. Du Clou, W. L. Van Niekerk, P. Gauché, C. Leonard, M. J. Mouzouris, R. Meyer, N. Van der Westhuizen, E. E. Van Dyk, and F. J. Vorster, "Sauran: A new resource for solar radiometric data in southern africa," *Journal of energy in Southern Africa*, vol. 26, no. 1, pp. 2–10, 2015.

[166] P. E. Labis, R. G. Visande, R. C. Pallugna, and N. D. Caliao, "The contribution of renewable distributed generation in mitigating carbon dioxide emissions," *Renewable and Sustainable Energy Reviews*, vol. 15, no. 9, pp. 4891–4896, 2011.

[167] Z. Abdmouleh, A. Gastli, L. Ben-Brahim, M. Haouari, and N. A. Al-Emadi, "Review of optimization techniques applied for the integration of distributed generation from renewable energy sources," *Renewable Energy*, vol. 113, pp. 266–280, 2017.

[168] A. Parida, S. Choudhury, and D. Chatterjee, "Optimized solar pv based distributed generation system suitable for cost-effective energy supply," in *2020 IEEE 9th Power India International Conference (PIICON)*. IEEE, 2020, pp. 1–6.

[169] J. Jaeger, "Explaining the exponential growth of renewable energy."

[170] P. T. Manditereza and R. Bansal, "Renewable distributed generation: The hidden challenges–a review from the protection perspective," *Renewable and Sustainable Energy Reviews*, vol. 58, pp. 1457–1465, 2016.

[171] M. Bajaj, A. K. Singh, M. Alowaidi, N. K. Sharma, S. K. Sharma, and S. Mishra, "Power quality assessment of distorted distribution networks incorporating renewable distributed generation systems based on the analytic hierarchy process," *IEEE Access*, vol. 8, pp. 145 713–145 737, 2020.

[172] J. Dong, Y. Wang, X. Dou, Z. Chen, Y. Zhang, and Y. Liu, "Research on decision optimization model of microgrid participating in spot market transaction," *Sustainability*, vol. 13, no. 12, p. 6577, 2021.

[173] H. Ding, P. Pinson, Z. Hu, and Y. Song, "Optimal offering and operating strategies for wind-storage systems with linear decision rules," *IEEE Transactions on Power Systems*, vol. 31, no. 6, pp. 4755–4764, 2016.

[174] Elia Group, "Grid data overview." [Online]. Available: https://www.elia.be/en/grid-data

[175] Nord Pool, "Market data," Nov. 1, 2021 [Online]. [Online]. Available: https://www.nordpoolgroup.com/Market-data1/#/nordic/table

[176] Y. Zheng, Z. Y. Dong, F. J. Luo, K. Meng, J. Qiu, and K. P. Wong, "Optimal allocation of energy storage system for risk mitigation of discos with high renewable penetrations," *IEEE Transactions on Power Systems*, vol. 29, no. 1, pp. 212–220, 2013.

[177] NationalGrid ESO, "Fast reserve." [Online]. Available: https://www.nationalgrideso.com/industry-information/balancing-services/reserve-services/fast-reserve

[178] R. D. Rappaport and J. Miles, "Cloud energy storage for grid scale applications in the uk," *Energy Policy*, vol. 109, pp. 609–622, 2017.

[179] N. Hansen, S. D. Müller, and P. Koumoutsakos, "Reducing the time complexity of the derandomized evolution strategy with covariance matrix adaptation (cma-es)," *Evolutionary Computation*, vol. 11, no. 1, pp. 1–18, March 2003.

[180] R. Biedrzycki, "A version of ipop-cma-es algorithm with midpoint for cec 2017 single objective bound constrained problems," in *2017 IEEE Congress on Evolutionary Computation (CEC)*, June 2017, pp. 1489–1494.

[181] A. Auger and N. Hansen, "A restart cma evolution strategy with increasing population size," in *2005 IEEE Congress on Evolutionary Computation*, vol. 2, Sep. 2005, pp. 1769–1776.

[182] U. Eminoglu and M. H. Hocaoglu, "Distribution systems forward/backward sweep-based power flow algorithms: a review and comparison study," *Electric Power Components and Systems*, vol. 37, no. 1, pp. 91–110, 2008.

[183] Elexon, "Imbalance Pricing," Accessed Oct. 18, 2021 [Online]. [Online]. Available: https://www.elexon.co.uk/operations-settlement/balancing-and-settlement/imbalance-pricing/

[184] K. Mongird, V. Viswanathan, P. Balducci, J. Alam, V. Fotedar, V. Koritarov, and B. Hadjerioua, "An evaluation of energy storage cost and performance characteristics," *Energies*, vol. 13, no. 13, p. 3307, 2020.

[185] M. Panteli and P. Mancarella, "The grid: Stronger, bigger, smarter?: Presenting a conceptual framework of power system resilience," *IEEE Power and Energy Magazine*, vol. 13, no. 3, pp. 58–66, 2015.

[186] N. Bhusal, M. Abdelmalak, M. Kamruzzaman, and M. Benidris, "Power system resilience: Current practices, challenges, and future directions," *IEEE Access*, vol. 8, pp. 18 064–18 086, 2020.

[187] F. H. Jufri, V. Widiputra, and J. Jung, "State-of-the-art review on power grid resilience to extreme weather events: Definitions, frameworks, quantitative assessment methodologies, and enhancement strategies," *Applied energy*, vol. 239, pp. 1049–1065, 2019.

[188] J. M. Bloemink and T. C. Green, "Increasing distributed generation penetration using soft normally-open points," in *IEEE PES General Meeting*. IEEE, 2010, pp. 1–8.

[189] W. Cao, J. Wu, N. Jenkins, C. Wang, and T. Green, "Operating principle of soft open points for electrical distribution network operation," *Applied Energy*, vol. 164, pp. 245 – 257, 2016.

[190] X. Chen, W. Wu, and B. Zhang, "Robust restoration method for active distribution networks," *IEEE Transactions on Power Systems*, vol. 31, no. 5, pp. 4005–4015, 2016.

[191] H. Saboori and S. Jadid, "Mobile and self-powered battery energy storage system in distribution networks–modeling, operation optimization, and comparison with stationary counterpart," *Journal of Energy Storage*, vol. 42, p. 103068, 2021. [Online]. Available: https://www.sciencedirect.com/science/article/pii/S2352152X21007763

[192] R. Ebadi, A. S. Yazdankhah, R. Kazemzadeh, and B. Mohammadi-Ivatloo, "Techno-economic evaluation of transportable battery energy storage in robust day-ahead scheduling of integrated power and railway transportation networks," *International Journal of Electrical Power & Energy Systems*, vol. 126, p. 106606, 2021.

[193] H. Saboori and S. Jadid, "Mobile and self-powered battery energy storage system in distribution networks–modeling, operation optimization, and comparison with stationary counterpart," *Journal of Energy Storage*, vol. 42, p. 103068, 2021.

[194] H.-P. Schwefel, *Numerische Optimierung von Computer-Modellen mittels der Evolutionsstrategie: mit einer vergleichenden Einführung in die Hill-Climbing-und Zufallsstrategie*. Springer, 1977, vol. 1.

[195] N. Hansen, "The cma evolution strategy: A tutorial," *arXiv preprint arXiv:1604.00772*, 2016.